Alma Mater Studiorum - Università di Bologna

DOTTORATO DI RICERCA IN

AUTOMOTIVE PER UNA MOBILITÀ INTELLIGENTE

Ciclo 36

Settore Concorsuale: 09/C1 - MACCHINE E SISTEMI PER L'ENERGIA E L'AMBIENTE

Settore Scientifico Disciplinare: ING-IND/08 - MACCHINE A FLUIDO

TWO STROKE CYCLE, NOVEL COMBUSTION CONCEPTS AND
ELECTRIFICATION FOR A NEW GENERATION OF INTERNAL COMBUSTION
ENGINES

Presentata da: Stefano Caprioli

Coordinatore Dottorato

Nicolò Cavina

Supervisore

Carlo Alberto Rinaldini

Co-supervisore

Enrico Mattarelli

Esame finale anno 2024

Table of Contents

List of Figures

List of tables

Abstract

Decarbonization and overall efficiency are two of the keywords for internal combustion engines development. Among the others, mobility sector is facing the need to improve energy conversion reducing the pollution. A portfolio of innovative technologies, tailored on the specific characteristics of each field of application, appears as the best way to get the climate neutrality of the transport sector in the short and medium term. The path of electrification of the whole mobility sector is still long and not really sustainable. Internal Combustion Engines (ICE) can still play a very important role, but it is necessary to implement innovative solutions and a mixing of technologies.

The aim of this research project is to study and analyse possible solutions to improve ICE efficiency reducing pollutant emissions, with respect of some conventional and already existing engines. More specifically Low Temperature Combustion (LTC) are taken into consideration as alternative combustion process such as Dual fuel combustion with diesel and natural gas or biogas. It is evaluated the addition of hydrogen and also the use of hydrogen as a fuel itself. 2-Stroke engines are compared to 4-Stroke layouts both with classic and hybrid configuration.

Low Temperature Combustion such as Dual fuel and Reactivity Controlled Compression Ignition (RCCI) combustion are effective in reducing emissions like Nitrogen oxides (NOx) or Soot as well as Carbon Dioxide (CO_2). Some possibilities are here tested like Dual fuel Diesel-Natural Gas with hydrogen addition up to 30%, able to reduce emissions and also increase combustion efficiency especially if compared to an experimentally tested engine at low load. RCCI Diesel-Gasoline engine is a promising solution both in a 4-Stroke and in a 2-Stroke engine, able to increase Brake Thermal Efficiency (BTE) in comparison to a standard diesel engine reducing specific NOx emissions.

Different 2-Stroke engine design configurations are analysed and compared to more common 4-Stroke solutions. Loop and uniflow scavenging system for both aircraft and vehicle application are optimised by means of CFD 1D and 3D, enhancing the importance of the high specific power output but also addressing some challenges in injection process to avoid short circuit through the exhaust. Some of the investigated 2-stroke engine configurations are then analysed as a part of a hybrid power unit.

Moreover, piston bowl shape for a Diesel engine converted to run in Dual fuel mode with Diesel-Biogas 65% is optimised to reduce NOx emissions and increase Brake Thermal Efficiency for both full and partial load.

Finally, unconventional and innovative 2-Stroke architectures are also analysed together with ultra-lean hydrogen combustion: reverse loop scavenged with valves for high performance car, opposed piston engine for electric generation and small loop scavenged engine for scooter application.

Acronyms

2S	2-Stroke
4S	4-Stroke
AFR	Air-Fuel Ratio
AVL GH14D	Cylinder Pressure Sensor
BDC	Bottom Dead Centre
BEV	Battery electric vehicle
BMEP	Brake Mean Effective Pressure
BSFC	Brake Specific Fuel Consumption
BTE	Brake Thermal Efficiency
CAD	Crank Angle Degrees
CE	Charging Efficiency
CFD	Computational Fluid Dynamics
CI	Compression Ignition
CNG	Compressed Natural Gas
CO	Carbon Oxide
CO2	Carbon Dioxide
DF	Dual Fuel
DR	Delivery ratio
EGR	Exhaust Gas Recirculation
EM	Electric Motor
ETAS LA4	Lambda Sensor
EVO	Exhaust Valve Overlap
FC	Fuel Cells
FMEP	Friction Mean Effective Pressure
GHG	Green House Gas
H2	Hydrogen
H2 DI	Hydrogen Direct Injection
HD	Heavy duty
HEV	Hybrid electric vehicle
HPDI	High-Pressure Direct Injection
ICE	Internal Combustion Engine
IMEP	Indicated Mean Effective Pressure
LPDI	Low-Pressure Direct Injection
LPSDI	Low-Pressure Scavenged Direct Injection
LTC	Low Temperature Combustion
NG	Natural Gas
NGI2	Bosch Natural Gas Injector
NOx	Nitrogen Oxides
OP	Opposed-Piston
PD	Perfect Displacement
PM	Perfect Mixing
PMA P30	Fuel Pressure Sensor

PMEP	Pumping Mean Effective Pressure
RCCI	Reactivity Controlled Compression Ignition
SE	Scavenging efficiency
SI	Spark Ignition
SOI	Start of Injection
STD	Standard Configuration
TE	Trapping Efficiency
UHC	Unburned hydrocarbon
WFR	Water-Fuel Ratio

1 Introduction

With escalating environmental challenges and growing energy demands, internal combustion engines have come under scrutiny for their significant contributions to air pollution and Green House Gas (GHG) emissions [1]. As engines continue to play a pivotal role in various sectors, it becomes imperative to seek innovative solutions that not only reduce their environmental impact but also improve their overall efficiency. It is imperative to investigate and explore the potential of cutting-edge technologies, including dual-fuel combustion, low-temperature combustion, hydrogen utilization, hybridization, and the modernization of 2-stroke cycle engines, to address these pressing concerns.

So far, human activities are responsible of an average global warming of about 1.0 ◦C, compared to the pre-industrial era [2]. In 2016, the road transport sector was responsible of about 12% of the global CO2 equivalent emissions. In order to mitigate its impact, many different paths have already been followed:

- Improvement of Internal Combustion Engine brake thermal efficiency: higher compression ratios, reduced pumping and frictions losses, waste heat recovery, innovative combustion concepts;
- Use of ultra-low-carbon print fuels: bio-fuels, e-fuels;
- Use of green hydrogen, pure or blended with other fuels in ICEs;
- Use of green hydrogen in fuel cells;
- Hybrid Electric Vehicles (HEV);
- Battery Electric Vehicles (BEV).

Every single technology is promising, but it is hard to believe that a unique solution may sweep away the others. As an example, Battery Electric Vehicles (BEVs) may strongly reduce GHG emissions from city traffic, especially when most of the electric energy comes from renewable sources and in presence of a widespread charging net. However, the same solution becomes highly questionable when these conditions are missing, or when the issues related to battery production and disposal are not adequately addressed. Moreover, the advantages of BEVs tend to vanish as the travel range and the installed power increase, such as in trucks, boats, aircraft, [3]

Therefore, the most likely scenario in the energy sector is the concomitance of different technologies, where the ICE can still play an important role, as both a stand-alone mover and in hybrid electric powertrains [4].

Diesel engines can still be a key, since they are characterized by higher Brake Thermal Efficiency compared to Spark Ignition (SI) engines, thus providing lower CO2 emissions. Furthermore, diesel engines show considerably lower carbon monoxide (CO) and Unburnt Hydrocarbons (UHC) emissions. The main technical drawback that affects diesel engines is represented by NOx and Soot emissions, which impose cumbersome and expensive after-treatment systems.

A way for reducing NOx and PM emissions of diesel engines without compromising BTE is represented by the Low Temperature Combustion (LTC) concepts [5]. Among them, Dual Fuel (DF) with Reactivity Controlled Compression Ignition (RCCI) has been analyzed for a wide variety of fuel combinations. Generally speaking, DF-RCCI combustion requires a high reactivity fuel, directly injected into the combustion chamber, for example diesel, in combination with a low reactivity fuel, typically injected into the intake ports in order to obtain a lean premixed charge within the cylinder. The most popular low reactivity fuels are: gasoline[6], methane or natural gas[7], ethanol, methanol, biogas with or without the addition of hydrogen [8]. The high reactivity fuel can be diesel, biodiesel, kerosene, DME.

The flexible nature of DF-RCCI combustion systems offers many potential benefits in terms of pollutant emissions and CO2 reduction and mitigation of fossil fuel dependence, minimizing. the formation of soot, and also increasing BTE, in comparison to conventional Spark Ignited and Diesel engines [9–13].

However, the researchers still have to address some issues, in particular the poor combustion efficiency that characterizes DF operation at low loads. In these operating conditions, the premixed NG-air mixture is too lean to guarantee the propagation of a stable and self-sustaining flame front, determining high CO and UHC emissions and low BTE, as observed by some authors [14,15]

In this thesis, the dual fuel combustion subject is divided into 3 main sections:

- full load: RCCI Diesel-Gasoline 4-stroke engine experimentally tested and then compared with a 2S solution;
- partial load: piston bowl shape optimization together with the injection strategy to reduce emissions of a dual fuel diesel-biogas engine
- low load: improvement of combustion stability and efficiency of a dual fuel diesel-natural gas engine experimentally tested by adding hydrogen up to 30%

The use of hydrogen as a fuel in ICEs has gained importance due to its potential to significantly reduce all types of emissions. Hydrogen ICEs theoretically produce only water vapor, even if real engines are also affected by the emission of NOx and Particulate Matter (PM), the last one deriving from the lubrication oil.

Due to the low availability of Hydrogen, the use of blends with CNG has been explored for both passenger cars and Heavy Duty (HD) engines: simulations and experimental tests have been conducted by several authors by adding a volumetric fraction of hydrogen up to 30%[16–18]. The main results of the substitution of CNG with H2-CNG mixtures are:

- BTE improvement and CO2 emissions reduction;
- lower cycle-by-cycle variability at low loads in stoichiometric conditions;
- extension of the high Air-to-Fuel ratio (AFR) limit of lean combustions;
- as the H2 content increases, CO and UHC emissions tend to decrease while NOx emissions rise.

The European Green Deal [19] for the decarbonization of transport strongly supports the use of green hydrogen, that is produced without generating CO2 emission. Hydrogen is conceived as an energy vector, able to store in a very efficient way the energy produced by renewable sources, when such energy is not immediately required by the electric power net. [20].

Using hydrogen as a stand-alone fuel can be very attractive for Spark Ignition (SI) 4-stroke engines, due to its high resistance to auto-ignition and knocking [21]. However it presents a wide number of challenges such as the reduction of volumetric efficiency, due to the bigger dimension of the H2 molecule, estimated to be up to 30% [22] when port injected. If it is injected directly in the combustion chamber the design of the cylinder head becomes more difficult and a proper mixing time has to be ensured.

Regarding the laminar flame speed of H2, it is almost an order of magnitude higher than gasoline: an experimental study shows that it is very hard to operate with equivalence ratio values higher than 0.5, without running into serious detonation issues[23].

One of the best compromises in terms of BTE and NOx emissions is found when lambda value is around 2.5-2.9. In this ultra-lean combustion NOx emissions drop to almost zero ad the BTE values may exceed 35%. Unfortunately, performances are strongly reduced and it is almost mandatory the use of a big turbocharger to provide the right amount of air [24,25].

An interesting option for the development of H2 engines is represented by the 2-stroke (2S) cycle: the double frequency, associated to a specific design of the combustion system, permits to recover power, without increasing pollutant emissions. Obviously, lost oil lubrication is not a practical proposition, due to the negative impact on soot emissions: therefore, 2S-H2 engines must adopt a lubrication system similar to 4-strokes, with the ensuing necessity of an external supercharger in order to pump the fresh charge into the cylinder.

2S engines are already widely used on large bore engines, adopting uniflow scavenging with inlet ports controlled by the piston and exhaust poppet valves, or on very small engines, with loop scavenging, without valves. In both cases, the application of the concept to a medium size engine is not so straightforward

Other less conventional solutions are represented by cylinders with loop scavenging provided by poppet valves for both intake and exhaust, or by the opposed piston design, where a piston controls the inlet ports, while the other controls the exhaust. The loop scavenging with poppet valves strongly simplifies the development of a prototype, due to its resemblance to a 4-stroke engine. Conversely, the opposed piston layout is very efficient in terms of scavenging, but it presents challenges in the design of the combustion chamber and of the piston-cylinder assembly.

Generally speaking, the main issue to be addressed when developing a 2S-H2 engine is the optimization of the scavenge process and the promotion of air-fuel mixing: air and fuel short-circuit must be limited as much as possible, while the exhaust gas should be completely swept away from the cylinder. The use of Hydrogen makes particularly dangerous the back flow of fuel in the inlet manifold, due to the risk of backfire.

In this thesis, some different 2-Stroke architectures are analyzed, assessing pros and cons, considering specific parameters for the characterization of the scavenge process. All the discussed paths are explored deeply.

Another topic discussed in this thesis is the hybridization of ICEs with electric motors. For a road vehicle, the synergy between these power sources improves drivability, enables energy recovery during vehicle braking, permitting higher fuel efficiency and lower emissions, in particular during urban driving conditions. Hybrid power units are interesting also for aircraft application, because they can deliver more power during take-off or in any emergency maneuver, enabling the installation of a more compact and efficient ICE (downsizing). Moreover, if a parallel layout is used, there is also the possibility to drive in full electric mode. A full section of the thesis is focused on this topic, presenting the optimization of 2-Stroke engines for aircraft application.

Finally, a section is dedicated to unconventional 2-stroke engine solutions. A reverse loop with poppet valves for both intake ad exhaust, designed to run on hydrogen and meet high performances and near zero NOx emissions is considered. A comprehensive comparison among different layouts is presented in term of performances, BTE and emissions. A 4-stroke H2 engine prototype is taken as reference for experimental measures. For electric power generation, the potential of an Opposed Piston engine fueled by hydrogen is evaluated. The engine has been optimized with the support of both 1D and 3D CFD simulations, reaching a maximum BTE of 50%. For low power applications, a numerical and experimental analysis has been carried out on a 50cc crankcase scavenged 2S engine running on H2. The optimization process is conducted in collaboration with the Technical University of Graz, owner of the experimental data, modifying the piston shape and the injector position to reduce the short-circuit through the exhaust.

2   2-Stroke engines architectures

The world of internal combustion engines seeks for a technological improvement of efficiency, power, and environmental friendliness. 2-stroke engines occupy a unique and captivating niche. Their simplicity, high power-to-weight ratios, and distinctive scavenging processes have made them a preferred choice for a wide array of applications, from small handheld tools to high-performance racing machines and even to high efficiency big-bore naval engines. Recently the interest in more eco-friendly alternatives like hydrogen-powered propulsion systems is raising together with the new technical solutions.

At the heart of the 2-stroke engine's simplicity lies its ingenious scavenging process, which is responsible for cleaning the combustion chamber from exhaust gases and replacing them with a fresh mixture of air, or air and fuel. The scavenging process is pivotal in determining an engine's efficiency, power output, and emissions characteristics.

In this section, the main 2-stroke engine architectures are presented, with a particular focus on four designs: loop scavenged, uniflow scavenged, reverse loop with poppet valves, and opposed piston engines.

2.1   Loop Scavenged

This configuration relies on the motion of the piston to create a dynamic loop of airflow within the engine, guiding exhaust gases out through the exhaust port and drawing in a fresh charge of air and fuel mixture through the intake port. The simplicity of this design has made it a popular choice for small, lightweight engines. While loop scavenged engines offer practicality and ease of maintenance, they are often associated with higher emissions and relatively lower efficiency when compared to more advanced designs.
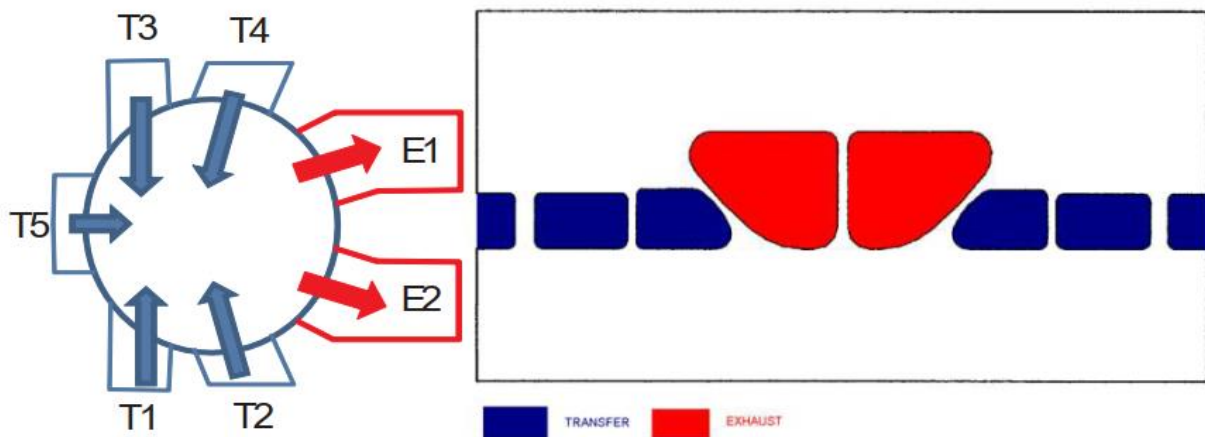
Figure 1 : Loop scavenged ports scatch [26]
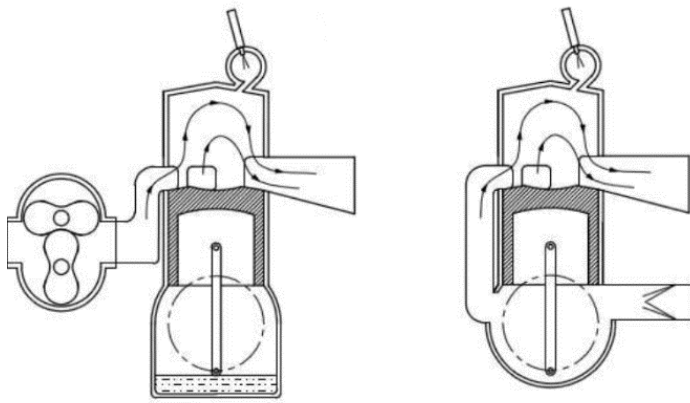
(a)   (b)

Figure 2: Loop scavenged layout, external blower(a) and crankcase pump (b)

In Figure 1 it is showed a typical port distribution for a loop scavenged made by 5 intake ports and 2 exhaust ports. The transfer ports 1-4 blow the fresh charge toward the wall opposite to the exhaust side, to reduce short-circuit. T5 is very necessary to orient upward the fresh charge, while the exhaust ports can be more freely designed, since they have to be as bigger as possible, also a single port is used. Moreover, it is important to notice the symmetry that characterize this type of engines that is also the reason for the formation of the tumble vortex.

The necessary delta-pressure between intake and exhaust can be guarantee from an external blower Figure 2(a) or by the moving piston itself in a more compact solution as depicted in Figure 2(b).

2.2   Uniflow Scavenged

In contrast to the loop scavenged approach, uniflow scavenged engines take a more refined path to scavenging excellence. These engines implement a dedicated system for exhaust and intake, ensuring that the flow of gases occurs in a continuous, one-way manner. The result is a generally improved scavenging efficiency, reduced emissions, and increased power output.
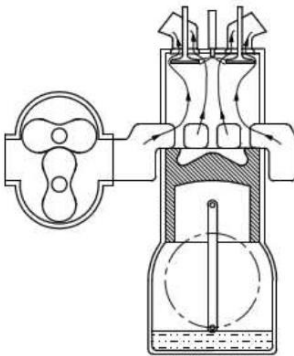
Figure 3: uniflow scavenged layout

In Figure 3 is reported a schematic view of a uniflow layout: intake ports surround the whole cylinder and their opening-closing time is controlled by the piston motion, generally they are specifically oriented to increase the swirl vortex formation. On the other side the exhaust valves are located in the cylinder head like a 4S engine. Some design guidelines can be provided:

For the exhaust valves the critical issue for permeability is the effective area. Even if the engine speed is low, the opening time correspond to 30% less than a 4S engine. For this point of view the higher is the number of the valves, the better. Not only to increase the effective area but also because they will be smaller, lighter and easier to cool down. Moreover, with more than 2 valves the injector can be located central in the head, very important for diesel injection.

Inlet ports can be strongly optimized by the use of CFD 3D simulations, regarding ports number, dimension, orientation angle and so on. Intake ports do not require an upsweep angle, since the piston skirt is already driving the flow toward the cylinder head, but the angle formed between the port axis and the radial direction is important. It is possible to increase the swirl motion, but a pocket of exhaust gas may remain in the cylinder core. In order to achieve a good scavenging efficiency in combination with low swirl, Hori [27] proposed an "alternate port" configuration, i.e. a sequence of one radial port and one swirling port, the former with an upward angle of elevation, the latter with a downward angle. In general the best trade off strongly depends on the cylinder geometry and operating conditions, since the scavenging process is guided by the pressure difference across the cylinder [26].

2.3 Reverse Loop with Poppet Valves

A fascinating departure from conventional 2-stroke engine design is the reverse loop with poppet valves configuration. This innovative approach combines elements of both 2-stroke and 4-stroke engine designs, incorporating poppet valves for both intake and exhaust. Reverse loop engines with poppet valves are particularly valuable for rapid prototyping and experimentation, as they can be directly derived from their 4-stroke counterparts with a brand-new design of the only cylinder head.
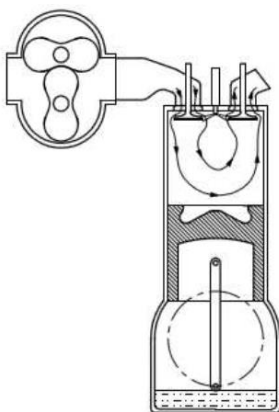
Figure 4: Reverse loop configuration
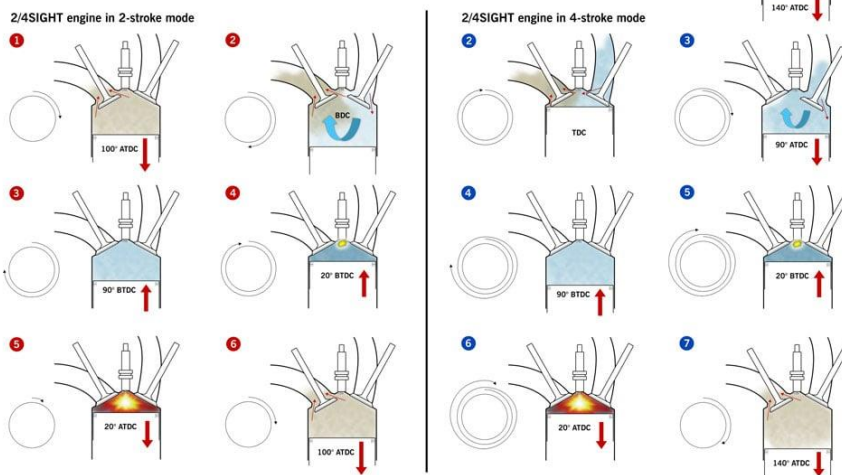
Figure 5: Ricardo 2-4 Sight concept[28]

Strong effort should be devoted to optimizing and design the valves actuation law and the intake ports shape.

The more is possible to decouple intake and exhaust valves the more is possible to increase trapping and scavenging efficiency reducing fresh air short-circuit. In Figure 4 is reported a possible reverse loop solution with external supercharger, while in Figure 5 is reported the 2-4 Sight concept developed by Ricardo [28] where is enhanced the quasi-vertical configuration of the intake duct. The air entering the cylinder is oriented toward the cylinder liner reducing the mixing with the exhaust gasses.

2.4 Opposed Pistons

Lastly, a design revered for its scavenging efficiency and power potential is the uniflow scavenged with opposed pistons. In this configuration, two pistons move toward each other within a single combustion chamber, effectively squeezing out exhaust gases and drawing in fresh air-fuel mixture Figure 6. The opposed piston layout poses challenges in terms of combustion chamber design, but the benefits in terms of scavenging efficiency and power output have made it known as the best configuration in the 2S engines. These engines are often found in high-performance scenarios, such as military vehicles and aerospace propulsion systems, where maximizing power and efficiency is paramount.
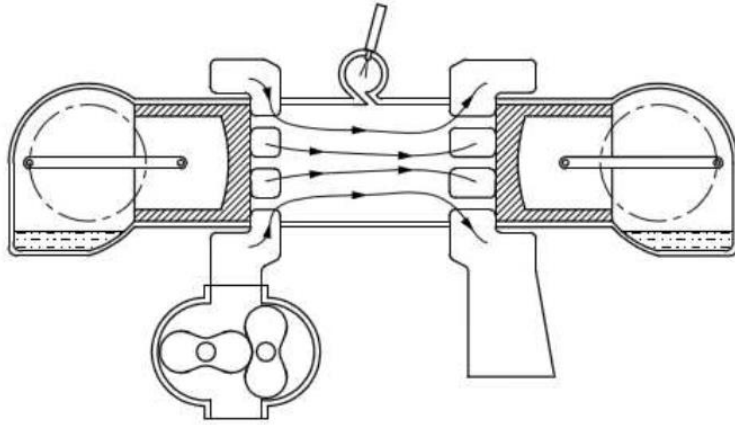
Figure 6: Opposed Piston configuration

Since intake and exhaust ports are far one from the other, the amount of fresh air that exits from the exhaust can be strongly reduced. Intake ports are similar to the Uniflow scavenged ones while for the exhaust ports is more important to have as much space as possible since it is mainly turbulent flow.

While the diverse landscape of 2-stroke engine architectures presents a wealth of advantages, it is not without its challenges. Issues such as scavenging efficiency, fuel short-circuiting, and pressure differentials between intake and exhaust require innovative solutions to optimize performance and meet stringent emissions standards. Moreover, the risk of backfires, especially when utilizing hydrogen as a fuel source, necessitates the incorporation of supercharging systems to ensure safe and reliable operation.

2.5   Scavenging Model

Evaluate the engine layout effectiveness and the scavenging process, as previously said, is one of the most important challenges facing a 2-Stroke engine. Generally speaking the scavenging process follow a path in between a Perfect Mixing (PM) and a Perfect Displacement (PD) process. The PM is an ideal process in which as soon as the fresh air is entering the cylinder, it mixes with the exhaust gasses, the mass-flow rate passing through the exhaust is an homogeneous mixture of residuals and fresh air. In the PD process, on the other hand, it is supposed that the fresh air "push" away the residuals from the cylinder through the exhaust, the air can slip out from the cylinder only when no residuals are left. It is quite evident that the PD is the best possible condition but in real cases, after an initial phase, air and residuals tend to mix together. Different 2S configuration try to delay this mixing process as much as possible.

Here will be analysed the fundamental hypothesis of the two models for a loop scavenged engine as in Figure 7, but it is valid for every layout:
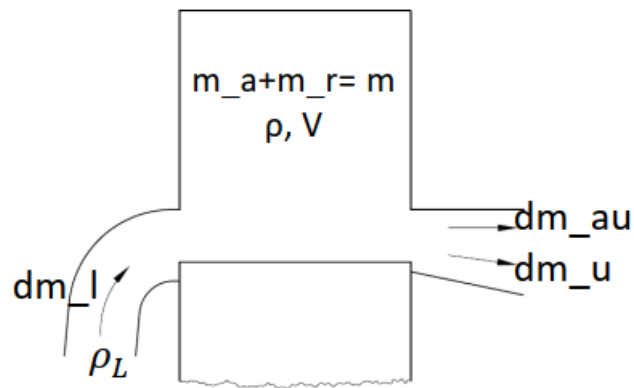
Figure 7: Scavenging model main variables

In Figure 7 are reported the main parameters used in the demonstration, where dm_l is the portion of mass entering from the intake, ρ_L is the density of the charge in the intake ports, m is the total mass inside the cylinder, composed by air (m_a) and residuals (m_r), dm_au is the infinitesimal mass of air exiting though the exhaust and dm_u is infinitesimal mass of exhaust gasses exiting though the exhaust.

2.5.1   Perfect Mixing Model

Hypothesis:

- Since the scavenging process starts before BDC and end after that, the piston is considered to be blocked at BDC, so that V is the constant cylinder volume;
- Constant pressure is considered upstream of the scavenge ports and downstream of the exhaust ports, no dynamic effects are considered;
- Constant temperature of the fresh charge that lead also to a constant fresh charge density, ρ_L;
- Average pressure upstream of the scavenge ports higher than the average pressure downstream of the exhaust port → no reverse flow;
- The volume of fresh charge entering the cylinder is equal to the volume leaving through the exhaust

$$\frac{dm_L}{\rho_L} = \frac{dm_{au}}{\rho}$$

(1. 1)

- Scavenge process starts at scavenge port opening and ends at their closure
- Perfect mixing hp: as the fresh charge enters the cylinder, it forms a perfectly homogeneous mixture with the exhaust gas

$$\frac{dm_{au}}{dm_u} = \frac{m_a}{m}$$

(1. 2)

20

$$(dm_l - dm_{au}) = dm_a$$

$$dm_{au} = dm_a * \frac{m_a}{m}$$

Combining (1.3) and (1.4):

$$dm_a = dm_l - dm_u * \frac{m_a}{m}$$

$$dm_u = \frac{\rho}{\rho_l} dm_l$$

Combining (1.5) and (1.6):

$$dm_a = dm_l \left[1 - \frac{\rho}{\rho_l} \frac{m_a}{m} \right] = dm_l \left[1 - \frac{1}{\rho_l} \frac{m_a}{V} \right]$$

Equation (1.7) is an expression that involve, for every infinitesimal moment, the delivered fresh air and the fresh air inside the cylinder. It is possible to further develop the expression to analyse this relation in the whole process:

$$dm_l = \frac{dm_a}{1 - \frac{m_a}{\rho_l V}}$$

$$\int_{TO}^{TC} dm_l = \int_{TO}^{TC} \frac{dm_a}{1 - \frac{m_a}{\rho_l V}}$$

$$M_l = -\rho_l V \log_e \left(1 - \frac{M_a}{\rho_l V} \right)$$

Where Ml is the total mass delivered and Ma is the amount of fresh charge inside the cylinder at the end of the scavenging process

$$M_a = \rho_l V \left[1 - \exp \left(-\frac{M_l}{\rho_l V} \right) \right]$$

Thanks to this definition of the perfect mixing process is it possible to define the efficiency parameters useful to define the effectiveness of a real engine.

2.5.2 Efficiency parameters

To evaluate the scavenging effectiveness in a 4 stroke engine is generally used the volumetric efficiency defined as the ratio between the air trapped into the cylinder and the ideal mass.

$$\lambda_v = \frac{m_{air,tr}}{\rho_a V_d}$$

In a 2-stroke engine this approach can be reductive since it is possible for example to have high trapping efficiency if the air delivered is very little, or it can happen to have very high ΔP across the cylinder, high delivered air flow rate and a high amount of air both in the cylinder and in the exhaust.

For this reason, 4 characteristic parameters are defined and will be used in the whole thesis:

- Delivery ratio (DR): mass delivered from the intake divided by the reference mass

$$DR = \frac{m_l}{\rho_l V_d}$$

- Trapping Efficiency (TE): mass of fresh air retained in the cylinder divided by the mass of fresh air delivered

$$TE = \frac{m_{air,tr}}{m_l}$$

- Scavenging Efficiency (SE): mass of fresh air retained in the cylinder divided by total in-cylinder mass (fresh +exhaust)

$$SE = \frac{m_{air,tr}}{m}$$

- Charging Efficiency (CE): mass of fresh charge trapped within the cylinder at a given crank angle, divided by the reference mass

$$CE = \frac{m_{air,tr}}{\rho_l V_d}$$

2.5.3 Perfect Displacement Model

The main hypothesis are the same as for the perfect mixing model, except for the last one:

Perfect displacement hp: no fresh charge lost at the exhaust until the cylinder is completely filled by fresh charge; at this condition m_l=ρ_l V

Starting from the fundamental hp the DR can be also written as:

$$DR = \frac{m_l}{\rho_l V_d} = \frac{\rho_l V}{\rho_l V_d} = \psi$$

Ψ defined in (1.13) is known as supercharging degree: a fixed number always grater than 1.

During the scavenging process, for values of the DR below Ψ, we have CE=DR and TE=1. For values of the DR above Ψ, we have CE= Ψ and TE= Ψ/DR.
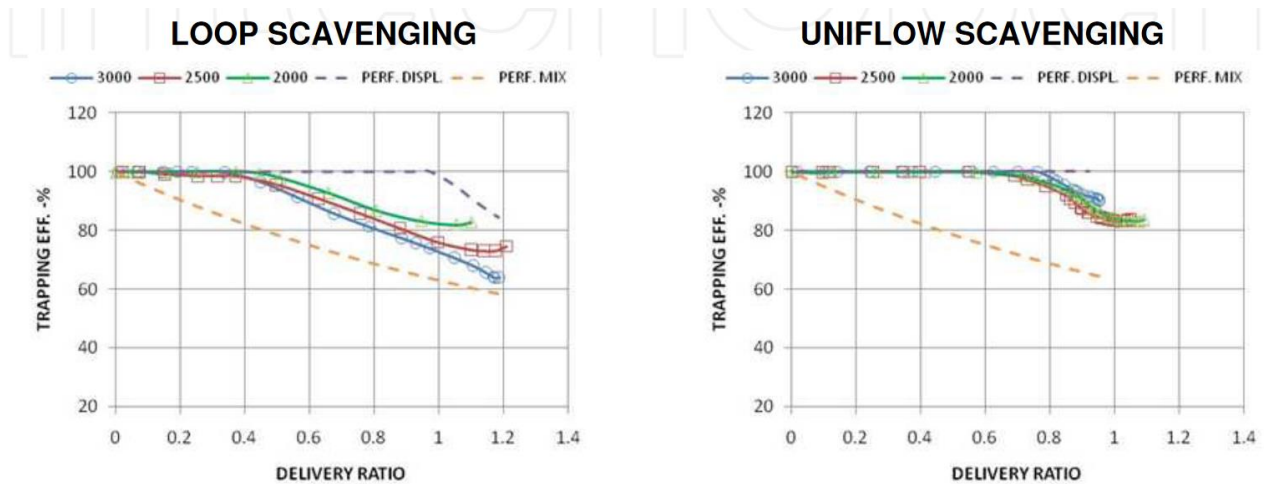
Figure 8: loop scavenging and uniflow scavenging TE comparison [27]

An interesting example of these parameters is given in Figure 8
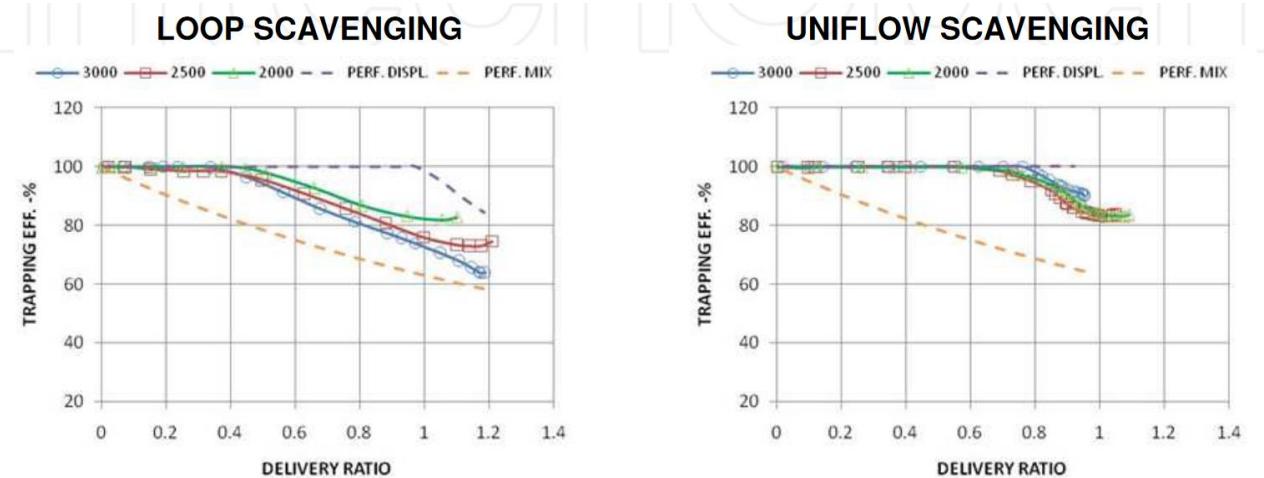
where the trapping efficiency of 3 operative points is compared between a loop scavenging and an uniflow scavenging engine of the same size [26]. It is quite evident that in the former the mixing process of fresh air and exhaust gasses started before than in the latter, at 0.5 of DR, shifting the process from an initial PD to a more realistic PM. The final trapping efficiency of this uniflow engine is therefore higher.

In order to find a simplified correlation among the average pressure drop across the cylinder (Δp) and the main engine parameters, the gas exchange process in a 2-Stroke engine can be idealized as a steady phenomenon, with the piston fixed at bottom dead centre and both inlet and exhaust ports partially open, so that the geometric area of each port corresponds to the average effective area, calculated over the cycle. As a further simplification, the flow is assumed as uncompressible.

$$DR = \frac{m_a}{\rho V_d} = \frac{\dot{m}_a}{\rho V_d n}$$

$$\dot{m}_a = \rho\, V_d\, n\, DR$$

Considering the displacement $V_d = A_p * S$ it is possible to derive the sequent:

$$\dot{m}_{eff} = A_{eff} * \sqrt{2\rho\, \Delta P} = \frac{\rho\, DR\, A_p\, u_p}{2}$$

Where $\dot{m}_{eff}$ is the average effective mass flow rate, A_{eff} is the average effective area of the all ports, ρ is the charge density, ΔP in the pressure difference across the cylinder A_p is the surface area of the piston and u_p is the mean piston speed.

It is possible to define the effective area as

$$A_{eff} = \frac{1}{\sqrt{\dfrac{1}{A_t^2} + \dfrac{1}{A_e^2}}}$$

Where A_e is the mean effective area of the exhaust ports and A_t is the mean effective area of the transfer ports.

Combining equation (1. 16) and (1. 17) the following correlation can be found:

$$\Delta P \propto \rho\, DR^2\, u_p^2 \left(\frac{A_p}{A_{eff}}\right)^2$$

Despite it is a simplified approach, some considerations can be made:

- the higher is the delivery ratio and the maximum mean piston speed, the more important is to have high values of effective area, in comparison to the piston area
- charge density plays an important role, thus supercharged engines are more demanding in terms of permeability than naturally aspirated units
- the ports average effective area can be increased both by reducing the flow losses and by increasing the opening area itself

3 CFD Software

3.1 Customized Software – Kiva 3V

Some of the CFD 3D calculations reported in this thesis are performed using a customized version of Kiva 3V code [29].

Kiva 3V is particularly useful to calculate injection and ignition in simple mesh such as diesel-like combustions.

The computational grid can be prepared with a dedicated tool named K3PREP [30]. In case of an axial-symmetric geometry of the combustion chamber, a sector corresponding to a portion of the whole combustion chamber can be used. The structured block mesh is then divided into 3 blocks corresponding to the piston bowl shape, the squish portion above the bowl and the squish portion above the flat piston, as it is reported in Figure 9. Then, for every block, every cell should be defined as a prism with its 8 vertexes and every vertex by its X,Y,Z coordinates. As an example the general methodology is reported for the definition of the bowl shape as in Figure 10:

1. define the block first corner at the down-left of a square to define the starting point
2. define the actual bowl outline as a combination of X,Z points
3. rotate the block through the selected angle to create the 3D grid
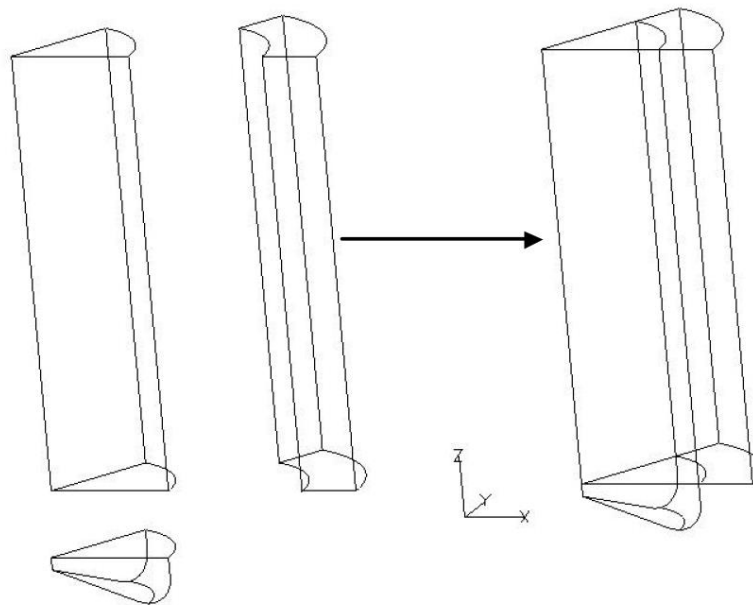
Figure 9: block mesh division of a K£PREP sector mesh
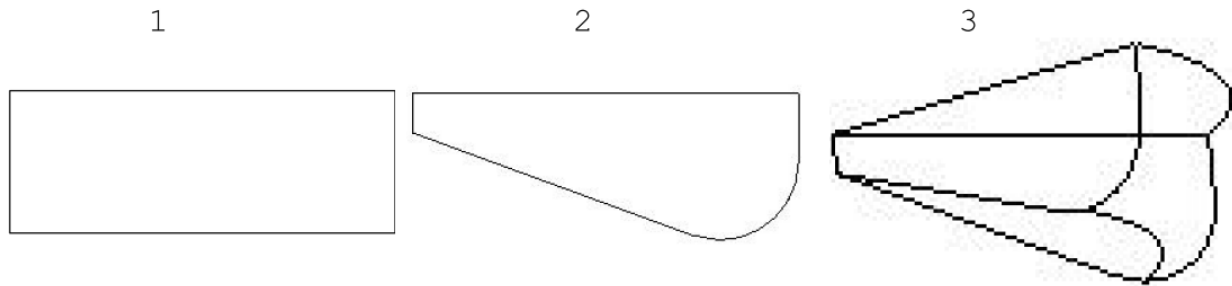
Figure 10: bowl mesh definition methodology

The customized version of the KIVA-3V code also includes the Hybrid Kelvin–Helmholtz/Rayleigh–Taylor (KH-RT) break-up model and a Droplet Collision model for the prediction of the spray evolution during injection phase [31]. The combustion process is based on detailed chemical reaction mechanism and, more specifically, for dual fuel application the model [32] is based on two sub-models: the generalised Partially Stirred Reactor (PaSR) model [33] and the Fame Propagation model [34].

The mechanism developed to simulate the DF NG-diesel combustion is made up of 81 species and 421 reactions. The validation of the chemical kinetic mechanism was carried out according to measurements of ignition delay times in shock-tube experiments and flame propagation data for constituent components of NG.

The Hybrid Kelvin–Helmholtz/Rayleigh–Taylor (KH-RT) break-up model proposed by Reitz [35–37] was implemented in the customized version of the KIVA-3V code. It includes two break-up modes. The KH and the RT modes. The Kelvin-Helmholtz instability is employed to model the breakup of a liquid jet or sheet due to velocity differences within the fluid, resulting in the formation of ligaments and eventually droplets. On the other hand, the Rayleigh-Taylor instability is utilized to describe the disintegration of a liquid column or sheet when a denser fluid is subjected to acceleration by a lighter one, as seen in spray formation under gravity or other external forces.

The Droplet collision model implemented in the customised version of KIVA-3V states that:

"Collision between two parcels occurs if their trajectories intersect and the intersection point is reached at the same time, and within the integration step" [31].

To reduce the computational cost of such a droplet collision model, two further conditions must be met:

1. parcels have a chance of colliding if they are travelling one towards the other.
2. the relative distance between parcels must be greater than their radius.

The generalised Partially stirred reactor model (PaSR) operates by breaking down the reactor or combustion chamber into a series of smaller, interconnected compartments known as Perfectly Stirred Reactors (PSRs). Each PSR represents a specific region or zone within the reactor, characterized by similar conditions of temperature, pressure, and chemical composition. Importantly, these PSRs are designed to capture different levels of mixing or stirring within the reactor.

The PaSR model considers the intricate interactions between these PSRs, accounting for the movement of reactants and products between them. This dynamic approach is crucial because combustion processes are

not uniform; instead, they involve varying degrees of mixing, heat transfer, and reaction rates across different regions of the reactor.

As far as the Flame Propagation model is concerned, the Turbulent Flame speed Closure (TFC) model proposed by Lipatnikov and Chomiak [34] was implemented in the customised version of KIVA-3V. this model is based on the PREMIX code [38] written in Fortran to calculate the laminar flame speed. This formulation is particularly suitable for dual fuel application.

First, the laminar flame speed is evaluated by means of the PREMIX code using the Natural Gas (NG) combustion mechanism consisting of 74 species that take part in 366 reactions, for values of ϕ between

0.5 and 1.5. The NG was assumed to be composed by a blend of CH4 C2H6 C3H8 and C4H10.

Then, the calculated laminar flame speeds were fitted to a polynomial correlation.

For the diesel injection a Diesel Oil Surrogate (DOS) model is used: it consists in representing the liquid diesel duel through a single-component with the chemical formula corresponding to C14H28 and with a corresponding fuel vapor modelled to be a 70/30 vol% blend of n-heptane C7H16 and toluene C7H8. The calculated Cetane Number (CN) of the DOS is 47, since n-heptane is about 56 and toluene is about 9.

Since the oxidation scheme of real diesel fuel is not known the single-component fuel is assumed to decompose in the two-component fuel vapor through the following:

$$1.5\ C_{14}H_{28} + 0.5\ O_2 = 2\ C_7H_{16} + H_2O$$
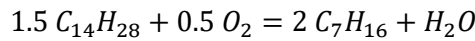
(1. 19)

The detailed chemical oxidation sub-mechanisms for n-heptane and toluene consists of 70 species taking part in 310 reactions.

The resulting oxidation mechanism of the diesel fuel model is able to adequately predict the ignition delay time of both n-heptane and toluene, as shown in Figure 11, which compares calculated ignition delay times for stoichiometric and lean n-heptane/air and toluene/air mixtures and shock-tube experimental data at high pressure conditions.
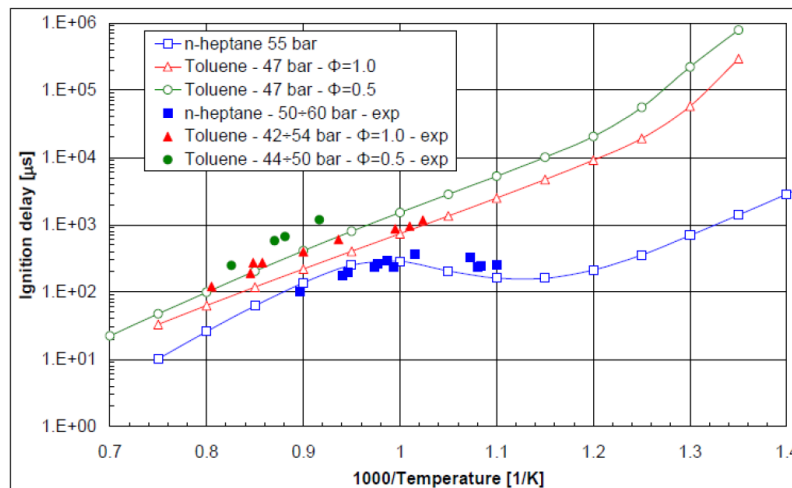
Figure 11: n-heptane and toluene ignition delay time, calculated and experimental comparison

Acenaphthylene (C12H8), referred to as A2R5, was selected as the soot precursor. Therefore, the chemical mechanism also includes the reaction path of the polycyclic rings formation that leads to A2R5, and then to soot, starting from the phenyl radical (C6H5).

In order to take into account the interaction between NO, NOx and combustion chemistry, which takes place when internal or external EGR is used, the Zeldovich reactions were added to the chemical mechanism:

$$NO + HO_2 \rightarrow NO_2 + OH$$

$$NO_2 + H \rightarrow NO + OH$$

$$NO_2 + O \rightarrow NO + O_2$$
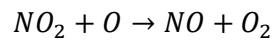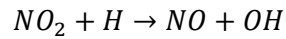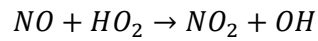
(1. 20)

3.2   Commercial Software

During my thesis, I extensively utilized GT-Power, developed by Gamma Technologies [39]. This powerful software proved to be an invaluable tool for simulating and analysing internal combustion engines and propulsion systems. Its comprehensive capabilities allowed me to model engine performances, and optimize various parameters through extensive CFD 1D models.

Another essential software was Forte, developed by Ansys [40]. Forte is specialized in detailed 3D modelling and simulation of combustion processes, particularly developed to be user-friendly and simple.

Additionally, Fire by AVL [41] is used during this thesis work. Fire is a well-regarded CFD 3D software in the field of engine and powertrain development, known for its versatility and efficiency. It enabled me to perform comprehensive simulations, assess various fuels and combustion strategies helping me developing both 4-Stroke and 2-Stroke engines.

4   LTC and Dual fuel

In the last decades, both the research community and engine manufacturers have exerted significant efforts to develop solutions aimed at inhibiting, or at the very least, mitigating the generation of NOx and soot emissions during the combustion process. Among the most promising techniques are Dual Fuel (DF) and Reactivity Controlled Compression Ignition (RCCI) combustions, given their ability to achieve ultra-low NOx emissions and exceptional Brake Thermal Efficiency (BTE). DF and RCCI combustion concepts prove especially attractive when utilizing renewable sources or fuels with low carbon content.

Natural Gas (NG) also stands out as an excellent low reactivity fuel, boasting several key advantages:

- It primarily consists of methane (CH_4), which possesses the highest hydrogen-to-carbon ratio among hydrocarbons, resulting in minimal Carbon Dioxide (CO_2) emissions.
- It can be readily substituted with bio-methane.
- Its Octane Number (ON) exceeds that of gasoline and alcohols, rendering it more suitable for operation with high compression ratios.
- It exhibits superior air mixing capabilities compared to liquids and is non-corrosive in nature.

Numerous authors have conducted investigations that demonstrate the favorable effects of employing NG in DF operations, particularly in terms of reducing NOx and soot emissions while enhancing BTE [42–44].

As previously stated, the addition of hydrogen in the NG mixture is an interesting field of analysis:

Rahnama at al. [45] conducted an investigation to assess the impact of hydrogen-enriched intake air, with the H2 volume fraction varying from 0% to 5%, in the context of a Heavy Duty (HD) Dual Fuel (DF) Natural Gas (NG)-diesel engine. Their findings at low loads revealed a significant reduction in specific CO emissions, with a reduction of approximately one order of magnitude, as well as in UHC emissions. Furthermore, with the increase in hydrogen content, both combustion efficiency and Gross Indicated Thermal Efficiency (GITE) exhibited substantial improvements, with GITE leaping from approximately 18.5% to about 50%.

A deeper comprehension of the DF H2-NG-diesel combustion process is provided by the work of Liu et al., [46] who conducted a study on the impact of hydrogen (H2) addition on combustion characteristics in an optically accessible single-cylinder engine, divided the combustion process into five phases. They demonstrated that H2 exhibits more pronounced effects during the early stages of combustion. The higher combustion speed and temperature of H2 itself contribute to the evaporation and ignition of other fuels.

Additionally, dual fuel combustion is highly suitable for the utilization of agricultural fuels, such as Biogas. As indicated in Table 1, the composition of biogas can vary significantly, contingent on the production process and materials used. An especially crucial aspect of biogas composition is the quantity of CO_2 present, which directly influences the laminar flame speed. [47]. A large fraction of CO_2 can greatly reduce it, making it difficult to obtain regular combustion in spark ignition (SI) engines. The development of a clean and efficient combustion system for a DF engine is typically based on the optimization of the composition of the premixed charge (air, BG and burnt gas) and the calibration of the injection strategy [48,49].

Table 1: Biogas general composition

Constituent	Range
Methane (CH_4) [vol%]	30–73
Carbon dioxide (CO_2) [vol%]	20–40
Nitrogen (N_2) [vol%]	5–40
Hydrogen (H_2) [vol%]	1–3
Oxygen (O_2) [vol%]	0–5
Physical Property	
Density [kg/m^3]	0.65–0.91
Octane number [-]	130
Auto-ignition temperature [°C]	632–813
Lower heating value [MJ/Nm^3]	10–25

A study on a RCCI engine fueled by diesel and NG demonstrates that as the engine load increases from low to medium, the control of RCCI combustion becomes more and more difficult [50]: the cylinder pressure tends to rise abruptly, generating high peaks and gradients, which increases the combustion noise and the risk of mechanical failures. Therefore, to operate at high load is convenient to adopt a high amount of EGR or reduce the compression ratio of the engine [51].

Other studies on RCCI combustion were focused on the different fuels that can be coupled to diesel fuel, such as DME/CH4 [52], methanol [53] and gasoline [54]. These studies demonstrated that the optimization of the diesel injection strategy is the key to decrease NOx and HC emissions over a wide range of DF configurations and operating conditions.

Nevertheless, regarding the design of the combustion chamber for RCCI combustion, when using methanol and gasoline as low-reactivity fuel, Dempsey et al. [55] proposed a shallow piston bowl and a flat cylinder head. For both gasoline/diesel fuel and methanol/diesel fuel operation, it was found that the modified piston yielded a 2–4% improvement in terms of the gross indicated efficiency.

Lee et al. [56] Researchers modified the combustion chamber geometry of a diesel engine to enable operation in the Dual Fuel (DF) gasoline-diesel mode. They conducted an analysis of the diesel start-of-injection (SOI) timing and its impact on spray tip penetration and ignition delay. The altered combustion chamber closely resembled the original design but was shallower, resulting in a 14% reduction in gross indicated specific fuel consumption (gISFC). Another experimental study on DF Biogas (BG)–diesel combustion was presented in[57]. This study involved a single-cylinder engine operating at low, medium, and high loads. Through the optimization of injection and ignition strategies, the researchers achieved a reduction in NOx emissions of up to 57% compared to the original diesel engine. However, it was observed that hydrocarbon (HC) emissions tended to increase. Moreover, at low loads, the lean BG–air mixture led to flame quenching.

Molina et al. [58] expanded the application of Reactivity Controlled Compression Ignition (RCCI) to high loads by reducing the compression ratio (CR). In addition, they introduced an early intake valve closing Miller cycle through the utilization of a hydraulic Variable Valve Actuation (VVA) system. The authors also adjusted the injection strategy based on the engine load. Their findings indicate that a dual diesel injection strategy is well-suited for RCCI combustion in the low (BMEP=6 bar) to medium load (BMEP=12 bar) range, while a single-shot injection strategy proves more effective for high loads (BMEP>17 bar).

Benajes et al. [59], beside reducing CR from 17.5:1 to 15.3:1, adopted a Dual-Mode Dual-Fuel (DMDF) strategy. At low loads, a highly-premixed RCCI combustion was successfully applied for decreasing emissions and improving fuel efficiency. At high loads, combustion switches to the diffusive dual-fuel mode, for complying with the mechanical constraints (limit of PPRR).

In this section, 3 different application of LTCs will be analysed. One solution is to adopt RCCI Diesel-Gasoline combustion in a 2-Stroke solution operating at high load condition and compare to a similar 4-stroke engine. For medium load on the one hand is evaluated a DF combustion with Diesel-biogas compared to an experimental diesel-NG, on the other side is optimized the combustion chamber geometry and injection strategy to increase the BTE reducing NOx emission in the diesel-biogas configuration. At very low load is evaluated the effectiveness of hydrogen addition to the NG mixture in the same engine up to 30 vol%.

4.1 RCCI Diesel-Gasoline engine: 2-Stroke VS 4-Stroke

In the current research project, the aim is to explore the application of RCCI combustion to a contemporary 2-stroke (2S) engine and make a comparative analysis with an equivalent 4-stroke (4S) RCCI engine. The study involves a comprehensive investigation conducted through experiments and computational fluid dynamics (CFD) combined with 1D simulation. The focus is on evaluating the potential of implementing the RCCI combustion concept in an automotive Diesel engine with the following specifications: 2.0 litres displacement, 4 cylinders, 4 valves per cylinder, 125 kW power output at 3500 rpm, and Euro VI compliance.

The experimental phase of the research is divided into two stages. First, a thorough characterization of the base engine (referred to as the "donor" engine) is carried out. In the second stage, modifications are made to the engine setup: three cylinders are configured to operate under standard Diesel conditions, while the fourth cylinder is specially calibrated for RCCI operation. The data obtained from these experiments is then utilized to create a GT-Power model for a complete RCCI version of the engine, where all cylinders operate in RCCI mode.

Additionally, through a combination of CFD-1D simulations and empirical assumptions, an equivalent 2-stroke RCCI engine is developed for comparison purposes. The final part of the research involves a numerical comparison between the 4-stroke and 2-stroke RCCI engines, focusing on their performance and emissions characteristics under full load conditions.

4.1.1 Experimental campaign

The experimental phase was conducted on a Euro VI 4-cylinder diesel engine, main characteristics reported in Table 2, manufactured by FCA, utilizing a steady dynamometer bench. This engine is equipped with several notable features, including a variable geometry turbine (VGT) and Charge Air Cooler (CAC) in the supercharging system, situated after the turbocharger compressor. The after-treatment components consist of a Diesel Oxidation Catalyst (DOC), a Diesel Particulate Filter (DPF), and a Selective Catalytic Reduction device (SCR). To further control emissions, two exhaust gas recirculation systems are employed: high-pressure (HP-EGR), connecting the exhaust manifold before the turbine to the intake manifold after the CAC, and low-pressure (LP-EGR), connecting the exhaust pipe after the DPF to the turbocharger compressor inlet. The intake ports incorporate a set of flaps, operated by an actuator known as the Variable Swirl Actuator (VSA), to enhance turbulence within the cylinders.

Initially, the Bosch Engine Control Unit (ECU) was replaced with an open ECU, which enabled flexible control of each cylinder, particularly important when dealing with unconventional combustion systems. This new ECU was meticulously tuned to match the performance of the original engine when operating in the conventional Diesel combustion mode, referred to as CDC.

Experimental data was gathered in CDC mode across various speeds and loads, facilitating the precise calibration of a CFD-1D engine model (GT-Power).

For the implementation of the RCCI combustion system, only one of the four cylinders was modified accordingly, while the remaining three cylinders continued to operate in CDC mode. Figure 12 (b) illustrates the new engine configuration in a "3+1" arrangement, while Figure 13 provide visual representations of the modified intake manifold and the RCCI exhaust piping.

Table 2:base engine specifications

Engine type	Diesel, 4-cylinder in-line
Homologation	Euro 6
Maximum Power	125 kW @ 3500 rpm
Maximum Torque	385 Nm @ 2000 rpm
Combustion pressure	170 bar
Bore x Stroke	83 x 90,4 mm
Connecting rod length	145 mm
Squish Height	0.72 mm
Pin Offset	0.3 mm
Displacement	1956 cc
Compression ratio	16.5:1
N° of valve per cylinder	4
Injection system	Common Rail
Inlet Valve Open	341 CA °ATDCF
Inlet Valve Close	-139 CA °ATDCF
Exhaust Valve Open	116 CA A°TDCF
Exhaust Valve Close	-340 CA °ATDCF

a)
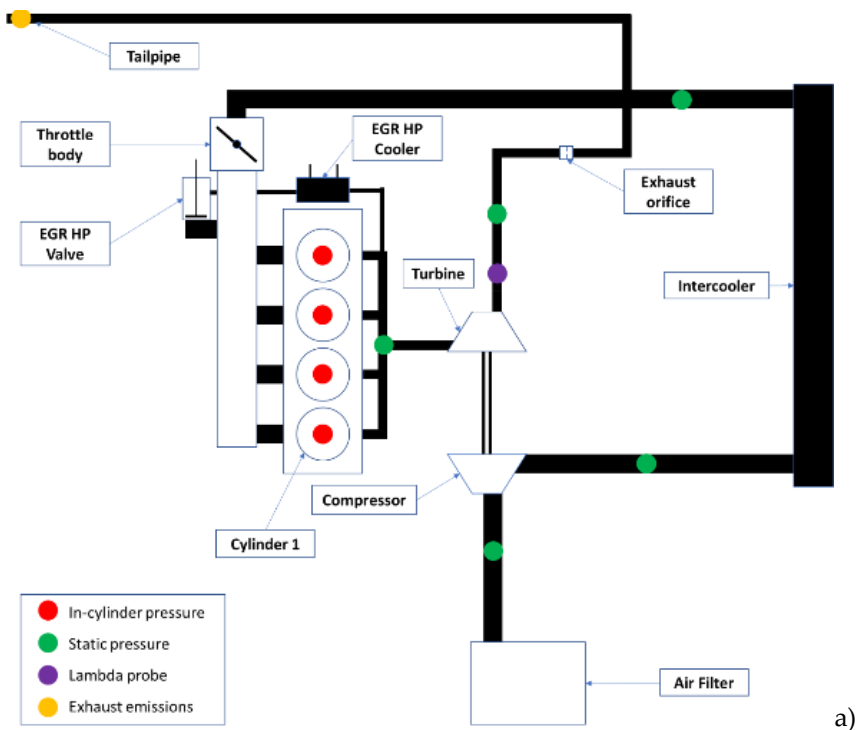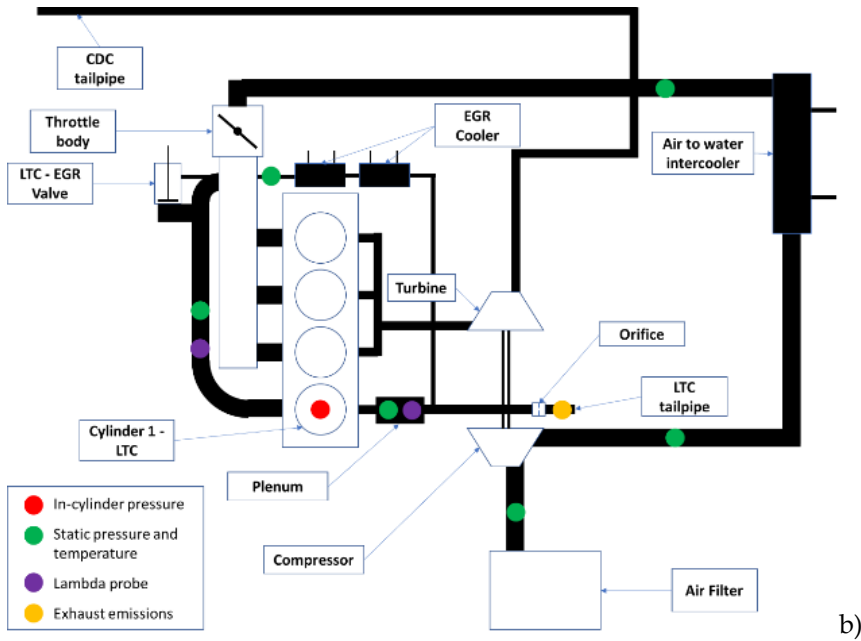
Figure 12: layout of the engine running in CDC mode (a) and when running in the "3+1" mode (b)

(a) (b)

Figure 13: picture of the modified intake manifold (a) and the exhaust pipeline of the RCCI cylinder (b)

As evident from the figures, there is a clear separation between the three cylinders operating in CDC mode and the RCCI cylinder. After passing through the Charge Air Cooler (CAC), the airflow is divided into two distinct paths. The Variable Geometry Turbine (VGT) is exclusively powered by the three CDC cylinders, while the fourth cylinder has its dedicated piping. In terms of exhaust gas recirculation (EGR), it is exclusively applied to the RCCI cylinder, with the original Low-Pressure EGR (LP-EGR) system remaining inactive. Figure 13 (b) illustrates the flow split downstream of the RCCI cylinder, where the front branch comprises the EGR pipe, featuring a liquid cooler and an EGR valve, while the rear pipe routes the gas to the ambient environment via a plenum and a back-pressure valve. The back-pressure valve is employed to adjust the EGR rate, working in conjunction with the EGR valve.

Regarding the intake system, an Additive Manufacturing-produced pipe is connected to the original manifold, as depicted in Figure 13 (a). At the end of this pipe, just upstream of the RCCI cylinder, a Pico

Racing fuel injector of type IWPR1 by Magneti Marelli is installed. Its nominal flow rate at 10 bar is 690 cc/min. To enhance air mixing, the EGR port is strategically positioned as far away from the cylinder as possible.

The composition of the charge within the RCCI cylinder is determined by measuring the mass flow rates of gasoline and diesel, as well as monitoring the oxygen concentration in both the intake and exhaust manifolds of the RCCI cylinders, achieved through the use of two Lambda sensors. Further insights are gained from the analysis of the exhaust gas.

Compared to a single-cylinder prototype, the 3+1 engine configuration offers several advantages. First, there's no need for a dedicated air feed system because the three CDC cylinders consistently meet the boosting requirements of the RCCI cylinder. Second, the engine remains operational even in the event of a misfire within the RCCI cylinder, which is common during the calibration phase. Lastly, and importantly, a 4-cylinder configuration is less susceptible to mechanical issues arising from torsional vibrations, which are typical concerns in single-cylinder setups.

The tests conducted on RCCI combustion cover a comprehensive range of critical operating conditions, including low load (GIMEP, up to 6 bar), medium load (GIMEP up to 9 bar), and high load (GIMEP up to 15 bar). The control of combustion relies mainly on three key factors:

Lambda (Air-Fuel Ratio): Maintaining the right air-fuel ratio in the premixed charge is crucial;

EGR Rate: The amount of exhaust gas recirculation in the premixed charge affects combustion smoothness and NOx emissions but slightly impacts PM, HC, and CO emissions.

Diesel Injection Strategy: Diesel injection, particularly Start of Injection (SOI), was studied along with injection pressure, the number of shots, and dwell time. Optimal SOI falls within 40° to 80° CA before TDC. High injection pressures are necessary to reduce ignition delay.

Overall, the incorporation of EGR in RCCI combustion helps improve combustion stability and reduce NOx emissions. However, it's essential to balance these benefits against the slight adverse effects on PM, HC, and CO emissions when considering RCCI as a combustion strategy.

Particular care was devoted to limit not only the peak cylinder pressure, Pmax, but also the peak pressure rise rate, $(dP/d\theta)max$. In commercial engines a maximum value of 10 bar/° can be tolerated. Considering racing applications, $(dP/d\theta)max$ may reach 20 bar/°. In this work, a maximum value of 13 bar/° is considered an acceptable limit.

The highest values of GIMEP were found with MFB50 close to TDC, rather than at 8-10° aTDC, as in conventional combustion systems. This optimum condition corresponds also to the limit of peak pressure rise rate. This outcome is explained by the very fast heat release rate, just after the onset of combustion

4.1.2 CFD-1D model of the RCCI 4-cylinder engine

The previously described experimental campaign is the base for the construction of a CFD-1D 4-stroke 4-cylinder engine model by GT-Power, where all the cylinders run in RCCI mode

Before the analysis of the complete engine, the numerical model of the single cylinder running in RCCI mode was calibrated, considering the set of experimental data shown in Table 3. The selected points include 5 engine speeds (1500, 2000, 2500, 3000, 3500 rpm) and 3 loads (L=low, M=Medium, H=High). Each operating point is numbered from 1 to 15, for the sake of brevity.

In the chosen operative point, EGR and Lambda settings are adjusted to reduce pollution and increase thermal efficiency. Under maximum load (H), the highest portion of diesel fuel in relation to the total fuel is 18%. The most effective engine performance occurs at 3000 rpm with a GIMEP of 14.6 bar.

The calibration mainly involved fine-tuning certain factors that affect fluid flow and heat transfer. The input data used were real measurements of injected fuel (both diesel and gasoline) and pressure traces inside the cylinder. Figure 14 compare these real values to the corresponding numerical ones. Volumetric efficiency and GIMEP match quite well, but there are some discrepancies in EGR rate (Figure 15), especially at point 7

The differences in EGR rate might partly stem from measurement uncertainties due to the complexity of the system. However, since the simulations are only performed under full load conditions, the accuracy of the computer model is considered quite good. The reliability of the CFD-1D model under high loads is also supported by the pressure measurements inside the cylinder, as shown in Figure 16.

The calibrated CFD model of the Reactivity Controlled Compression Ignition (RCCI) cylinder was employed to simulate a 4-cylinder engine. The overall layout of this engine matches that of the original diesel engine, but it necessitates a few key modifications.

Firstly, the new model incorporates a set of gasoline injectors. Secondly, a mechanically-driven supercharger is added, which is powered by the engine. This supercharger is introduced to provide support to the turbocharger under specific critical operating conditions, such as low engine speed and high EGR rates. When not required, the supercharger can be bypassed. Thirdly, the turbocharger is scaled to ensure a better match with the new operating conditions

The full load points for the 4-cylinder, 4-stroke engine correspond to cases: 3,6,9, 12 and 15 (Table 3). The recirculated gas is supplied by the standard LP-EGR system, while the Start of Combustion is slightly adjusted to align with the constraints regarding peak pressure rate rise and peak cylinder pressure.
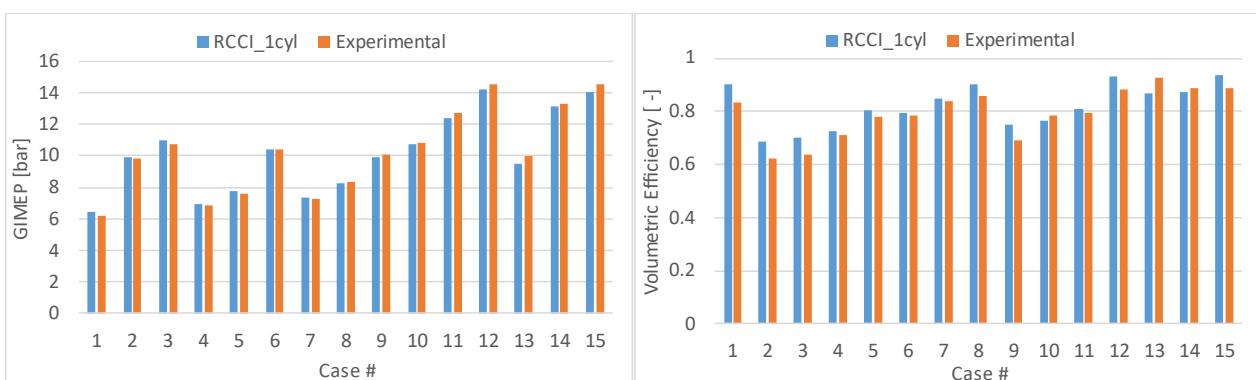
Figure 14: Gross IMEP and Volumetric efficiency: comparison between the calibrated 1D model and the experimental data

Table 3: Operating conditions of the cylinder running in RCCI mode, selected for the calibration of the Gt-Power engine model

Case #	Load	RPM	EGR %	Lambda	$\dfrac{m_{diesel}}{m_{tot}}$	GIMEP [bar]
1	L	1500	0	2.25	10.16	6.19
2	M	1500	42	1.09	12.19	9.87
3	H	1500	45	1.02	12.19	10.77
4	L	2000	22	1.74	18.26	6.2
5	M	2000	35	1.21	8.13	8.65
6	H	2000	45	1.07	10.16	12.21
7	L	2500	17	1.96	16.24	7.26
8	M	2500	42	1.26	10.16	10.06
9	H	2500	38	1.06	8.13	13.96
10	L	3000	39	1.12	20.29	10.87
11	M	3000	36	1.06	20.29	12.73
12	H	3000	35	1.03	18.26	14.57
13	L	3500	32	1.46	10.16	10.00
14	M	3500	46	1.09	14.22	12.61
15	H	3500	38	1.06	18.26	13.33
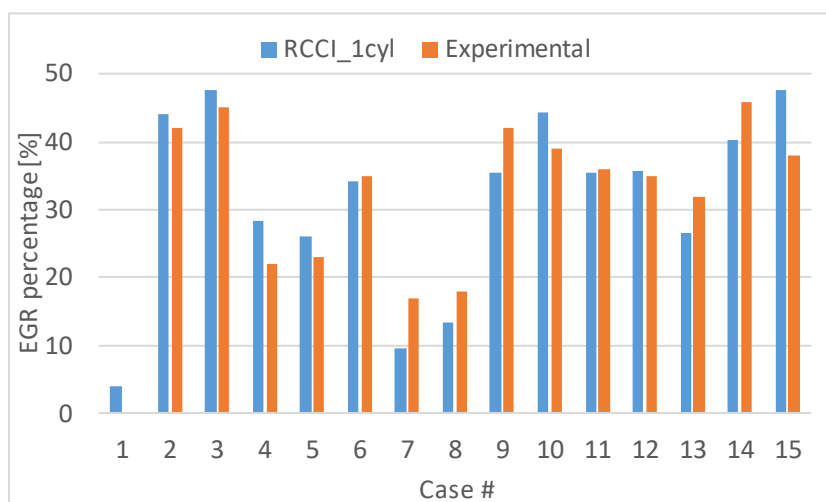
Figure 15: EGR percentage comparison between calibrated 1D model and experimental data
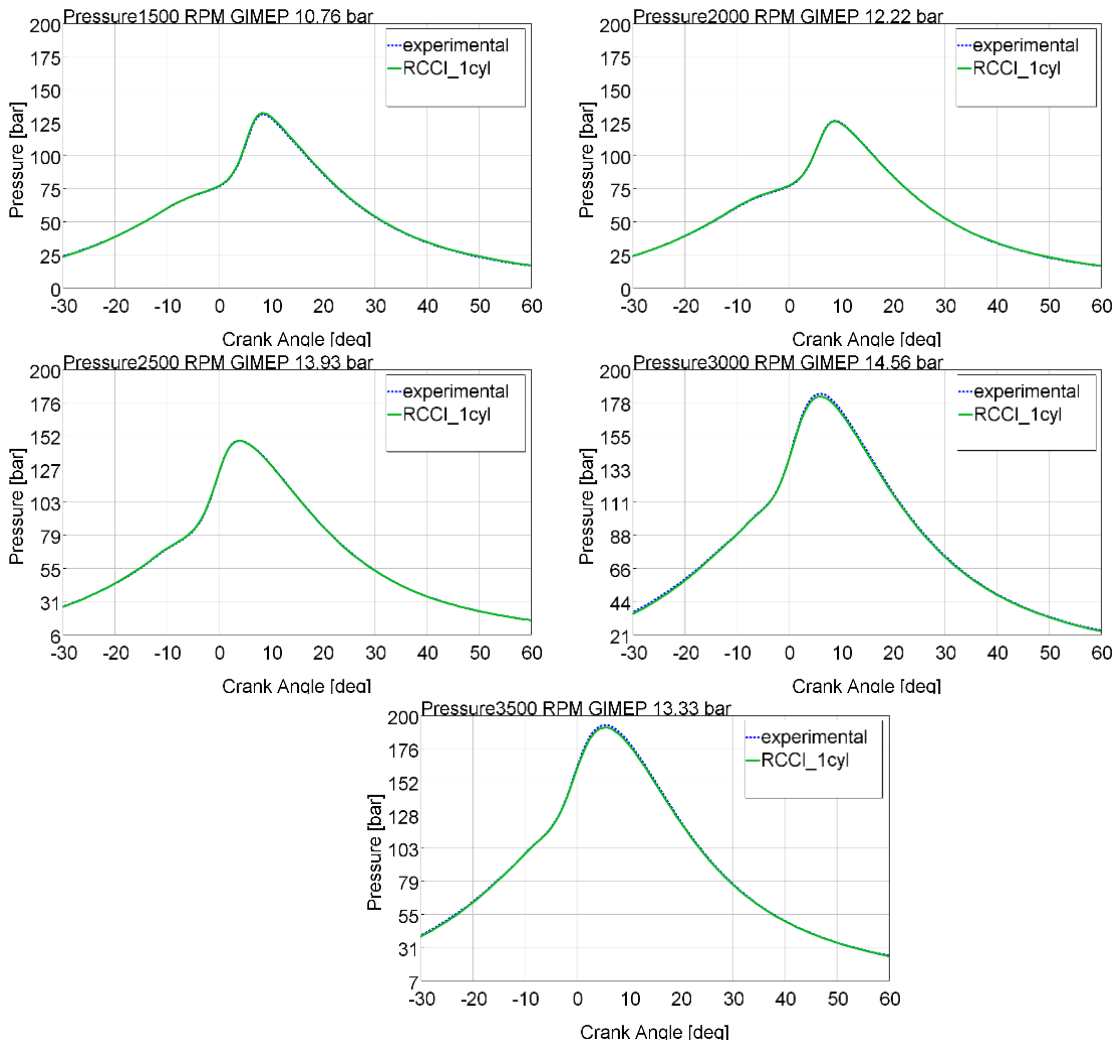
Figure 16: In cylinder pressure, comparison between experimental data and simulated RCCI cylinder full load from 1500 RPM to 3500 RPM at full load

4.1.3   The 2-Stroke model engine

The primary objective of the virtual 2-stroke (2S) engine proposed in this study is to extend the benefits of Reactivity Controlled Compression Ignition (RCCI) combustion to higher levels of brake torque. To ensure consistent combustion characteristics when transitioning from a 4-stroke (4S) to a 2-stroke engine, maintaining the same engine speed and fuel rate, the following hypotheses are put forth:

1. Both engines share common characteristics, including bore, stroke, the number of cylinders, and the geometry of the combustion chamber (including the shape of the bowl and cylinder head, squish clearance). The 2-stroke engine configuration follows a Uniflow design with exhaust valves and piston-controlled intake ports.
2. The exhaust valve lift profile and timing of the 4-stroke engine are adjusted to operate according to the 2-stroke cycle, which involves double the rotational speed, shorter opening duration, and maximum lift around BDC.
3. The intake valves and ports of the 4S engine are converted into exhaust valves for the 2-stroke engine.
4. The set of inlet ports for the 2-stroke engine is designed to create the same Swirl Ratio within the cylinder as in the 4-stroke cycle, occurring at the point of Intake Valve Closing.

In addition to maintaining consistent combustion patterns, it is essential to replicate the in-cylinder pressure diagram observed in the RCCI single-cylinder demonstrator. This necessitates the design of a specific gas-dynamic system for the 2S engine.

The key aspects considered in the project are outlined as follows:

- Inlet ports and manifold: Each cylinder is equipped with a set of 12 piston-controlled ports, which are supplied by a compact manifold wrapped around the liner, as depicted in Figure 17
- Supercharging system: This system comprises a Variable Geometry Turbocharger, coupled with a mechanical supercharger. The supercharger is installed after the dynamic compressor and the first intercooler. A second intercooler is positioned between the supercharger and the intake plenum. This combined system offers the ability to regulate the gas flow rate across the cylinders by adjusting both the turbine rack and the area of the by-pass valve installed on the supercharger.
- Exhaust manifold, upstream of the turbine: To optimize engine performance and maintain efficient gas flow, especially with an even firing interval of 90 degrees, the shape of the exhaust manifold is meticulously designed. The goal is to prevent any negative effects of interference among cylinders while avoiding unnecessary damping of the kinetic energy in the exhaust flow that feeds the turbine.
- Exhaust gas recirculation: In addition to the conventional low-pressure EGR system, which links the turbine outlet to the compressor inlet through a cooler, the quantity of burnt gas within the cylinder is also influenced by the actuation law of the exhaust valves. This EGR system plays a significant role in managing combustion characteristics and emissions control.

The calibration of the gas-dynamic system in the context of varying engine speed and mass flow rates of gasoline and diesel fuel is a complex task. It involves numerous control parameters that need precise adjustment, which include:

1. Turbine rack: The positioning of the turbine rack.
2. Opening of the by-pass valve on the supercharger: Managing the by-pass valve to control airflow.
3. EGR valve opening area: Regulating the area of the EGR valve for effective exhaust gas recirculation.
4. Opening of the exhaust flap: Adjusting the exhaust flap, a valve installed after the turbine, to control low-pressure EGR.
5. Timing of the exhaust valves: Determining the timing of exhaust valve operation.

The calibration process is intricate due to the high number of these control parameters, and the use of CFD-1D simulation proves to be the most suitable tool to address their configuration and assist in designing the engine components.

The modelling of the scavenging process is based on CFD-3D simulations conducted on a two-stroke engine with a similar cylinder design. When transitioning from a 4-stroke to a 2-stroke cycle, it is assumed that the Friction Mean Effective Pressure is halved. Additionally, the burn rate at each operating condition aligns with the experimental curve measured on the RCCI prototype.

Once the numerical model is constructed at full load (defined by the maximum fuel amount in RCCI mode), several parameters are optimized to maximize brake thermal efficiency. These parameters include the height of the inlet ports (timing), opening duration, and maximum lift of the exhaust valves, as well as the size of the turbocharger and the size and transmission ratio of the supercharger. Furthermore, the layout and characteristic dimensions of intake and exhaust manifolds before the turbine are evaluated, and a comprehensive summary of these characteristics is provided in Table 4.

Even maintaining the Uniflow design, the combustion chamber could be redesigned for the new combustion patterns, some other improvement and optimization can be made. However, the purpose of the study is not to develop the best possible 2-stroke RCCI design, but to evaluate the advantages for an RCCI engine, when switching from four to two stroke cycle, maintaining all the other conditions as close as possible.

Table 4: Main characteristics of the optimized 2S engine

Parameter	Unit	
Bore x stroke	mm	83 x 90.4
Compression ratio	#	16.5
N° of cylinders	#	4
Total displacement	L	1.96
N°of exhaust valves	#	4
Exhaust valve diameter (inner seat)	mm	20
Exhaust valve opening duration	°CA	156
Exhaust valve max. lift	mm	7.6
Exhaust Valve Opening	°ATDC	96
Exhaust Valve Closing	°ATDC	252
N° of inlet ports	#	12
Width of each inlet port	mm	14
height of each inlet port	mm	9.7
Inlet Port Opening	°ATDC	135
Inlet Port Closing	°ATDC	225
Max. Reduced mass flow rate of the Supercharger	kg/s*K^0.5/bar	3.36
Max. Reduced mass flow rate of the Compressor	kg/s*K^0.5/bar	4.04
Max. Reduced mass flow rate of the Turbine	kg/s*K^0.5/bar	1.95
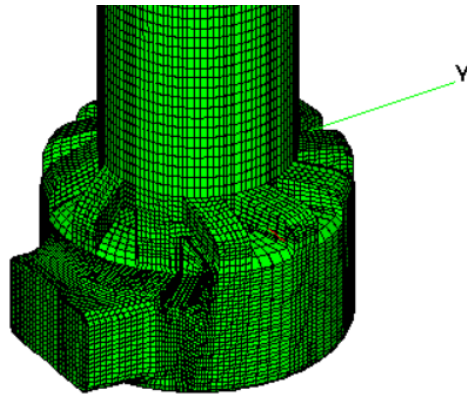
Figure 17: Inlet manifold and ports

4.1.4   2S vs 4S RCCI engine at full load

In this section, a comparison at full load among the standard 4-stroke diesel engine (referred to as 4S_STD, blue), the modified 4-stroke RCCI unit (4S_RCCI, red) and the new 2-stroke RCCI solution (2S_RCCI, green) is presented.

The operating conditions applied to all the simulations are:

- Engine speed from 1500 rpm to 3500 rpm, by steps of 500 rpm
- EGR% and Lambda from Table 3
- Experimental burn rates

The engines also share the following constraints:

- in cylinder peak pressure: 190 bar
- peak of pressure rate rise: 13 bar/deg

Figure 18 shows the brake performance (torque and power) of the engines. As expected, at low speed the brake output of 4S_RCCI is about halved, in comparison to 4S_STD; the 2-stroke cycle helps to recover a part of the gap, but not all of it. At high speed, 2S_RCCI yields the best performance, also in comparison to 4S_STD
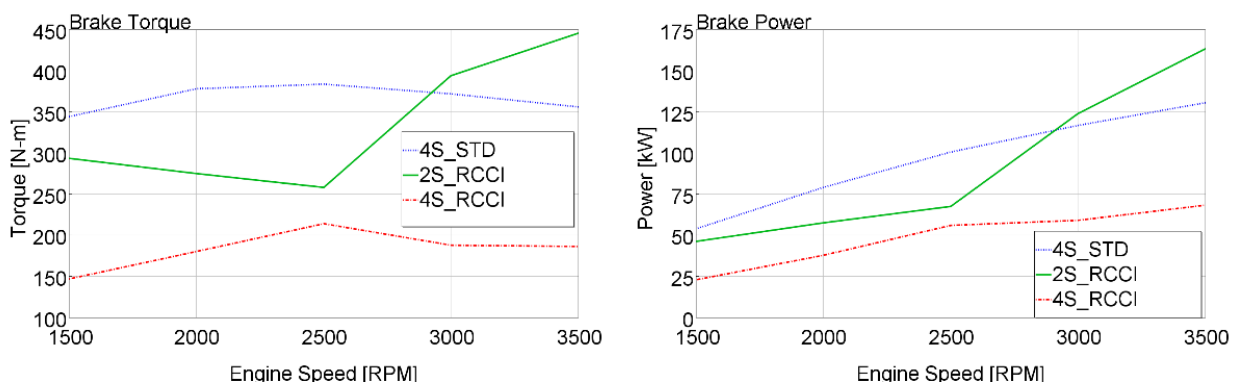
Figure 18: brake torque and brake power comparison, base diesel engine, 4-stroke RCCI engine and 2-stroke RCCI engine. Operating point 1500-3500 RPM full load

In Figure 19 the advantages of the 2-stroke configuration at high speed become evident when examining the Brake Mean Effective Pressure (BMEP) and Gross Indicated Mean Effective Pressure (GIMEP) curves. Despite the higher brake torque and power, the cylinder mechanical load, as expressed by GIMEP, is significantly lower in the 2-stroke engine compared to the 4-stroke standard (16-17 bar vs. 26 bar) and slightly lower than in the 4S_RCCI.

In terms of thermal efficiency, Figure 20, the highest values of the gross indicated parameter belong to 4S_RCCI. The curve corresponding to 2S_RCCI is slightly lower but consistently above 4S_STD, except at 1500 rpm. This outcome can be explained by the fact that RCCI combustion enhances the efficiency of the thermodynamic cycle, with heat release closer to the isochoric process. However, in the 2-stroke cycle, the expansion stroke is truncated earlier by the opening of the exhaust valves.

When considering friction and pumping losses, which affect the transition from gross indicated thermal efficiency to brake thermal efficiency, the situation varies somewhat. At high speeds, the 2-stroke cycle yields the highest brake efficiency due to its lower friction and pumping losses (see also Figure 21 However, at medium and low speeds, 2S_RCCI is penalized by the fresh charge slipping through the exhaust during the scavenging process. Although the amount of lost gasoline is negligible, the work done by the mechanical supercharger to push the excess air and recirculated exhaust gas into the cylinder burdens the pumping efficiency of the engine.

Regarding mechanical efficiency, Figure 21, shows relatively low values for 4S_RCCI due to a higher ratio of friction work to indicated work. While the former is nearly independent of brake output, the latter is low when the brake torque is low.

Finally, Figure 22 presents a comparison of the three engines in terms of brake-specific emissions. For the diesel engine, these parameters are directly measured on the dynamometer bench, while for the RCCI versions, they are calculated. The calculations are based on experimental measurements on the RCCI prototype of the gross indicated specific quantity (i.e., the mass flow rate of pollutants divided by the gross indicated power) and GT-Power's calculations of pumping and mechanical efficiencies. It is assumed that the gross indicated specific emissions remain unchanged when transitioning from the 4-stroke to the 2-stroke cycle. This assumption is supported by the fact that both engines share the same combustion chamber, trapped charge composition, flow field within the cylinder, diesel injection strategy, and thermodynamic conditions at the combustion onset. Therefore, combustion patterns should be nearly identical. Brake-specific emissions are calculated by dividing gross indicated specific emissions by the product of pumping and mechanical efficiency.

The key results of this comparison include:

- The 2-stroke engine maintains a significant advantage in terms of NOx and soot emissions, confirming that RCCI combustion is nearly free of these pollutants.
- The drawback of both RCCI engines lies in the substantial increase of hydrocarbons (HC) and carbon monoxide (CO), a common outcome reported in the literature. However, in absolute terms, the concentration of these pollutants is lower or comparable to a conventional spark-ignition (SI) engine at full load, and they can be effectively managed by using a specific oxidation catalyst.
- CO2 emissions are almost directly proportional to brake thermal efficiency, owing to the similar chemical composition of gasoline and diesel fuel. Therefore, at low and medium speeds, 4S_RCCI has the lowest carbon footprint, while at high speed, 2S_RCCI takes the lead.
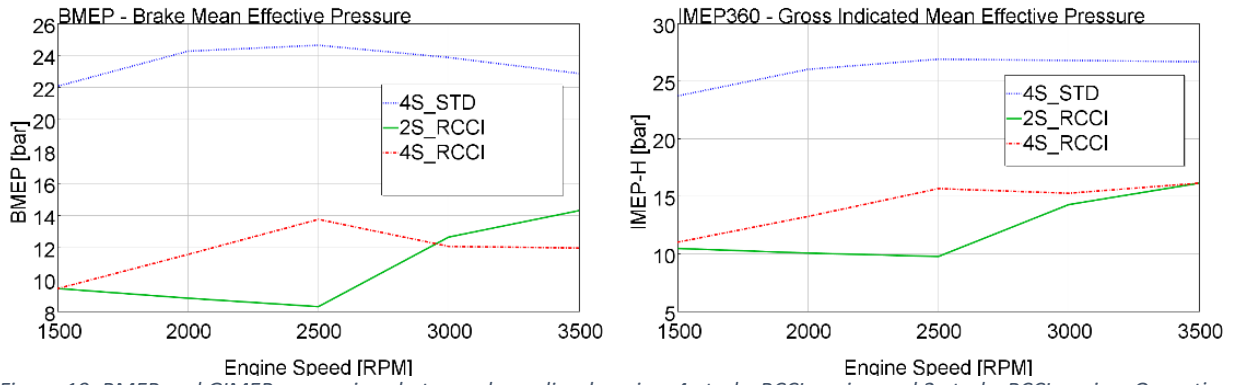
Figure 19: BMEP and GIMEP comparison between base diesel engine, 4-stroke RCCI engine and 2-stroke RCCI engine. Operating point 1500-3500 RPM full load
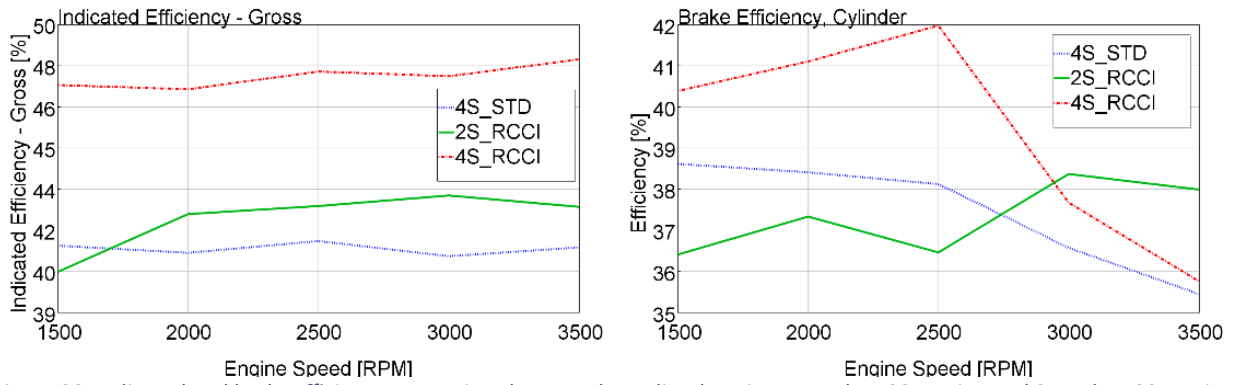
Figure 20: Indicated and brake efficiency comparison between base diesel engine, 4-stroke RCCI engine and 2-stroke RCCI engine. Operating point 1500-3500 rpm full load
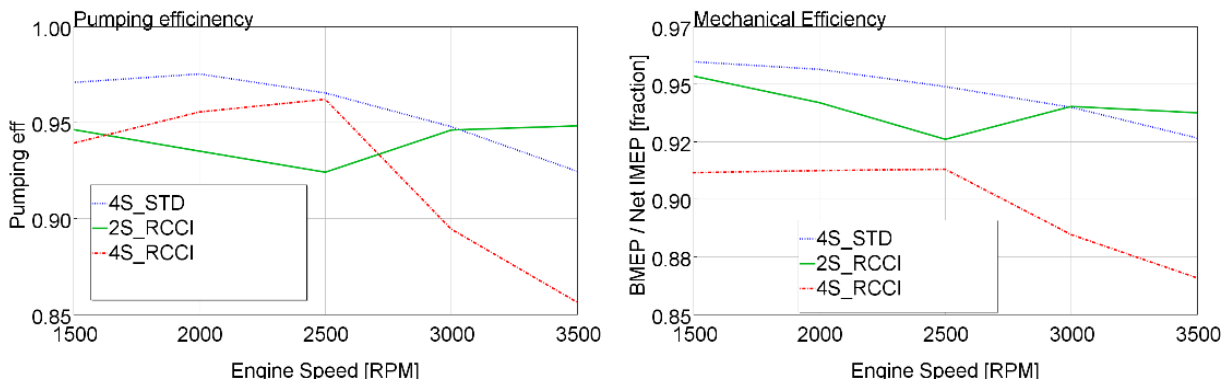
Figure 21: Mechanical and pumping efficiency comparison between base diesel engine, 4-stroke RCCI engine and 2-stroke RCCI engine. Operating point 1500-3500 rpm full load
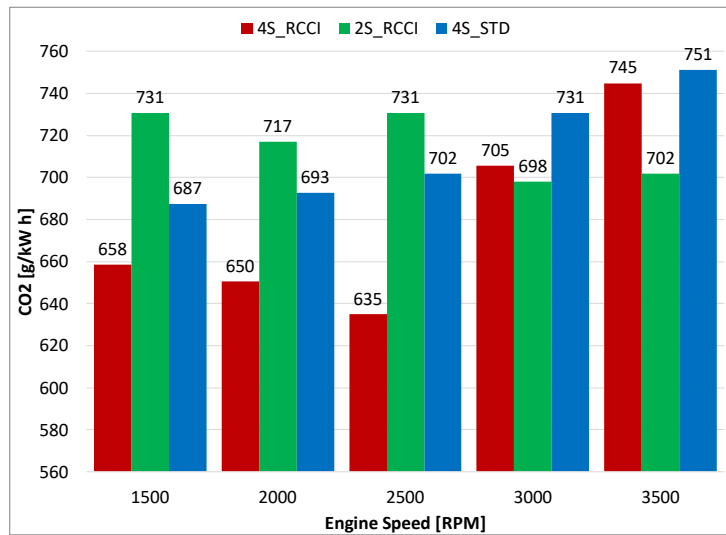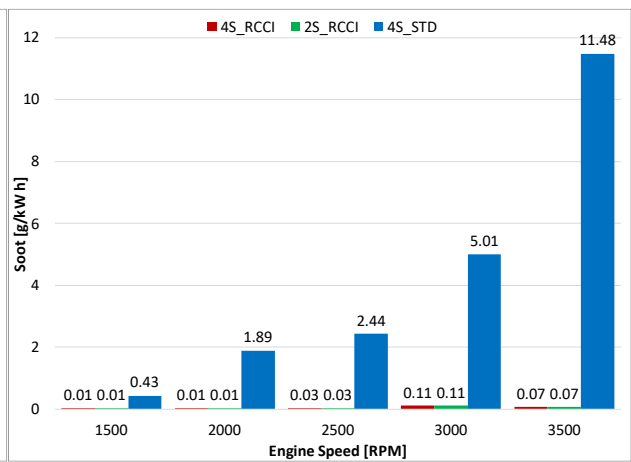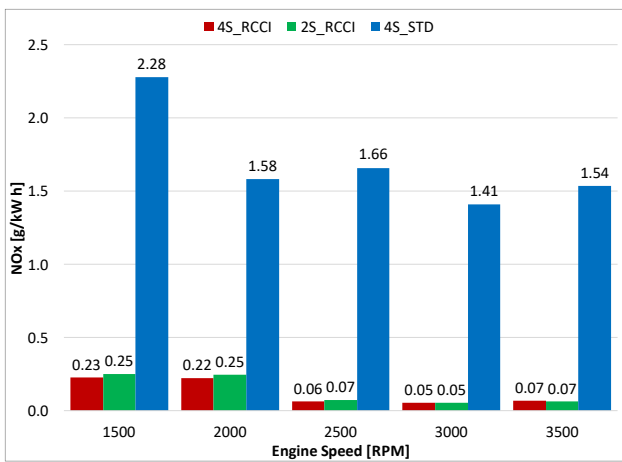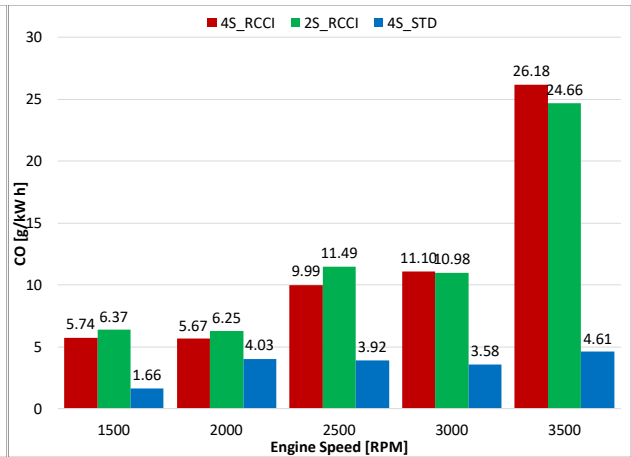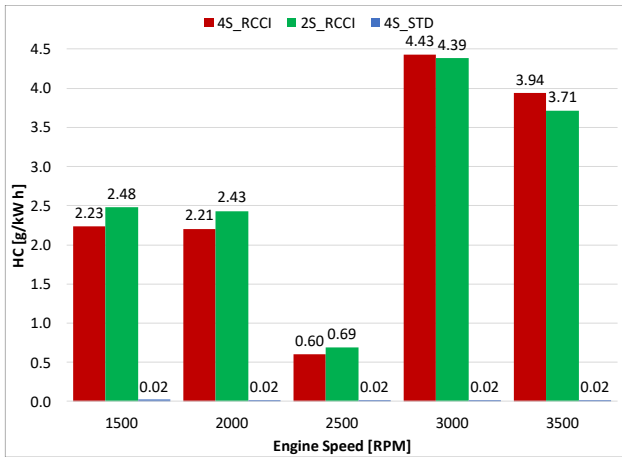
Figure 22: Brake specific emissions comparison

4.2 Combustion chamber optimization for a Dual Fuel gen set application

The focus of this section is on studying the combustion process of a dual-fuel engine that uses both diesel and biogas, operating at two different loads. The main goal was to analyze the impact of key factors related to the design of the combustion chamber. Specifically, the shape of the piston bowl, the position of the injector tip, and the angle at which the diesel spray is directed.

Radius of the piston bowl: 23 mm, 28 mm, 33 mm, and 38 mm are tested.

Axial position of the injector tip: moving the tip ranging its depth from 2 mm to 10 mm, with increments of 1 mm.

Tilt angle of the spray: angles between 30° and 120°, in steps of 15°.

The study was conducted on a four-cylinder, 2.8-liter turbocharged common rail engine that had been modified and experimentally tested to run on a dual-fuel mode with NG. Unlike most dual-fuel engines, this one started as a commercial light-duty engine with relatively high power output.

The engine is capable to deliver a brake power output of 55.6kW @3000RPM BMEP=8bar, that is the maximum limit for micro-cogeneration plant. The numerical simulations here presented consider the engine running on biogas with 65% of methane instead of methane. The considered operative conditions are BMEP=8bar, called Full Load (FL) despite is not the full load condition for the engine is the maximum allowed for micro-cogeneration, and BMEP= 4bar, called Partial Load (PL).

For PL configurations, also diesel injection strategy is evaluated.

4.2.1 Turbulence assessment

The combustion chamber geometry of a typical diesel engine is meticulously crafted to enhance air-fuel mixing during the latter stage of the injection process. This design employs an axially symmetric piston bowl with a distinctive "omega" shape, which serves to bolster swirl motion during the final part of the compression stroke. Additionally, the flat cylinder head is intended to generate a radial flow, often referred to as "squish," around the top dead center (TDC).

However, this design, optimized for conventional diesel combustion, is not ideal for Dual Fuel (DF) combustion. In DF combustion, the diffusive phase is significantly less pronounced in comparison to the premixed phase, especially when a substantial portion of diesel is replaced with natural gas (NG). In this scenario, numerous flame fronts result from the ignition of a small quantity of high-reactivity fuel within a homogeneous, lean mixture of low-reactivity fuel and air. For efficient premixed combustion, a high level of turbulence intensity (beyond just high swirl) is required to increase the surface area of the flame front, consequently enhancing the burn rate.

Compactness is another crucial aspect of an optimal DF combustion chamber design. A more compact chamber leads to a shorter average flame path, which is advantageous for ensuring the completeness of the combustion process. Furthermore, a compact chamber typically boasts a high volume-to-surface-area ratio, which aids in reducing hydrocarbon (HC) emissions, minimizing heat losses through the chamber walls, and consequently enhancing the engine's overall efficiency.

Creating an ideal DF combustion chamber design involves considering both the cylinder head and the piston bowl. However, modifying the cylinder head may not be practical, as it would necessitate a comprehensive

overhaul of the engine's layout. In contrast, a redesign of the piston bowl appears to be a more viable approach.

To establish theoretical guidelines for designing a Dual Fuel combustion chamber, a simplified approach was adopted. The design considered a basic cylindrical bowl with a flat cylinder head. The axis of the bowl aligned with the cylinder axis. Furthermore, the injection process was assumed to be axially symmetric. It was also taken into account that both the compression ratio and the squish clearance (the minimum distance between the piston and the cylinder head) were maintained at constant values. Consequently, as the depth of the cylindrical bowl increased, the following trends could be observed:

- The squish velocity increased [60];
- The heat transfer area of the chamber increased.

These two trends had opposite effects. The higher the squish intensity, the higher the turbulence intensity, thanks to the interaction between the radial flow and the swirl motion within the bowl, which generates a dissipation of kinetic energy [61]. Moreover, the centrifugal radial motion after TDC speeds up the propagation of the flame fronts. On the other hand, the larger the surface area associated with the strong turbulence, the larger the heat losses.

Assuming that ignition takes place near the injector nozzle, the compactness of the combustion chamber can be evaluated by determining the maximum distance between the injector and the wall of the piston bowl at Top Dead Center (TDC). This parameter reflects the maximum distance that the flame front must travel to fully traverse the entire chamber. This distance, denoted as "l," can be expressed as follows:

$$l = \sqrt{h^2 + \frac{d^2}{4}}$$

where h is the depth of the bowl and d is its diameter.

The hypothesis of the constant volume of the bowl (to maintain the same compression ratio) yields

$$\frac{d^2}{4} = \frac{V_{bowl}}{\pi\, h}$$

where V_{bowl} is the volume of the bowl.

Therefore, combining Equations (1. 21) and (1. 22):

$$l = \sqrt{h^2 + \frac{V_{bowl}}{\pi\, h}}$$

The depth of the bowl that minimizes the parameter l is

$$h = \sqrt[3]{\frac{V_{bowl}}{2\pi}}$$

In conclusion, the discussion above demonstrates that the design of a piston bowl for a DF combustion presents conflicting issues; therefore, it must be supported by accurate numerical analyses and/or experiments. Moreover, the outcome strongly depends on the goals of the optimization, as well as on the constraints of the problem, in particular, the compression ratio, squish clearance, bore, et cetera.

4.2.2   3D-CFD Code

For the numerical analysis of the DF combustion process on alternative combustion systems, the previously presented version of the 3D-CFD KIVA-3V code was used. To characterize the mesh size a previous paper based on the same engine is used [62]. In this paper the characteristic cell size was varied between 0.5 and 1.7 mm. Based on the most important outputs of the simulations (total heat released) and the computational cost, the best global cell size was determined. The computational grid built for the study is shown in Figure 23.

This grid consisted of approximately 80,000 cells at the Bottom Dead Center (BDC) and around 24,000 cells at the Top Dead Center (TDC). This variation in cell count was a result of the piston's motion from BDC to TDC (and vice versa), where cells were either compressed or stretched to the point where a cell layer was either removed or added to the grid.

The combustion simulations were conducted within the time frame between the intake valve closing (IVC) at -130 degrees Crank Angle (CA) after Top Dead Center (aTDC) and exhaust valve opening (EVO) at 112 degrees CA aTDC. Initial conditions for these simulations, including pressure, temperature, trapped mass, and charge composition, were directly acquired from experimental data.

Additionally, an initial flow field was imposed as a rigid vortex around the cylinder axis. The intensity of this vortex, characterized by a swirl ratio of 1.8, was determined through a previous 3D Computational Fluid Dynamics (CFD) simulation of the intake stroke. This flow field information was essential for capturing the initial conditions and dynamics within the combustion chamber.
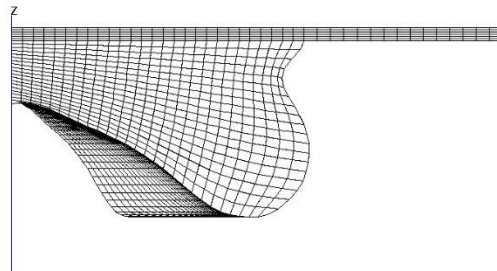
Figure 23: Computational grid at the TDC.

4.2.3   Numerical Model and Validation

The reference engine used for the analysis was an automotive high-speed direct-injection (HSDI) diesel engine manufactured by FCA–VM Motori, whose main characteristics are listed in Table 5.
The authors made modifications to the engine to enable it to operate in Dual Fuel NG–diesel fuel mode, and they conducted an extensive experimental campaign to optimize DF combustion across a wide range of operating points. Subsequently, they developed and validated a 3D CFD model of the combustion system.
For the sake of brevity and focused presentation, the paper reported model validation for a specific operating point. This operating point corresponded to the micro-cogeneration peak power condition, which was characterized by the following parameters:
- Power Output: 55.6 kW
- Engine Speed: 3000 rpm
- BMEP: 8 bar

It's important to note that at this micro-cogeneration peak power operating point, the authors achieved a substantial 80% reduction in diesel fuel mass compared to the corresponding diesel-only case. This specific

condition was chosen for model validation to provide a detailed insight into the behavior and accuracy of the 3D-CFD model in a critical operating scenario.

The main engine parameters used for the validation of the numerical model are listed in Table 6. Figure 24(a) reports the comparison between the simulation and experimental results in terms of the in-cylinder pressure and rate of heat release (RoHR). As can be noticed, the numerical results were in reasonable agreement with the experiments. For a full description of the results of the experimental campaign and the whole validation of the numerical model, the reader is referred to [62–64].

Following the successful validation process, the model was then utilized for simulating the co-combustion of diesel fuel and biogas. To account for the composition of BG, adjustments were made to the initial composition of the premixed charge. Specifically, the composition of the premixed charge was recalculated to accommodate the characteristics of BG. This typically involves determining the ratios and quantities of individual components within the premixed charge, including methane, which is a primary component of both natural gas and biogas. Table 7 shows the main operating point features, while Figure 24(b) shows the comparison between the combustion of NG and BG. Despite having the same energy content, BG resulted in slightly lower pressure due to a slower combustion process caused by a lower air quantity in the mixture.

Table 5: Main technical data of the VM diesel engine

Engine type	HSDI 4-S diesel, EURO IV
Cylinders	4 in-line
Total displacement [L]	2.78
Bore × stroke [mm]	94 × 100
Compression ratio	17.5:1
No. of valves per cylinder	4
Air metering	Turbocharger with VGT + intercooler
Injection system	Common rail
Number of injector holes	6
Injector hole diameter [mm]	0.153

Table 6: Main engine parameters of the experimental validation case

Trapped mass [mg/cycle/cyl]	918.63
Air mass [mg/cycle/cyl]	801.90
NG mass [mg/cycle/cyl]	24.86
Diesel fuel mass [mg/cycle/cyl]	6.62
Diesel fuel injection pressure [bar]	1050
Diesel fuel pilot SOI [°CA AFTDC]	−21.66
Diesel fuel pilot duration [°CA]	3.25
Diesel fuel pre SOI [°CA AFTDC]	−13.92
Diesel fuel pre-duration [°CA]	3.60
Diesel fuel main SOI [°CA AFTDC]	−6.00
Diesel fuel main duration [°CA]	6.85
Diesel fuel in pilot injection [mass%]	14.90
Diesel fuel in pre-injection [mass%]	18.40
Diesel fuel in main injection [mass%]	66.70
Residuals [mass%]	10
EGR [mass%]	0
Swirl ratio [-]	1.8

	(a)	(b)
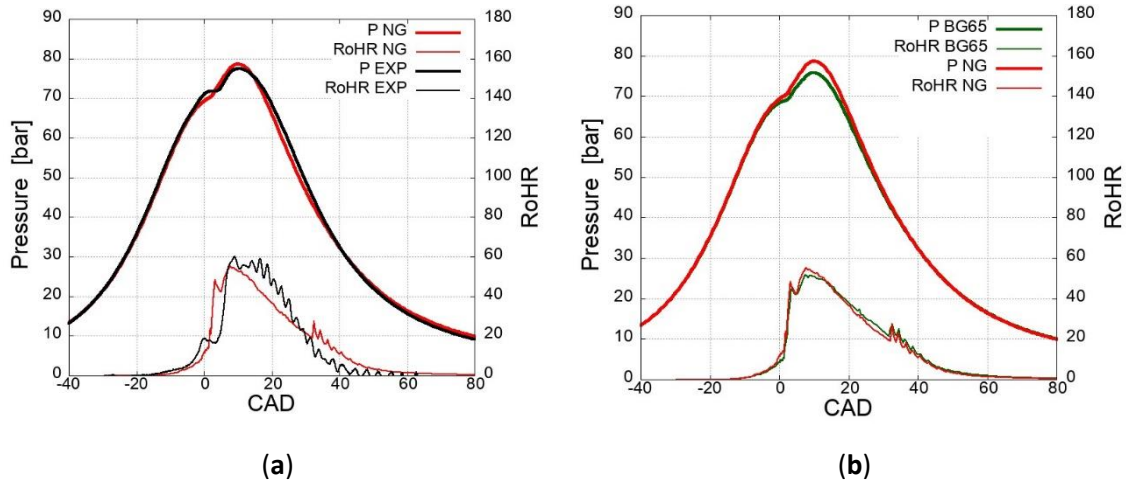
Figure 24: Comparison between the experimental and numerical results (a). Comparison between the Natural gas-Diesel and Biogas-diesel numerical results (b)

Table 7: Base operating points

	NG	BG
Engine speed [rpm]	3000	3000
BMEP (brake torque) [bar (Nm)]	8 (177)	8 (177)
Power [kW]	55.6	55.6
Diesel fuel mass [mg/cycle/cyl]	7.60	7.60
CH_4 mass [mg/cycle/cyl]	24.25	25.26
Air mass [mg/cycle/cyl]	765.22	739.13

4.2.4 Combustion System Design Criteria

In the pursuit of developing a new combustion system for Dual Fuel (DF) combustion, the primary focus was on optimizing the design of both the piston bowl geometry and the injector tip, while the cylinder head retained its flat configuration, consistent with the original engine design.

The piston bowl was designed with a cylindrical shape and a rounded bottom. The entire combustion chamber, including the six-hole injector nozzle, was characterized by perfect axial symmetry. This symmetry allowed for the use of a 60° sector mesh, which was consistent with the mesh employed in the simulations for the diesel engine.

The most critical geometric parameter examined in the study was the radius of the piston bowl, which ranged from 23 to 38 mm in increments of 5 mm (four cases). It's important to note that the bowl's depth was adjusted to maintain a consistent compression ratio with that of the reference engine.

Additionally, a secondary geometric parameter considered in the study was the radius of the bottom edge of the bowl, with values analyzed at 3, 5, and 8 mm. These geometric variations were integral to the study's investigation of the combustion system's performance and behavior in DF combustion.

Figure 25 shows the new combustion chambers in comparison to the original one, while *Table 8* reviews their main features. Each geometry was identified by 2 numbers: the first was the bowl radius (in millimeters), while the second, preceded by "R", was the bottom edge radius (in millimeters). As an

example, "23R3" means that the radius of the cylindrical bowl was 23 mm, while the radius of the bottom edge was 3 mm.
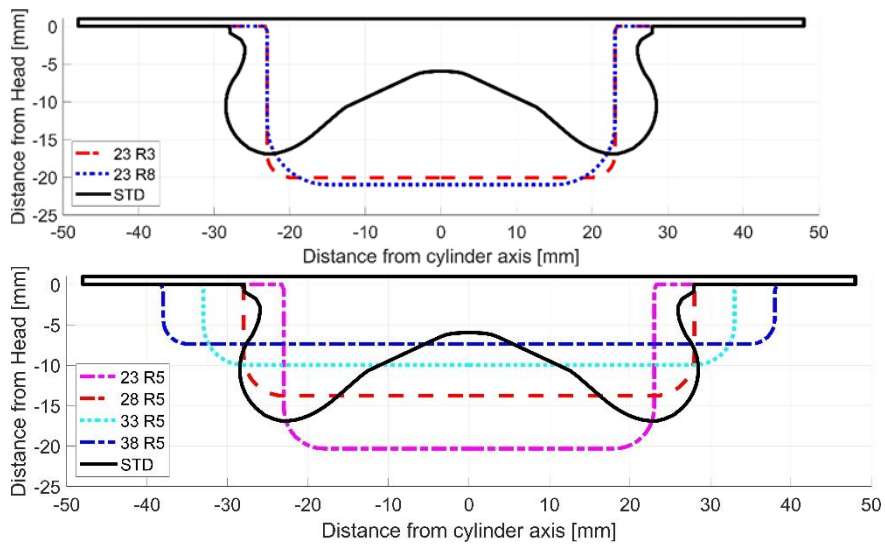
Figure 25: Bowl geometries

As far as the injector nozzle is concerned, for each design of the bowl, two parameters were considered: the distance along the cylinder axis from the injector hole to the cylinder head (nozzle offset) and the tilt angle, i.e., the angle formed by the spray axis with the cylinder axis Figure 26. The first parameter was varied from 2 to 10 mm (in steps of 1 mm) and the second from 30° to 120° (in steps of 15°). A minimum clearance of 3 mm between the piston and the injector tip was imposed; obviously, the configurations that could not comply with this constraint were discarded.
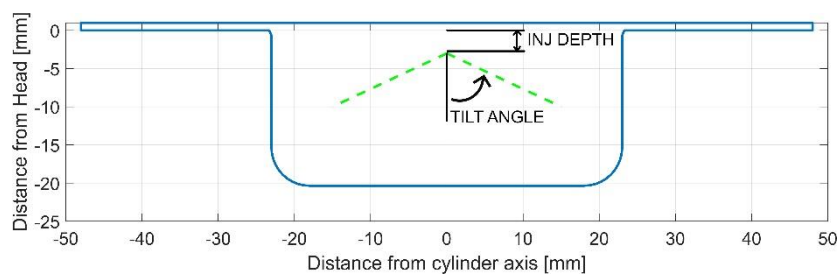
Figure 26: Injector depth and tilt

Table 8: Details of the analysed combustion systems

Name	Bowl Radius [mm]	Bottom Edge Radius [mm]	Bowl Depth [mm]	Nozzle Offset [mm]	Tilt Angle [°]
Ref. engine	28.00	–	6.04–16.86	3	75
23R3	23.00	3.00	20.05	2–10	30–120
23R5	23.00	5.00	20.35	2–10	30–120
23R8	23.00	8.00	21.00	2–10	30–120
28R5	28.00	5.00	13.80	2–10	30–120
33R5	33.00	5.00	9.97	2–7	30–120
38R5	38.00	5.00	7.55	2–4	30–120

For each geometry under investigation, the computational grid was generated using the K3PREP pre-processor. The criteria employed for constructing the grid were consistent with those used for the base engine mesh. A 60° sector grid was utilized, and a typical cell size of 0.8 mm, the same as the original mesh, was adopted. The computational grids of the new combustion chambers are shown Figure 27.

23R3

23R5

23R8

28R5

33R5

38R5
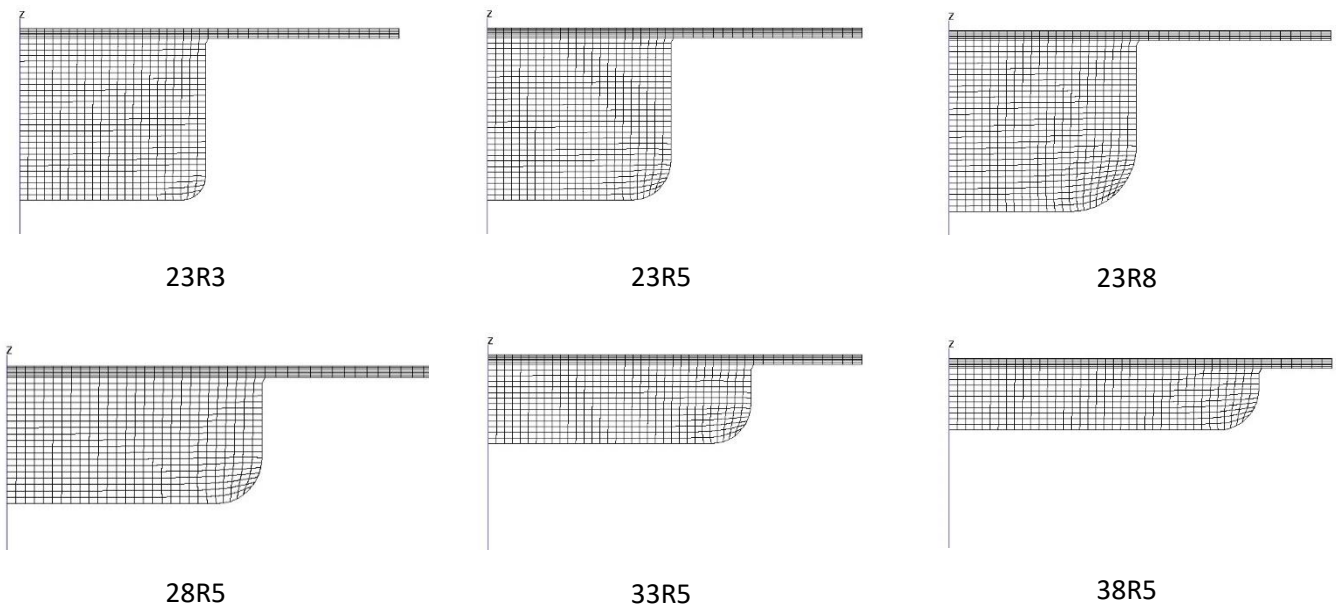
Figure 27: Computational grids of the tested bowls

As previously mentioned, the composition of BG can vary significantly. However, for the purposes of this study, the fraction of CH4 in BG was assumed to be 0.65. This assumed composition is an average value and can be obtained without the need for extensive refinement while still maintaining a favorable lower heating value. The simulations were carried out at two different operating points as reported in Table 9:

FL: "Full load"—BMEP = 8 bar, brake torque = 177 Nm and engine speed = 3000 rpm. At this operating point, the engine delivered a brake power output of 55.6 kW, corresponding to an electrical power of about 50 kW, which is the limit for micro-cogeneration.

PL: "Partial Load"—BMEP = 4 bar and engine speed = 3000 rpm (50% of maximum load). To achieve this target, the fuel rate needed to be reduced by 40%. The air/fuel ratio increased from 22 to approximately 31.

Table 9: Full load and partial load initial conditions

	Total Mass	O_2	Diesel Fuel	CH_4	(A/F) Premix	(A/F) Tot
	[mg]	[mg]	[mg]	[mg]	[–]	[–]
FL	830.567	170.0	7.60	25.66	28.81	22.23
PL	663.54	139.1	4.50	14.71	41.10	31.47

4.2.5   Results and Discussion – Full load

In this section, the results of combustion simulations conducted to optimize the piston bowl geometry and injector tip are presented and discussed. The primary objective of this optimization was to identify a configuration that achieved a favorable balance between thermal efficiency and NOx emissions at both full and partial loads. Other pollutant emissions such as soot, hydrocarbons (HC), and carbon monoxide (CO) were not a focus of the design process because they were either very low (soot) or could be effectively managed with a standard oxidation catalyst (HC and CO).

The initial phase of the simulations was carried out at peak power, characterized by a BMEP of 8 bar, an engine speed of 3000 rpm, and a brake power output of 55.6 kW. For this phase, the same injection strategy was applied across all cases. This strategy was determined based on experimental data obtained from a very similar version of the Dual Fuel engine running on natural gas and diesel fuel with the standard diesel bowl [65].

The initial set of simulations did not yield a single configuration that outperformed the original design for several reasons. First, the existing diesel bowl design was effective at full load due to experimental calibration. Second, the diesel fuel injection strategy was not optimized for all the alternative bowl designs. However, from these simulations, the most promising configurations for both the bowl and injector tip were identified for further investigation.

The second round of simulations focused on partial load conditions. In this phase, the diesel injection strategy was optimized for each specific configuration. The optimization of the injection pattern was carried out using a Design of Experiment (DOE) approach, involving the adjustment of the Start of Injection (SOI) within a range of -7 °CA to +5 °CA, in 2 °CA steps.

Furthermore, the best combustion chamber design for partial load conditions was then subjected to simulations at full load, with further refinement of the injection strategy. To provide an overview of the key results from this first round of simulations, a NOx-IMEP diagram was considered. Given that the amount of injected fuel remained constant, IMEP was directly proportional to the indicated thermal efficiency (ITE), providing a clear indicator of Brake Thermal Efficiency (BTE). Additionally, the quantity of NOx emissions was expressed as a specific quantity, denoting the mass flow rate of incomplete NOx combustion. This approach facilitated a concise assessment of the combustion performance.

Figure 28(a) focuses on the impact of the piston bowl radius, with values of 23, 28, 33, and 38 mm, while keeping the radius of the bowl bottom edge constant at 5 mm. Each set of data points with the same color corresponds to a specific bowl geometry, and the differences between these points are solely due to variations in the injector nozzle. The purple star symbol indicates the reference bowl of the diesel engine. As expected, most points tended to fall close to the Pareto front since rapid and complete combustion is generally associated with high values of the IMEP and NO$_x$ and vice versa.

To enhance the clarity of the results, the Y-axis was reversed. In fact, as can be noticed from Figure 28(a), the dashed green lines divide the graph into four regions: The optimal region is located near the origin of the axis, where IMEP increased, and NOx emissions decreased compared to the reference case. Conversely, the worst region is situated in the top-right quadrant, where IMEP decreased, and NOx emissions increased. This representation aids in interpreting the trade-off between thermal efficiency and NOx emissions for different bowl geometries and injector tips. From Figure 28 (a) it becomes evident that only the 23R5 bowl configuration resulted in an improvement in thermal efficiency, with indicated mean effective pressure (IMEP) values surpassing those of the base case for a significant portion of the injector setups. However, this gain in IMEP was counterbalanced by a notable increase in NOx emissions.

The best compromise across all configurations was found with a specific setup of the 28R5 bowl, which was characterized by a nozzle offset of 8 mm and a spray tilt angle of 90° (referred to as 28R5_90_8). This particular configuration delivered performance that was approximately on par with the original diesel bowl. This outcome was somewhat expected, as the new bowl shared the same radius as the baseline.

When considering the bottom edge radius (Figure 28(b)), which varied from 3 to 8 mm on the bowl having a radius of 23 mm, it is quite evident that the influence of this parameter was very weak: in fact, the series tended to superpose, at least for high values of the IMEP. Therefore, the parameter seemed not worthy of further investigations, and it was set at 5 mm for the next simulations.

Figure 28 provides information on the influence of the injector, which was characterized by the distance of its tip from the cylinder head and by the tilt angle. For the sake of brevity, only the 23R5 bowl was considered. Figure 29 (a) maps the IMEP as a function of the two injector parameters, while Figure 29(b) displays NO$_x$ with the same graphical format. In both figures, the red-dotted lines correspond to the values obtained with the original bowl. Figure 29 clearly demonstrates that the tilt angle had a stronger influence than the position of the injector tip. However, between 60 and 105 degrees, the values of the IMEP and NO$_x$ did not change very much.
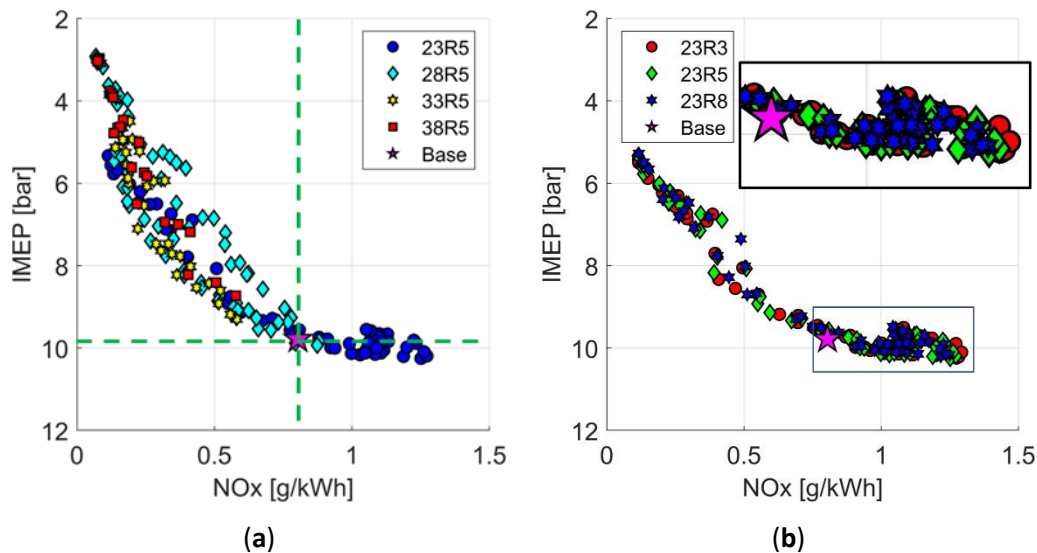
Figure 28: (a) FL with all bowls; (b) FL with a focus on R23
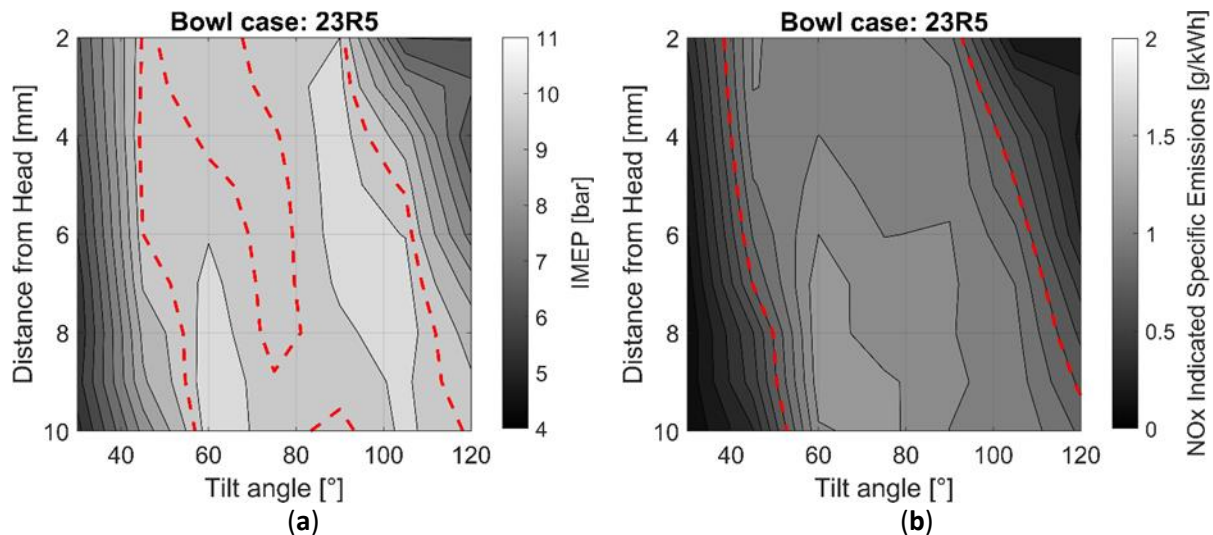
Figure 29: Bowl 23R5 IMEP and a specific NOx plot with standard bowl isolines

In summary, the results from the first round of simulations revealed the following key findings:
- At peak power, achieving a better trade-off between NOx emissions and thermal efficiency than what the original diesel bowl provided proved to be a challenging task.
- The bowl's diameter emerged as the most sensitive parameter. Deeper bowls characterized by a short radius appeared to be more efficient. This advantage became particularly relevant at partial load conditions, where combustion in the original bowl tended to be incomplete.
- The position of the injector tip along the cylinder axis seemed to have less significance compared to the tilt angle. Nevertheless, there was a wide range of possibilities for adjusting the tilt angle, and it had a relatively minor impact on both NOx emissions and IMEP.
- Two promising directions for the development of the combustion system emerged from the simulations. The first was the 28R5_90_8 bowl configuration, which offered the best trade-off between NOx emissions and IMEP. The second was the 23R5 bowl, which showed promise for various injector setups.

4.2.6 Results and Discussion – Partial load

At partial load conditions, the injection strategy played a significant role, and it required individual optimization for each analysed configuration. To maintain simplicity, the shape of the diesel fuel injection rate and the dwell angle between injection shots remained constant, with the primary focus on adjusting the start of injection (SOI) angle.
The following parameter ranges were examined:
- The SOI of the main injection pulse was varied from -7 to +5 °CA aTDC (in 2 °CA steps).
- The injector offset was adjusted within the range of 4 to 10 mm (in 1 mm increments).
- Four different injection tilt angles were considered: 60°, 75°, 90°, and 105°.

The two bowl geometries subjected to investigation were the 28R5 and 23R5 bowls. However, for the 28R5 bowl, only one injector setup was explored, with a tilt angle of 90° and an injector offset of 8 mm.
The first round of simulations at partial load aimed to compare the behavior of the reference bowl to that of bowl 28R5 while sweeping the SOI angle. Figure 30 shows this comparison in terms of the IMEP and specific NOx. It is quite evident that the new bowl did not provide any real advantage in comparison to the original one. Therefore, the attention was focused on the deeper bowl (23R5).
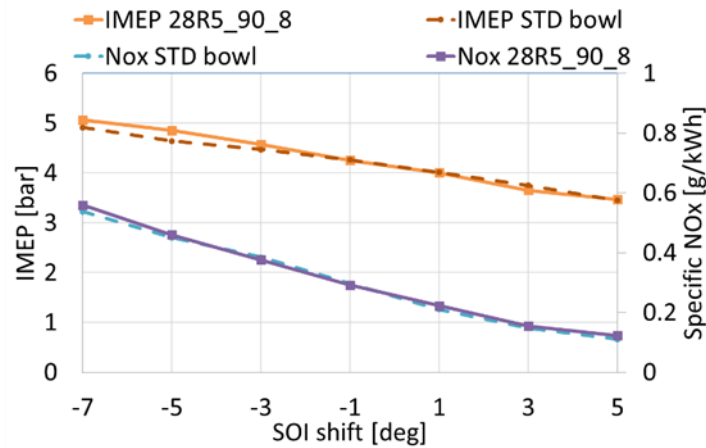
Figure 30: Comparison at PL between the standard bowl and 28R5_90_8 bowl in terms of the IMEP and specific NOx.

For the sake of clarity, the PL simulation results for the 23R5 bowl, shown in Figure 31, were divided into four plots, with each one corresponding to a single tilt angle (a = 60°, b = 75°, c = 90°, d = 105°). The baseline is represented by purple stars.

| (a) | (b) | (c) | (d) |
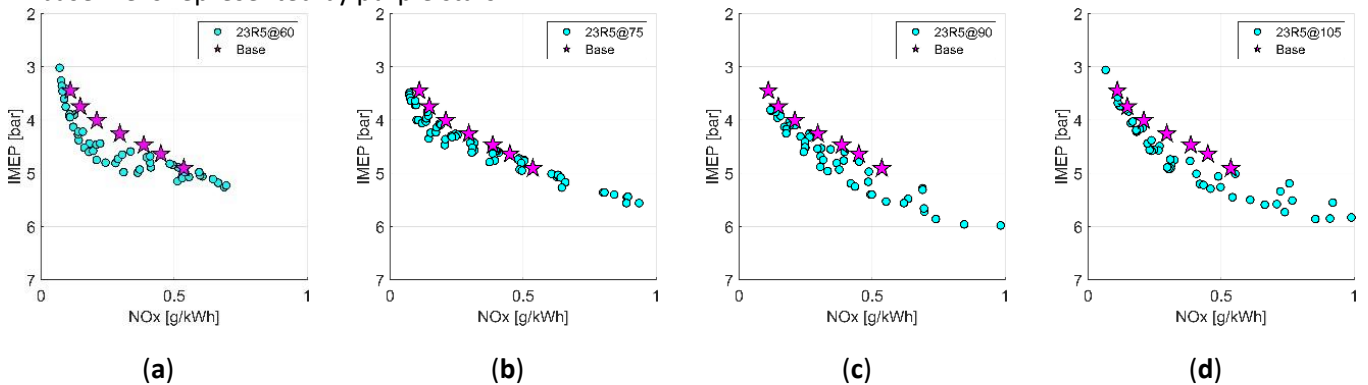
Figure 31: Comparison at PL between the standard bowl (purple stars) and the 23R5 bowl (cyan circles) in terms of varying the tilt angle, depth and SOI. Tilt: 60 deg (a); 75 deg (b); 90 deg (c); 105 deg (d)

The results of the analyses can be summarized as follows:
- The best trade-off achieved with the standard bowl design was specific NOx emissions of 0.5 g/kWh and an indicated mean effective pressure (IMEP) of 4.9 bar.
- Several new configurations were identified that maintained the same IMEP but achieved lower NOx emissions. Notably, the configuration with a tilt angle of 90° and an offset of 4 mm reduced specific NOx by 38% (from 0.54 to 0.33 g/kWh) compared to the baseline while maintaining the same IMEP of 4.9 bar.
- If a lower IMEP value than 4.9 bar was acceptable, the advantage in terms of NOx reduction with the new bowl design at partial load became even more significant, although some penalties at full load were expected.
- For configurations accepting NOx values higher than 0.5 g/kWh, the new bowl design demonstrated greater efficiency, achieving IMEP values of up to 6 bar, which was 20% higher than the baseline.
- The optimization of start of injection (SOI) led to the following final configurations: STD bowl (SOI at -7 °CA aTDC), 23R5_90_4 (SOI at -1 °CA aTDC), and 28R5_90_8 (SOI at -5 °CA aTDC). These configurations represented the most promising solutions for achieving the desired trade-off between NOx emissions and IMEP at partial load.

4.2.7 Final Optimization

In this section, two more promising configurations at PL (23R5_90_4 and 28R5_90_8) were further investigated and compared with the original geometry (STD bowl).

First, it was observed that the original injection strategy at FL of 23R5_90_4 led to higher values of both the IMEP and NOx than the STD bowl (see Figure 32 (a)) with the specific tuning of the injection parameters, it was possible to reduce both the IMEP and NOx emissions to find a new trade-off that was almost perfectly equivalent to the base engine.

Figure 32 shows a comparison between the 23R5_90_4 (with optimized injection strategy), 28R5_90_8 and STD bowls. At FL, the IMEP and NOx were almost the same; however, at PL, the NOx emissions were reduced by 14.5% (28R5) and 38% (23R5) with equivalent IMEPs.

(a) (b)
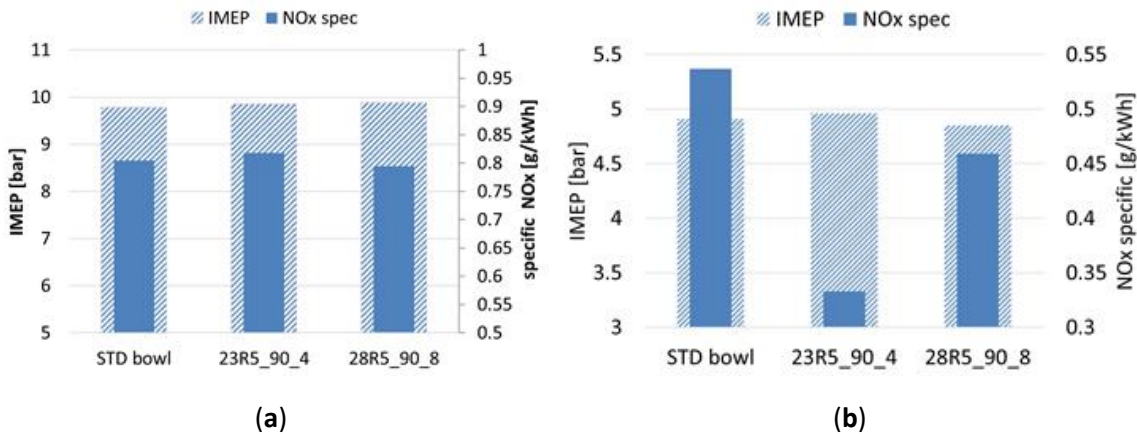
Figure 32: Comparison between the bowls at full load (a) and partial load (b): IMEP and NOx emissions.

For a more detailed insight into the combustion process, Figure 33 and Figure 34 present the traces of the in-cylinder pressure, temperature and rate of heat release (RoHR) at both full and partial loads. At FL, the behavior of the 28R5 bowl design closely resembled that of the diesel geometry, while the 23R5 design generated a higher pressure peak. This difference was primarily attributed to the more pronounced contribution of the pilot injections, which combusted before reaching TDC, leading to an increase in the Rate of Heat Release. It is likely that the 23R5 design promoted a reduction in the diffusion of the diesel fuel jets, enhancing the localized formation of the ignitable mixture prior to TDC.

However, it's noteworthy that the higher peak pressure did not correspond to a higher peak temperature. As a result, the final NOx emissions for both configurations were comparable, indicating that the differences in peak pressure did not significantly affect NOx formation.

(a) (b)
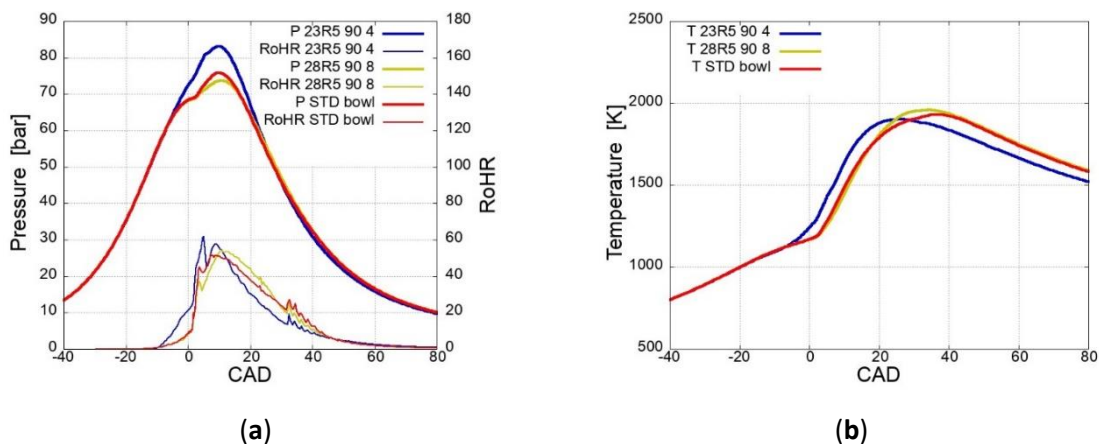
Figure 33: In-cylinder pressure and rate of heat release (a) and temperature (b) at FL (BMEP = 8 bar, 3000 rpm).

(a)   (b)
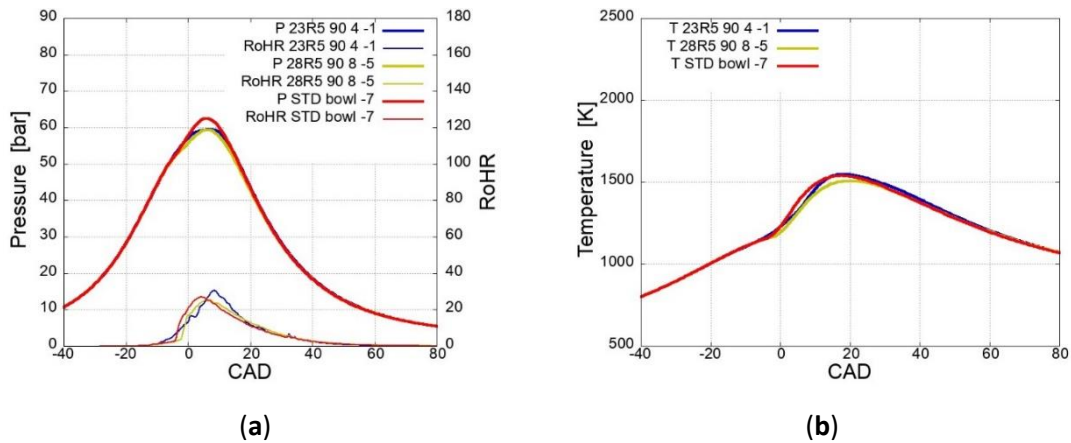
Figure 34: In-cylinder pressure and rate of heat release (a) and temperature (b) at PL (BMEP = 4 bar, 3000 rpm).

At partial load (PL), the advantage in terms of NOx reduction offered by the new bowl design could not be solely explained by the peak cylinder temperature, as it was nearly equivalent for both configurations, as depicted in Figure 34. It's important to note that the cylinder temperature represents an average parameter, while the formation of NOx is predominantly influenced by local temperature variations. Therefore, Figure 35 illustrates a temperature map on a radial cross-section at the crank angle corresponding to the peak of average temperature (18° aTDC).

In this temperature map, it becomes evident that the region with high local temperatures, indicated by yellow and red colours, was significantly smaller for the 23R5 configuration. Consequently, it can be concluded that the reduction in NOx emissions at PL achieved by the 23R5 bowl design was associated with a more uniform distribution of local temperatures, which effectively limited the formation rate of the pollutant. This demonstrates the significance of local temperature distribution in influencing NOx emissions.

(a)   (b)   (c)
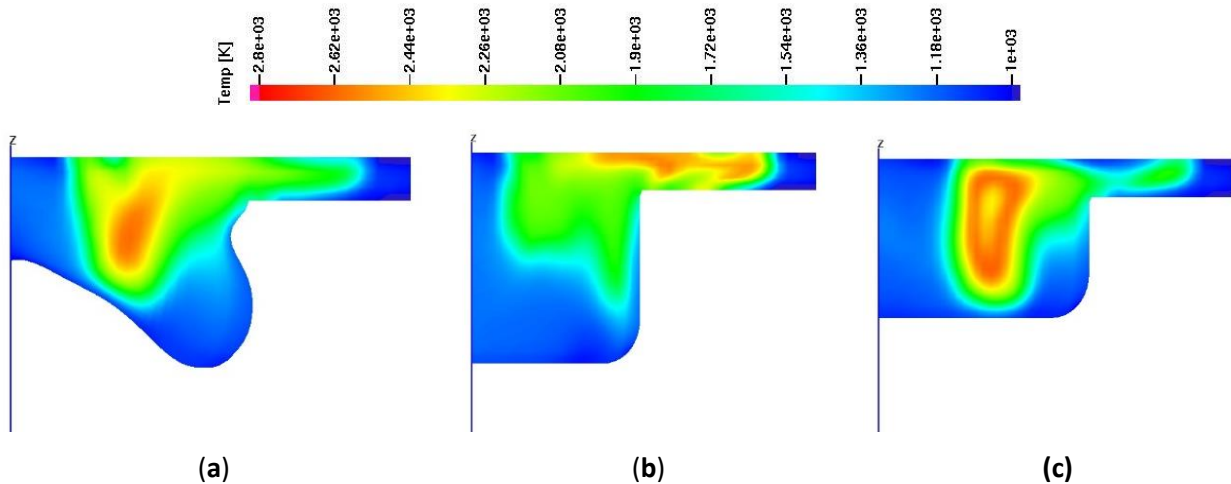
Figure 35: Temperature distribution at PL in the following configurations: STD (a), 23R5 (b) and 28R5 (c).

In conclusion, the best configuration found with respect to the standard diesel bowl geometry at partial load was the 23R5_90_4, which was a cylindrical-shaped bowl characterized by a 23 mm radius, 5 mm bottom edge radius, 90° injection tilt angle, 4 mm injector tip depth and −1 °CA SOI.

4.3   CH4+hydrogen blends for a Dual Fuel low load condition

This section is dedicated to the same DF engine, but it delves into a scenario of very low load conditions: specifically, 3000 rpm with a BMEP of 44 Nm, resulting in 2 bars. The research revolves around a light-duty turbocharged Diesel engine, which the authors modified to operate in DF NG-diesel mode, as previously described. In this project, the validation of the numerical model is accomplished using a commercial CFD-3D tool (Ansys Forte). At this operational state, the DF NG-diesel combustion becomes notably critical, resulting in elevated levels of CO and UHC due to an incomplete process. Consequently, Brake Thermal Efficiency (BTE) is adversely affected.

Using the calibrated model, a series of simulations were conducted to explore the impact of varying H2-CNG blends within a range from 0% to 30% of hydrogen volumetric concentration. The findings, covering aspects such as combustion stability, thermal cycle efficiency, and emissions, are presented and discussed.

4.3.1   Experimental setup

As in the previous section, the so-called donor engine has already been described in the context of the experimental campaign for the modified diesel-NG engine. Specifically, four NG injectors, each with a nominal flow rate of 1.5 g/s at 3 bar, were installed on the engine's inlet pipe, positioned just downstream of the intercooler and approximately 500 mm ahead of the intake manifold. This extended routing fosters the creation of a homogeneous NG-air mixture and its even distribution among the four cylinders. Furthermore, the EGR valve remained consistently closed, so the impact of charge dilution with exhaust is not considered in this study.

The entire experimental campaign was conducted at four different operating points, all characterized by an engine speed of 3000 rpm but varying medium-low loads (BMEP = 2, 4, 8, and 12 bar, corresponding to brake torques of 44, 88, 177, and 265 Nm, respectively). For each operating point, the full diesel mode is referred to as Conventional Diesel Combustion (CDC). Starting from CDC, the amount of diesel fuel injected per cycle was gradually reduced and replaced by NG, all while maintaining constant brake torque through the application of closed-loop control to the engine pedal.

The parameter X_NG is employed to quantify the fraction of energy provided by NG in DF mode, as compared to the energy supplied by diesel fuel in the corresponding CDC operation:

$$X_{NG}[\%] = \frac{m_{NG} * LHV_{NG}}{m_D * LHV_D} * 100$$

where m_{NG} is the mass per cycle of NG in DF mode, m_D is the mass per cycle of Diesel fuel in CDC mode, LHV_{NG} is the Lower Heating Value of NG and LHV_D is the Lower Heating Value of Diesel fuel. The fraction of energy provided by diesel in DF mode is evaluated by means of the following formula:

$$X_D[\%] = \frac{m'_D}{m_D} * 100$$

Where m_D' is the mass per cycle of Diesel fuel in DF operation.

Comparing X_{NG} to the reduced diesel energy (100-X_D) in DF mode, the variation of engine efficiency can be evaluated: if X_{NG} is greater than (100-X_D), then BTE is lower, and vice versa.

Figure 36 depicts the effect pf the dual fuel combustion on BTE, if no specific optimization is applied. Except for the case corresponding to the higher load (265 Nm) and the higher substitution rate of diesel with NG (80%), BTE dropped in all DF cases.
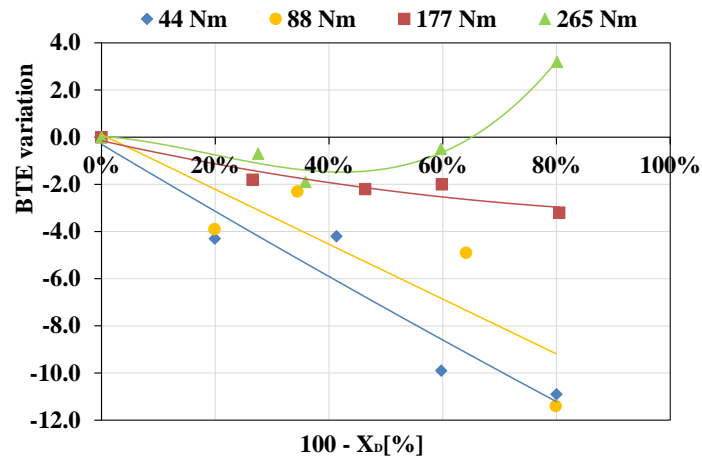
Figure 36: Impact of DF combustion on BTE

Therefore, an optimization of the diesel injection strategy was conducted, in terms of rail pressure and SOI. The goal of the optimization was to recover the lost efficiency, maintaining the reduction of diesel energy while minimizing the amount of NG.
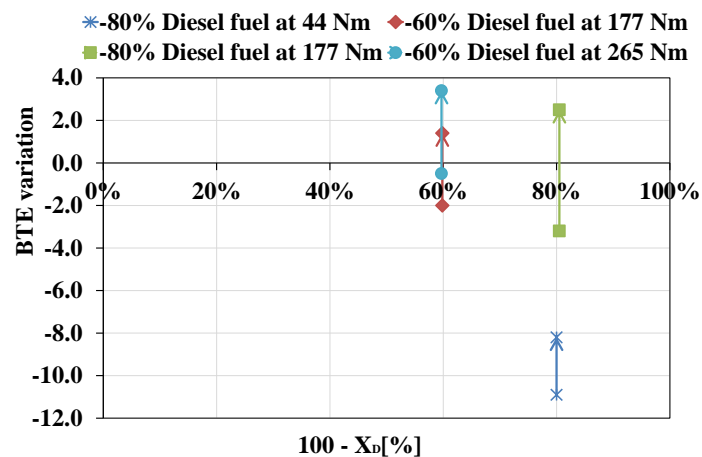
Figure 37: Impact of diesel injection strategy on BTE for the cases at higher reduction of diesel energy

It's important to note that optimization was exclusively carried out for cases involving a more substantial reduction of diesel energy, specifically at 60% and 80%. As depicted in Figure 37, favourable results in terms of engine efficiency recovery were achieved across all the scenarios examined. Moreover, in all the Dual-Fuel (DF) cases with a BMEP equal to or greater than 8 bar, the calibration led to an enhancement in BTE, surpassing even the BTE values in CDC mode. The sole exception was the lowest load condition (44

Nm/BMEP = 2 bar), where it was not possible to surpass or match the BTE value attained in the corresponding CDC operation.

Being the lowest load (44Nm/BMEP = 2 bar) the most critical condition for DF NG-diesel combustion, it was decided to numerically investigate at this operating point the effect of various H2-NG blends.

4.3.2 Computational model and validation

The CFD-3D tool used in the present work is Ansys Forte [40].

The main models adopted for the simulations are summarized in Table 10.

Table 10: Main models used for the CFD-3D DF combustion modelling.

Turbulence model	RANS RNG k-ε
Wall Slip model	Law of the Wall
Droplet collision model	Adaptive Collision Mesh model
Breakup model	Kelvin-Helmholtz/Rayleigh-Taylor coupled with Unsteady Gas-Jet model
Fuel vaporization model	Discrete Multi-Component model
Wall Film model	Particle Numerical model
Combustion model	G-Equation coupled with chemical kinetics

The chemistry set utilized in the numerical model comprises 191 distinct species. The diesel fuel is represented as a 2-component surrogate, consisting of n-decane (67% by weight) and 1-methyl naphthalene (33% by weight), possessing a Cetane Number (CN) of 55. Soot is simplistically modelled as a gaseous species, taking into account the following aspects:

- Nucleation pathways through benzene and phenyl.
- Growth predominantly governed by the HACA mechanism.
- Oxidation facilitated by O_2 and OH.

Each simulation commences at Intake Valve Closing (IVC), with NG or H2-NG blends thoroughly mixed with air and residuals (the latter set at 10%). The assumption of a homogeneous charge at IVC is quite realistic, given that the gas injectors are positioned a considerable distance from the intake manifold, allowing ample time for the gaseous fuel to thoroughly mix with the incoming air.

The compositions of NG and H2-NG blends are reported in Table 11, along with the corresponding physical properties.

Passing from DF NG-diesel to DF H2-NG-diesel combustion, the energy associated to the premixed charge is kept constant.

As the amount of H2 increases, the total mass of fuel progressively decreases, since NG is replaced by a fuel having a higher LHV (120 vs 47 MJ/kg).

		NG	NG+5%H$_2$	NG+10%H$_2$	NG+15%H$_2$	NG+20%H$_2$	NG+25%H$_2$	NG+30%H$_2$
Composition [%vol]	CH$_4$	96.0%	91.2%	86.4%	81.6%	76.8%	72.0%	67.2%
	C$_2$H$_6$	2.5%	2.375%	2.25%	2.125%	2.0%	1.875%	1.75%
	C$_3$H$_8$	0.5%	0.475%	0.45%	0.425%	0.4%	0.375%	0.35%
	N$_2$	1.0%	0.950%	0.9%	0.85%	0.8%	0.75%	0.7%
	H$_2$	0.0%	5.0%	10.0%	15.0%	20.0%	25.0%	30.0%

The computational grid was constructed using the Sector Mesh Generator Utility, an integral component of Ansys Forte. Owing to the axial symmetry of the piston bowl and the uniform spatial distribution of the six injection orifices, a 60° sector mesh was employed (see Figure 38) Non-axial-symmetric intricacies in the cylinder head and piston crown were disregarded, as their impact on the combustion process is minimal. The average cell size was established at 1.3 mm, aligning with industry-standard best practices. A minimum of four cell layers was enforced in the squish region at TDC, with an additional three cell layers located between the piston and liner. It's noteworthy that the crevice above the top piston ring was slightly widened and deepened compared to the actual dimensions, done to maintain the correct compression ratio without altering the squish height. Ultimately, the computational grid encompasses 21,760 cells at TDC and 105,728 cells at BDC.
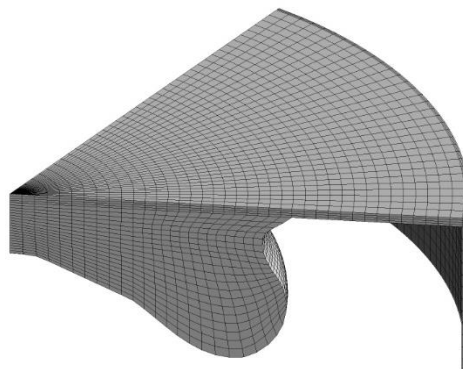
Figure 38: Computational grid at TDC made with Forte

The main engine parameters of the experimental reference case are reported in Table 12. The case considered for the experimental validation corresponds to the highest substitution rate of diesel (diesel energy reduced by 80%) with NG at 3000 rpm – 44 Nm/BMEP = 2 bar.

NG mass [mg/cycle/cyl]	21.11
diesel mass [mg/cycle/cyl]	2.42
diesel injection pressure [bar]	670
diesel pilot SOI [CA °AFTDC]	-18.56
diesel pilot duration [CAD]	4.0
diesel pre SOI [CA °AFTDC]	-10.28
diesel pre duration [CAD]	4.0
diesel main SOI [CA °AFTDC]	-2.00
diesel main duration [CAD]	5.5
diesel in pilot injection [%]	25.6
diesel in pre injection [%]	25.6
diesel in main injection [%]	48.8
residuals [%]	10
EGR [%]	0
Swirl Ratio	1.8

The experimental validation of the CFD-3D model is conducted with a focus on in-cylinder pressure and the Apparent Heat Release Rate (AHRR). As for pollutant emissions, they are excluded from the validation process, given that the default models integrated into Ansys Forte are expected to provide adequate accuracy, particularly in capturing the relationship between hydrogen volumetric fraction and emissions. The experimental-numerical comparison shown in Figure 39 reveals a satisfying agreement between measurements and simulation. This outcome is further confirmed in Table 13, by the values of IMEP* and peak cylinder pressure. IMEP* is calculated by the following formula, where V_d is the engine displacement

$$IMEP^* = \frac{1}{V_d} \int_{IVC}^{EVO} p \, dV$$

(1. 27)
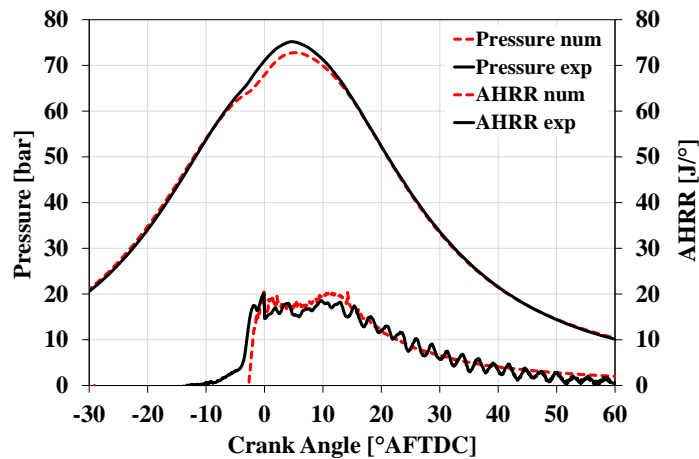
Figure 39: Comparison between experimental and numerical in-cylinder pressure and AHRR 3000RPM 44 Nm BMEP=2bar

	Experimental	Numerical	Error %
IMEP* [bar]	3.84	3.89	1.36
Max Pressure [bar]	75.19	72.77	3.21

4.3.3 Results and discussion

In this section, the results of the numerical simulations are analysed.

Figure 40 shows the calculated in-cylinder pressure and the AHRR for different volume fractions of hydrogen (from 0% to 30%, by steps of 5%). The CDC is also reported, for a straightforward comparison. As hydrogen increases, the peak pressure always increases: the maximum variation is of about 11%, from 72.8 bar to 80.7 bar. This behavior is the direct consequence of the higher heat release rates, due to the increasing content of hydrogen in the premixed charge.

Combustion patterns in Dual-Fuel (DF) operations differ significantly from the standard diesel combustion. In the latter case, the Apparent Heat Release Rate (AHRR) exhibits three distinct peaks, corresponding to the combustion of the pilot, pre, and main injections, respectively. However, in DF cases, the effects of individual injections are not discernible since heat release is primarily governed by the propagation of the flame within the charge, which is ignited by minimal quantities of diesel fuel (the latter being reduced by 80% when transitioning from Conventional Diesel Combustion or CDC to DF operation).

Furthermore, in DF mode, combustion is shifted away from Top Dead Centre (TDC), resulting in a minimum increase of 8.5% in peak cylinder pressure when moving from CDC to a DF case with 0 vol% of H2.
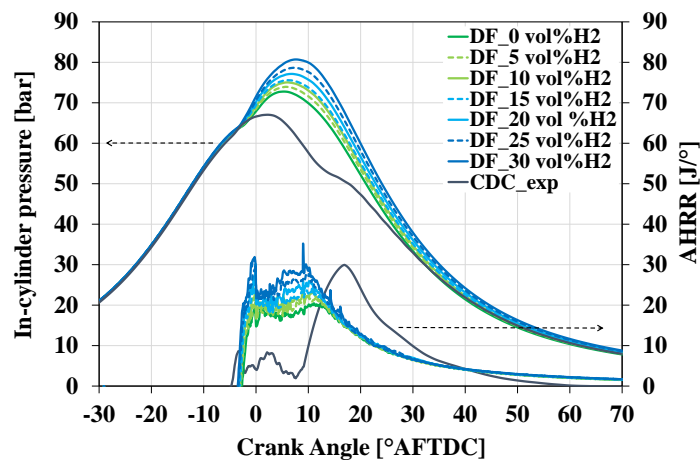
Figure 40: Influence of hydrogen content on in-cylinder pressure and AHRR

As the H2 fraction increases, combustion becomes faster: as visible in Figure 41 , the angle at which 50% of fuel is burnt (CA50) goes from 10.4° to 8.7°. This outcome is due to the combination of two effects:

- the reduction of the ignition delay, calculated as the difference between the pilot SOI and the angle at which 5% of fuel is burnt (CA5): this angle passes from 18.1 to 17.2 CAD;
- the reduction of the main combustion duration, defined as the angular window during which the burnt fuel raises from 10 to 90%: this angle varies from 28.35 CAD to 26.10 CAD(see Figure 42);

The reduction of combustion duration is also responsible of a slight increase of Peak Pressure Rise Rate (PPRR), reaching its maximum when the hydrogen content in the NG-air mixture is equal to 30 vol%. However, this maximum value of PPRR (2.6 bar/°) is well below the top limit (typically: 10-13 bar/°).
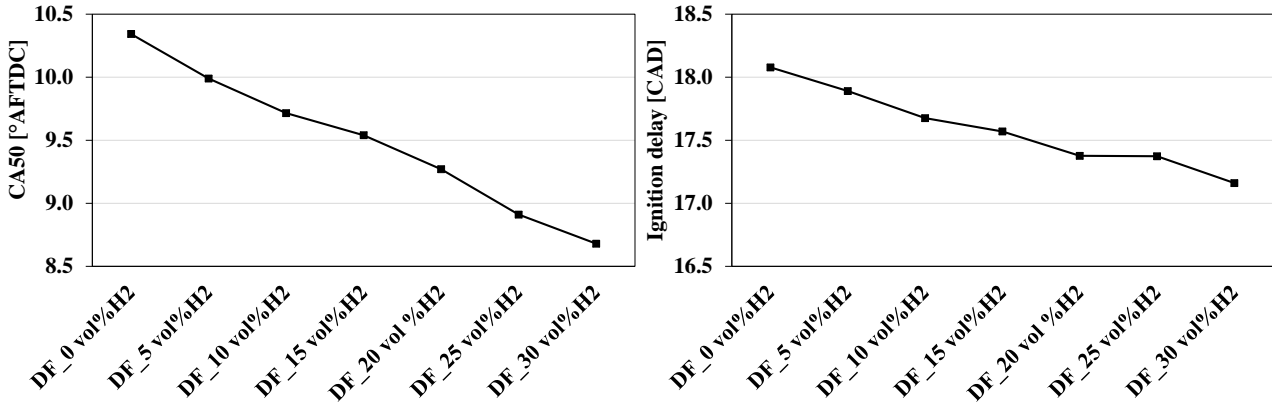
Figure 41: influence of hydrogen content in CA50 and ignition delay
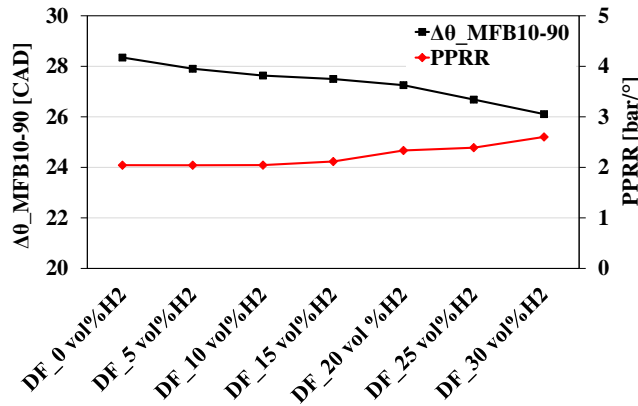
Figure 42: influence of hydrogen content in CA10-90 and PPRR
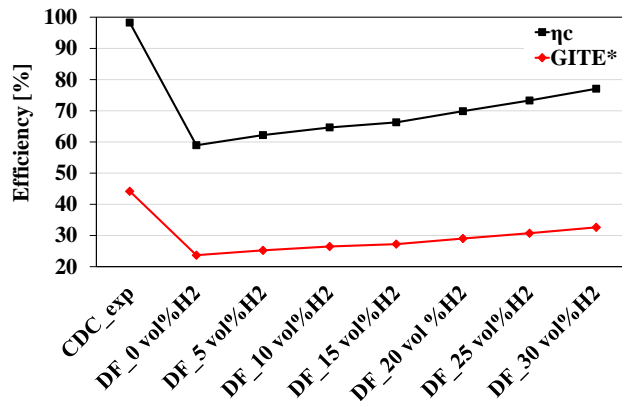
Figure 43: influence of hydrogen content in combustion and thermal efficiency

The addition of hydrogen to the NG-air mixture not only speeds up the combustion process, but it also enhances its completion: this result may be observed in Figure 43, reporting the combustion efficiency (η_c). η_c is evaluated by means of the following formula:

$$\eta_c = \frac{E_{in} - m_{UHC}\ LHV_{UHC} - m_{H2}\ LHV_{H2} - m_{CO}\ LHV_{CO}}{E_{in}} * 100$$

Where:

$E_{in} = m_D\ LHV_D + m_{NG+H2}\ LHV_{NG+H2}$ is the energy provided by the Diesel fuel and the NG-H2 mixture;

m_{NG+H2} is the mass per cycle of the NG-H2 mixture;

LHV_{NG+H2} is the Lower Heating Value of the NG-H2 mixture;

m_D is the mass per cycle of Diesel fuel;

LHV_D is the Lower Heating Value of Diesel fuel;

m_{UHC} is the mass per cycle of Unburnt Hydrocarbons at Exhaust Valve Opening;

LHV_{UHC} is the Lower Heating Value of Unburnt Hydrocarbons;

m_{H2} is the mass per cycle of Hydrogen at Exhaust Valve Opening;

LHV_{H2} is the Lower Heating Value of Hydrogen;

m_{CO} is the mass per cycle of carbon monoxide at Exhaust Valve Opening;

LHV_{CO} is the Lower Heating Value of carbon monoxide.

Figure 43 clearly illustrates the decline in η_c (combustion efficiency) when transitioning from CDC to DF operations. However, the introduction of hydrogen partially mitigates the loss in efficiency. The combustion efficiency penalty decreases from 40% when comparing CDC with DF_0 vol% H2 to 21.6% when considering DF_30 vol% H2. In other words, a 31% improvement in combustion efficiency is observed when moving from DF_0 vol% H2 to DF_30 vol% H2.

A similar trend is observed for Gross Indicated Thermal Efficiency (GITE*), which represents the ratio of the indicated work calculated between IVC and EVO to the fuel energy. The improvement associated with the highest H2 content is 37.8%. This improvement is not only due to enhanced combustion efficiency but also to a more efficient cycle (faster combustion). Nonetheless, the efficiency gap between CDC and DF operations cannot be fully recovered.

Positive developments arise in terms of CO2 emissions, as demonstrated in Figure 44. They can be significantly reduced in DF mode by the addition of hydrogen. A 36.4% enhancement is observed from CDC to the DF case characterized by the highest H2 content. This outcome was anticipated since 80% of diesel fuel is replaced by CH4 (which has the highest H-to-C ratio among hydrocarbons) and H2, both of which do not produce CO2.

Due to the presence of hydrogen in the premixed mixture, CO2 emissions decrease by up to 30.7% when increasing the hydrogen volume fraction from 0 vol% to 30 vol%. However, it's essential to note that this

advantage will diminish when adopting an oxidation catalyst due to the conversion of Unburned Hydrocarbons (UHC) and CO into CO2."
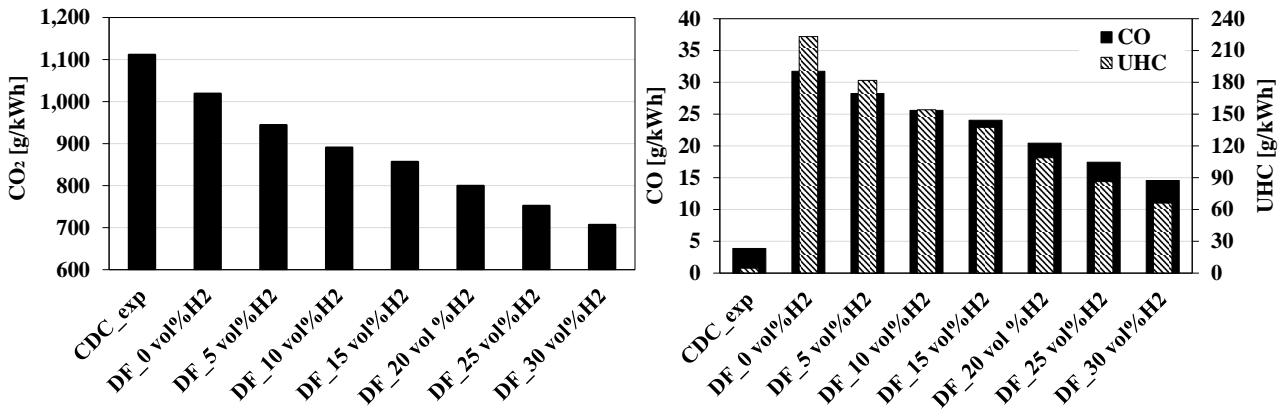
Figure 44: influence of hydrogen content in CO2, CO and UHC emissions

As far as pollutant emissions are concerned, the improvement of the DF NG-diesel combustion process when adding hydrogen is confirmed. CO and UHC decrease by 54.1% and 70.4%, respectively, when comparing the DF_0 vol% H2 case to the DF_30 vol% H2 case. However, even with the higher rate of H2 the CDC emissions are lower.

The reduction of CO and UHC depends on the increase of the OH radical pool, related to the hydrogen content. Figure 45 clearly shows the correlation between the unburned CH_4 - that represents the main constituent of UHC emissions in DF mode - and the concentration of OH.
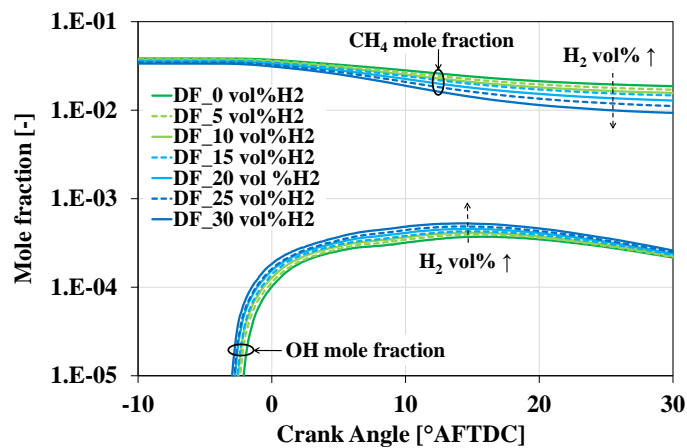
Figure 45: Influence of hydrogen content on OH concentration and methane oxidation

It is worth noting that, in DF NG-diesel combustion mode, most of the UHC is generated by the quenching of the flame at the periphery of the combustion chamber, in the so called "end gas". This phenomenon can be viewed in Figure A. 1, in the Appendix. The figure presents the distribution of Temperature, n-C10H22 CH4 and OH concentrations on two cut planes coincident with the diesel spray axis, at different crank angles, during the combustion process. The choice of n-C10H22 for representing the concentration of diesel

66

fuel is due to the fact that this hydrocarbon is the main constituent of the diesel surrogate used in the numerical model.
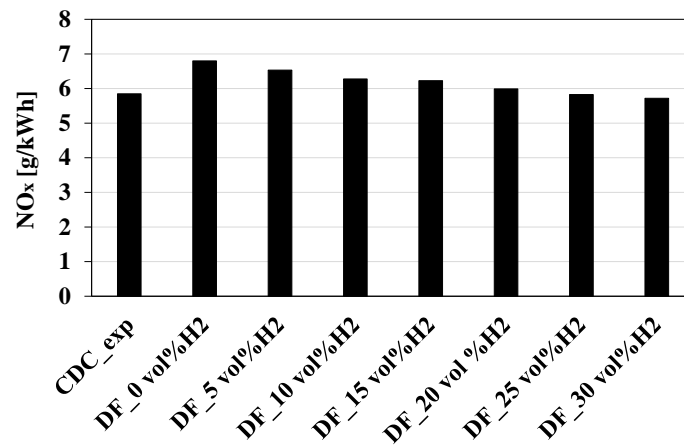
Figure 46: influence of hydrogen content in NOx emissions

Despite the cylinder peak pressure tends to increase in DF mode when the hydrogen content in the NG-air mixture grows up, NOx emissions follow the opposite trend (see Figure 46). As H2 increases from 0% to 30%, NOx emissions are reduced by 15.9%. NOx emissions in DF mode with 30 vol% hydrogen are also slightly lower than that of CDC operation (5.72 g/kWh and 5.85 g/kWh, respectively).

Finally, the strong reduction of diesel fuel in the DF operations (-80%) permits to almost cancel soot emissions, which fall at values lower than 0.001 g/kWh. The addition of H2 further reduces this ultra-low value.

It can be concluded that the addition of H2 to the NG-air mixture is an effective way to improve DF NG-diesel combustion at low loads, and such an enhancement grows as the hydrogen mole fraction increases.

4.4   Conclusions

First, my project was centred on an experimental campaign involving a 4-cylinder, 4-stroke 2.0L diesel engine. I conducted performance and emissions measurements for two configurations: standard diesel and "3+1," where one cylinder operated in RCCI mode (a combination of gasoline and diesel), while the other three used diesel. With the obtained experimental data, I built and calibrated a CFD-1D engine model for an RCCI 4-stroke 4-cylinder engine. I also virtually developed a 2-stroke engine with the same specifications as the 4-stroke counterpart. I aimed to replicate combustion patterns observed in the tested RCCI engine, including the combustion chamber geometry, charge composition, in-cylinder flow field, and diesel injection strategy. The results were promising. Transitioning from standard diesel to RCCI, whether in a 4-stroke or 2-stroke engine, consistently led to significant reductions in NOx and soot emissions. Despite an increase in hydrocarbon (HC) and carbon monoxide (CO) emissions, these remained manageable and could be efficiently addressed using cost-effective Oxidation Catalysts. Furthermore, switching to RCCI consistently improved brake thermal efficiency, presenting the 2-stroke RCCI engine as a compelling choice, especially at full load and high engine speeds.

Secondly, I ventured into the intricacies of combustion chamber design for a dual-fuel (DF) engine. My focus was on micro-cogeneration applications with a maximum electric power output of 50 kW. I sought to optimize the trade-off between Brake Thermal Efficiency (BTE) and NOx emissions across a range of loads. My approach involved extensive 3D CFD simulations, assessing various bowl shapes, injector positions, and spray angles. The outcomes were as follows: at full load, new cylindrical bowl shapes did not provide significant advantages over the original design in terms of the IMEP-NOx trade-off. The "28R5" bowl configuration showed a modest improvement, with a 1% increase in IMEP and a 1.26% reduction in specific NOx emissions. A deeper bowl ("23R5") held promise, with numerous injector configurations improving IMEP and overall thermodynamic cycle efficiency. At partial load, "23R5" exhibited a substantial 14% reduction in specific NOx emissions compared to the original bowl design, while "28R5" demonstrated a remarkable 38% improvement. These findings highlighted that the standard piston bowl design offered a near-optimal balance between thermodynamic efficiency and pollutant emissions at full load, but a deeper cylindrical bowl with a smaller radius became particularly advantageous at partial load, enhancing the engine's performance characteristics.

Lastly, my third project utilized CFD-3D simulations to investigate the impact of hydrogen addition to a lean premixed mixture in DF natural gas (NG)-diesel combustion. I focused on a specific operating point characterized by low load and high speed (3000 rpm, 2 bar BMEP), aiming to mitigate high CO and UHC emissions observed in previous experiments. The introduction of hydrogen into NG-H2 blends yielded significant outcomes. In-cylinder peak pressure increased by 11% due to reduced ignition delay and combustion duration. CA50 (crank angle) shifted from 10.3° to 8.7° after top dead centre (CA°AFTDC). Pressure rise rate (PPRR) increased by 27.4%, with the maximum value (2.6 bar/°) staying well below the critical limit (10-13 bar/°). CO2 specific emissions decreased by 30.7%, owing to a lower carbon content and increased thermal efficiency. Notably, CO and UHC emissions dropped significantly by 54.1% and 70.4%, respectively, primarily due to the higher concentration of the OH radical. Hydrogen addition proved highly effective in promoting combustion at the chamber's periphery, reducing early flame quenching. These reductions in emissions translated to a 31% increase in combustion efficiency. Furthermore, NOx emissions decreased by 15.9%, demonstrating the overall environmental benefits of hydrogen addition.

In summary, my research uncovered the potential of the 2-stroke cycle as an effective platform for RCCI combustion systems, showcasing significant reductions in emissions and fuel consumption without compromising brake performance. It also emphasized the significance of optimizing combustion chamber design for DF engines, providing insight into the trade-off between BTE and NOx emissions. Lastly, it

highlighted the effectiveness of hydrogen addition in mitigating emissions and enhancing combustion stability in DF NG-diesel combustion, particularly at low loads.

5 Aircraft powertrain

The development of modern aircraft engines has been driven by a quest for high-performance and efficiency, in pursuit of safe, reliable, and environmentally friendly aviation. When designing an aircraft engine, several key factors come into play. One of the foremost requirements is achieving a high power-to-weight ratio. This is a critical parameter as it directly impacts the aircraft's performance, allowing it to climb swiftly, cruise efficiently, and respond promptly to dynamic flight conditions.

Aircraft engines must also possess compact overall dimensions, enabling installation without the need for significant modifications to the aircraft bodywork. This factor is crucial to minimize aircraft downtime and maintenance costs, as well as to enhance the adaptability of the engine across various airframes.

Low fuel consumption is another pivotal goal in aircraft engine design. Fuel efficiency contributes to longer operational ranges, extended mission durations, and reduced operating costs, all while diminishing the environmental footprint of aviation.

For military applications, the ability to run on Jet Fuel (JP-8) is of utmost importance. This fuel compatibility ensures logistical simplicity and versatility for military aircraft.

Nowadays, the most successful aircraft piston engines run on the 4-Stroke (4S) cycle, burning kerosene[66] or gasoline.[67,68] It is interesting to notice that these engines are specifically designed for aviation, they are not derived from automobile or motorcycle units.

In this scenario, the 2-Stroke cycle yields several advantages, compared to a standard 4-Stroke, 2S engines have demonstrated to be able to reach very high brake thermal efficiencies: the big naval CI engines can easily exceed 50 % [69].

There are several examples of 2S CI aircraft engines, starting from the Junkers JUMO developed before World War II, and the slightly more recent Napier Deltic, both of them adopting the Opposed Piston design.[70] Among the modern propositions, some success was achieved by the WAM engine developed by Wilksch Airmotive, and described in some technical papers.[71,72] The WAM engine is a 3-cylinder in line, 1.8 L, Indirect Injection (IDI) turbocharged engine; it uses a Uniflow scavenging system, with a set of inlet ports along the cylinder liner, and 2 exhaust poppet valves on the cylinder head. The engine weights about 100 kg, and it's able to deliver up to 90 kW at 2600 rpm, in the version described in.[71]

Other 2S CI aircraft prototypes have been developed by DeltaHawk[73] and Zoche[74].

The absence of certified 2S CI aircraft engines on the market (at least at the moment of writing this thesis) demonstrates that the practical application of this concept is far from trivial.

Since their inception in the 1930s, 2-stroke diesel engines have made a significant impact in the field of aviation, offering a distinct set of advantages over their 4-stroke counterparts. These advantages have made them a preferred choice in many aircraft applications.

- Downsizing: The increased cycle frequency allows for the downsizing of the engine. This means that a 2-stroke engine can deliver the same power output as a 4-stroke engine of larger displacement, resulting in a superior power-to-weight ratio. Aircraft engineers can achieve higher power density without adding excessive weight
- Downspeeding: 2-stroke diesel engines can operate at lower rotational speeds while maintaining their power output. This eliminates the need for a reduction drive, a common component in 4-stroke aircraft engines.

- Smoother Torque Output: The double cycle frequency leads to a smoother torque output. This consistent torque curve is highly advantageous for maintaining steady aircraft performance, even with varying operational conditions

Another significant advantage of 2-stroke diesel engines is the absence of poppet valves, a defining feature of 4-stroke engines. This design difference leads to several benefits, among them the elimination of poppet valves results in a simpler engine design with fewer moving parts. Fewer components mean reduced maintenance and a lower likelihood of component failure, leading to enhanced reliability.

Hybrid aircraft, which combine both traditional thermal engines and electric motors, offer several compelling advantages over their fully electric counterparts. One of the key benefits lies in the ability to decouple the thermal engine from the electric motor, especially in a parallel layout. This decoupling leads to a range of advantages, including the flexibility to operate in either a fully electric mode or a full thermal mode, presenting a versatile solution for various flight scenarios. In addition to this flexibility, hybrid aircraft also enjoy enhanced power during critical phases of flight, such as takeoff maneuvers. Furthermore, one must consider that fully electric aircraft face the significant challenge of dealing with the substantial weight of batteries, which can result in a massive overall aircraft weight, potentially limiting their efficiency and performance. These advantages collectively make hybrid aircraft an attractive proposition for the aviation industry, offering a balance between traditional and electric propulsion technologies while addressing some of the limitations associated with full electrification.

Pros:

- Efficiency and Performance: The hybrid 2-stroke power unit can harness the benefits of electric propulsion, such as instant torque and efficient power delivery. This results in improved efficiency and performance. Electric motors can provide an additional power boost during take-off and climb, optimizing the aircraft's performance in critical phases of flight.
- Emissions Reduction: By combining electric propulsion with an internal combustion engine, it's possible to significantly reduce emissions, especially during low-power and cruise phases.
- Wide Operating Range: ICEs have a broader operating range compared to some other propulsion technologies. This means the hybrid system can efficiently adapt to various flight conditions, from low-speed taxiing to high-speed cruising and rapid climb phases.
- Technology Transfer: technologies from the automotive sector can be adapted and transferred to the design and development of hybrid 2-stroke power units for light aircraft. This can potentially expedite advancements and reduce development costs.

Cons:

- Weight Increase: The addition of electric components, such as batteries and electric motors, can increase the overall weight of the aircraft. This added weight can offset some of the advantages gained from electric propulsion, particularly if it results in reduced payload capacity or increased fuel consumption.
- Complexity and Cost: Integrating a hybrid power unit into an aircraft introduces complexity in terms of system design, integration, and maintenance. This complexity can lead to higher manufacturing and maintenance costs, which might not be feasible for some operators, especially in the light aircraft sector.
- Reliability: The reliability of a hybrid power unit can be a concern. It introduces more components and systems, increasing the risk of failures or maintenance issues. Ensuring the reliability of a complex hybrid system is crucial for aviation safety.

5.1 Uniflow scavenged engine performance optimization

One of the most critical aspects is the design of the supercharging system. In a standard 4-stroke turbocharged engine, volumetric efficiency mainly depends on the pressure within the intake manifold. However, in 2-stroke engines, the gas exchange process, determined by the geometry of each cylinder, is governed by the pressure difference between the inlet and exhaust ports. Therefore, the efficiency of each turbo-machinery component, along with the turbine back-pressure, holds a more significant role in 2-strokes. Additionally, when selecting a turbocharger, one must consider the entire range of altitudes at which the aircraft operates.

The proposed 2-stroke engine adopts a Uniflow scavenging system, featuring two exhaust poppet valves on the cylinder head and a set of inlet ports along the cylinder liner. The details of the scavenging system design are supported by 3D-CFD simulations. The combustion system, consisting of an axisymmetric piston bowl and a Common Rail injector positioned nearly coincident with the cylinder axis, mirrors that of a 4-stroke engine.

During the engine's development, several critical design issues were addressed. These included mitigating blow-by between the piston and liner, which is caused by liner deformation and the presence of scavenge ports at the cylinder's bottom. Another significant concern was the cooling of the cylinder head, as it experiences twice the frequency of the 2-stroke cycle. This latter issue can be partially addressed by maintaining a high air-fuel ratio and operating at lower combustion temperatures and pressures.

CMD S.p.a., a LONCIN company, is developing a new CI 2S aircraft engine, named GF56, whose features are listed in Table 14. the engine may have two different layouts: configuration A (twin turbochargers, intercooler, twin Roots superchargers), and configuration B, that differs from the previous one only for the presence of a single turbocharger. Both configurations are of interest, for different aircraft applications (different layout constraints). The engine can be easily installed on many different aircraft, thanks to the compact layout of cylinders (flat 6), and the reduced overall dimensions and weight. In comparison to the best in class certified CI engine, CD-300, by Continental Engines,2 GF56 is lighter (220 vs. 265 kg), and more powerful (360 vs. 300 HP), with similar or smaller overall dimensions. A fair comparison is not possible at the moment, since GF56 has still to receive its certification.

Table 14: Main features of the new 2S CI aircraft engine by CMD

GF56 engine features	
Layout	6-cylinder, boxer
Bore [mm] x Stroke [mm]	106 x 105
Total displacement [cm^3]	5560
Compression Ratio [-]	17.2
Fuel	Diesel Fuel or Jet A-1
Supercharging A	Twin turbochargers, intercooler, twin Roots superchargers
Supercharging B	Single turbocharger, intercooler, twin Roots superchargers
Scavenging type	Uniflow, with exhaust valves and piston controlled scavenge ports
Exhaust valves per cylinder	2
Cooling	Liquid-cooled
Alternator [V]	24
Dry weight [kg]	220
Dimension L x H x W [mm]	1016 x 628 x 912
Target power (sea level) [HP@rpm]	360@2400

5.1.1 Numerical – experimental validation: CFD 1D

The analyzed 2S engine has been modelled using the 1D-CFD software GT-Power. To facilitate this modelling, the software requires certain input data, such as the discharge coefficients of the scavenge ports, which are needed as a function of the port opening degree and pressure ratio across the port. Additionally, for the Zero-Dimensional (0D) modelling of the scavenging process, a correlation between the fraction of combustion products in the exhaust flow and the concentration of exhaust gas within the cylinder is essential.

The analysis reveals that the scavenging process patterns are relatively independent of the gas-dynamic conditions across the cylinder and the position of the cylinder within the air-chest. Furthermore, the quality of the scavenging process in the optimized cylinder configuration is excellent. There is no loss of fresh charge through the exhaust valves until half of the cylinder is emptied, and the concentration of air in the exhaust flow consistently remains much lower than in the cylinder until the fraction of exhaust gas within the cylinder drops to less than 10% [75].

The GT-Power model for the GF56 engine is calibrated using experimental data collected from a prototype that is similar to, though not identical to, the final configuration known as "A" of the engine. The primary differences between the prototype and the final engine configuration lie in the sizes of the turbochargers and Roots blowers, as well as in some geometric details of the scavenge ports.
The engine's operating conditions are defined with consideration for its coupling with a propeller. This means that the load increases with speed. The maximum speed, which is 2400 rpm, corresponds to the maximum power delivered by this older version of the engine. The measurements obtained include the pressure traces of each cylinder, which are ensemble-averaged over 100 cycles.
During the simulation, the engine's performance is evaluated by imposing the experimental operating conditions, including ambient pressure and temperature, engine speed, fuel mass, and intercooler outlet temperature. Additionally, combustion is represented based on the experimental burn rates, which have been measured at various speeds. To account for friction losses, the Chen-Flynn approach is employed, and parameters are configured to align with the experimental values of FMEP.
In the calibration process, one of the crucial parameters considered is the blow-by during compression. This is modelled using a calibrated orifice located between the cylinder and air chest. It's important to note that this aspect represents a significant difference between the calibration of a 2-stroke (2S) and a 4-stroke (4S) turbocharged engine.
Figure 47 show a comparison between experimental and simulation results, considering some fundamental thermo-fluid-dynamic parameters: turbocharger speed (a), turbine inlet pressure (b),air flow rate (c), air-chest pressure (d), Turbine Inlet Temperature (TIT) (e), BMEP (f), in-cylinder pressure trace at 2400 rpm, high load (g), in-cylinder pressure trace at 1800 rpm, low load (h).

The calibrated numerical model demonstrates a high level of accuracy and physical consistency in predicting both average and instantaneous parameters. While generally the agreement between numerical results and experimental measurements is good, there are a few areas with minor discrepancies. For instance, there is a wider gap between numerical results and experimental measures for TIT. Additionally, the instantaneous cylinder pressure at the opening of the exhaust valve appears to be slightly underpredicted, which suggests a potential overestimation of the exhaust valve permeability at low lifts.
Despite these minor differences, the overall agreement between the numerical model and experimental data can be considered quite satisfactory.
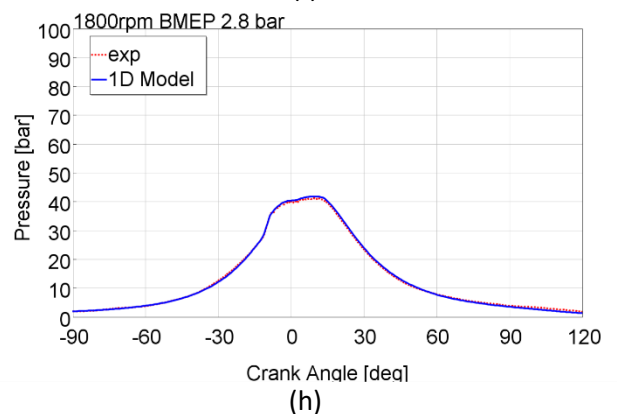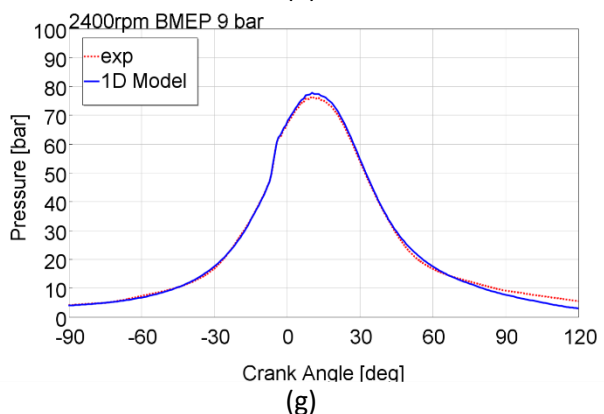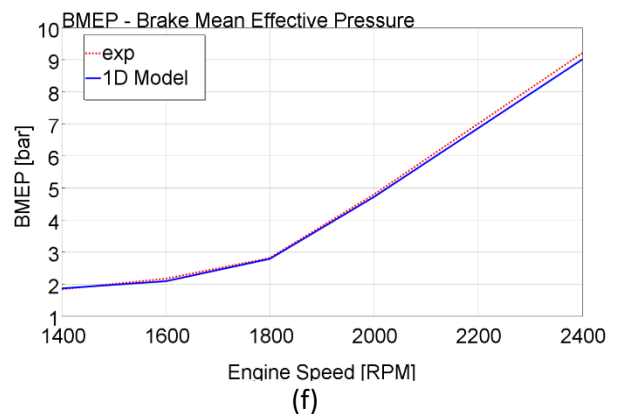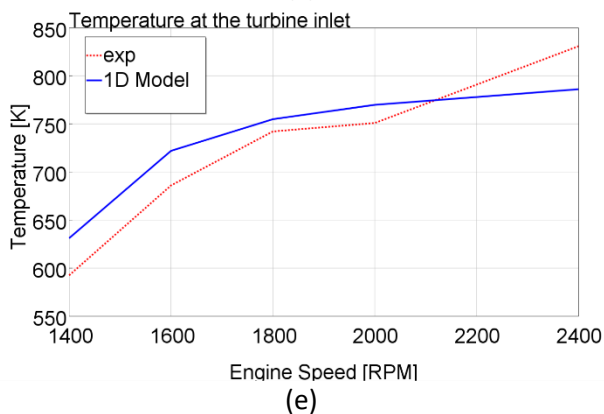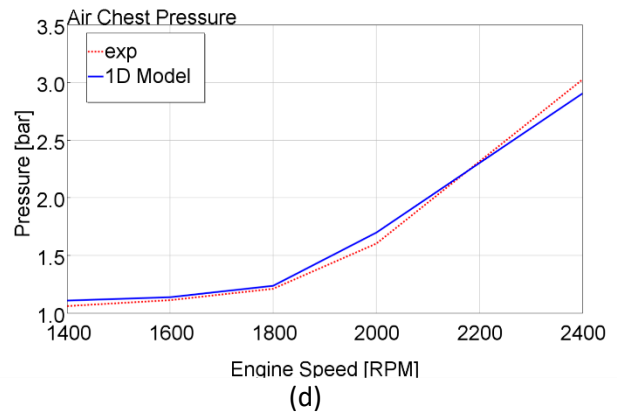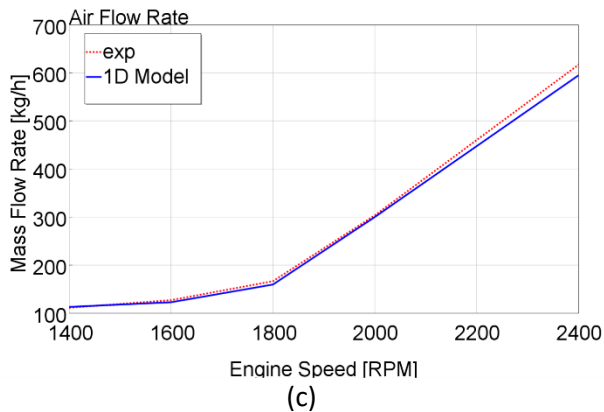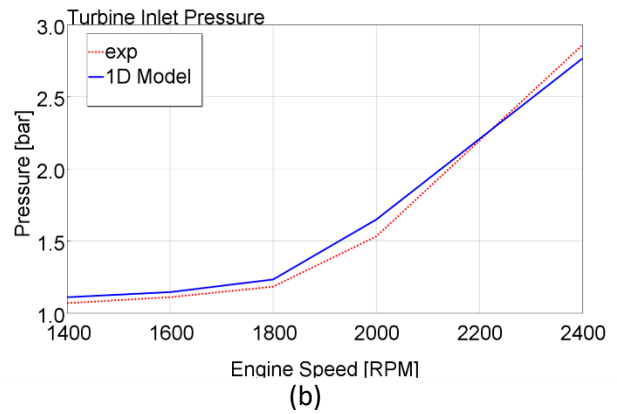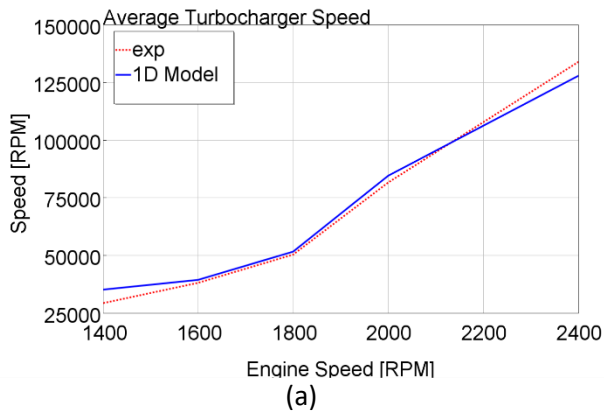
Figure 47: comparison between experimental and numerical results of the calibrated GF56 model

5.1.2   Numerical – experimental validation: CFD 3D

The optimization of the combustion system is supported by 3D-CFD simulations, employing a customized version of the KIVA-3V code.

Due to the almost perfect symmetry of the combustion chamber and the injector nozzle, a sector mesh is considered, the computational grid is depicted in Figure 48.

It's important to note that obtaining an experimental measure of the composition of the charge trapped within the cylinder in 2S engines can be challenging. Exhaust gas analysis alone does not provide a straightforward means of determining the portion of air that bypasses the cylinder during the scavenging process. Additionally, the composition of the trapped charge in 2S engines may vary significantly from one cylinder to another due to the strong dependence on the local dynamics of the inlet and exhaust manifolds.
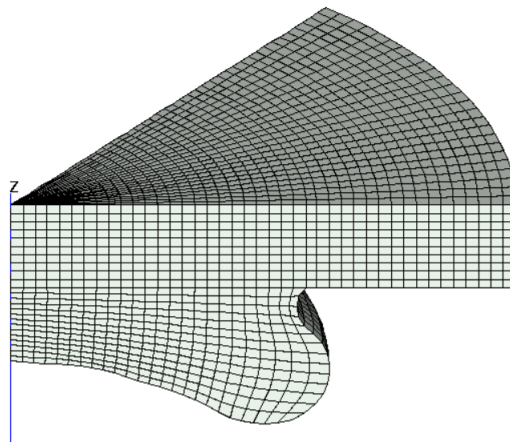
Figure 48: GF45 sector mesh computational grid

To address this challenge, the calibrated 1D-CFD model, supplemented by the results from the 3D-CFD scavenging analyses, plays a crucial role. The 3D-CFD analyses also provide the initial flow field for the combustion analysis, which commences from the closure of the exhaust valves and concludes at their opening.
In Figure 49 , the experimental validation of the 3D-CFD model is presented in terms of pressure traces within the cylinder. This validation covers two engine speeds (1800 and 2000 rpm) and two alternative injection strategies (pilot and main injection, as well as main injection only), all while maintaining the same calibration parameter settings. The comparison between simulations and experiments for all four different points demonstrates a reasonable agreement.
It's important to consider that when comparing experimental pressure traces to simulations, both the experimental measurements and the simulation results are unavoidably influenced by a variety of small uncertainties. For instance, each fuel injector may have slight differences, and the same can be said for the turbochargers and the Roots compressors. The accumulation of these small variations makes it nearly impossible to achieve a perfect match between theory and practice.
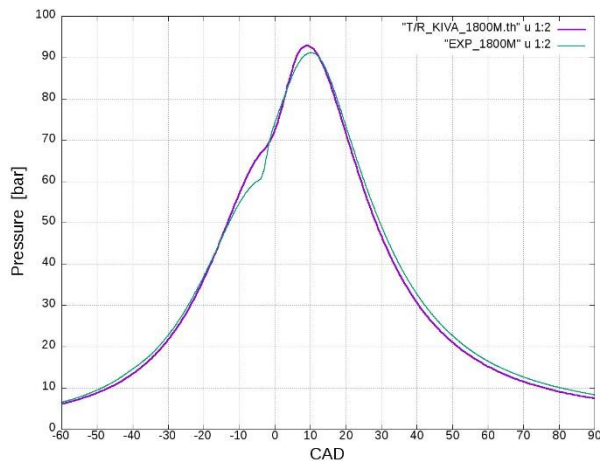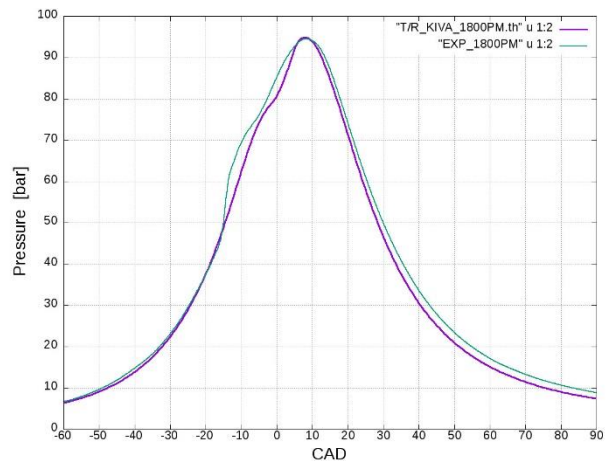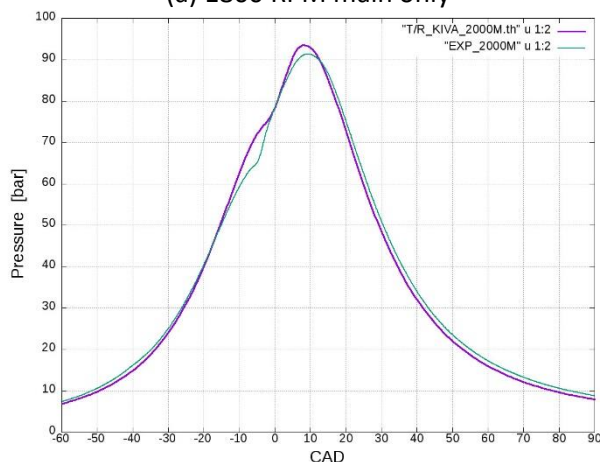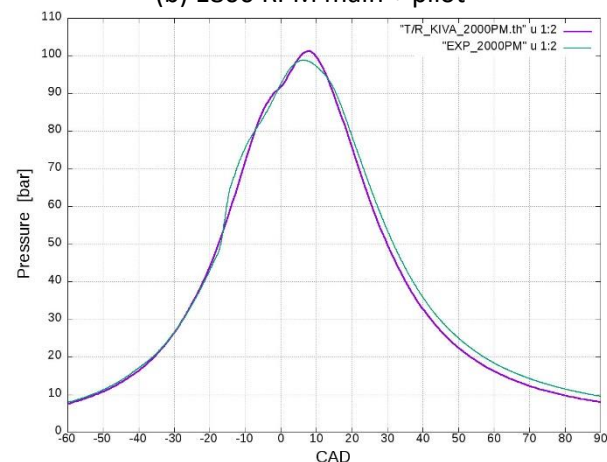
Figure 49: Comparison between numerical (purple line) and experimental (green line) in-cylinder pressure

The experimental results obtained from the initial prototypes have indicated that the geometry of the combustion chamber does not necessitate significant modifications. Additionally, the design of the injector nozzle appears to be reasonable. Consequently, the numerical development of the combustion system was primarily focused on optimizing the injection strategy.

Particular attention was dedicated to take-off conditions, during which the engine operates continuously at maximum load and maximum speed for several minutes. This operating point generates the highest mechanical stress, not only on the engine but also on the propeller. The objectives at this stage are two-fold: first, to ensure complete and efficient combustion from a thermodynamic perspective, and second, to maintain strict control over peak cylinder pressures and PPRR. The specified limits for these parameters are 110 bar and 5 bar/°, respectively.

In evaluating combustion quality, several aspects are taken into consideration:

1. Combustion efficiency, which is the ratio of heat released by combustion to the fuel energy (mass of injected fuel multiplied by its lower heating value).
2. Adiabatic efficiency, which is the ratio of net combustion heat (energy released by combustion minus the heat rejected through the walls) to the total heat released by combustion.
3. IMEP*, which represents the work done by the gas on the piston at closed valves (from exhaust valve closing to exhaust valve opening) divided by the cylinder displacement.

It's worth noting that engine brake power and specific fuel consumption are directly influenced by IMEP*, as the total fuel quantity remains constant for all the analyzed strategies. Furthermore, both adiabatic and combustion efficiencies are crucial for various reasons. Higher adiabatic efficiency results in less heat being rejected through the walls, which in turn allows for smaller, lighter, and less cumbersome coolant radiators, highly advantageous features for aircraft. The completeness of combustion has a direct impact on pollutant emissions, particularly in terms of soot. While this aspect may not currently be regulated, it is highly valued by customers for its contribution to reduced visible smoke emissions.

For compactness of notation, the following symbols are employed:

- M_s#: Main injection only, Start of injection # degrees before TDC
- M&M: Injection split into two similar shots (Main & Main)
- PPM: Split injection made up of 3 shots: Pilot, Pre and Main
- PPPM: Split injection made up of 4 shots: Pilot1, Pilot 2, Pre, and Main

The amount of fuel and the timing of each shot are indicated according to the following notation:

PPPM_Pxx_yy_Pzz_ff_Pgg_hh_Mii_jj

where:

xx: advance of pilot 1 injection from TDC;

yy: percent of fuel introduced in pilot 1 injection;

zz: advance of Pilot 2 injection from TDC;

ff: percent of fuel introduced in Pilot 2 injection;

gg: advance of Pre injection from TDC;

hh: percent of fuel introduced in Pre injection;

ii: delay of Main injection from TDC;

jj: percent of fuel introduced in Main injection.

As an example: PPPM_P40_11_P28_8_P17_8_M2_73 means:

Pilot injection 1: SOI at 40° BTDC, 11% of total fuel;

Pilot injection 2: SOI at 28° BTDC, 8% of total fuel;

Pre injection: SOI at 17° BTDC, 8% of total fuel;

Main injection: SOI at 2° ATDC, 73% of total fuel.

Table 15 shows that the maximum values of IMEP* are obtained by using a single Main injection, phased around TDC. M_s0 provides an indicated work corresponding to 8.6 bar, complying with the limit on peak cylinder pressure (≈106 bar <110 bar). IMEP* cannot be improved without exceeding the limit on peak cylinder pressure.

Table 15: analysed injection strategies at 2400RPM - full load

Name	Swirl Ratio [-]	Total Injected Mass [mg]	Injected mass Pilot1 [%]	SOI Pilot 1 [°CA]	Injected Mass Pilot2 [%]	SOI Pilot 2 [°CA]	Injected mass Pre [%]	SOI Pre [°CA]	Injected Mass Main [%]	SOI MAIN [°CA]	IMEP* [bar]	Pmax [bar]	CA max. pressure [°]
M_s0	2.0	56	0%	-	0%	-	0%	-	100%	0	8.60	105.61	13.6252
M_s2	2.0	56	0%	-	0%	-	0%	-	100%	2	8.77	116.22	10.8743
M&M_M3_37_M5_63	2.0	56	0%	-	0%	-	37%	-3	63%	5	8.33	107.61	11.5726
PPM_P40_10_P15_10_M1_80	2.0	56	10%	-40	0%	-	10%	-15	80%	1	7.90	104.58	11.6334
PPM_P40_16_P16_16_M2_68	2.0	56	16%	-40	0%	-	16%	-16	68%	2	8.23	110.53	10.5403
PPPM_P40_11_P28_8_P17_8_M2_73	2.0	56	11%	-40	8%	-28	8%	-17	73%	2	8.42	104.81	11.8037
PPPM_P40_8_P28_6_P17_6_M1_80	2.0	56	8%	-40	6%	-28	6%	-17	80%	1	8.11	101.60	12.6336
PPM_P40_16_P6_21_M2_63	2.0	56	16%	-40	0%	-	21%	-6	63%	2	8.59	109.64	10.8405

Unfortunately, Table 16 reveals also that PPRR is well over the threshold (9.1 bar/°>5bar/°). Moreover, the heat rejected through the walls is relatively high, getting a lower than average adiabatic efficiency of 84%.

The M&M injection strategy seems to improve PPRR (6.6 bar/°), but not it is not sufficient to meet the limit.

A 3-shot injection (Pilot-Pre-Main, PPM) produces a clear step forward in terms of combustion roughness, but its efficiency is strongly related to the timing of Pre-injection and to the fuel distribution between Pre and Main. The optimum combination is found by merging the end of Pre with the beginning of Main, the last one set at 2° after TDC (PPM_P40_16_P6_21_M2_63). IMEP* is equivalent to the single injection strategy M_s0, with the following further advantages:

- PPRR is strongly lower (3.4 vs 9.1 bar/°);
- the rejected heat is about 1/3 (136 vs 391 J)

The last aspect has a very positive impact on the thermal stress of the cylinder components; moreover, it leaves more energy available for the turbine. This additional energy, if properly used, can reduce the work spent by the positive displacement compressor to pump the air toward the cylinders

The smoothness of combustion can be further improved with a second pilot injection (strategy PPPM), but IMEP* tends to drop a little bit. As an example, with PPPM_P40_8_P28_6_P17_6_M1_80, the minimum values of peak cylinder pressure are obtained (102 bar) and PPRR (3.0 bar/°), but IMEP* falls from 8.59 to 8.11 bar.

	Heat Release [J]	Comb. Eff. [%]	CA 10% [°CA]	CA 50% [°CA]	CA 90% [°CA]	Max T [K]	Heat to walls [J]	Adiab. Eff. [%]	Adiab. x Comb. Eff [%]	PPRR [bar/°]
M_s0	2494.35	100	8.12	12.29	31.59	1885.5	391.1	84.32	84.32	9.08
M_s2	2484.51	100	5.73	9.56	30.13	1897.3	405.7	83.67	83.67	10.32
M&M_M3_37_M5_63	2389.84	99.25	5.03	10.99	36.79	1813.7	366.1	84.68	84.04	6.62
PPM_P40_10_P15_10_M1_80	2319.15	96.31	1.90	11.24	42.48	1731.5	90.3	96.11	92.56	2.93
PPM_P40_16_P16_16_M2_68	2346.58	97.45	-2.89	10.23	39.32	1785.9	347.6	85.19	83.02	3.58
PPPM_P40_11_P28_8_P17_8_M2_72	2444.82	100	-2.85	11.80	38.03	1787.4	78.1	96.80	96.80	3.48
PPPM_P40_8_P28_6_P17_6_M1_79	2416.79	100	1.00	12.63	40.70	1752.1	83.8	96.53	96.53	3.05
PPM_P40_16_P6_21_M2_63	2436.91	100	1.51	10.84	36.07	1812.0	135.9	94.42	94.42	3.43

In Figure 50 a visual representation of the combustion development for the best injection strategy during take-off, labeled as PPM_P40_16_P6_21_M2_63, is depicted. Oxygen concentration is illustrated on two cross-sectional planes: the first is a radial plane that includes the cylinder axis and the axis of one of the injector holes, while the second is a horizontal plane, perpendicular to the cylinder axis and passing through the injector hole.

At 2 degrees before TDC, combustion is just initiating along the hole axis, not far from the injector nozzle. A pale blue region, indicating the presence of fuel vapor, is observed at the far end of the bowl, in the direction of the hole axis. This region serves as the storage location for most of the fuel injected by the pilot, accounting for about 16% of the total fuel quantity.

Between 6 degrees and 20 degrees after TDC, combustion predominantly occurs within the main bulk of the bowl, surrounded by a layer of air, especially over the piston and along the liner. This air "cushion" functions as a thermal barrier, contributing to the exceptional adiabatic efficiency of the system, which exceeds 94%. The influence of the counterclockwise swirling flow is evident in the deformation of the combustion plume, causing it to divert from the hole axis and bisect the sector.

At 60° after TDC combustion is complete, leaving no unburnt fuel. The residual Oxygen is due only to the excess of air (trapped $\lambda \approx 1.45$)
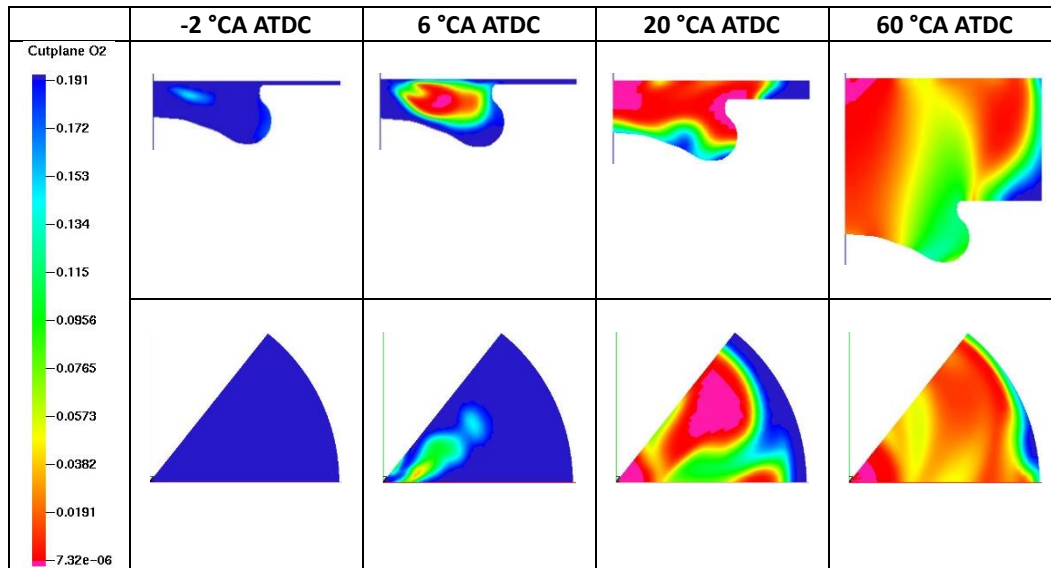
Figure 50: Combustion development in the sector mesh injection strategy PPM_P40_16_P6_21_M2_63. O2 molar fraction

5.1.3   Engine performances optimization at sea level

The calibrated engine model was used to optimize some fundamental design parameters, in particular:

- height of the scavenge ports (defining also the timing and the mean effective area available for the inlet flow);
- phase and lift profile of the exhaust valves (defining also the timing and the mean effective area of the exhaust flow);
- transmission ratio between engine and Roots superchargers;
- size of the turbocharger (swallowing capacity of turbine and compressor).

The main goal of the optimization is to achieve the performance targets (in particular the rated power of 360 HP at 2400 rpm, sea level) minimizing fuel consumption and complying with all the design constraints. As far as the last ones are concerned, the most important are:

- no radical change to the engine design concepts, only refinements (in order to maintain and possibly improve the lightness of construction);
- peak cylinder pressure at continuous full load conditions <110 bar, for the same reasons mentioned above;
- peak cylinder pressure at maximum load for a limited amount of time (overload conditions) <125 bar
- peak TIT <800 °C (for turbine reliability and durability);
- peak charge temperature at the supercharger outlet <150 °C (for supercharger reliability and durability);
- mass flow rate unbalance among cylinders <5 % (for smooth and repeatable engine operations).

The design of the supercharging system stands out as one of the most critical aspects. In a standard 4-stroke turbocharged engine, volumetric efficiency is primarily influenced by the pressure within the intake manifold. However, in 2-stroke engines, the gas exchange process is dictated by the pressure difference between the inlet and exhaust ports, which is determined by the cylinder geometry. Consequently, the efficiency of each component of the turbo-machinery and the back-pressure of the turbine play a more

significant role than in 4-stroke engines. Moreover, when selecting a turbocharger, it's essential to consider the entire range of altitudes at which the aircraft may operate.

The proposed 2-stroke engine utilizes a Uniflow scavenging system, featuring two exhaust poppet valves on the cylinder head and a set of inlet ports along the cylinder liner. The design of the scavenging system was aided by 3D-CFD simulations. The combustion system comprises an axisymmetric piston bowl and a Common Rail injector positioned almost coincidentally with the cylinder axis, resembling that of a 4-stroke engine.

Throughout the engine's development, significant efforts were dedicated to addressing issues such as blow-by between the piston and liner, which is caused by liner deformation and the presence of scavenge ports at the cylinder bottom. Another challenge was cooling the cylinder head due to the higher frequency of the 2-stroke cycle. The cooling challenge can be partly mitigated by maintaining a high air-fuel ratio, resulting in lower combustion temperatures and pressures.

The engine's compact cylinder layout, in a flat-6 configuration, and reduced dimensions and weight make it highly adaptable to various aircraft. When compared to the best-certified CI engine, the CD-300 by Continental Engines, the GF56 engine is both lighter (220 kg vs. 265 kg) and more powerful (360 HP vs. 300 HP), with similar or smaller overall dimensions. However, it's important to note that a fair comparison is currently not possible as the GF56 is awaiting certification.

The 2-stroke engine under analysis has been modelled using the 1D-CFD software GT-Power. To perform the simulation, the software requires input data, including discharge coefficients of the scavenge ports in relation to the port opening degree and the pressure ratio across the port. Furthermore, for Zero-Dimensional modelling of the scavenging process, a correlation between the fraction of combustion products in the exhaust flow and the concentration of exhaust gas within the cylinder is crucial. The analysis reveals that scavenging process patterns remain mostly consistent and independent of gas-dynamic conditions across the cylinder and its position within the air chest. Additionally, the optimized cylinder configuration exhibits commendable characteristics, with no loss of fresh charge through the exhaust valves until half of the cylinder is emptied, and the concentration of air in the exhaust flow consistently lower than in the cylinder until the fraction of exhaust gas within the cylinder is less than 10%.

The GT-Power model of the GF56 engine is calibrated using experimental data from a prototype that closely resembles the final engine configuration (Configuration A), with some variations primarily relating to the size of the turbochargers, Roots blowers, and specific geometric details of the scavenge ports. The engine's operational conditions are defined with consideration for its coupling with a propeller, where the load increases with speed. The simulation is executed by applying the experimental operating conditions, including ambient pressure and temperature, engine speed, fuel mass, and intercooler outlet temperature. Furthermore, combustion is represented using experimental burn rates, while friction losses are modelled using the Chen-Flynn approach, with parameters set to match the experimental values of FMEP.

The calibrated numerical model exhibits accuracy and physical consistency in predicting both average and instantaneous parameters. Although some minor discrepancies may exist, the agreement between numerical results and experimental measurements can be considered satisfactory.

It is worth noting that obtaining an experimental measure of the charge composition trapped within the cylinder in 2-stroke engines poses challenges since exhaust gas analysis doesn't readily reveal the portion of air bypassing the cylinder during the scavenging process. Moreover, the charge trapped in 2-stroke engines can significantly vary from one cylinder to another due to local dynamics in the inlet and exhaust manifolds.

To tackle this challenge, the calibrated 1D-CFD model, coupled with the outcomes from 3D-CFD scavenging analyses, proves to be an invaluable tool. The 3D-CFD simulations furnish the initial flow field for the

combustion analysis, commencing at the moment of exhaust valve closure and concluding upon their opening. Experimental validation of the 3D-CFD model, as depicted in Figure 49, illustrates reasonable agreement between simulations and experiments across various engine speeds and injection strategies.

In 2-stroke engines, the distribution of flow among cylinders plays a pivotal role, and this aspect is often more critical than in 4-stroke engines. This trend was also observed in the initial prototypes of the GF56 engine. The absence of distinct exhaust and intake strokes in 2-stroke engines means that the gas exchange process is entirely dictated by the fluid-dynamic conditions unique to each cylinder, which may exhibit non-uniform behavior. Consequently, meticulous attention was devoted to designing equivalent flow paths for all cylinders and ensuring symmetry between the two cylinder banks. The deployment of a single turbocharger offers advantages in addressing this issue.

Roots superchargers, situated after the intercooler and directly delivering air into the air chests, make significant contributions to maintaining the regularity and uniformity of the flow. Although the engine can operate without them in most operating conditions, it is impractical to remove or bypass them at full load. To minimize the power absorbed by these machines, a suitable transmission ratio is selected for each displacement. In the case of an ideal turbocharger capable of delivering the target air mass flow rate independently, the pressure ratio across the supercharger should be precisely 1 under conditions of maximum brake power. This configuration would result in zero work being imparted to the charge, with the power subtracted from the engine being solely that required to offset the mechanical losses linked to rotor motion.

At full load conditions, the installation of a charge cooler between the turbocharger compressor and the mechanical blower becomes imperative to prevent rotor overheating. This cooling process not only prevents rotor overheating but also increases the airflow rate due to the higher gas density entering the cylinders. Although the possibility of adding a second intercooler, positioned between the Roots compressor and the air chest, was considered, it was eventually rejected due to design complexity, increased dimensions, and added weight.

Selecting the appropriate turbocharger poses a significant challenge for an aircraft engine, especially one designed to operate over a wide range of altitudes, including altitudes as high as 18,000 ft (5486 m). Ensuring a brake power exceeding 270 HP (equivalent to 75% of the rated power) at this maximum altitude represents a fundamental objective. The size of the turbocharger and the transmission ratio of the superchargers are influenced by this goal. As altitude increases, air density decreases, and because there is no waste-gate for turbine control, the operating point on the compressor map shifts to higher turbocharger speeds and pressure ratios. When the choke limit is reached, it becomes necessary to reduce the fuel rate and brake power to prevent over-speeding of the turbocharger. To maintain an effective engine-turbocharger match, the operating points on the compressor map at sea level should remain significantly distant from the choke limit, allowing for adjustments within the map as altitude increases. Consequently, the greater the altitude to be reached, the higher the swallowing capacity required by the turbocharger. It is essential to bear in mind that high-altitude performance is balanced by high fuel consumption at sea level.

The engine's operation encompasses two primary sets of conditions: full load and propeller load. Under full load, brake outputs are mainly constrained by the minimum trapped air-fuel ratio necessary for achieving complete and smokeless combustion, with burn rates directly predicted from CFD 3D simulations. Another critical limitation pertains to the maximum cylinder pressure, particularly at high speeds (2200-2600 rpm), where there is a defined limit set at 125 bar. In the case of the propeller curve, a cubic curve is employed, with a maximum value of 320 HP at 2400 rpm, specifically tailored for typical aircraft applications.

The choice between a single turbocharger and a pair of twin turbochargers has minimal influence on 1D-CFD results, as both configurations offer equivalent air intake capacity. The slightly greater inertia of a single

turbocharger is not a significant concern for steady-state simulations. However, the analyzed configuration involves twin turbochargers, with the turbomachinery represented by experimental maps for both the compressor and turbine. It is assumed that the intercooler employs the same system as used in experimental tests, thus eliminating the need for adjustments to the calibrated 1D-CFD engine model. Figure 51(a)shows the pressure differential across the cylinders, depending on the turbocharger balance (compressor outlet and turbine inlet pressure), as well as on the contribution of the supercharger (visible in Figure 51(b)). Differently from a 4S, the airflow rate delivered by the engine is mainly controlled by this pressure differential, in combination with cylinder permeability. It is observed that the supercharger provides a PR higher than 1 (up to 1.2) only at medium-high speeds (>2000 rpm), while at lower speeds it is almost "transparent" (but it helps to keep the flow regular, stabilizing the oscillations of turbocharger speed). Even when the supercharger plays an active role on scavenging at sea level, its efficiency remains quite low. However, it should be considered that this component is designed to be light and compact, more than efficient; moreover, as altitude increases, its efficiency improves.
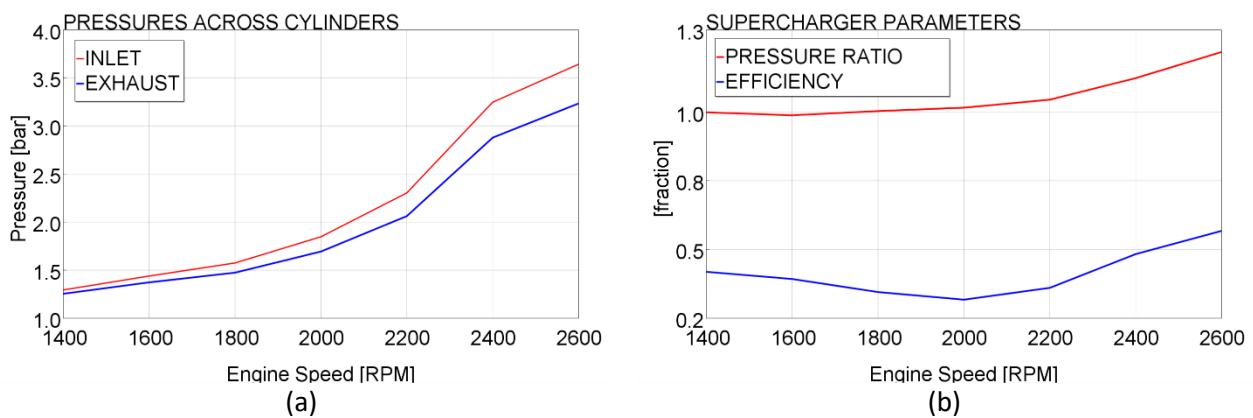
Figure 51: simulation at full load, sea level, cylinder delta-pressure and supercharger behavior

The air available for combustion is much lower than the delivered mass(Figure 52(b)): trapping efficiency is about 0.5 (Figure 52(a)), meaning that one half of the air pumped into cylinders goes to the exhaust.

At the speed corresponding to the maximum power output (2400 rpm), the charging ratio stands at approximately 1.35, while the scavenging efficiency reaches 87%. Notably, the composition of the trapped charge at maximum power for the GF56 engine bears a qualitative resemblance to the composition within the cylinder of a typical 4-stroke Diesel engine operating at medium load with 13% of EGR. As a result, it is reasonable to expect that no substantial distinctions will arise in terms of combustion when compared to a conventional 4-stroke CI engine.
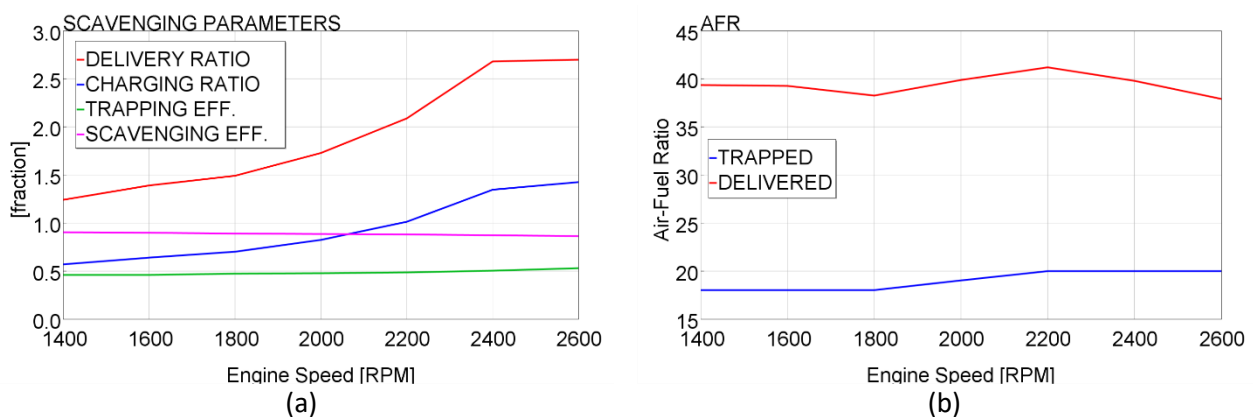
Figure 52: simulation at full load, sea level, scavenging parameters (a) and air-fuel ratio (b)

The operations of both compressor and turbine for each bank of cylinders may be analyzed by plotting the operating points on the corresponding maps: Figure 53 shows both the compressor and the turbine. The graphs show that all the operating points of interest fall in high efficiency areas, demonstrating that the matching between engine and turbocharger is very good.
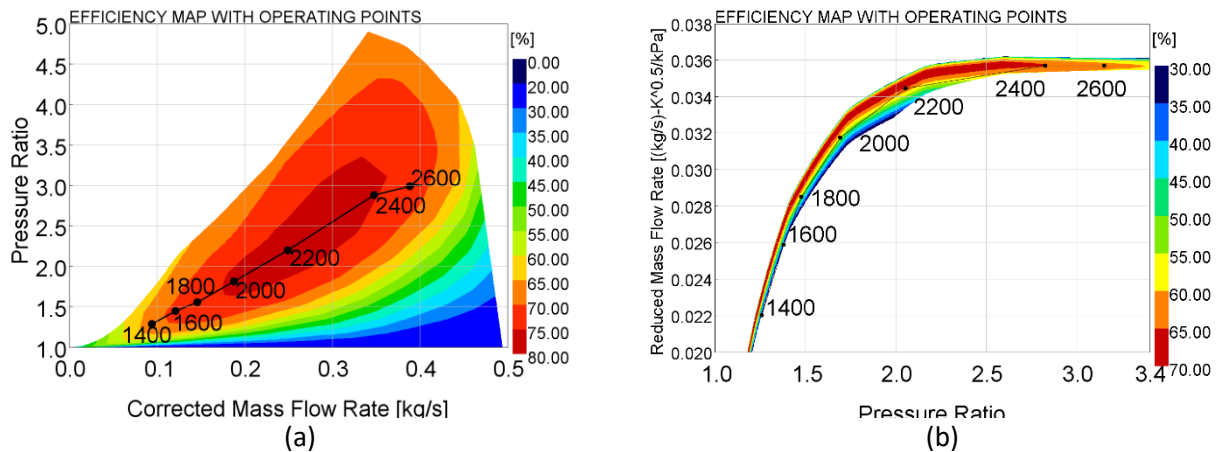
Figure 53: simulation at full load, sea level, efficiency map for compressor (a) and turbine (b)

Figure 54 reported different set of characteristic parameters. As expected, at maximum power the values of IMEP and BMEP (Figure 54(a)) are quite low for a turbocharged engine (15 and 12.5 bar, respectively), and comparable to the typical values of a naturally aspirated 4S SI engine. The value of AMEP (Figure 54(b)) at 2400 rpm (1.5 bar) is similar to the one observed at full load, high speed on a 4S CI marine engine, equipped with a turbine controlled by a waste-gate valve.18

The FMEPs are roughly halved when compared to those typically encountered in 4-stroke Diesel engines with the same mean piston speed and in-cylinder peak pressure. In terms of standard brake parameters, including torque, power, BSFC and BTE, are presented in Figure 54(c-d). t's worth noting that the power target at 2400 rpm surpasses the expected value by approximately 16 HP, equivalent to a 4% increase, and further enhancements of up to 24 HP can be achieved by elevating the propeller speed to 2600 rpm. This surplus power could be employed to optimize down-speeding, leading to reduced fuel consumption, diminished mechanical strain on rotating components, and a reduction in propeller noise.

Figure 54 (e) presents a check on two fundamental constraints, for engine reliability and durability: TIT and cylinder peak pressure. It is noted that the TIT is much lower than the limit, because of the dilution with fresh air, during the scavenging process.

As far as the performance along the propeller curve is concerned, Figure 54(f) illustrates BSFC and power concerning engine speed. The decrease in fuel-specific consumption during cruising conditions, compared to full-load operations, can be attributed to the following factors:

- The trapped air-fuel ratio is significantly higher, resulting in lower average combustion temperatures and peak cylinder pressure, thereby reducing thermal and mechanical losses.
- During part-load conditions, the power consumed by the Roots blowers is minimal.

In the crucial cruising conditions, particularly at 55%, 65%, and 75% of the maximum propeller power (320 HP), the BSFC is approximately 211 g/kWh. This is a remarkable achievement when compared to the typical values found in 4-stroke spark-ignition engines (250-300 g/kWh).
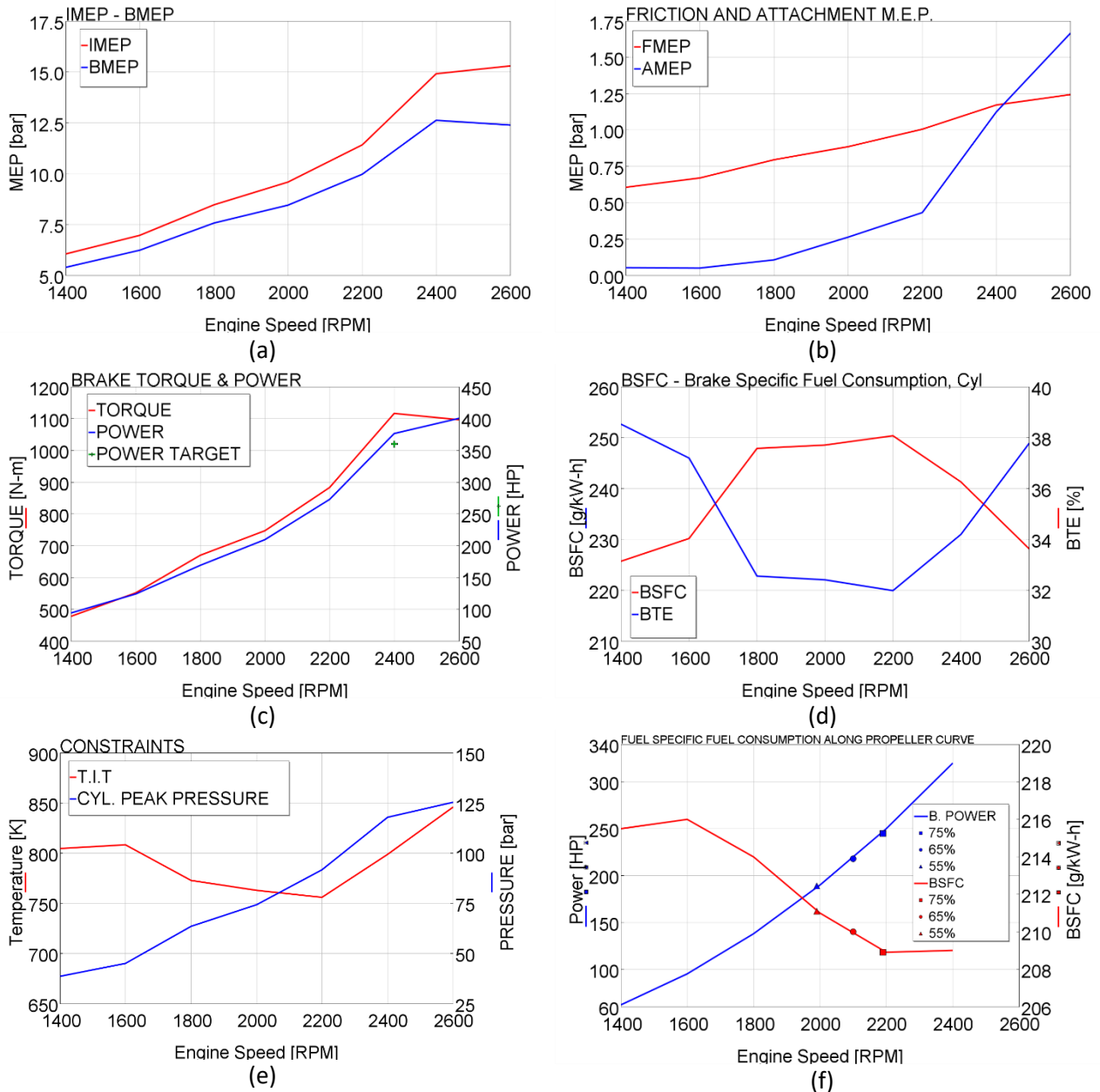
Figure 54: simulation at full load, main engine parameters

5.1.4   Engine performances optimization at high altitude

As noted earlier, an aircraft engine needs to produce substantial power even at high altitudes, where the air is much less dense. Since turbochargers in such engines do not possess direct control features like a waste-gate valve or a variable geometry turbine, it becomes imperative to precisely calibrate fuel rates at various altitudes. This calibration is necessary to maximize power output while avoiding the risk of over-speeding. By carefully selecting the appropriate turbocharger and fine-tuning the transmission ratio between the

engine and supercharger, it's possible to maintain adherence to the smoke limit, which is enforced at sea level and extended up to 18,000 feet, with trapped Air-Fuel Ratios ranging between 18 and 20. Figure 55(a) shows how the operating conditions are shifting on the turbocharger compressor map, as altitude increases. The operating conditions of the supercharger, Figure 55(b), are modified by altitude: as it increases, pressure ratio increases, along with the machine efficiency.
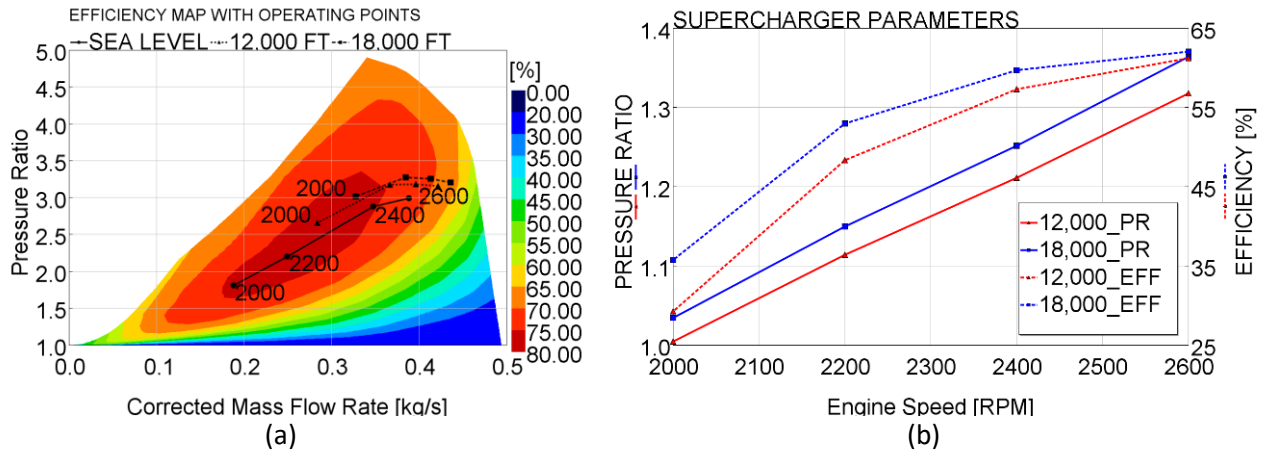
Figure 55: simulation at full load, high altitude, efficiency map for compressor (a) and supercharger (b)

Figure 56 illustrates the impact of altitude on brake power and BSFC. While the latter is only mildly affected, peak power decreases with increasing altitude. For instance, at 12,000 feet, the GF56 can still deliver 325 HP at 2600 rpm, while at 18,000 feet, the peak power is 280 HP. The design objective of achieving 75% of rated power at 18,000 feet, equivalent to 270 HP, has been met with a small margin.

Notably, the engine's efficiency at typical cruise speeds (2000-2200 rpm) consistently outperforms that at peak power across all altitudes. This is a positive outcome since aircraft engines primarily operate in cruise mode, making the overall range significantly dependent on efficiency in this condition rather than at maximum power.
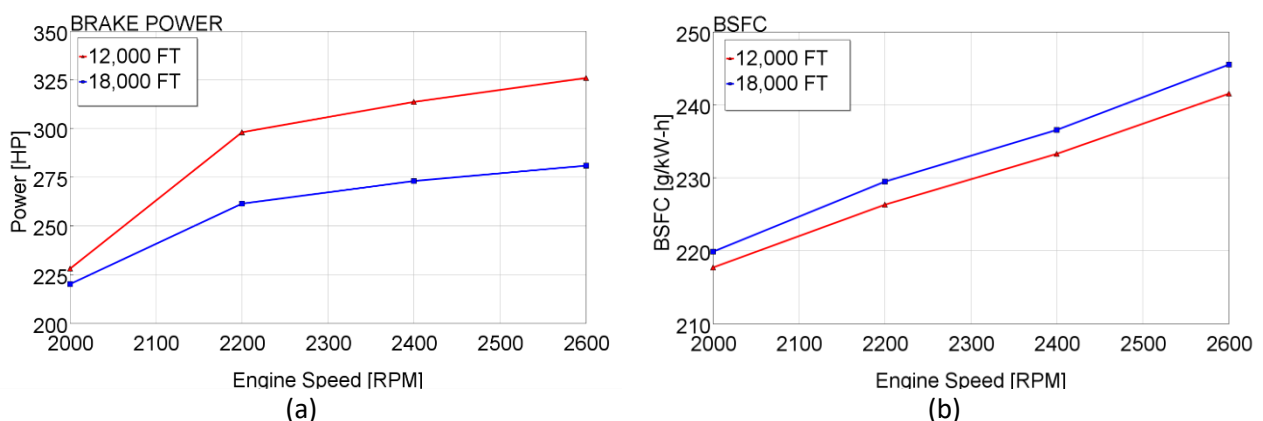
Figure 56: simulation at full load, high altitude, brake power (a) and BSFC(b)

5.2 Loop scavenged engine injection optimization

In this section, a new compact, lightweight, environmentally friendly, and efficient 2-Stroke Spark Ignition hybrid engine is proposed. It features an innovative semi-direct fuel injection system that has been optimized using CFD simulations. The reference for this design is the 850cc E-TEC 2-stroke DI engine developed by BRP-Rotax for snowmobiles. This reference engine is known for its excellent power-to-weight ratio (121 kW/42.2 kg) and its advanced solutions for scavenging and the combustion system [76].

The proposed ICE is expected to weigh less than 60 kg, deliver 110 kW at 6000 rpm, and maintain a low Brake Specific Fuel Consumption of under 260 g/kWh under various operating conditions. One of the key challenges with this type of engine is the loss of fresh charge at the exhaust due to the short circuit. To address this issue, a specific injection system has been developed to maximize fuel trapping and ensure proper charge stratification at the beginning of combustion [77].

5.2.1 Engine design: target and constrains

The engine's total displacement is determined by limitations on maximum BMEP and engine speed. A BMEP of 10 bar ensures a balance between thermal and mechanical loads, while an engine speed of 6000 rpm matches the requirements of the Electric Motor (EM) and propeller. To achieve a maximum brake power of 110 kW at 6000 rpm, the engine's total capacity must be at least 1.1 liters.

For the scavenging system, the crankcase pump is rejected due to emissions related to lubricant oil in the exhaust. An external supercharger is chosen to push air into the cylinders. Since the maximum BMEP target is relatively low, neither a turbocharger nor a charge air cooler is necessary. A commercial centrifugal compressor, mechanically coupled to the engine through integrated reduction gears, is selected for its compact size, low weight, and installation flexibility.

The choice of an in-line triple-cylinder configuration is considered ideal, providing a balance between reducing unit displacement and achieving smooth instantaneous torque output. A loop scavenge system with piston-controlled ports is preferred over a uniflow system to avoid a camshaft system and reduce friction losses. A loop configuration offers more design flexibility for the combustion chamber and enhances the tumble vortex, facilitating charge stratification and premixed combustion.

The bore-to-stroke ratio of this engine type is set close to 1, as higher values limit cylinder permeability, while lower values increase overall dimensions and mean piston speed. Following the example of the Rotax 850 E-TEC engine, the bore and stroke are set at 82 and 80.4 mm, respectively.

In 2S engines, designing ports involves a balance between two competing requirements. On one hand, large scavenge and exhaust ports are essential to minimize pumping losses and reduce cylinder peak pressures and temperatures. On the other hand, enlarging these ports can weaken the cylinder liner excessively. The recommended trade-off in best engineering practice is to maintain a ratio of port width to liner width (approximately π times the bore) at about 0.8. Scavenge ports should occupy a portion of the cylinder liner approximately three times larger than that of the exhaust ports. It is crucial to ensure that the width of each port remains less than 20% of the liner width to prevent damage to the piston rings. [78,79].

The engine design includes five scavenge ports and one primary exhaust port, with an additional pair of smaller exhaust ports, known as boosters, placed above the scavenge ports closest to the main exhaust. The heights of these ports are critical for meeting performance goals, and they have been optimized through 1D CFD simulations.

One of the key project constraints is that the charge temperature at the supercharger outlet should remain below 70°C to avoid the need for a charge cooler.

Regarding the exhaust system, various designs have been evaluated, with a focus on the main geometric parameters of the exhaust pipes and the silencer. Several designs were compared, including:

a) Separated exhaust lines for each cylinder.
b) A log manifold with a single exhaust pipe fed by short ducts from each cylinder and a single terminal pipe.
c) A 3-in-1 manifold with three equally long exhaust ducts joined to the terminal through a junction.
d) A log manifold with two terminals.

Option (a) provides maximum power at high speeds but is bulky and heavy. Option (b) is compact and lightweight but may introduce some variations in delivered air among cylinders. Option (c) can minimize differences among cylinders, provided each pipe is bent to have the same length as the others. Finally, option (d) is seen as the best compromise, allowing for a compact and efficient exhaust system with good uniformity among cylinders. The layout of the engine and its main characteristics are presented in Figure 57 and Table 17. The exhaust system includes also a silencer, not shown in the picture.

Table 17: proposed loop engine main characteristics
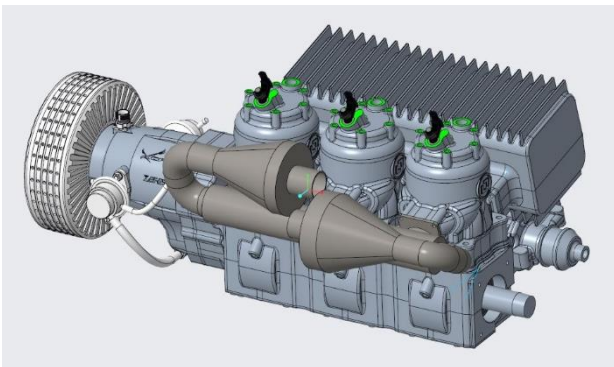
Figure 57: CAD model of the proposed loop Powertrain (ICE+EM)

Bore x Stroke [mm]	82 x 80.4
Number of cylinders	3
Compression ratio	11.6:1
Total displacement [cm^3]	1243
Total Dry weight [kg]	50
Lubrication System	Forced, dry sump
Dimensions LxHxW [cm]	93x45x62
Air supply	Mechanical Supercharger (Rotrex C30-94), w/o charge cooler

5.2.2 Scavenging process optimization

The first step of the project was the analysis of the design solutions adopted on the BRP-Rotax 850 cc E-TEC engine. A CFD-1D model of this engine was built by using GT-Power and calibrated against experiments, at both full and partial loads [76]. Engine main characteristics are reported in Table 18, as it possible to see the dimensions are similar to the proposed virtual engine.

Table 18: BRP Rotax 850cc E-TEC engine main characteristics

Engine type	2-stroke, SI, DI, crankcase scavenging, reed valves
Bore x Stroke [mm]	82 x 80.4
Cylinders	2 in-line (180°)
Total displacement [cm^3]	849
Compression ratio	12.5:1
Rated power@8000rpm [kW]	121
Max. bmep@7800rpm [bar]	10.7

Figure 58(a) shows a comparison between simulation and experiments in terms of brake torque and power at wide open throttle. Figure 58(b) offers an additional comparison, taking into account partial load operations. It illustrates the alignment between the predicted and measured parameters, such as brake power and specific fuel consumption, against the snowmobile speed. The agreement between the two sets of data is notably satisfactory.
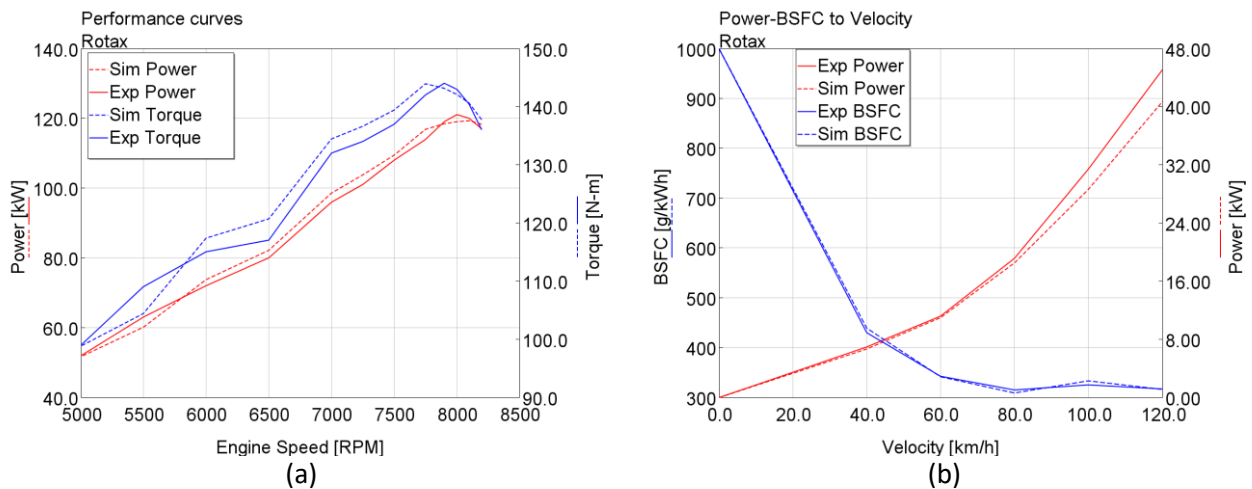
Figure 58: Experimental calibration of the BRP Rotax 850cc CFD 1D model. WOT (a) and snowmobile speed (b)

The initial CFD-1D model of the aircraft engine was originally derived from the calibrated model of the reference snowmobile unit. It served as the foundation for establishing the necessary boundary and initial conditions for conducting a simplified 3D analysis of the scavenging process, excluding fuel injection. In this analysis, the fresh charge was represented by O2, while Nitrogen (N2) was used to represent the exhaust gas. The multidimensional simulation covered the time from the opening to the closing of the exhaust ports.

An iterative approach was followed, which involved adjusting the initial pressure if the mass of the charge trapped at the closing of the exhaust ports did not align with the cylinder conditions defined at the beginning of the calculation.

The primary focus was on the operating condition corresponding to maximum brake power and maximum engine speed (6000 rpm, full load). This condition is particularly critical for an aircraft engine as it allows for minimal time for air-fuel mixing and involves the maximum injected fuel quantity.

The results of the 3D simulations at maximum power were employed in three main ways:

- They provided in-depth insights into the flow patterns through the ports and within the cylinder, highlighting strengths and weaknesses in the existing design. This information was instrumental in addressing evident issues and enhancing the overall system.
- The scavenging process patterns observed in the 3D simulation were used to develop a precise zero-dimensional model, which was incorporated into the CFD-1D engine model, thereby improving its accuracy.
- Flow rates through the ports, as calculated by both the 3D and 1D simulations under identical conditions, were compared. This comparison led to the correction of the discharge coefficients in the 1D model to align with the 3D simulation results, enhancing the model's accuracy.

As an example of the optimization carried out on the cylinder ports, Figure 59 shows a geometric comparison between the first configuration, named "base", and the final one, referred to as "EVO". As visible, the volume of the manifold wrapped around the cylinder has been increased, in order to get a smoother path between the inlet plenum and the set of scavenge ducts.
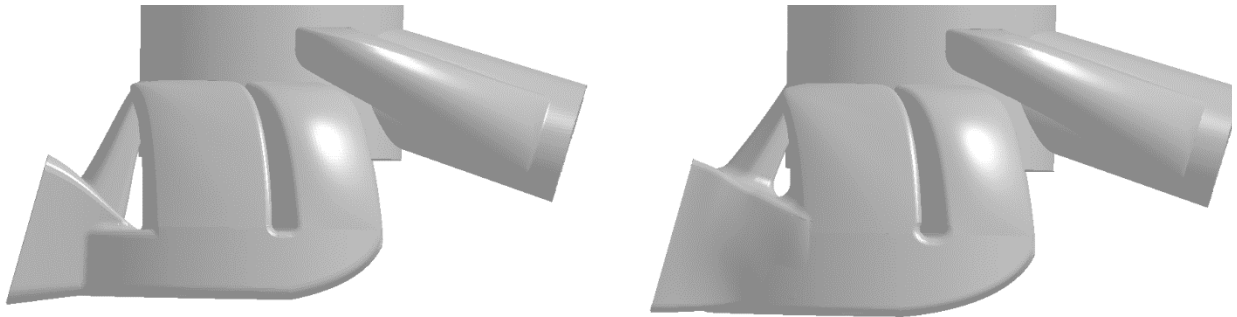
Figure 59: CAD model of the two configurations: base (a) and EVO (b)

Figure 60, illustrates trapping efficiency, charging efficiency, and scavenging efficiency as they relate to the delivery ratio. Notably, the EVO configuration outperforms the base configuration, displaying higher permeability, which results in an improved charging and scavenging efficiency. It also exhibits slightly better retaining/trapping efficiency. This observation is further supported by analyzing the fraction of residual gas in the exhaust flow concerning the fraction of residual gas within the cylinder.
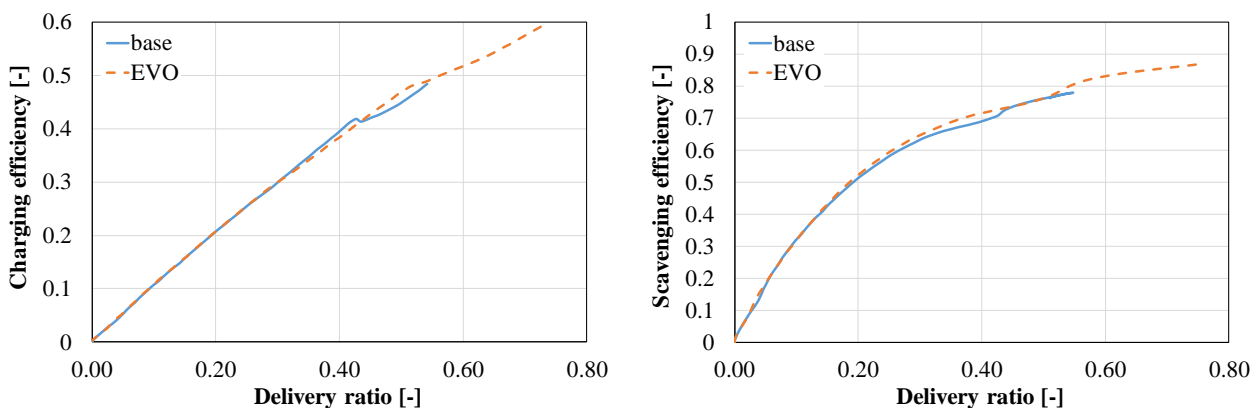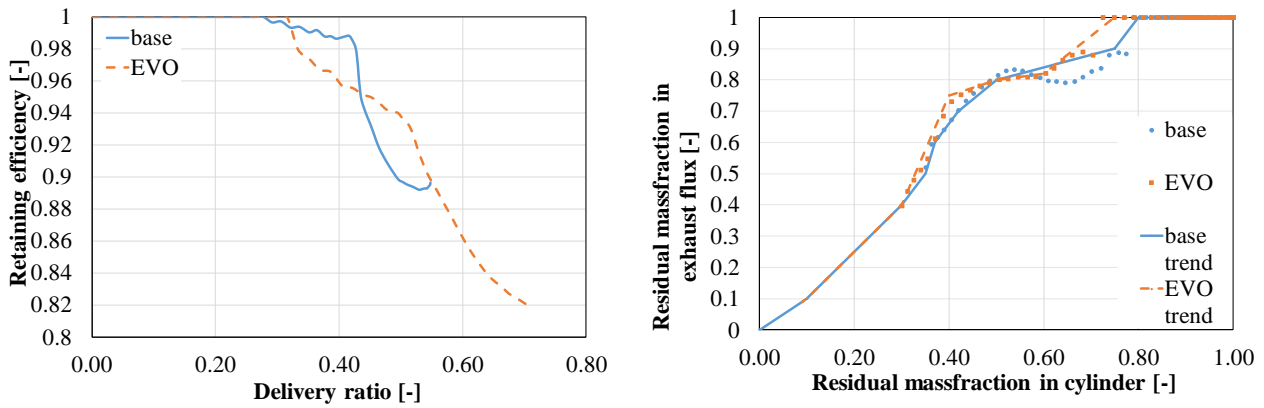
Figure 60: comparison between CFD 1D base and EVO model in term of scavenging efficiency parameters

Figure 61 shows a comparison between results of the calibrated GT-Power 1D model and those of the 3D Forte model. Table 19 presents the same comparison, in terms of average quantities (delivery ratio, trapping efficiency, charging efficiency, scavenging efficiency). The accuracy of the CFD-1D model is very satisfactory: the maximum error is 2.9%, on the fraction of residual gas.
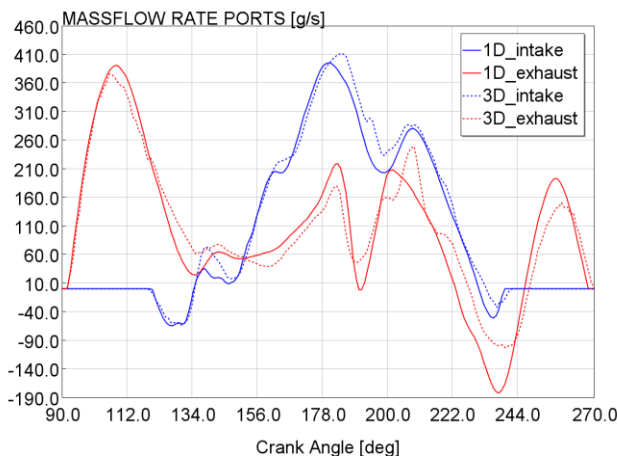
Figure 61: Comparison between the results of the calibrated 1D model and the outputs of the 3D scavenging simulation in term of mass flow rate

Table 19: Comparison between the results of the calibrated 1D model and the outputs of the 3D scavenging simulation in term of main scavenging parameters

	DR	TE	CE	SE	EGR%
CFD 3D	0.787	0.750	0.591	0.850	0.150
CFD 1D	0.791	0.739	0.585	0.846	0.154
Err [%]	-0.5	1.5	1.0	0.5	-2.9

The calibrated CFD-1D engine model was used to configure the optimization of scavenge and exhaust port timings, determine the transmission ratio between the engine and supercharger, and design the exhaust system, which includes the silencer. Additionally, combustion was modelled similarly to the Rotax 850 engine, with identical burn rate curves specified using a Wiebe's function.

5.2.3 Injection system development

For fuel injection system different solutions are taken into consideration. The most interesting alternatives are:

1. High Pressure Direct Injection (HPDI): one injector installed on the cylinder head, close to the spark plug, as on spray-guided 4S GDI engines;

2. Low Pressure Direct Injection (LPDI): two low-pressure injectors installed on the cylinder liner;

3. Low Pressure Semi-Direct Injection (LPSDI): one or two low-pressure injectors installed in the scavenge ports, very close to the cylinder;

4. Port injection: one or two injectors installed in the scavenge manifold;

5. A combination of direct and semi-direct injection.

All these configurations have their pros and cons, the choice depends on the specific goals of the project.

HPDI yields the best fuel efficiency at low and medium speed, but it is expensive, heavy (because of the high-pressure pump that must be driven by the engine), and it requires a careful setup in order to guarantee a good performance at high speed, high load (it is difficult to achieve a proper composition of the charge at the combustion onset while minimizing exhaust fuel losses)
LPDI is a cost effective and compact solution, very efficient at high speed, high load, as demonstrated by many researchers [80] [81]. The only drawback is the heating of the tip of the injectors, facing the cylinder and exposed for a short time to the high temperatures of the combustion products.
A successful application of the LPDI concept has been implemented by the Institute for Internal Combustion Engines and Thermodynamics, Graz University of Technology [82–84] for motorcycle engines characterized by displacements ranging from 50 to 300 cm3. Such an injection system permits to strongly reduce fuel short-circuit improving Brake Specific Consumption (BSFC) and power output, making 2-Stroke engines competitive with modern 4-Stroke ones.
Low-Pressure Semi-Direct Injection offers several advantages over LPDI, including the prevention of injector tip overheating. However, optimizing LPSDI is a complex task that requires the support of CFD-3D simulations.

Conversely, standard Port Fuel Injection (PFI) offers a relatively simpler approach to implementing electronic fuel injection in 2-stroke engines. However, it does pose the challenge of preventing fuel short-circuiting. While current aircraft engine emissions remain unregulated, future regulations are anticipated, likely mandating the use of a catalyst. In such a scenario, any fuel escaping into the exhaust must be avoided, as the presence of O2 can ignite the escaped fuel and harm the catalyst.

A promising solution for the next generation of regulated 2-stroke aircraft engines combines High-Pressure Direct Injection (HPDI) and Low-Pressure Scavenged Direct Injection (LPSDI). This system permits the controlled introduction of fuel into the cylinder during the scavenging process, preventing any losses at the exhaust. This fuel has ample time to mix with air and residual gas, resulting in a homogeneous, lean, and diluted charge within the cylinder. The remaining fuel is injected at high pressure after the exhaust port closes, creating a stratified charge with a rich zone near the spark plug.

Table 20 shows a qualitative comparison among all the injection system candidates, summing up the previous considerations. Each solution has been rated by a mark, ranging from 1 to 4 (1: poor; 2: medium; 3: good; 4: excellent). In the initial comparison of all five solutions, LPSDI and LPDI received the highest rate

after the splited injection in direct and indirect. Then, LPSDI was selected for the implementation of the first engine prototype due to its higher rating.

Table 20: Qualitative comparison among different injection systems (Marks: 1: poor; 2: medium; 3: good; 4: excellent)

	HPDI	LPDI	LPSDI	PFI	DIR+SEMI
Fuel trapping efficiency at WOT	4	3	3	1	4
capability to stratify the charge at high speed, WOT	3	2	2	1	4
capability to get homogeneous charge at high speed, WOT	2	3	3	4	4
Wall impingement risk	2	4	3	2	4
Injector tip thermal stress	4	1	3	4	3
AVERAGE VALUE	3	2.6	2.8	2.4	3.8

The optimization objectives for the injection system in a 2-stroke engine can be succinctly outlined as follows:

Minimize fuel loss through the exhaust, setting a minimum target of 90% of trapped fuel.

Attain a suitable composition of the trapped charge at the end of the compression phase. The ideal composition includes a slightly rich mixture around the spark plug and within the bulk of the combustion chamber, alongside a slightly lean mixture elsewhere.

Ensure complete fuel vaporization before the commencement of combustion and mitigate the formation of fuel puddles. It's important to note that only the development of an LPSDI system is discussed here. The final layout, which incorporates two symmetric multi-hole injectors installed on the scavenge ports, is presented in Figure 62. Each injector features 12 holes, with a diameter of 0.29mm and a cone angle of 20°. The injection pressure may vary from 3 to 8 bar. Fuel is injected only during the opening of the scavenge ports, for approximately 60 CAD, to prevent wall impingement. The injector orientation is fundamental: fuel should be directed toward the cylinder head and the middle of cylinder, as far as possible from the exhaust ports and from the liner walls. An angle of 20° for both the planes shown in Figure 62 was found to be the best compromise between fluid-dynamic effectiveness and simplicity of installation.
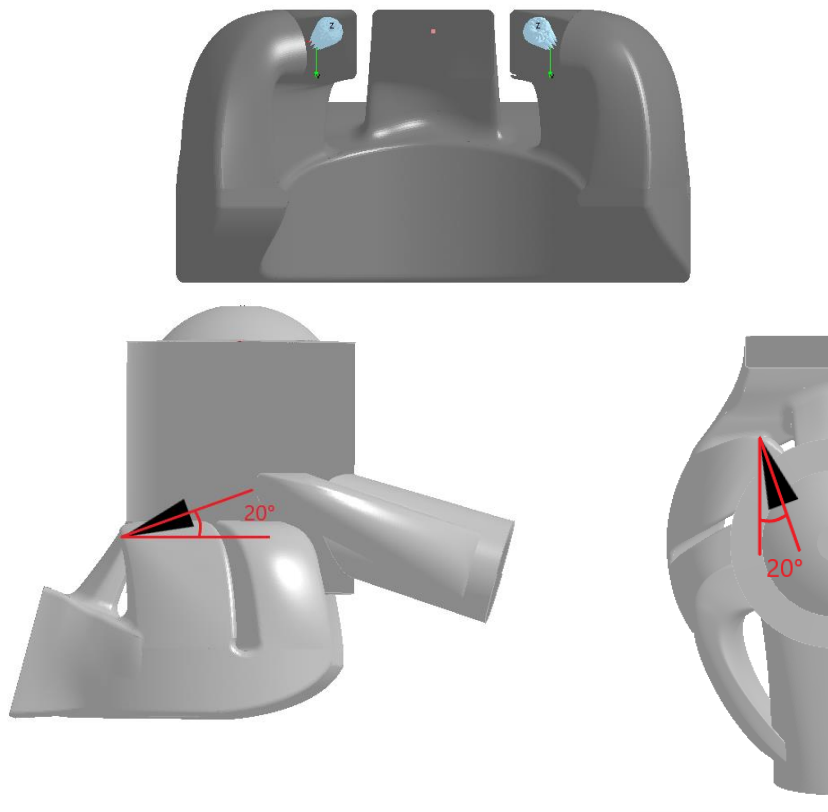
Figure 62: CFD-3D view of the semi-direct injectors

The CFD-3D simulation has been carried out between 90 CAD and 330 CAD aTDC, still considering the operating condition of maximum power (6000 rpm, WOT).

The fundamental characteristics of the computational mesh are reported in Table 21. The grid was generated by using the auto-mesh tool of Ansys Forte: the spatial domain is made up of cubic elements with an average size of 2 mm, except in the refinement zones. The number of cells varies from a minimum of 310,000 up to a maximum of 1,344,000 cells.

The intake region has been initialized with O2, the exhaust with carbon dioxide (CO_2) and the cylinder with N2. The injected fuel is iso-Octane (i-C_8H_{18}). These simplifications help the post-processing of results without penalizing the accuracy of the scavenging analysis.

	Cell size	Refinement method	Activation interval
Global Mesh	2 mm	-	-
Wall boundaries refinement	1 mm	1 layer	Always active
Open boundaries refinement	1 mm	2 layer	Always active
Wall boundaries port refinement	1	2 layer	Always active
Booster-intake interface refinement	0.25 mm	16 mm radius sphere	btw 90-93 CAD aTDC
Booster-intake interface refinement	0.25 mm	16 mm radius sphere	btw 265-270 CAD aTDC
Evaporation refinement	0.5 mm	Gradient of fuel vapor mass fraction	btw 160-220 CAD aTDC
Velocity magnitude refinement	0.5 mm	Gradient of velocity magnitude	btw 118-220 CAD aTDC

Moreover, a sensitivity analysis has been carried out, varying the global mesh size from 1.5 mm to 3 mm. As visible in Table 22

Table 25 , the influence of cell size on volumetric efficiency is absolutely negligible, while it is quite important when considering the Tumble Ratio (TR-y). Confirming the User's manual recommendations, the best compromise between computational time and accuracy is found between 2 and 2.25 mm

Global Mesh Size (mm)	# core	Max cell num	Comp time	Mean TR-y	Mean TR-y %diff	Vol eff	Vol eff %diff
1.5	4	829489	21 h 37 min	-1.76 E-03	0.000	2.020	0.000
1.75	4	581856	14 h 22 min	-1.63 E-03	7.503	2.016	0.200
2	4	429487	10 h 52 min	-1.83 E-03	-3.998	2.015	0.238
2.25	4	324241	9 h 7 min	-1.81 E-03	-2.832	2.023	-0.129
2.5	4	255662	7 h 13 min	-1.94 E-03	10.069	2.016	0.187
2.75	4	207741	6 h 16 min	-1.51 E-03	14.121	2.016	0.208
3	4	245275	5 h 23 min	-1.54 E-03	12.286	2.019	0.045

The numerical sub-models selected for the simulation are reviewed in Table 23 and the boundary conditions are derived from the CFD 1D engine model.

Table 23: Forte spray numerical models

Equation of state	Ideal gas
Turbulence model	RANS RNG k-epsilon
Droplet collision model	Adaptive collision mesh model
Droplet size distribution	Rosin-Rammler distribution
Spray brake up model	KH-RT + unsteady gas jet model

The three cases analyzed in this paper are identified by the injection advance with respect to the transfer port closing. For example, LPSDI-49 signifies that injection begins 49 CAD before the effective closure of the scavenge port, precisely when the fuel jet starts to touch the piston.

Table 24 outlines the primary characteristics of the analyzed strategies. The total amount of injected fuel, distributed evenly between the two injectors, remains constant at 27 mg, as does the fuel temperature at 330 K. The Duration of Injection (DOI) is 32.3° for the first two strategies, corresponding to an injection pressure of 5 bar, and 25.5° for the last case at an injection pressure of 8 bar. Start of Injection (SOI) is delayed by 15 CAD from the first to the second case and by a further 8 CAD from the second to the third, with the aim of reducing fuel short-circuiting.

Table 25 provides a comparison of the results for the three strategies. It's important to note that a small portion of the fuel injected into the cylinder is rejected into the intake manifold. In the subsequent cycle, the fuel re-enters the cylinder, with only a fraction of it (10-20%) exiting. Therefore, the actual fuel trapping efficiency is calculated considering two consecutive cycles. As SOI is further delayed, fuel trapping efficiency increases. However, it's only with the injection pressure increased to 8 bar that the 90% threshold can be surpassed (achieving 94%).

In order to assess the quality of the mixture at the combustion onset, the global value of the relative air-fuel ratio is not sufficient. It is necessary to determine a value of Lambda weighted on the basis of the volume of each region of the combustion chamber occupied by a homogeneous mixture. For this purpose, a mean effective value of Lambda, Λ_{eff} , is considered, according to the following formula:

$$\Lambda_{eff} = \frac{\sum_{i=1}^{N} \lambda_i V_i}{\sum_{i=1}^{N} V_i}$$

(1. 29)

λ_i, V_i are the values of the relative air-fuel ratio and of the volume of each cell, N is the total number of cells within the cylinder mesh at -30° aTDC.

The RMS variation of Λ_{eff} is also calculated throughout the combustion chamber, in order to assess the non-homogeneity of the charge. The ratio of RMS to Λ_{eff} should fall between 10 and 20%: on the one hand, lower values implicate a weak stratification; on the other hand, higher values may result in a poor combustion efficiency, due to the formation of unburned HC in the ultra-lean region.

Finally, the value of the relative air-fuel ratio within a sphere of diameter =10 mm, centered on the spark plug, is calculated.

All the stratification parameters shown in Table 25, demonstrate that strategy LPSDI-26 is the most effective one not only in terms of trapped fuel, but also in terms of quality of the air-fuel mixture.

By adopting this configuration, we anticipate a high-speed laminar flame front at the beginning of combustion, resulting in a rich mixture around the spark plug. This should lead to low cycle-by-cycle variations. Additionally, the lean mixture at the chamber's periphery, combined with the chamber's compact shape, allows for the adjustment of larger spark ignition advances, enhancing thermodynamic efficiency while reducing the risk of knocking.

Finally, the distribution of Lambda for strategy LPSDI-26 is shown by the pictorial view of Figure 63 : the results find a further confirmation. Other plots of Lambda, at different crank angles, can be found in FigureA.2 in the Appendix.

Table 24: Semi-Direct injection setup, 3 different strategies

	LPSDI-49	LPSDI-34	LPSDI-26
Inj mass [mg]	27		
SOI [deg]	160	175	183
DOI [deg]	32.3	32.3	25.5
Mass flow rate [g/s]	15.05	15.15	19.06
ΔP [bar]	5	5	8
Fuel temperature [K]	330		
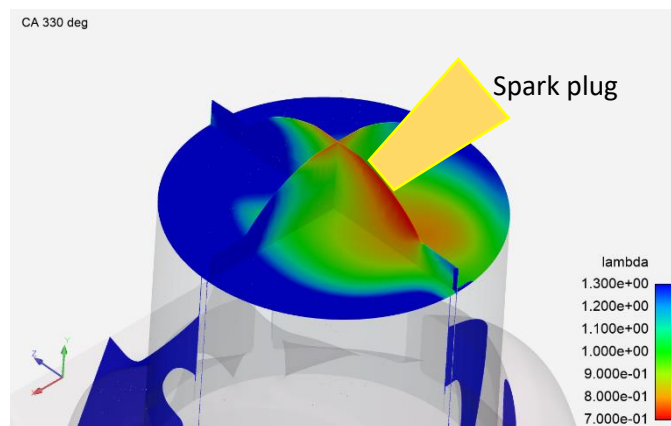
Figure 63: Lambda distribution at 330 CAD, strategy LPSDI-26

Table 25: CFD-3D results of the Semi-Direct injection simulation, 3 different strategies

	LPSDI-49	LPSDI-34	LPSDI-26
Trapped fuel mass into cylinder [mg/cyl/cycle]	21.71	20.95	23.76
Trapped fuel mass into intake volume [mg/cyl/cycle]	2.38	3.80	2.33
Apparent Trapping efficiency (1 cycle)	0.80	0.78	0.88
Actual Trapping efficiency (2 cycles)	0.87	0.88	0.94
Lambda (global)	1.12	1.11	1.04
Effective Lambda (Λ_{eff})	1.04	1.01	0.97
RMS (Effective Lambda)	0.12	0.14	0.15
RMS/Λ_{eff} [%]	11.66	13.59	15.17
Lambda at spark plug	0.95	0.90	0.85

5.2.4   Performance analysis

The primary design objective was to achieve the performance target of 110 kW at 6000 rpm while adhering to specific constraints, notably the maximum air temperature within the intake manifold (70 °C) and the maximum proportion of residual gas within the cylinder (20%). This objective was met through the optimization of the scavenging process at maximum engine speed.

A crucial factor in this optimization is the timing of the "plugging" wave, which is the compression wave arriving at the exhaust port just after the scavenge port closes. In this engine, equipped with a log exhaust manifold, this wave is generated by the blowdown process occurring in the cylinder 120 CAD after the current one. The plugging wave significantly enhances trapping efficiency and promotes uniform mixing between the fresh charge and exhaust gas, preventing the formation of residual gas "pockets." For a more detailed depiction of the complete scavenging process, along with these waves, please refer to Figure A.3 in the Appendix.

Subsequently, CFD-1D simulations are employed to project engine performance at full load, covering the range from 1500 rpm to 6000 rpm in 500 rpm increments.

Figure 64 provides insight into the instantaneous mass flow rates through the scavenge and exhaust ports in the final engine configuration at maximum power. Notably, there is a noticeable backflow of exhaust at scavenge port closing (240 CAD aTDC), underscoring the efficacy of the plugging wave.

Additionally, the introduction of fresh charge into the cylinder commences at approximately 45 CAD bBDC, occurring once nearly half of the exhaust gas has exited the cylinder. This timing is of significance as it impacts the work expended by the external compressor in sweeping the cylinder.

With increasing engine speed, both the delivered and trapped air quantities grow, even though trapping efficiency remains relatively low, averaging around 50%, with a peak value of 63% at 6000 rpm. Conversely, the proportion of fresh charge remains consistently above 90% at medium-high speeds and never falls below 82%.
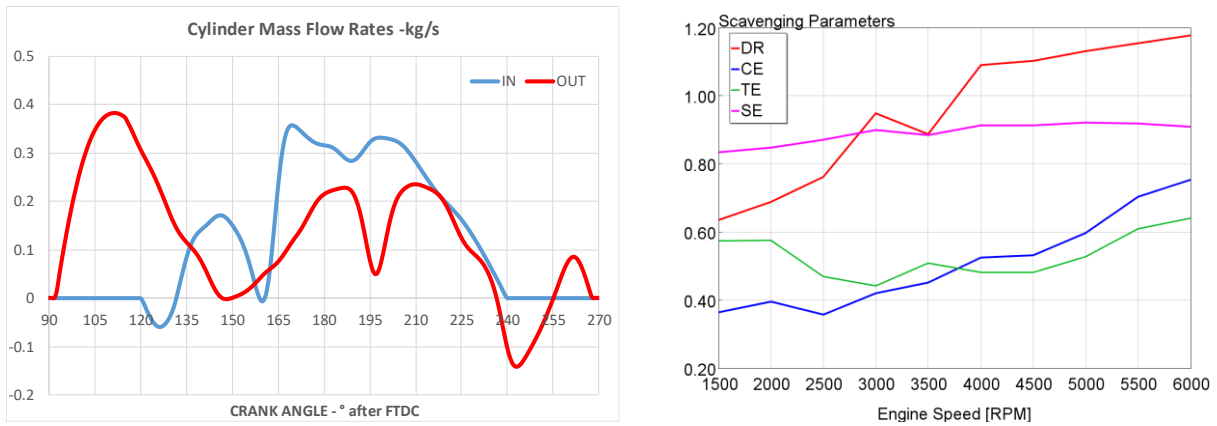
Figure 64: cylinder instantaneous mass flow rates and related scavenging parameters

Figure 65 illustrates the plots for Indicated and Brake Mean Effective Pressures (IMEP and BMEP, respectively). The third curve in green represents the combined effect of Friction and Pumping Mean Effective Pressure (FMEP and PMEP, respectively; in the context of a 2-stroke engine, PMEP refers to the specific work required to drive the external compressor). Notably, the maximum BMEP value is slightly below 9 bar, whereas the IMEP peak is just over 10 bar. These values are considerably lower than those typically observed in naturally aspirated 4-stroke engines with a similar brake power. Moreover, friction and pumping losses are also reduced.
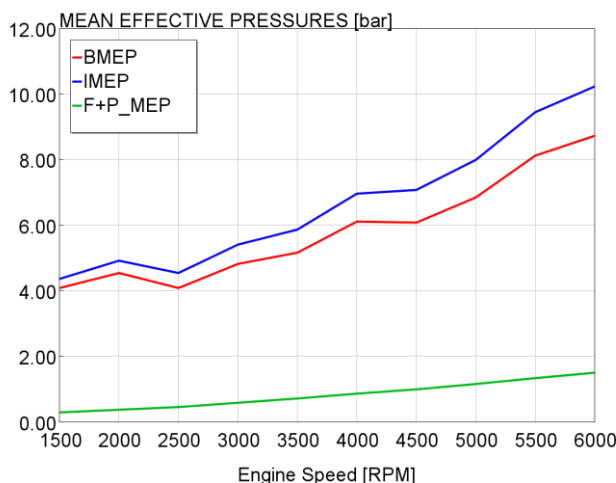
Figure 65: Brake, Indicated, Friction + Pumping Mean Effective pressures as a function of engine speed, at WOT

Figure 66 shows the curves of Indicated and Brake Thermal Efficiency (ITE and BTE, respectively). The average value of BTE at medium-high speed is about 32%.
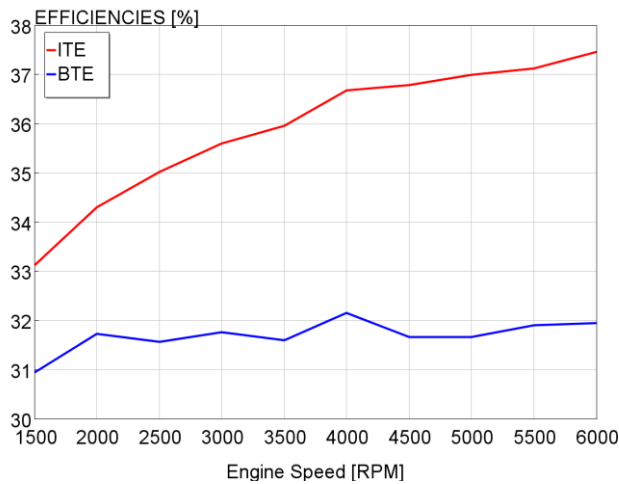
Figure 66: Indicated and Brake Thermal Efficiencies as a function of engine speed, WOT

The remarkable thermal efficiencies can be elucidated by examining the graphs in Figure 67 . The mechanical + pumping efficiency is calculated as BMEP/IMEP. Adiabatic efficiency denotes the ratio of the effective heat available for the thermodynamic cycle to the heat released during combustion. Combustion efficiency, on the other hand, is the ratio of the heat released by combustion to the energy associated with the mass of injected fuel.

At medium to high speeds, both efficiency parameters surpass 85%, underscoring that in this 2-stroke engine, pumping, friction, and heat losses are minimal, while the combustion process is more complete compared to an equivalent 4-stroke engine. The primary drawback of the 2-stroke engine appears to be the thermodynamic cycle, whose efficiency is constrained by the early and abrupt opening of the exhaust port, interrupting the expansion stroke.
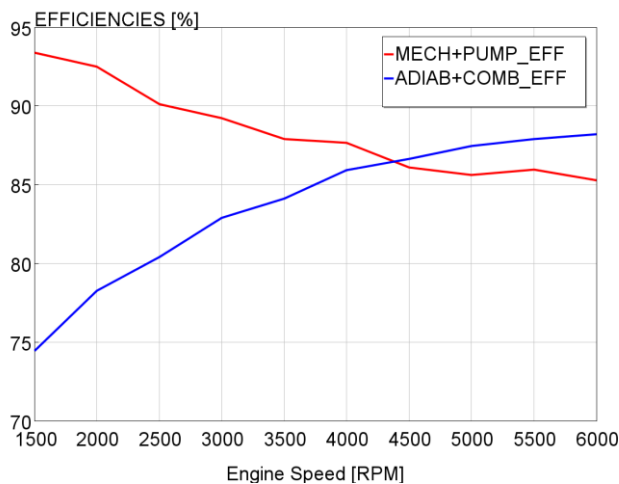
Figure 67: Mechanical+Pumping efficiency, adiabatic and combustion efficiency as a function of engine speed, WOT

Figure 68 shows the trends of average pressure and temperature in the intake manifold, downstream of the compressor. The supercharging ratio is kept quite low, in order to avoid the installation of a charge cooler.
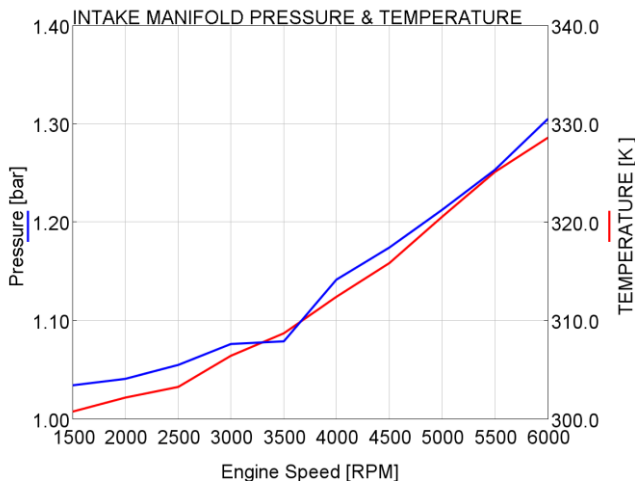
Figure 68: Average value of pressure and temperature in the intake manifold, as a function of engine speed, WOT

In Figure 69, the operating points at WOT are plotted on the compressor map. The chosen compressor and the setup of the transmission ratio are the results of many compromises. On the one hand, a compressor with a smaller swallowing capacity could provide higher internal efficiencies; on the other hand, a small compressor must rev at higher speed, requiring a higher transmission ratio, thus a lower mechanical efficiency.

From the map in Figure 69, it may be observed that the values of efficiency at high speed are over 50%, not a bad result considering the low values of pressure ratio (using a positive displacement compressor the efficiency is similar or worse)
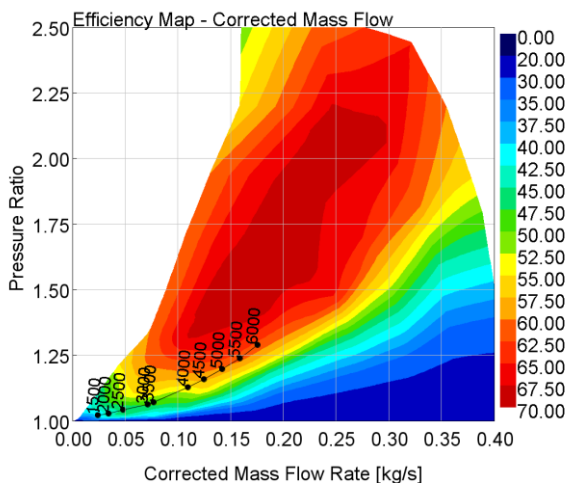
Figure 69: Compressor map with operating points at full load, WOT

Engine brake performance in terms of torque and power are presented in Figure 70. Engine brake performance in terms of torque and power are presented in Figure 70. It should be considered that this engine is coupled to an EM and to an aircraft propeller: for this application, low end torque has no importance, since the engine is operated always at high speed (never below 4000 rpm), and in case of emergency is supported by the EM.
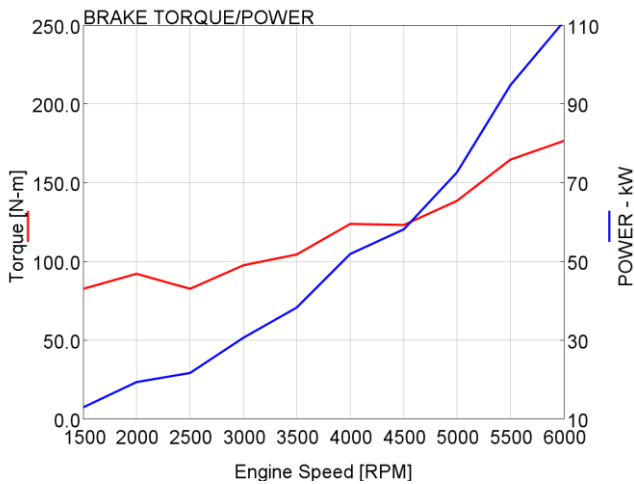
Figure 70:Brake power and torque plotted as a function of engine speed, at WOT

Finally, Figure 71 examines the BSFC and the average peak cylinder pressure. At high speeds, BSFC is quite good, although not at the level of diesel engines. It's important to note that combustion parameters have not been fully optimized yet. The relatively low values of average peak cylinder pressures (less than 60 bar) suggest that there is still room for improving BTE.

.
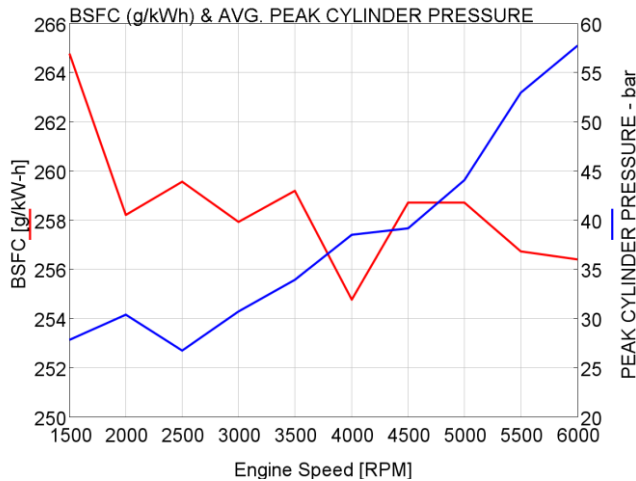
Figure 71: Brake specific fuel consumption and average peak cylinder pressure, plotted as a function of engine speed, at WOT.

5.3   Conclusions

In the aviation industry, the near future is expected to usher in stricter emissions regulations, even though significant legislation in this regard is currently almost absent. Improving engine overall efficiency and fuel consumption, along with exploring different fuel applications, has become almost mandatory. In this chapter, two distinct aircraft applications of 2-stroke engines specifically designed for aviation purposes are presented.

The first section introduces a 2-stroke, 6-cylinder Compression-Ignition (CI) aircraft engine with a total displacement of 5.6 litres. This engine can deliver up to 400 HP for a short duration at 2600 rpm and is directly coupled to the propeller. Notably, it boasts a low Brake Specific Fuel Consumption (BSFC), expected to be around 210-215 g/kWh during typical cruise conditions. Additionally, it features a peak cylinder pressure of less than 100 bar along a typical propeller curve. This engine can be easily adapted to run on alternative fuels like kerosene, making it suitable for military applications. The engine has been simulated for both sea-level and high-altitude conditions, with optimizations in turbo-matching and compressor operation to ensure it remains well below the choke limit.

The second section discusses a 2-stroke, 3-cylinder Spark Ignition (SI) aircraft engine with a displacement of 1.2 litres, rated at 110 kW @ 6000 rpm. This engine employs a parallel hybrid configuration, an external centrifugal compressor, and an innovative semi-direct low-pressure fuel injection system. Notable numerical results from CFD-1D simulations at full load include low average peak cylinder pressure (less than 60 bar), low thermal loads (Brake Mean Effective Pressure, BMEP, less than 9 bar), and good Brake Thermal Efficiency (BTE) of approximately 32% at high speed. The engine also achieves a low BSFC of less than 260 g/kWh at high-medium engine speed and a high scavenge efficiency of over 90% at medium-high speed.

Since it is a spark ignition engine running on gasoline, special attention has been given to the optimization of the injection strategy. Two low-pressure injectors are positioned in the intake ports, facing the cylinder. The optimized injection system exhibits a fuel trapping efficiency of 94% and an average lambda value of 0.97 at 30° before Top Dead Centre (bTDC).

6 2-Stroke hydrogen solutions

As widely recognized, hydrogen (H2) produced from renewable sources, often referred to as green H2(green H_2 [85,86]), has the capability to significantly reduce both CO2 emissions and pollutant emissions from internal combustion engines[87]. Among these pollutants, the most challenging to address are NOx emissions, which necessitate either expensive after-treatment systems or specialized combustion control strategies.

H2 stands out as an appealing choice for SI engines [88]. due to its high resistance to auto-ignition and knocking, with a research octane number (RON) exceeding 130.

Nonetheless, the transformation of a conventional gasoline 4-stroke engine into a hydrogen-powered one is a complex task, even without considering the associated challenges of on-board hydrogen storage [89]. One initial issue is the reduction of volumetric efficiency caused by the larger volume occupied by hydrogen when injected into the intake manifold or cylinder with open valves, resulting in an expected decrease of around 30% compared to gasoline [90].

Notably, introducing hydrogen into the intake manifold when the intake valves are closed is not feasible due to its broad flammability range, posing a higher risk of backfire. Conversely, DI of gaseous fuel into the cylinder after IVC presents two main challenges: the design of the cylinder head, which must accommodate a relatively large gas injector, and the increasing difficulty of forming a homogeneous air-fuel mixture before ignition as engine speed rises, due to time constraints [91,92].

Another significant challenge is the laminar flame speed of hydrogen, which is nearly an order of magnitude higher than that of standard gasoline under the same conditions. A recent experimental study [93] shows that operating with equivalence ratios higher than 0.5 without encountering serious detonation issues is difficult, potentially affecting engine-specific performance unless the airflow rate is substantially increased.

Additional challenges in implementing a hydrogen combustion system based on a conventional SI chamber design include [94]:

1. The shorter "quenching" distance, compared to gasoline, leading to more complete combustion but also higher heat losses and the potential for partial combustion of lubricant oil on the walls, resulting in increased particulate matter, CO, and THC emissions.

2. Hydrogen's lower ignition energy, making it more susceptible to "hot spots" and unintended auto-ignitions.

3. The higher auto-ignition temperature, which enhances resistance to detonation but can worsen cold engine starts.

An optimal balance between BTE and NOx emissions is typically found when operating with equivalence ratios (Φ) in the range of 0.35 to 0.40 [95]. Researchers [96,97] have developed turbocharged 4-stroke, 4-cylinder, DI hydrogen engines that achieve near-zero NOx emissions (<20 ppm) while delivering excellent BTE across a wide range of operating conditions through the exploration of the Miller cycle, ignition timing, and injection strategies.

However, one challenge with 4-stroke hydrogen engines running on lean mixtures is the requirement for very high volumetric efficiency values to meet performance targets. Supercharging may not be sufficient,

especially for high-speed engines, and achieving high values of low-end torque and peak power simultaneously without a complex and costly two-stage supercharging system is nearly impossible.

For small engines, adopting the double frequency of the 2-stroke cycle may offer a solution to retain the aforementioned advantages without compromising steady and dynamic performance [98,99].
Liu et al [100] provide an extensive analysis on backfire occurrence depending on injection strategy in a DI 4-stroke engine. While on 4-strokes Hydrogen direct injection is generally adopted to improve volumetric efficiency and to prevent backfire in the intake system ([101] [102], [103] [104]), in the 2-stroke application it is mandatory, in order to avoid the short circuit of fuel during the scavenge process.
This section discusses various unconventional 2-stroke engine solutions running on pure hydrogen, including:
1. An opposed-piston engine designed for gen-set applications, involving a numerical study to evaluate its potential, considering a single-cylinder electric generator capable of delivering a maximum power of 45 kW at 3000 rpm.
2. A reverse loop scavenged engine equipped with poppet valves for both intake and exhaust ports, designed for high-performance vehicles. A comprehensive comparison is made among three different solutions and a reference 4-stroke engine.
3. A small LPDI loop scavenged engine tested to run on hydrogen and then optimized to enhance injection trapping efficiency.

6.1 Reverse loop with poppet valves hydrogen engine

Among the other 2-stroke designs, a very interesting concept appears to be the one characterized by loop scavenging with intake and exhaust poppet valves, a solution already explored by Toyota in the '90s [105]. The main advantage of this solution is the minimum number of modifications required to build a prototype starting from a correspondent 4-stroke engine. Only the cylinder head, including the ports and the valves actuation system, must be designed from scratch, in order to optimize the scavenging process.

For this purpose, hydrogen should be injected when the valves are closing, or even better when they are already closed.

The combustion pattern and the further comparison is made with a prototype 4-Stroke engine found on literature [96,97]

The development of a 2-stroke hydrogen engine, starting from the basis of a 4-stroke turbocharged prototype, is far from trivial. First of all, the turbocharger must be supported by a further compressor, in order to start the engine and guarantee a positive pressure differential across the cylinder at any operating condition. This compressor may be either mechanical (connected to the crankshaft) or driven by an electric motor. The reason for choosing an electric supercharger instead of a mechanical one is the high flexibility of engine control: the air flow rate delivered by the engine can be varied by modifying the compressor speed. The electric drive of the compressor also enhances the engine response during transient operations. Finally, on a hybrid powertrain, the energy recovered from vehicle braking can be used to drive the electric supercharger, further improving the efficiency of the system.

A cheaper and more compact alternative to the two-stage systems is a single mechanical supercharger, featuring a by-pass valve for load control. In terms of fuel efficiency, this solution is quite penalizing at full load.

The size of the machines and their layout must be carefully chosen, in order to reach the performance targets and to minimize fuel consumption. Due to the relatively low exhaust gas temperature, a Variable Geometry Turbine (VGT) can be selected: this choice has the further advantages to improve the flexibility of engine control and to reduce the turbine back-pressure at full load, high speed.

Another fundamental issue to be addressed in 2-strokes with poppet valves is the tendency to short circuit during the scavenging process. Even if no fuel is lost, the work spent by the electric supercharger for compressing the short-circuited charge penalizes the engine efficiency. This problem can be mitigated in many ways: optimization of the intake ports geometry; optimization of the valves actuation law and reduction of the overlapping period; tuned exhaust manifold and designing a shroud in between intake and exhaust valves to orient the air entering the cylinder.

The proposed $2SH_2$ engine is a 3-cylinder with intake and exhaust poppet valves, 0.9L, Direct Injection (DI) Spark Ignition (SI) supercharged unit, numerically optimized to meet both high performance targets (max. specific power >80 kW/l, max. specific low-end torque: 200 Nm/l) and ultra-low emissions limits (NOx<20 ppm).

The CFD 1D engine was supported by CFD 3-D simulations, for the design of the scavenge system and for providing fundamental information for the modelling of the in-cylinder processes, in particular scavenging and fuel injection. Combustion was not investigated in depth, as the chosen combustion system is very similar to the one typically implemented on 4-strokes (after the closure of the valves, during the compression stroke, the geometry of the chamber is the almost the same, except for a few details). Therefore, burn rates have been calculated by using a quasi-dimensional predictive model, embedded in GT-Power (SI-Turb), experimentally calibrated on the $4SH_2$ reference engine.

6.1.1 Cylinder geometry optimization

The main characteristics of the optimized 2-stroke cylinder geometry are reported in Table 26, while Figure 72 shows the geometry of the valves and ports. Besides the valves timing, the most relevant differences from a conventional 4-stroke can be summarized as follows:

- higher bore-to-stroke ratio (2.0 vs 1.0) for maximizing the dimensions of the valves and helping the scavenging process;
- exhaust valves larger than the intake ones, for the peculiarities of the scavenging process in the 2-stroke cycle;
- vertical orientation of the intake ports, for generating a reverse tumble within the cylinder and limiting the mixing between fresh charge and residuals;
- valves masking: a shroud along a portion of the intake valves orients the fresh charge flowing through the curtain toward the cylinder liner, in the attempt to reduce the short-circuit and promote the intensity of the reverse tumble vortex;
- "smooth" path for the intake and exhaust flows, for limiting flow losses;
- "aggressive" valve actuation laws for maximizing permeability and reduce the parasitic work of the supercharger.

Concerning the valve lift profiles, their design is directly driven by the mechanical constraints of the system (maximum/minimum accelerations, maximum velocity); the only small advantage of the 2-stroke cycle consists in the large distance between the valves and the piston, as scavenging occurs at BDC.

The space for the hydrogen injector can be easily between the intake valves and the liner, at least with the proposed dimensions of the cylinder.

It may be noted that the proposed geometry is more similar to the old Toyota concept than to the modern design developed by Ricardo for its "2-4 Sight" concept [106]. The reason for this choice is to comply with the requirements of the project, which limit the overall dimensions of the cylinder head.
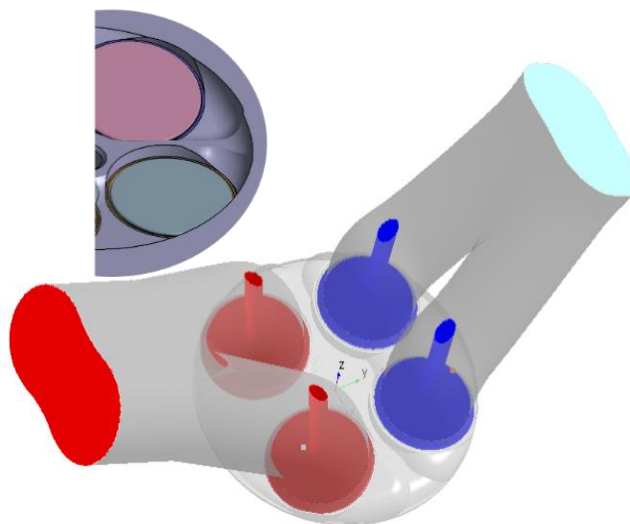
Figure 72: Optimized 2-Stroke engine ports

Table 26: 2-stroke cylinder main parameters

Bore	91.4 mm
Stroke	45.7 mm
Conrod length	115 mm
Compression ratio	16:1
Displacement (per cylinder)	299.8 cm^3
Intake valves seat diameter	2 x 29.5 mm
Exhaust valves seat diameter	2 x 31.5 mm
IVO-IVC	126-258 @0.2mm
EVO-EVC	85-244 @0.2mm
Max. Intake lift	9.6 mm
Max. Exhaust lift	11.4 mm
Max. engine speed	7000 RPM

The 3D CFD scavenge simulation was performed by using Fire-M by AVL. The simulated operating point is WOT and maximum engine speed (7000 RPM). This condition is expected to be the most critical, due to the minimum time available for the scavenging process.

The CFD-1D engine model (GT-Power) calculates the initial and boundary conditions for the 3D analysis, while the latter provides fundamental information to calibrate the sub-models employed to represent the scavenging process in the 1D simulation.

For each cycle, the simulation starts at 70° after firing TDC, when all the valves are closed, and it terminates at -60° after TDC, before the beginning of combustion. The initial pressure within the cylinder is adjusted to get a coherent value of trapped mass (the mass of exhaust gas at exhaust valve opening must be equal to the mass of air entering the cylinder during the scavenging process, plus the mass of Hydrogen). It should be noted that the employment of crank-based boundary conditions provided by a cfd-1d simulation allows the designer to take into account the complexity of the whole engine layout, including the dynamic effects occurring within the intake and exhaust manifolds even if only a small portion of the ports are considered in the computation volume.

As the main goal of the numerical study is the characterization of the scavenging process, several simplifications are made. First, Hydrogen injection is not considered; second, we supposed a homogenous composition of the charge within the cylinder, at the beginning of the simulation; third, to facilitate the post-processing analysis, exhaust gas within the cylinder is represented by pure N_2, while the fresh charge entering from the intake port is modelled as pure O_2.

The CFD-3D software allows the user to deactivate the parts of the volume that are not involved in the simulation: in particular, the intake and exhaust ports are active only when their valves are open. The computational grid, made up of poly elements, was built with the help of the automatic Fire-M mesher: the average cell size is equal to 2 mm, refined at the walls with 2 layers of 0.2 mm each. Further refinements are enforced in the curtain of the valves, where the average cell size is 0.5 mm (see Figure 73). The total number of cells varies from 165,000 at TDC to about 1,634,000 at BDC. From Figure 73 is also possible to see a shroud to perform a masking between the intake and the exhaust port, in order to reduce the short-circuit.

Turbulence is modelled according to a RANS approach, selecting the k-zeta-f method embedded in FIRE.
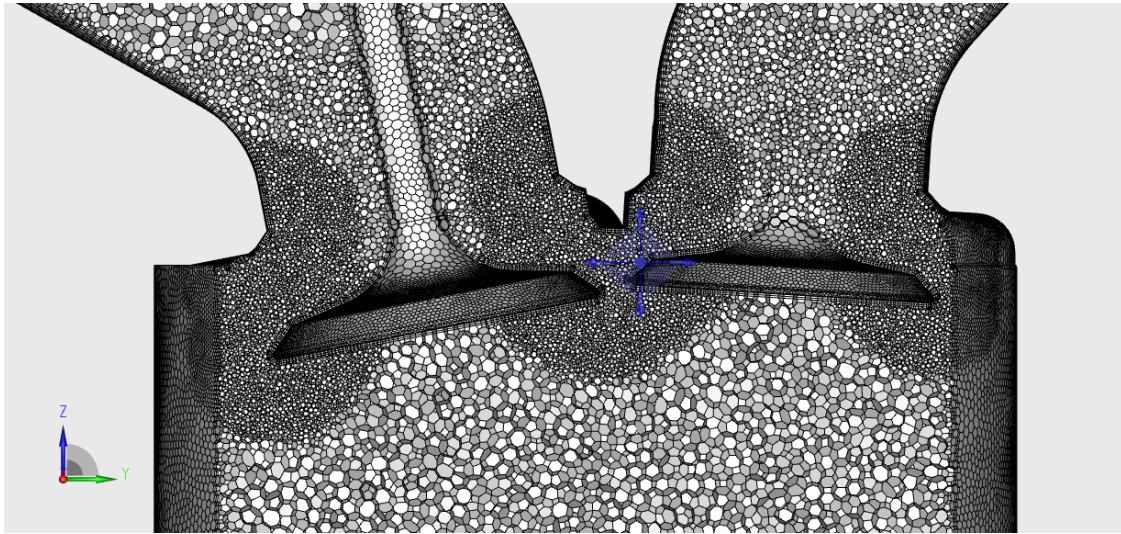
Figure 73: Computational Grid at BDC

For the characterization of the scavenging process, the already introduced 2S efficiency parameters are considered:

- Delivery Ratio, DR: mass of fresh charge flowed through the intake valves divided by a reference mass;
$$DR = \frac{m_{int}}{m_{ref}}$$
- Charging ratio, CR: mass of fresh charge retained into the cylinder, divided by a reference mass;
$$CR = \frac{m_{tr}}{m_{ref}}$$
- Trapping ratio, TR: mass of fresh charge retained into the cylinder, divided by the mass of fresh charge flowed through the intake valves;
$$TR = \frac{m_{tr}}{m_{int}}$$
- Scavenging ratio, SR: mass of fresh charge retained into the cylinder, divided by the total mass into the cylinder;
$$SR = \frac{m_{tr}}{m_{cyl,tot}}$$
- Reference mass: product of the gas density in the intake ports and cylinder capacity (displacement);
$$m_{ref} = \rho_{int} * V_d$$

Figure *74* presents the trends of CR, TR and SR as a function of DR, while Figure *75* shows also the Tumble Ratio. All the curves of Figure *74* clearly show that at the beginning of the scavenging process some short-circuit occurs. The results from Figure *74* are compared with two different dotted lines that represent the extreme conditions for the scavenging process: perfect mixing (PM) and perfect displacement (PD). These lines serve as benchmarks to evaluate the performance of the observed data. This result was expected, because the fresh charge enters the cylinder very close to the exhaust valves, and the valves masking cannot completely avoid the problem. Furthermore, the geometry of the intake ports makes it very difficult to generate a compact front of fresh charge that uniformly sweeps the cylinder. However, as the charge

continues to enter the cylinder, the impact tends to reduce and the process becomes slightly better than a perfect mixing.

A strong help to the improvement of trapping ratio comes from the exhaust backflow, generated by a compression wave traveling toward the cylinder, due to the firing event in a neighbouring cylinder. Figure *76* shows the moment (200 cad aTDC) in which both intake and exhaust flows are directed toward to the cylinder. The relatively homogeneous distribution of O_2 mass fraction, also depicted in Figure *76*, confirms that the scavenging process is closer to a Perfect Mixing than to a Perfect Displacement. A complete set of pictures, from 90° to 240° after TDC by step of 10°, showing O_2 concentration and gas velocity vectors, is reported in the Appendix, Figure A.4.

(a)   (b)

(c)
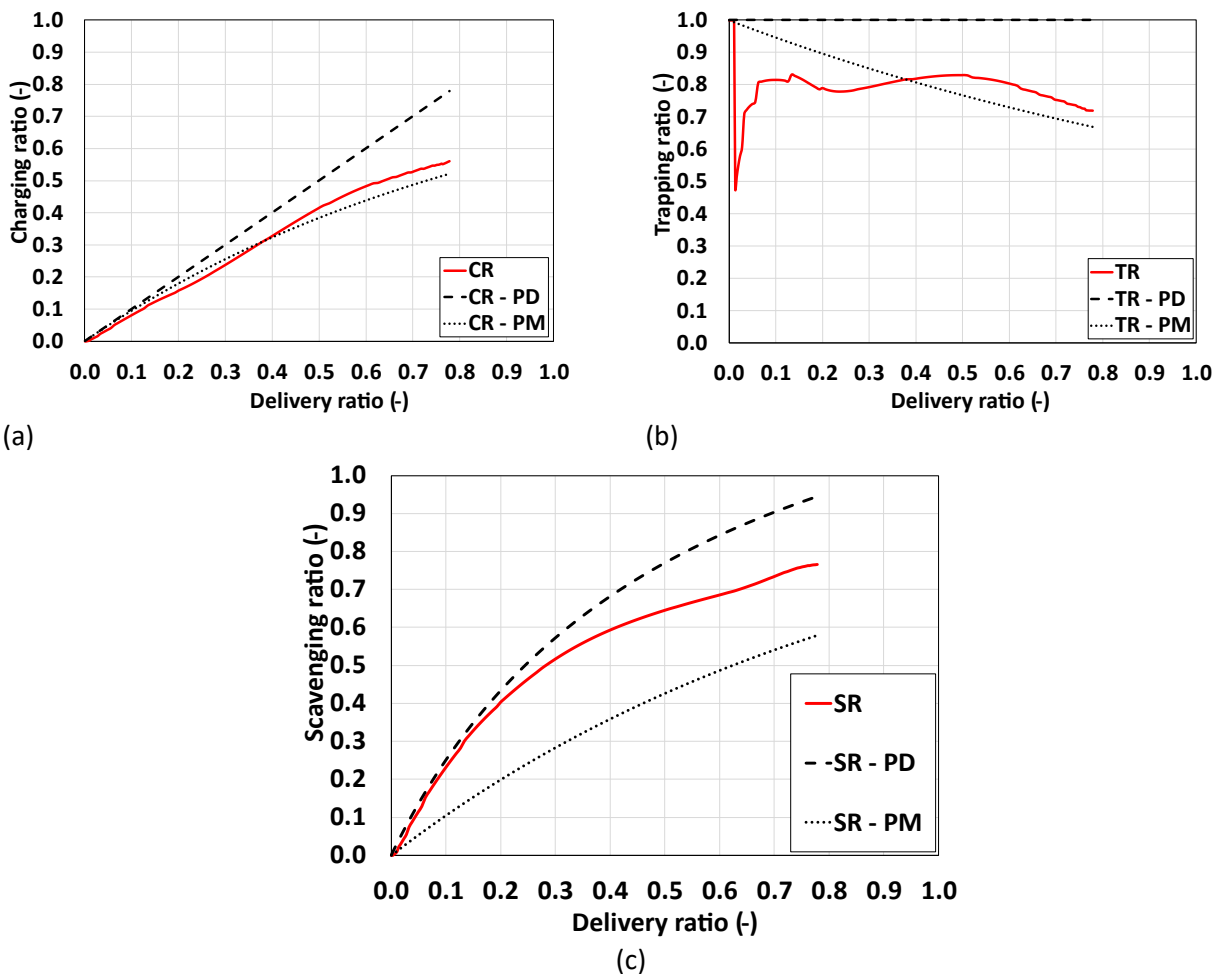
Figure 74: CR (a), TR(b) and SR(c) plotted as a function of DR at 7000 rpm, WOT

From Figure *75* and Appendix Figure A.4 it is also possible to assess the formation and development of the Tumble vortex. The Tumble ratio reaches its maximum value (≈1.22) just before the closure of the intake valves, more or less at the arrival of compression wave at the exhaust port. It may be noted in Figure *76* that the flow entering the cylinder from the exhaust side generates a counter-rotating vortex, that limits the intensity of Tumble ratio, but it should be very effective to support the mixing between fuel ad fresh charge. In general, from a qualitative point of view, turbulence appears to be higher than in a correspondent 4-stroke engine.

Figure 75: Tumble Ratio plotted as a function of DR at 7000 rpm, WOT
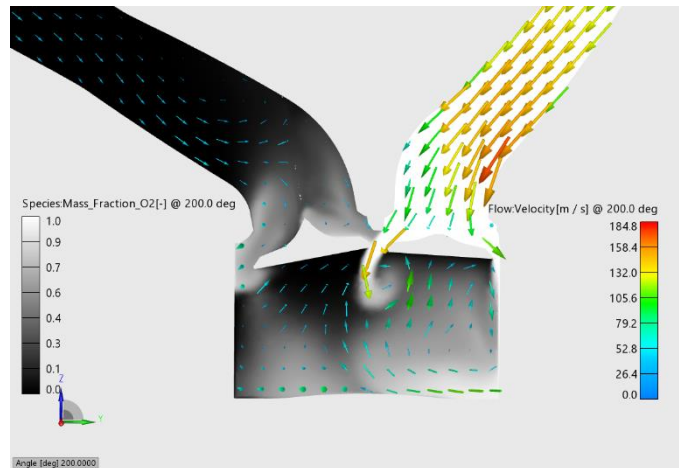
Figure 76: Fresh charge concentration and flow velocity plotted at 200° after TDC. Operating condition: 7000 rpm, WOT

6.1.2   CFD 1D Combustion calibration

Since the injection of hydrogen and its combustion are not fully analysed by means of CFD 3D simulations, the 1D numerical models have been experimentally calibrated, at least for the prediction of Hydrogen combustion and the formation of NOx.

Reference was made to the work of Bao et al. [107,108], who developed a turbocharged 4-Stroke, 4-cylinder, DI Hydrogen engine, finding near zero NOx emissions (<20 ppm) and excellent BTE values over a broad range of operating conditions. The main characteristics of the investigated engine are listed in Table 27.

Table 27: Main Features of the 4Sreference engine

Engine Type	DI-SI 4S Hydrogen
Cylinders	4 in-line
Bore x Stroke [mm]	88 x 82
Compression ratio	13:1
N. of valves per cylinder	4
Exhaust valve opening [CAD bBDC]	40
Intake valve opening [CAD bTDC]	4
Exhaust valve closing [CAD aTDC]	18
Intake valve closing [CAD bBDC]	20
Engine speed [RPM]	1000-3500
Air Metering	Turbocharger with VGT + Intercooler

First, a GT-Power model of the engine was built on the basis of the published data; the layout of the model is visible in Figure 77.
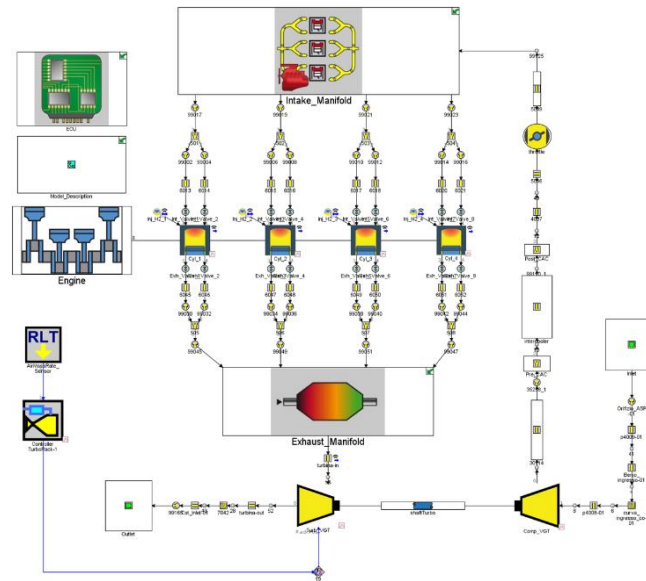
Figure 77: Layout of the 4S model engine

Bao et al. [107,108], experimentally demonstrated that the best trade-off between Brake Thermal Efficiency (BTE) and NOx emissions can be found when operating with equivalence ratios (Φ) in the range between 0.35 and 0.40. They also investigated the impact of the Miller cycle, ignition timing, and injection law following two approaches: "ultra-lean" combustion (λ=2.8, Φ=0.36) with standard spark timing and lean "delayed" combustion (λ=2.5, Φ=0.40) with delayed spark timing.

"Delayed" combustion was found to be the best strategy to maximize brake performance outputs, while keeping NOx<20ppm: the centre of the burn curve (CA50) typically falls at values of 15-20 CAD aTDC. This setup provides a smooth and regular combustion without knock. Moreover, the maximum in-cylinder temperature is comparable to that obtained with ultra-lean mixtures (Φ=0.36), resulting in low NOx formation rates and minimal heat losses, without penalizing cycle-to-cycle variability. Finally, the enthalpy of the exhaust gas entering the turbine is increased, compared to ultra-lean combustion, resulting in higher turbocharger speed and higher airflow rates. This combination of high volumetric efficiency and high equivalence ratio leads to improved engine brake outputs (torque and power), with a very slight penalization on BTE.

"Ultra-Lean" combustion allows to achieve the maximum values of BTE, while maintaining very low concentrations of NOx. Since this strategy slightly reduces full load performance, it is more suitable at medium and low loads.

The efficiency map of the compressor, including the operating points of the 4-stroke prototype calculated by GT-Power at full load (solid red and green circles), is presented in Figure *78*. The maximum flow rate of the compressor (0.17 kg/s) is very high, when compared to the engine displacement (2.0 L) and the maximum

engine speed (3500 rpm). These results suggest that 4SH2 engines require larger turbochargers than their gasoline counterparts.
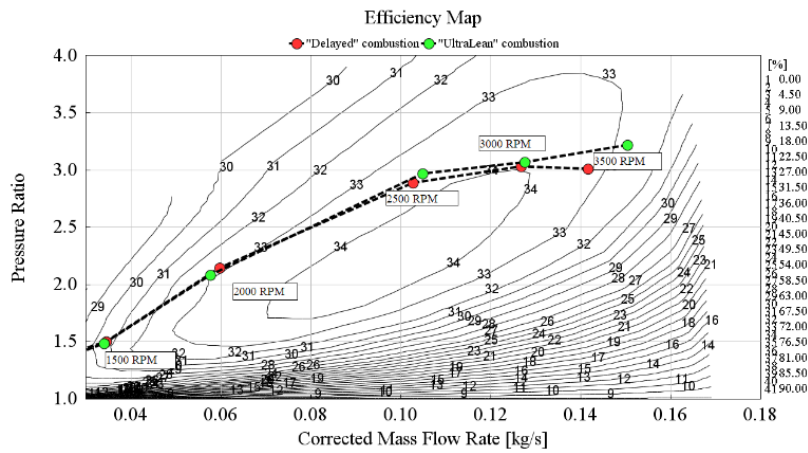
Figure 78: Experimental efficiency map of the compressor installed on the reference 4S engine with corresponding operating points (red=delayed, green=ultra-lean

)

The predictive combustion model was employed only after the calibration of the key performance parameters (VE, BMEP, BTE) at full load. In the first round of simulations, combustion was modelled entering experimental burn rate profiles; when experimental data was not available, the burn rate curves were extrapolated from nearby operating conditions, with the support of empirical assumptions.

The subsequent step consisted in the integration and tuning into the engine model of a predictive combustion model, embedded in the software (SI Turb). SI Turb [109] is a two-zone combustion model designed to simulate turbulent flame propagation in a spark-ignited combustion process. The model assumes a spherical propagation of the flame front within the actual combustion chamber geometry, while also accounting for the wrinkling effect of turbulence on the flame front. The model considers several parameters, such as flame front surface area, unburned gas density, turbulent and laminar flame speeds (TFS and LFS), and mass flow rate of unburned mixture entrained in the flame front. For LFS, the model employs a specific correlation for hydrogen that has been validated at approximately 2000 operating points, using detailed chemistry simulations. A standard k-ε model is employed to solve the turbulence kinetic energy (k) and its dissipation rate (ε) equations.

The calibration of the SI-Turb model for the 4S engine was limited to a set of three parameters (Flame Kernel Growth Multiplier, Turbulent Flame Speed Multiplier, Taylor Length Scale Multiplier), whose numerical values are shown in *Figure 79*: Delayed and Ultra lean combustion engine model calibration comparison

Table 28. The parameters remain constant as the operating conditions change.

Finally, the SI Turb combustion model was integrated with a NOx emissions model that uses the Extended Zeldovich Mechanism (EZM). The EZM model was calibrated and validated by Gamma Technologies against experimental data obtained from hydrogen combustion. In this study, a further calibration was performed by adjusting a single multiplier (N2 Oxidation Activation Energy Multiplier), also reported in Figure 79: Delayed and Ultra lean combustion engine model calibration comparison

Table 28.

Figure 79 shows a final comparison between the experimental and the simulation results, considering both a Delayed Combustion strategy (left column) and an Ultra Lean Combustion Strategy (right column)

The first row of pictures presents the comparison in terms of key performance parameters (VE, BMEP, BTE): the agreement is very good, especially for the delayed combustion.

The second row of pictures shows the instantaneous values of in-cylinder pressure and Apparent Rate of Heat Release for the following conditions:

- BMEP=13.9 bar, 2500 RPM, λ=2.5, ϕ=0.40 (delayed combustion).
- BMEP=12.8 bar, 2500 RPM, λ=2.8, ϕ=0.36 (Ultra-lean combustion).

Finally, the third row of pictures shows a comparison in terms of NOx concentration.
For all the parameters, the agreement is very satisfactory, keeping into account the limits of a quasi-dimensional approach and the use of single set of calibration values.
The calibration model parameters used for the 4-Stroke reference engine will be used also in the 2-Stroke model engine.
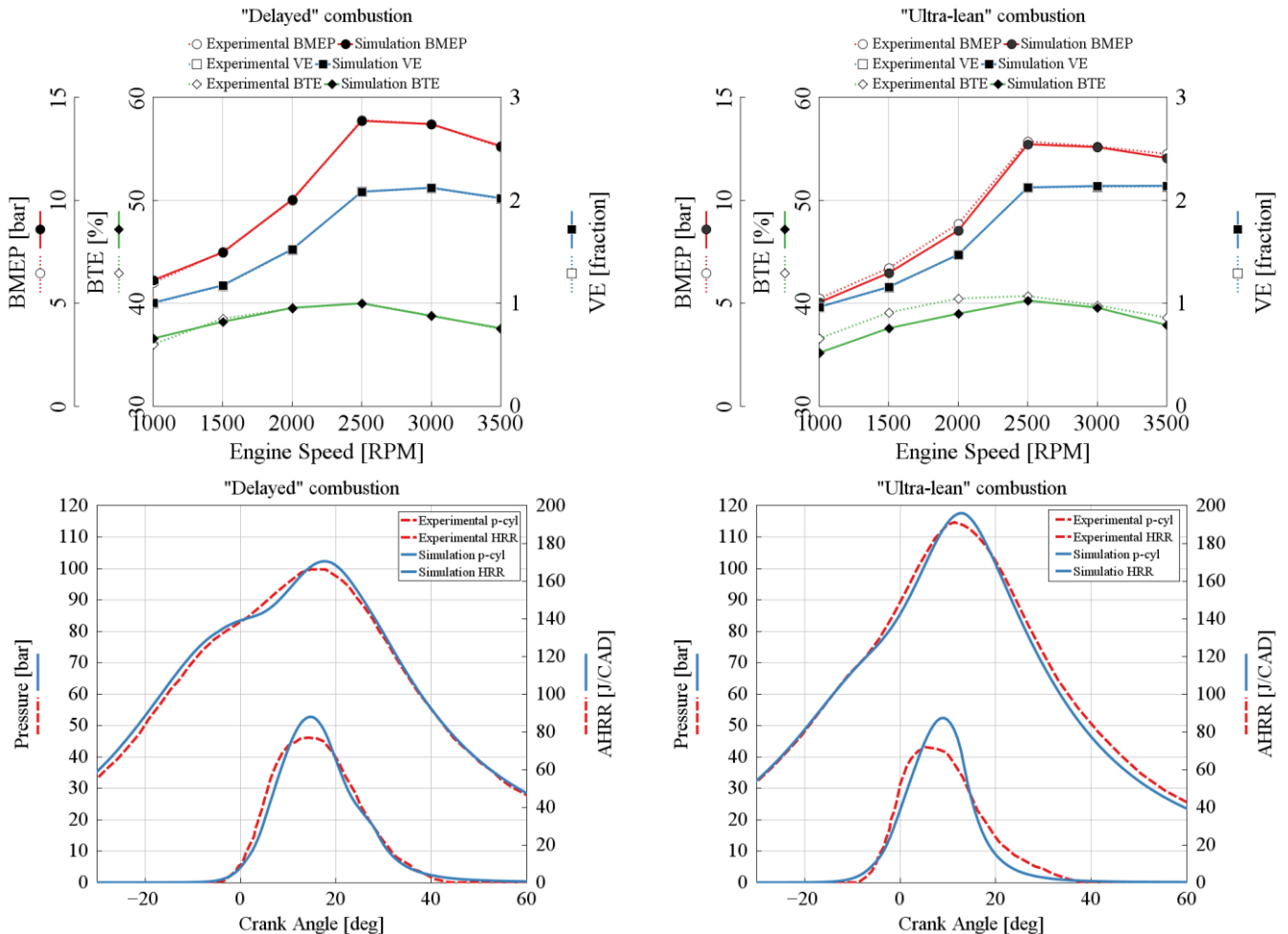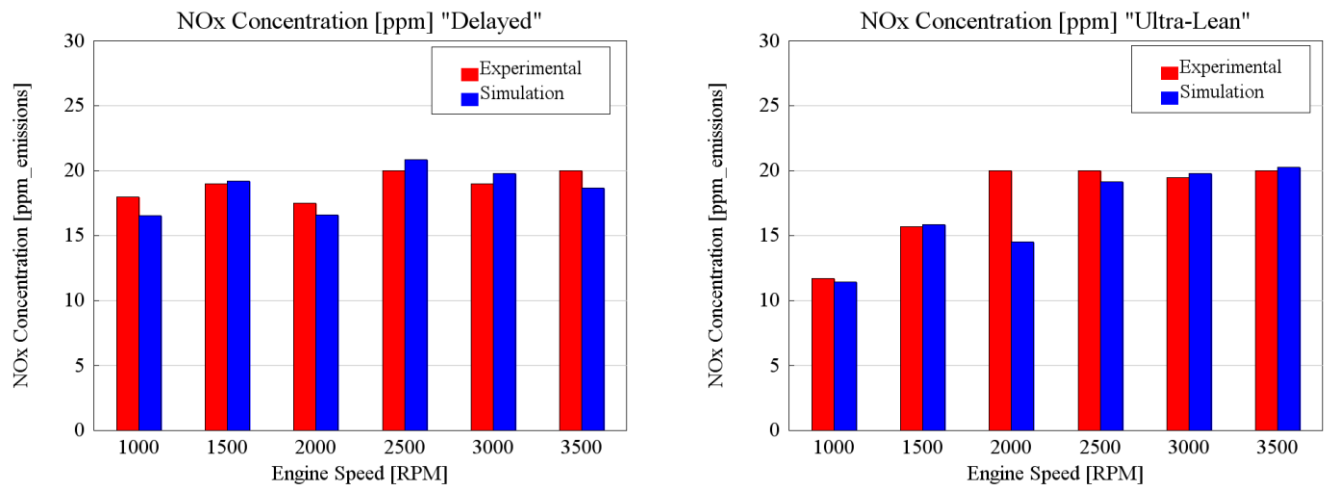
Figure 79: Delayed and Ultra lean combustion engine model calibration comparison

Table 28:Setup of the predictive combustion model (main parameters which are not set as default)

Flow	
Initial Tumble Ratio [-]	0.88
Initial Turbulent length scale [-]	1
Initial Normalized Turbulent Intensity [-]	0.1
Combustion	
Initial Spark Size [mm]	1
Initial Laminar Flame Speed model	Artificial Neural Networks trained on H_2 experimental data
Flame Kernel Growth Multiplier	5.3
Turbulent Flame Speed Multiplier	0.53
Taylor Length Scale Multiplier	0.69
NOx Emissions	
N2 Oxidation Activation Energy Multiplier	0.825

6.1.3   2-Stroke engine model layouts

The CFD-1D model of the 2Sengine is based on the calibrated model of the 4S reference engine, with delayed combustion. The changes, described below, are strictly limited to the specific requirements of the 2-stroke cycle. Therefore, no modification is made to the predictive combustion model and to the heat transfer parameters.

In order to achieve a maximum brake power comparable to the 4Sprototype (73 kW), a 3-cylinder in-line layout is chosen. Therefore, the total displacement of the engine is 899 cc. The maximum speed is set at 7000 rpm, corresponding to a maximum mean piston speed of 10.7 m/s: in comparison to the 4-Stroke engine, this parameter is very close if consider 3500RPM maximum speed (vp=9.6 m/s). For a more straightforward comparison with the reference 4-Stroke engine, a reduction gear of 2:1 is considered: therefore, the maximum output speed of the 2-stroke engine is identical to the speed of the 4-stroke at maximum power (3500 rpm). The output torque is calculated considering a mechanical efficiency of the gear reduction equal to 0.98.

The dimensions of the pipes are scaled in order to obtain identical flow losses at peak power conditions. Moreover, a supercharger and a further charge cooler is included in the intake system.

Concerning the mechanical losses, it is supposed that friction mean effective pressures in the 2-stroke engine are halved, due to the double cycle frequency. Considering the same geometry of the engine, the above hypothesis implies that the mechanical losses at each revolution of the crankshaft are the same.

The CFD-1D optimization of the virtual 2S engine is mainly focused on the gas exchange process. Three different supercharging systems are considered and depicted Figure *80*:

1. Two-stage, with a variable geometry turbocharger supported by an electric supercharger, two charge coolers (one after each compressor) (named 2S_VGT+eSC)
2. Two-stage, with a variable geometry turbocharger supported by a mechanical supercharger, two charge coolers (one after each compressor); electronic by-pass valve on the supercharger (named 2S_VGT+SC)
3. Single stage, mechanical supercharger, with electronic by-pass valve, one charge cooler (named 2S_SC)
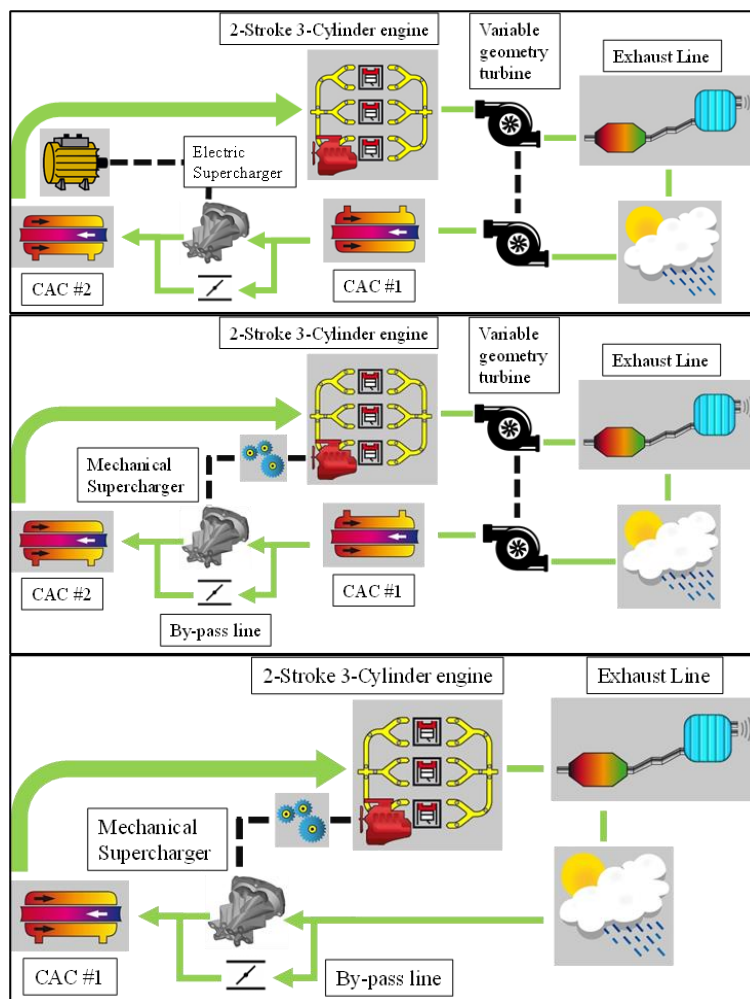
Figure 80: 2-Stroke model engines layout: two-stage electric supercharger (middle), two-stage mechanical supercharger (top), single stage (bottom).

The first solution allows a flexible and efficient control of the engine, the third is much less expensive and more compact. The second one is a sort of compromise.

As far as the electric supercharger is concerned, it is supposed that the energy required to drive the machine is taken from the engine crankshaft, with an efficiency equivalent to that of the mechanical transmission. This simplification is motivated by the empirical consideration that a part of the electric energy is free of charge (recovered during vehicle braking), but the remaining part is subtracted to the engine crankshaft at a relatively

low efficiency, due to the multiple steps in the energy transfer (from engine to the electric motor of the supercharger, passing through the electric generator, the inverter, the battery, …). A more accurate estimation of this aspect is outside the scope of the current work.

Without the energy recovery provided by the turbine, the fuel efficiency of the mechanical supercharging system is expected to drop at full load. However, the differences in terms of BTE should be more limited at partial load.

The choice of the components of the supercharging system was aimed to achieve high efficiency operations at medium-high engine speed, full load, where the gas exchange process has the stronger impact on fuel consumption.

For the single stage system, the map of the selected mechanical supercharger is presented in Figure *81*.

For the 2-stage systems, the map of the turbocharger compressor is shown in Figure *82*, while the map of the supercharger is presented in Figure *83*. In order to reduce the number of variables, the same supercharger is adopted for both electric and mechanical drive.

Figure *84* finally reports some characteristic curves of the VG Turbine, at different rack positions.
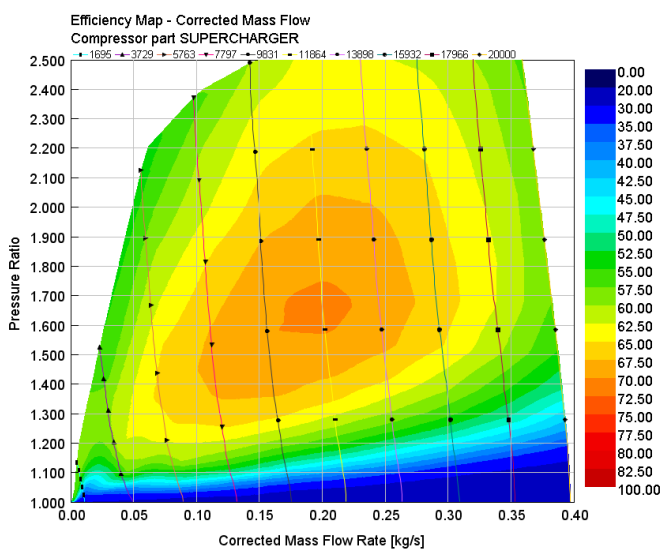
Figure 81: performance map of the mechanical supercharger employed in the single stage system
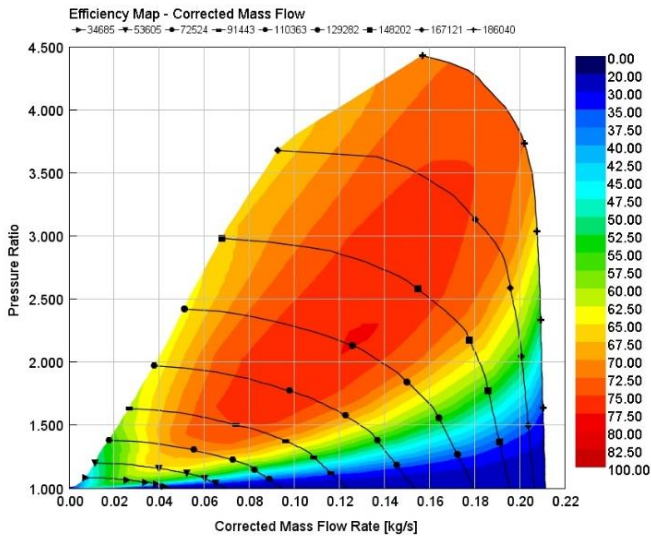
Figure 82: compressor map of the turbocharger, employed in the two-stage system
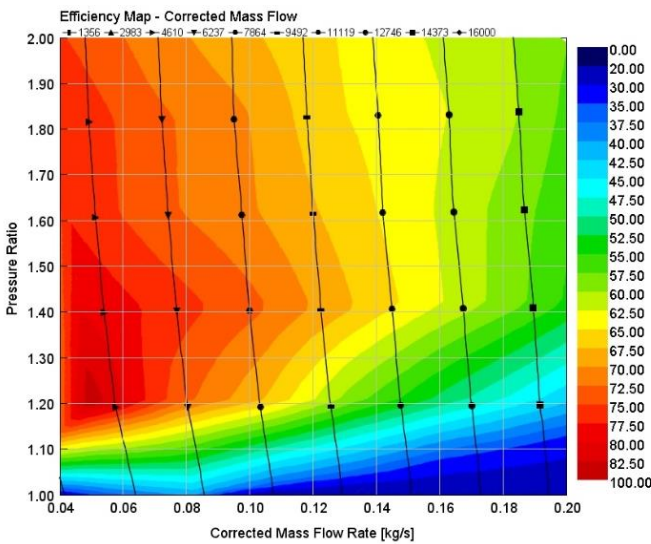
Figure 83: electric supercharger map, employed in the two-stage system
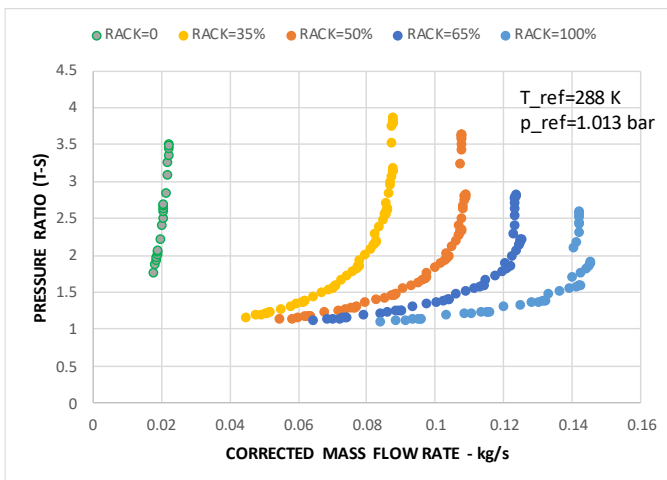
Figure 84: Characteristic curves of the Variable Geometry Turbine

For the single stage configuration, the three most important optimization parameters are: 1) the transmission ratio between supercharger and engine; 2) the effective area of the supercharger by-pass; 3) the effective area of the back-pressure valve, installed in the exhaust system. While the first parameter is constant, the others are calibrated for each operating condition. It should be noted that the by-pass valve has the same function of the throttle valve in a conventional 4S engine: as the by-pass valve opens, the mass flow rate delivered to the engine decreases, and vice versa.

This type of control is also quite effective in transient conditions, for two main reasons: first, at partial load, pressure in the intake manifold never goes below the atmospheric value, since it must be always higher than the average exhaust pressure; second, as soon as the by-pass is closed, the supercharger can immediately deliver to the engine the whole volume of air corresponding to its displacement.

When considering the 2-stage system, with the electric supercharger, the by-pass valve and the back-pressure valve are not strictly required, as load can be simply controlled by varying the speed of the supercharger. This parameter is fundamental also for optimizing the full load performance, along with the position of the turbine rack.

For each 2S configuration, the valve lift profiles have been also optimized considering the adoption of a Variable Valve Timing (VVT) device for both Intake and Exhaust. As the scavenging process occurs at BDC, the only constraint considered in the study is the maximum variation range of the phase (30°).

6.1.4   Results and comparison

This section presents a comparison among the reference 4-stroke engine (referred to as "4S-Testcase") and the three configurations of the 2-Stroke engine (referred to as "2S_SC", "2S_VGT+SC" and "2S_VGT+eSC", respectively), at both full and partial load.

All the configurations are calibrated to have NOx emissions lower than 20 ppm; as a further constraint, the peak cylinder pressure is set at 150 bar for the 2-stroke engines.

Figure *85* presents a comparison at full load, in terms of specific torque and power (the output brake torque or power is divided by the total displacement). As expected, the 2-stroke cycle strongly improves performances, in particular when associated to a 2-stage supercharging system: the specific low-end torque (at 1500-2000 rpm) is more than doubled (from 70 to 160 Nm/l), while the advantage in terms of maximum specific power is even higher. Even for the compact supercharged version (2S_SC), the specific torque curve is flatter and higher than the 4S-Testcase; the maximum specific power is 83 kW/l, vs. 38 kW/l.
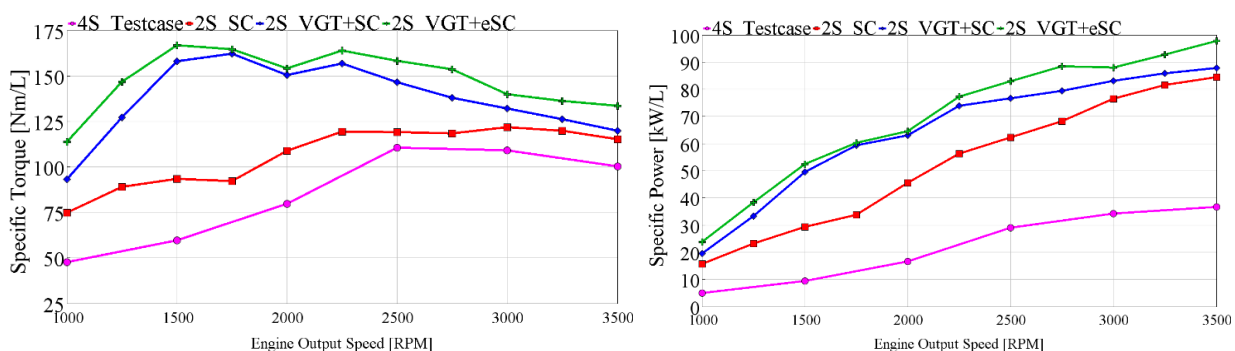
Figure 85: Specific brake torque (top) and power (bottom) at full load.

Figure *86* shows the setting of the supercharging systems, for each configuration, considering the volumetric efficiency and the average pressure in the intake manifold. In comparison to the reference 4-S, all the 2-S engines require a higher amount of air at medium low engine speed (<2500 rpm), due to the fresh charge escaping the exhaust during the scavenging process. Consequently, also boost pressure is higher at these conditions.

At high speed (>2500 rpm), the engines behavior changes. In the turbocharged 2-strokes, trapping efficiency improves significantly (see Figure 86), reducing the air requirement.
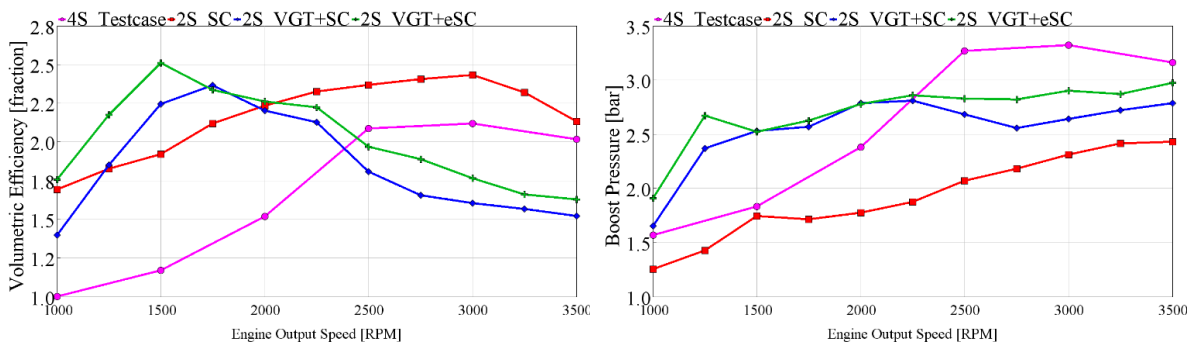
Figure 86: Trapped volumetric efficiency (top) and boost pressure (bottom) at full load.

However, boost pressure remains about constant, in order to compensate the rapidly increasing exhaust backpressure generated by the turbine. The last effect cannot be found for the configuration 2S_SC, without the turbine; in this case boost pressure monotonically increases, as engine speed (and, as a consequence, pressure losses across the cylinders) increase. As far as the 4-S engine is concerned, the results should be interpreted at the light of the adoption of an early intake valve closing strategy, aimed at the implementation of the Miller cycle. Therefore, the achievement of high volumetric efficiencies can be obtained only by rising boost pressure.

Two fundamental parameters for the 2S engines are the trapping efficiency and the fraction of residual gas at the beginning of the cycle, both presented in Figure *87*. As already observed in the CFD-3D analysis, the scavenging process with valves is less effective than other solutions, especially in presence of high values of volumetric efficiency. In particular, it is very difficult to find a good trade-off between high trapping efficiency and low residual fraction. At full load, for the 2S configuration with the mechanical supercharger, a significant amount of fresh charge is lost at the exhaust, especially at low engine speed. However, supposing a proper calibration of the fuel injection system, the lost charge does not contain fuel, so that the poor values of trapping efficiencies are not affecting the thermal efficiency. Moreover, the low fraction of residual gas helps the regularity of the combustion process.

Both the 2-stage supercharging systems allow a more flexible control of the scavenging process: in this case, the calibration was aimed to maximize performance, so that trapping efficiencies are significantly higher than in the mechanical supercharger version. On the other hand, the amount of residual gas is much higher.
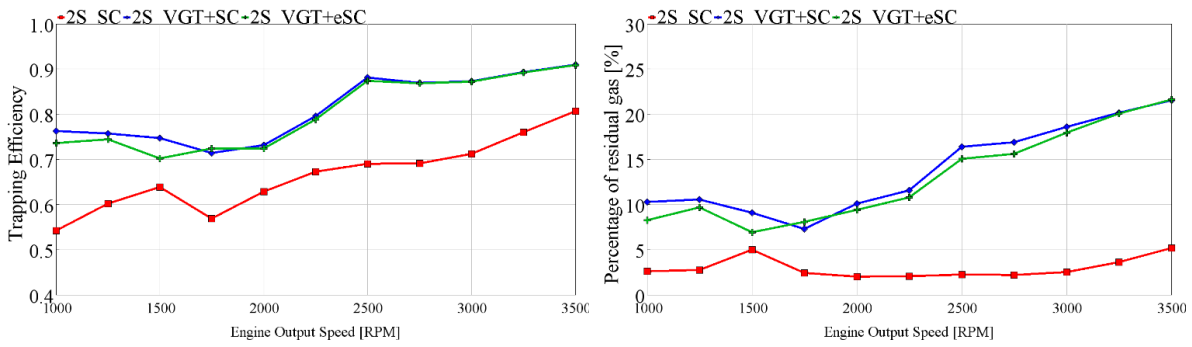
Figure 87: Trapping efficiency (top) and fraction of residual gas (bottom) at full load, for the 2-stroke engines

Figure 88 compares the brake efficiency (BTE) of all the configurations, at full load. The 4S engine shows a slight advantage in comparison to the turbocharged 2-strokes. The gap is much wider when the supercharged version is considered, in particular at high-medium engine speed. The penalization is directly related to the power adsorbed by the supercharger: the higher the contribution to boost pressure provided by the supercharger, the lower the efficiency of the system.
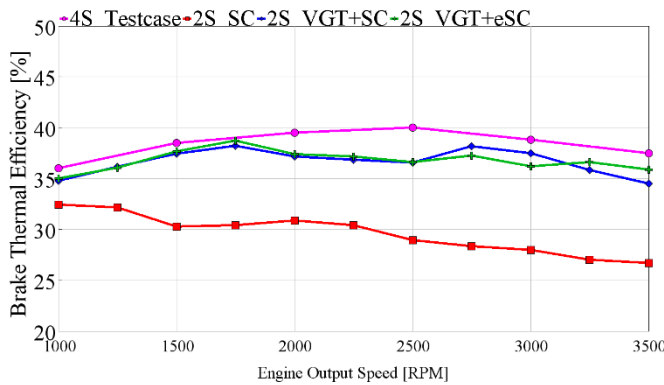
Figure 88: BTE at full load

Finally, a comparison is made in terms of BTE at partial load (Figure 89). It is supposed that all the engines are installed on the same car and the most representative operating conditions are defined by a grid of 12 points: engine speed: 1500, 2000, 2500 rpm; brake torque: 50, 100, 150, 180 Nm. For the 2S engines, each operating point has been calibrated, considering all the constraints, with particular attention to the concentration of NOx emissions (<20 ppm). For the reference 4S engine, the values of BTE at medium load (150 and 180 Nm) correspond to the experimental ones; for the low load points (50 and 100 Nm), the values have been calculated by using the calibrated CFD-1D model.

Figure 89 shows that at partial load the differences in terms of thermal efficiency are strongly reduced: the maximum variation is found at 180 Nm, between Testcase 4S and 2S_SC (about 15%)

At low loads (50 and 100 Nm), the most efficient configuration is 2S_VGT+eSC, while the reference 4S engine provides the best BTE at medium loads (150 and 180 Nm). The reason of this outcome is that this 2S configuration minimizes the relative weight of friction losses at low load, thanks to the small engine displacement (downsizing effect); however, as load increases, the 2S is penalized by the increasing power adsorbed by the supercharger.

It is interesting to notice that the electric supercharger provides a very small efficiency improvement (<5%), compared to the VGT version, with the mechanical supercharger. Furthermore, this small advantage is limited only to low loads (50 and 100 Nm). This outcome demonstrates that the use of the by-pass on the supercharger permits a quite efficient control of the load, even if it cannot completely cancel the losses associated to the supercharger at low loads.
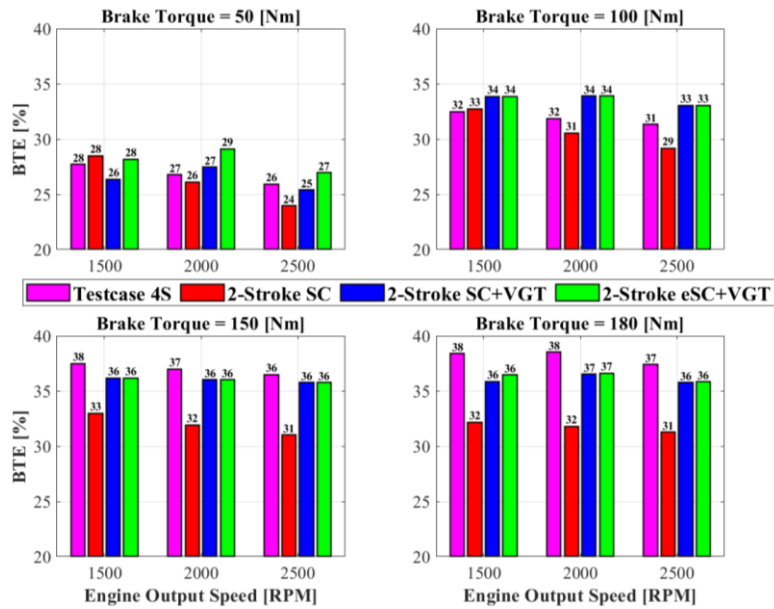
Figure 89: BTE at partial load.

6.2 Opposed piston hydrogen engine

An alternative path for the development of a H2 engine is represented by the 2-stroke (2S) cycle, and in particular, by the opposed piston (OP) design. This specific configuration with two pistons facing each other is far from a novelty, having been introduced at the end of the 19'30s on aircraft. Most of the existing OP engines work with compression ignition, but Spark ignition and direct fuel injection can be implemented quite easily [110,111]. The potential advantages provided by 2S OP engines, compared to 4-Strokes, are listed below [112–114]:

- Double Cycle Frequency: The engine's double cycle frequency allows for meeting performance targets with a smaller displacement (downsizing), lower speed (down-speeding), or a lower value of BMEP (downrating).
- Reduced Heat Losses: OP engines have reduced heat losses due to the smaller surface area of the combustion chamber, which is defined by the two piston crowns and the portion of the liner between them, eliminating the need for a cylinder head.
- Lower Mechanical Losses: The absence of valves in OP engines reduces mechanical losses. Engine airflow is regulated by two sets of ports, which open or close based on the motion of the two pistons.
- High In-Cylinder Turbulence: OP engines generally exhibit very high in-cylinder turbulence. This enhances the air-fuel mixing process and accelerates combustion.
- Improved BTE: The combination of the above-mentioned advantages leads to improved BTE, making OP engines more efficient.
- Lower Production Cost: When targeting the same performance goals, OP engines tend to have a lower production cost. This is due to the reduced number of components and lower thermal and mechanical stresses in the design.

The main issues to be addressed in the development of an OP H2 engine can be summarized as follows:

- Optimal Hydrogen Injection Timing: To prevent hydrogen short-circuiting during the scavenge process, it's essential to inject hydrogen into the cylinder as late as possible, ideally when the exhaust ports are already closed. However, this can be challenging, especially at high engine speeds, due to the limited time available for air-fuel mixing.
- Minimizing Lubricant Oil Combustion: There is a concern about the combustion of lubricant oil, which can generate CO2 emissions. To mitigate this issue, it's necessary to limit blow-by between the cylinder and the two crankcases. A well-designed liner-piston assembly can help achieve this goal, reducing oil consumption and emissions. Proper piston ring design and material selection can also play a significant role in minimizing oil consumption and combustion.

ICE, such as the Opposed-Piston engine, and Fuel Cells (FC) represent two competing technologies for hydrogen-powered vehicles. Each has its advantages and challenges:

Advantages of Internal Combustion Engines (2S OP):

- Lower Complexity and Cost: 2S OP engines are typically less complex and have cost advantages over fuel cells, making them more accessible in terms of production and maintenance.
- Lower Hydrogen Purity Requirements: 2S OP engines can operate with hydrogen at purity levels of 98% to 99%, which can be more cost-effective and easier to produce and distribute.

Challenges of Internal Combustion Engines (2S OP):

- Efficiency: To remain a practical alternative to fuel cells, 2S OP engines need to match or come close to the efficiency of fuel cells. While fuel cells have high peak efficiency (around 60%), ICEs typically have lower efficiency, and optimizing them for better efficiency can be a significant challenge.
- Emissions: Achieving low or zero emissions is essential for internal combustion engines to compete with fuel cells, especially in terms of environmental regulations and concerns.
- Hydrogen Combustion: The combustion of hydrogen can lead to issues like pre-ignition and high nitrogen oxide (NOx) emissions, which must be addressed in 2S OP engines.

While 2S OP engines have cost advantages and can operate with slightly impure hydrogen, they will need to make significant strides in terms of efficiency, emissions, and reliability to remain competitive with fuel cell technology in the rapidly evolving field of hydrogen-powered vehicles. The choice between these technologies will depend on various factors, including cost, efficiency, emissions, and regulatory requirements.

Measures indicate [115] that the average efficiency of the fuel cell stack is below 50%, and the fuel cell system efficiency drops below 40% at high loads due to the parasitic losses associated to the air compressor and other system accessories. Therefore, 2S OP H2 engines may be particularly well suited for commercial vehicles operating at high load. Other fields of interest may be stationary power generation, off road vehicles, boats, industrial machinery, et cetera.

The project is focused on a relatively simple application, i.e. a single cylinder electric generator delivering a maximum power of 45 kW at 3000 rpm. the study is mainly carried out by means of CFD 1D simulations for the whole layout definition and optimization. Particular care is devoted to the combustion process:

Firstly it is implemented a SI-Turb predictive model derived from the previous study, then the calibration parameters are slightly adjusted in order to represent a CFD 3D combustion process on a preliminary version of the same OP engine.

For the modelling of the scavenge process, reference is made to a previous CFD-3D study, carried out on an almost identical cylinder design [116].

6.2.1 1D-CFD engine model

A GT-Power model of the new OP 2S H2 engine was built, including the calibrated SI-Turb combustion model. The geometric characteristics of the engine are listed in Table 29, while the whole layout from the air intake inlet to the exhaust system outlet is illustrated in Figure 90.

It's important to highlight that the engine's load is regulated through the use of a by-pass valve, which is integrated into the supercharger. This valve effectively takes on the role typically performed by the conventional throttle body found in 4-stroke engines. Additionally, a backpressure valve is employed to provide an extra level of control over the flow through the cylinder. These components play a critical role in governing the engine's performance and optimizing its operation.

Table 29: Main Features of the Opposed piston model engine.

Engine Geometry	
Bore [mm]	84.5
Stroke [mm]	109.5
Con. rod length [mm]	223
Total Displacement [L]	1.2
Cylinder | Pistons [#]	1|2
Scavenge Design	
TPO [CAD bBDC]	44
TPC [CAD aBDC]	44
EPO [CAD bBDC]	60
EPC [CAD aBDC]	60
Height Transfer Ports [mm]	12
Height Exhaust Ports [mm]	22

To precisely manage the internal cylinder composition, a dedicated controller has been developed for the hydrogen and water injectors. This advanced controller was deemed necessary due to the limitations of the standard controller, particularly when striving to achieve the desired composition, especially when the trapping ratio deviates from unity.
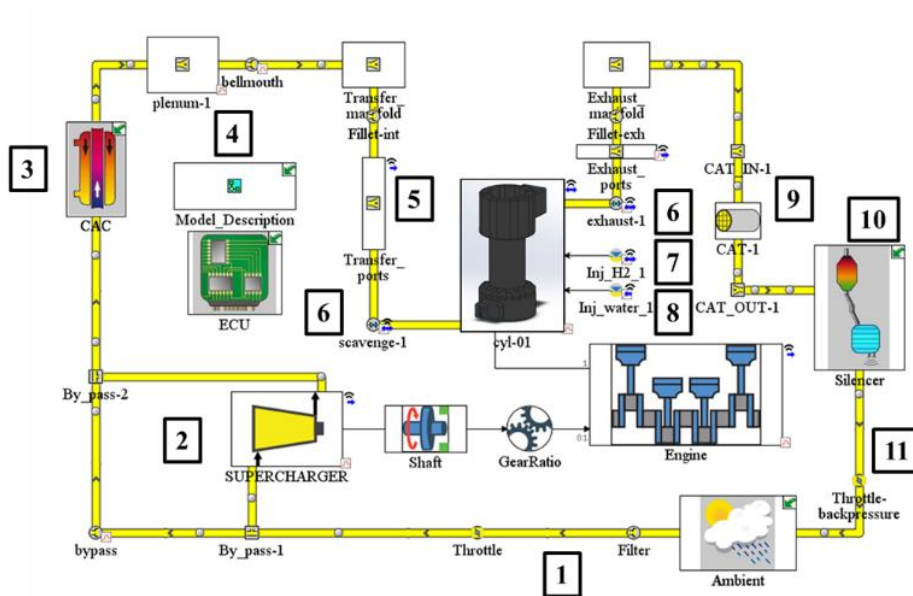
Figure 90: One-Dimensional model of the OP2S in the Gamma Technologies INC. environment

1. Air filter and inlet duct with secondary throttle valve
2. Mechanical Screw Supercharger with bypass circuit
3. Charge Air Cooler (CAC).
4. Intake Plenum.
5. Intake manifold wrapped around the cylinder
6. Scavenge and Exhaust ports.
7. Direct water injector into the cylinder
8. Direct hydrogen injector
9. Oxidation catalyst
10. Muffler volume

11.   Back-pressure valve

The cylinder geometry, including the design of scavenge and exhaust ports and manifolds, was optimized in a previous numerical study of the authors, fully described in [116]. The flow field within the cylinder during the scavenge process (when the exhaust ports are open) was calculated on an almost identical geometry by using a customized version of the KIVA-3V code.

A typical representation of the scavenging process characteristics is provided in Figure 91 which illustrates six different operating conditions. Each operating condition is defined by the engine speed and the setup of boundary conditions across the cylinder. The curves in the graph depict the amount of residual gases in the exhaust with respect to the quantity of residuals within the cylinder. The scavenging process begins at the top-right point of the graph and progresses to the left as the residual gases exit the cylinder. Figure 91 demonstrates that engine speed and the setup of boundary conditions have a minimal effect on the shape of the characteristic curves. Therefore, a single interpolation curve can effectively represent all these cases. It also reveals that for nearly the entire scavenging process, only residuals exit the cylinder, and no fresh air is lost.
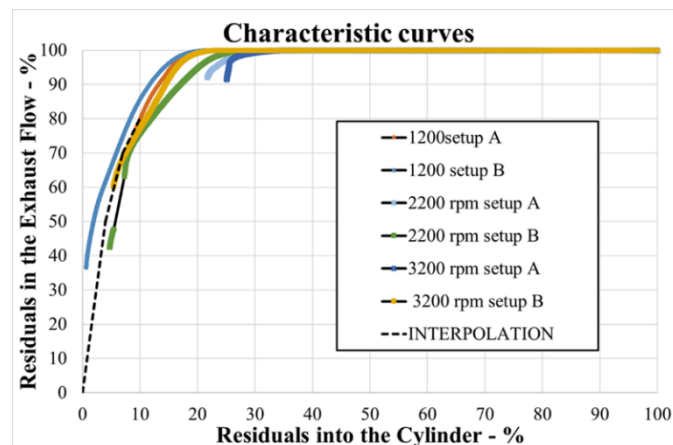
Figure 91: Scavenging characteristic curves calculated in a previous 3-D CFD study

The simulation of the scavenging process performed by KIVA-3V is used in the current study for the setup of the discharge coefficients of the ports and for the definition of the scavenging sub-model required by GT-Power. Moreover, the flow field at exhaust port closing is the starting point of the detailed combustion analysis, that will be presented in the next section.

6.2.2   3D-CFD Combustion Analysis

The combustion process in the OP H2 engine, whose main features are given in Table 29, is numerically investigated by means of the CONVERGE tool [117].

The primary purpose of this 3D-CFD analysis is to assist in calibrating the SI-Turb model, offering a more direct comparison for the new combustion process within the actual engine geometry. While the results of the combustion analysis may carry some degree of uncertainty without experimental data, they do provide a solid physical foundation for the calibration of a quasi-dimensional combustion model. Simulations are carried out

from Exhaust Port Closing (EPC) to Exhaust Port Opening (EPO), considering a homogeneous composition of the charge. Therefore, the modelling of intake and exhaust manifolds is not required. The computational grid of the cylinder after exhaust port closure is shown in Figure 92. On the basis of the previous CFD-3D simulations, a swirl ratio of 3 is set to initialize the in-cylinder flow field. The burnt gas fraction is set at 7.36 mass%.
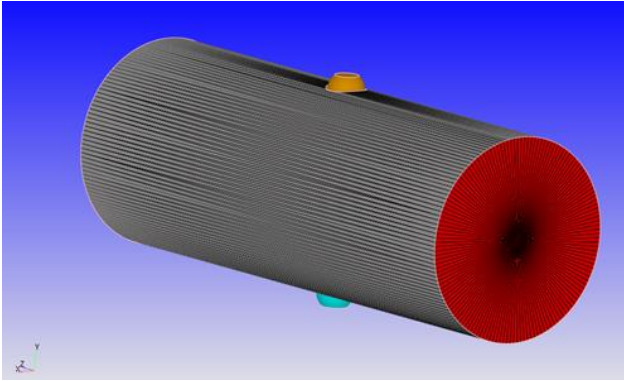
Figure 92: Opposed Piston CAD geometry used for CFD 3D simulations

Table 30: Main models employed in the 3D-CFD analysis

Equation of state	Redlich-Kwong
Turbulence model	RANS RNG $k - \varepsilon$
Wall heat transfer model	O'Rourke and Amsden
Near wall treatment	Standard wall function
Combustion model	SAGE detailed chemistry solver + adaptive zoning
Reaction mechanism	13 species and 25
NOx model	Thermal (Extended Zeldovich) + Prompt

Converge adopts the SAGE detailed chemistry solver, in conjunction with a multi-zone model, which reduces the computational effort without any penalization on the accuracy of the results. A chemical mechanism composed by 13 species and 25 reactions is used. As far as NOx emissions modelling is concerned, both Thermal (Extended Zeldovich) and Prompt models are employed.

Finally, the well-established RNG $k - \varepsilon$ turbulence model with wall-functions is used. Table 30 reviews the main models used in the 3D-CFD combustion analysis.

Based on the Base Grid Size (BGS) analysis performed in the previous simulations, a BGS of 1 mm is used, coupled with an Adaptive Mesh Refinement (AMR) on velocity field that produces a maximum mesh refinement of 0.5 mm. A second AMR, based on spatial gradients in temperature, is applied from SOI to end of simulation (i.e., EPO), with maximum mesh refinement of 0.5 mm.

Furthermore, specific mesh refinements are applied to the pistons and cylinder liner boundaries, where two-cell layers with a size of 0.5 mm are applied. Finally, two concentric sphere refinements, centred between the spark electrodes, are used to accurately capture the first stages of combustion, when the flame kernel is formed. In detail, the first sphere refinement consists in a spherical region with a radius of 4 mm and a cell size of 0.25 mm, while the second sphere refinement is characterized by radius of 2 mm and a cell size of 0.125 mm.

The setup of the engine parameters for combustion simulation is summarized in Table 31. As it can be noticed, the value of lambda (2.38) is similar to the one used on the 4S H2 engine presented in the previous section.
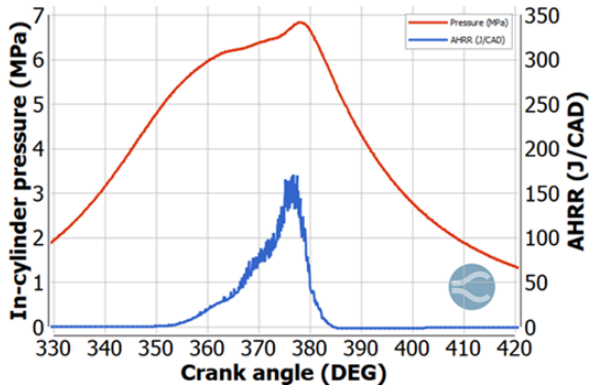
Figure 93: In-Cylinder pressure and AHRR predicted by the CFD-3D Opposed piston simulation

Engine parameters	Value
Pressure @ EPC [MPa]	0.15
Temperature @ EPC [K]	419
Total mass trapped	1370.7
H_2 mass [mg/cycle/cyl]	15.5
Lambda [-]	2.38
Residuals [mg/cycle/cyl]	100.9
EGR [%]	0
Swirl Ratio [-]	3
Start of Ignition [°CA ATDC]	-15

Figure 93 displays the in-cylinder pressure and AHRR as predicted by the 3D-CFD model. Even though the SOI is set at -15 CAD after TDC, combustion primarily occurs during the expansion stroke. However, the Peak Pressure Rise Rate is low (1.74 bar/CAD) due to the rapid increase in cylinder volume. This, combined with the very lean H2-air mixture, results in extremely low NOx emissions, specifically 11 ppm. These findings underscore the effectiveness of lean and delayed combustion in OP engine technology, which not only yields ultra-low NOx emissions but also excellent combustion efficiencies (ηc = 100%).

6.2.3 SI-Turb Calibration Analysis

The SI-Turb model calibrated for the 4S engine requires some modifications, in order to match the CFD-3D results on the OP engine. The new values of the multipliers are presented in Table 32. It is interesting to observe that with the new calibration the model parameters are close to the default values, demonstrating the physical soundness of the predictive combustion model.

After this calibration, the agreement between 1D and 3D results is quite perfect, also in terms of NOx emissions, as shown in Figure 94.

(a)

(b)
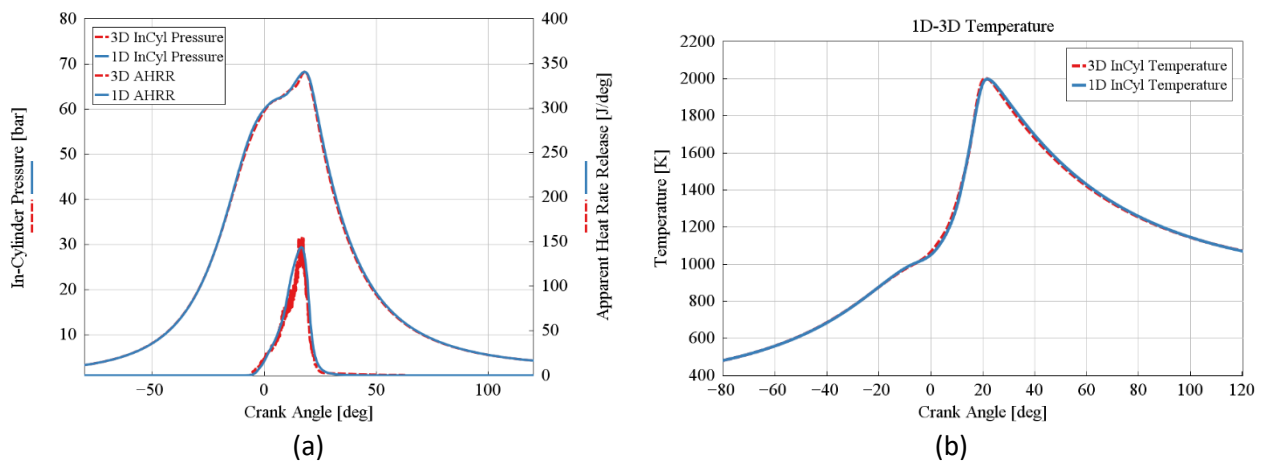
Figure 94: OP in cylinder pressure, AHRR (a) and in cylinder temperature (b) comparison 1D-3D

128

Flame Kernel Growth Multiplier	1
Turbulent Flame Speed Multiplier	1.75
Taylor Length Scale Multiplier	3
N2 Oxidation Activation Energy Multiplier	0.99

6.2.4 Hydrogen Opposed-Piston Engine Optimization

The numerical optimization process in this study aims to maximize BTE while adhering to the constraints outlined in Table 33. The optimization process is conducted iteratively and involves several key steps:

- Selection of the supercharger and determination of the transmission ratio between the engine and compressor.
- Optimization of the timing for the exhaust and scavenge ports, as well as the design of the manifold geometry.
- Calibration of the primary combustion parameters, including Spark Timing, Water-Fuel Ratio (WFR), Water Injection Timing, Air-Fuel Ratio (AFR), Hydrogen Injection Timing, and Compression Ratio.
- Optimization of the exhaust system's geometry, including the control of the backpressure valve.

Iterations continue until the optimized parameters reach a stable state with no further changes. It's worth noting that water injection in this project primarily serves the purpose of reducing NOx emissions rather than controlling knocking.

Table 33: OP2S Optimization constraints.

Lambda range	(2.4 – 2.8)
Trapping Ratio [%]	>90
Maximum cylinder pressure [bar]	<150
PPRR [bar/CAD]	<6
Minimum power output [kW]	30
bsNOx emission [g/kWh]	<0.25
EGR at combustion start [%]	<15
Burn Duration 10-90 [CAD]	<50
(Maximum Water Flow Rate / Maximum Hydrogen Flow Rate) [-]	<1.25

The performances of the optimized OP 1.2 L H2 engine have been calculated at both full and partial loads. Brake Torque, Power and Thermal Efficiency at full load, are presented in Figure 95, along with Trapping Efficiency.
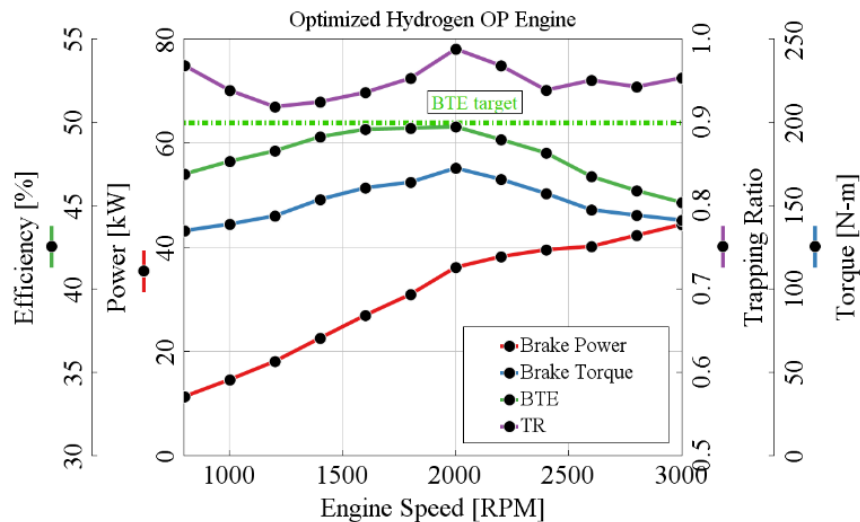
Figure 95:Main results for the optimized OP engine, in terms of Trapping Ratio, BTE, Torque and Power

The OP engine presents a quite flat torque curve, with a peak of about 170 Nm (BMEP=8.9 bar) at 2000 rpm. The good quality of the scavenge system optimization is evidenced by the high values of trapping ratio (always higher than 90%).

The power density (37 kW/l, comparable to the reference 4-S engine) is satisfactory, considering the simplicity of the supercharging system and the low maximum engine speed. The most outstanding result is the value BTE, always higher than 45% and with a peak of about 50%.

Figure 96 Figure 97 shows the maps of BTE and specific NOx calculated for all the operating conditions of the engine, in terms of load and speed. The control strategy at partial loads can be described as follows.

- Starting from full load, as load decreases the equivalence ratio can be reduced, up to the combustion stability limit (ϕ=0.36, λ=2.8).
- For lower loads, the by-pass valve on the supercharger should open, in order to reduce the mass flow rate entering the cylinder.
- Water injection is suppressed for Load<50%, due to the already low values of NOx.

The BTE map of Figure 96 shows how the efficiency of the engine remains very high over a wide range of operating conditions. This outcome is fully coherent with the experimental results presented by Achates Power for the OP Diesel Engine [118].

Also, the values of specific NOx (Figure 97) are low (never over 0.25 g/kWh), confirming that the engine can be used also in applications where operating conditions change widely, as on a vehicle.
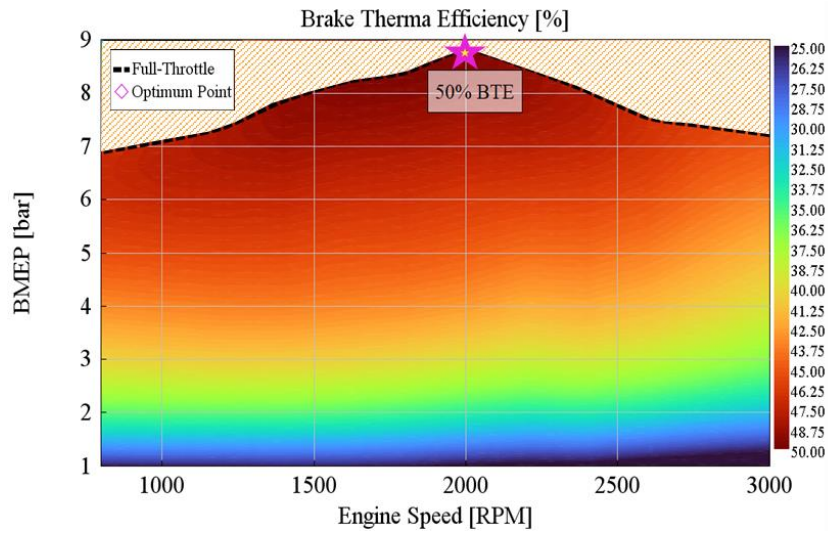
Figure 96: BTE calculated for all the operating conditions of the engine, in terms of load and speed.
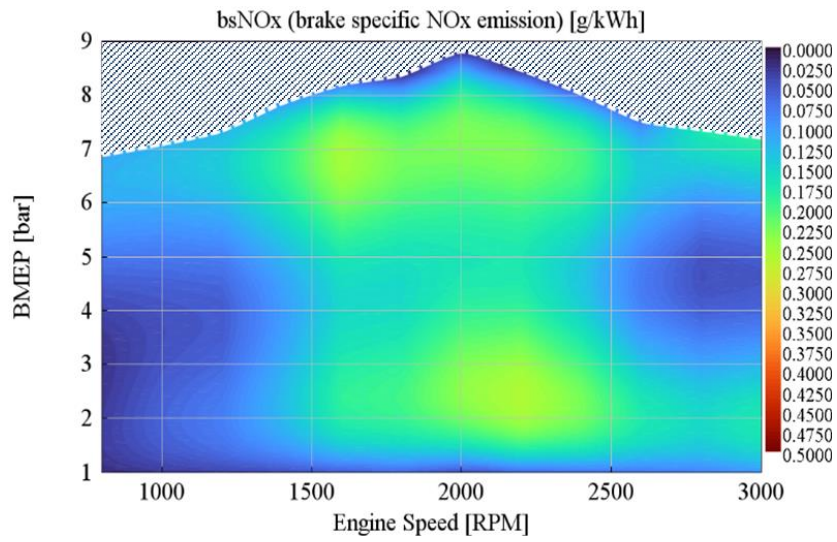
Figure 97: Specific NOx calculated for all the operating conditions of the engine, in terms of load and speed.

6.3 Small Loop hydrogen engine – injection characterization

Small loop-scavenged engines, such as 50cc scooter engines, are designed for compactness, simplicity, and reliability. However, they face challenges related to low trapping efficiency and significant fuel losses through the exhaust. Depending on the chosen injection method and intake port design, it's possible to mitigate these fuel losses [119]. These engines can evolve from traditional carburettors to more sophisticated low-pressure direct injection systems, increasing trapped fuel and playing a role in the ongoing powertrain technology transition.

This project, conducted in collaboration with the University of Graz's Institute of Internal Combustion Engines and Thermodynamics, focuses on their patented 50cc loop-scavenged engine. This engine can run on conventional gasoline, methane, and has undergone testing with hydrogen as well.

Leveraging experimental data from a 50cc prototype running on hydrogen with a patented LPDI injection system, an extensive 3D CFD campaign has been executed. The aim is to enhance hydrogen trapping efficiency through system modifications, including injector positioning and piston shape adjustments.

6.3.1 Motivation of the study

The Low pressure direct injection system developed by the Technology University of Graz [84,119,120] features a unique design. It utilizes a single injector positioned above the intake boost port. Notably, the injector's tip is strategically placed to ensure that the piston opens the exhaust port before the injector activates. This configuration serves to significantly reduce the pressure and temperature of the exhaust gases, minimizing the risk of damaging the injector tip. To accommodate this placement above the boost port, the injector is inclined downward, facing the piston.

Figure 98 a cross-section of the engine layout, referred to as 2TE3, is presented. One key feature to highlight is the piston, colored in orange, which incorporates a drilled hole in the skirt. This hole allows for dual injection methods. As depicted in Figure 99, fuel can be injected during the scavenging process, when the piston is in motion around the BDC. Conversely, it is also possible to inject fuel when the piston closes the transfer ports, directly into the crankcase through the drilled hole in the piston. This versatile design offers flexibility in the injection timing and process.
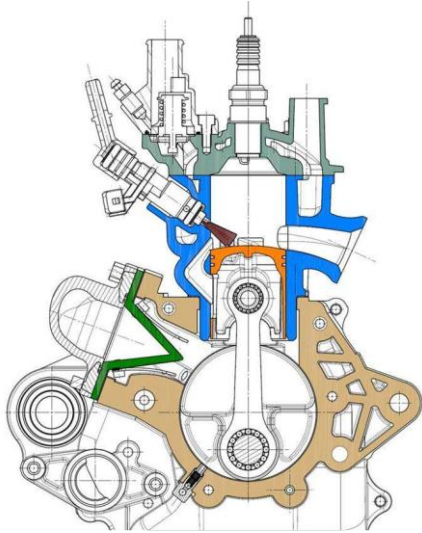
Figure 98: cross section of the LPDI 50cc engine 2TE3
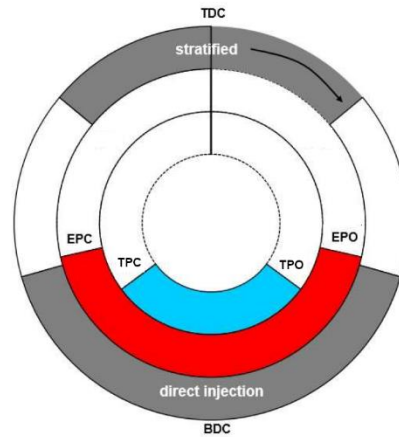
Figure 99: polar diagram of the LPDI 50cc 2TE3 engine

The experimental setup for the 50cc LPDI 2-Stroke engine is equipped with an array of advanced sensors and components aimed at monitoring and controlling its performance. This comprehensive setup includes:

- Fuel Pressure Sensor (PMA P30): This sensor ensures precise measurement of fuel pressure, contributing to the engine's efficiency and reliability.
- Cylinder Pressure Sensor (AVL GH14D): It plays a critical role in monitoring cylinder conditions, providing essential data for performance analysis.
- Fuel Coriolis Mass Flow Measurement System: This system accurately measures fuel flow, which is vital for optimizing the engine's fuel delivery.
- Lambda Sensor (ETAS LA4): Lambda sensor measurements are conducted to maintain optimal air-fuel ratios, a key factor in engine efficiency.
- Bosch Natural Gas Injector (NGI2): This injector is used for low-pressure fuel injection, enhancing the engine's combustion process.

In the interest of safety and reliability, a unique feature has been incorporated. In the event of a backfire in the crankcase, a safety mechanism is in place, which involves creating a hole in the crankcase and securing it with a cover plate. This setup allows the cover to dislodge if necessary, facilitating the safe release of excess pressure into the surrounding environment. This additional safety measure ensures the overall integrity of the experimental setup and the safety of its operation (Figure 100) .

Figure 100: Hole in the crankcase of the 2TE3 in case of backfire

Experimental data are mainly referred to 3 different injection pressure: 3 bar, 5 bar and 10 bar. These configurations are compared to the standard gasoline engine. In Figure 101 are reported the experimental Lambda Value (Fig. (a)) and the brake power (Fig. (b)), some main results can be summarize as follow:

- moving from gasoline to hydrogen there is an expected power loss up to 10-15%;
- the 3 hydrogen setup obtain similar lambda values and similar power output values;
- moving from 5 bar to 10 bar, with the same lambda value, the former seems to be slightly better

Analyzing Table 34 where are reported the main data only at 6000RPM for the 3 H2 injection strategies is interesting to notice also from here that the brake performances are similar, 5 bar injection pressure seems to have a better IMEP, while 10 bar injection pressure has the lowest despite the higher amount of hydrogen injected, nevertheless lambda values are very close.

The aim of the subsequent simulations is to better understand the hydrogen behavior and distribution during the injection process.

Table 34: 2TE3 experimental data @6000RPM WOT

Engine speed	Power output	BMEP	IMEP	FMEP	MF_air_in	MF_h2_in	P_injection	DOI	Lambda	Injected mass
RPM	KW	bar	bar	bar	Kg/h	Kg/h	bar	deg		mg
6023.22	2.19	4.32	5.05	0.73	15.15	0.6150	10.14	55.53	1.205	1.70
6015.08	2.16	4.28	5.15	0.88	15.04	0.3544	7.06	52.82	1.455	0.982
6040.74	2.57	5.06	6.08	1.02	18.12	0.3568	5.02	61.87	1.363	0.984

(a)   (b)
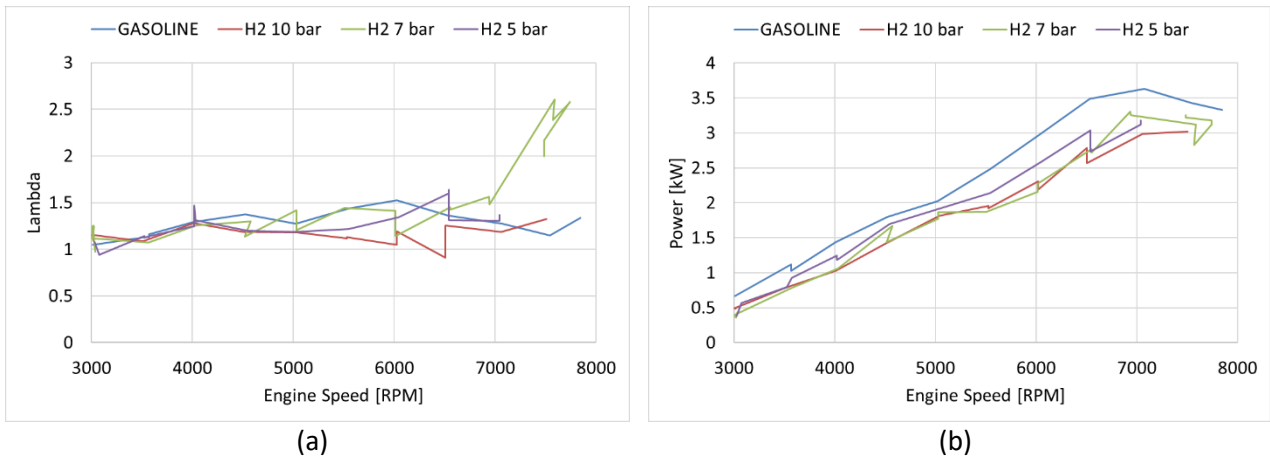
Figure 101: experimental results of the 2TE3 engine gasoline VS hydrogen in term of Lambda (a) and Brake Power (b)

6.3.2   CFD 3D simulation methodology

To obtain the proper hydrogen distribution and then optimize the trapping ratio is necessary firstly to characterize the injector. The injector tip has been reproduced with a 3D CAD software and it's been prepared a spray bomb simulation with a big cylinder. Doing so it's been possible to analyses the mass-flow dependency from injection pressure and chamber backpressure, as well as the injector discharge coefficient.

This process is fundamental to further reproduce the injection pattern in the engine simulation since the testbench gives us only the mean mass flow rate value, but during the simulations is needed the specific opening and closing ramps.

After the injector characterization the mesh of the engine it's been prepared for a full cycle simulation, using the symmetry of the system to reduce the number of the cell and the computational cost.

Multi-cycle simulations are made for a single case, 6000RPM WOT for injection pressure 5 bar, 7 bar and 10 bar, reinitializing pressure, temperature and EGR inside the cylinder every cycle to obtain convergence in term of in cylinder mass of air and fuel. The comparison with the experimental data is made by means of some main results and then the fuel trapping efficiency s optimized following the most promising path instead of using a design of experiments (DOE) to reduce the computational cost.

6.3.3   Injection characterization

The injector bosh NGI2 is a typical natural gas injector for injection pressure between 2 and 10 bar. In the experimental campaign is fueled with hydrogen with injection pressure between 5 and 10 bar. From the Figure 102 (b) is possible to reproduce the injector tip in a CAD environment while from Figure 102 (a) is possible to calculate the opening time (1.7-2 ms) and closing time (0.2-0.4 ms).

From the testbench it is possible to measure the mean mass flow rate value on a full cycle, and from the injection duration imposed by the ECU is possible to calculate the injected mass per cycle.

To define the "real" injection pattern some information are needed:

- injection start and end crank angle from the ECU

135

- injected mass calculated from the mean mass flow rate and the injection duration
- max mass flow rate for a certain injection pressure
- injector real opening and closing ramp

(a)

(b)
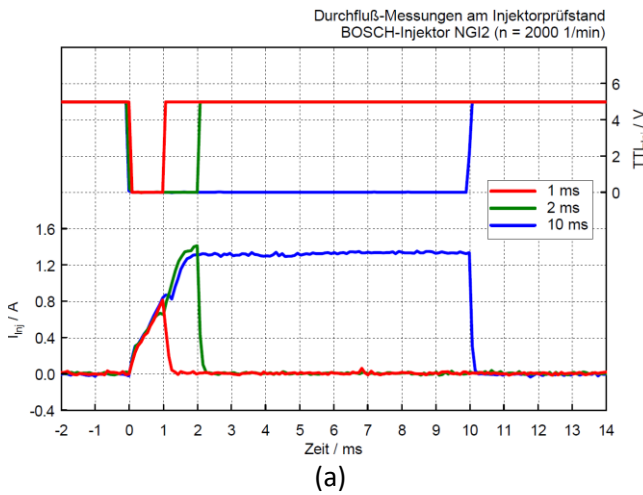
Figure 102: injector Bosh NGI2 characteristic curves (a) ad tip picture (b)

From the experimental data is quite clear that the amount of injected hydrogen is too low to allow the injector to fully open. In Table 35 the injection duration is converted to ms, even with 5 bar of injection pressure the longest opening time is 1.7ms, the real injection pattern will be closer to the triangular red line in Figure 102 (a) instead of the blue line. For that reason, a bunch o injection pressures are selected to be simulated, to be sure to fully catch the behavior of the injector:

Selected injection pressure: $3 - 5 - 7 - 10$ bar

Selected chamber backpressure: $1 - 1,5 - 2 - 3 - 3,5 - 4 - 4,5$ bar

Table 35: 2TE3 experimental injection duration

P_inj	DOI	DOI
bar	deg	ms
10.14	55.53	1.536
7.06	52.82	1.464
5.02	61.87	1.707

For the simulation the injector is positioned at the top of a big chamber of 100mm diameter in order to avoid the influence of the chamber walls on the injected flow. The CFD 3D analysis are made with the commercial software AVL Fire already described. The mesh is made by hexahedral elements from 0.1mm of mean mesh size in the injector tip to 3mm at the very periphery. The simulations are time depending and the injection pressure rises from very low value at the beginning to the final value with the injector fully open for the whole simulation, this strategy enhance simulation stability.

In the first set of simulations the injection pressure is varied and the chamber back pressure is constantly set to 1 bat. No specific ramps are imposed, since the focus is the tip discharge coefficient and the maximum static mass flow rate comparison between the calculated one and the simulated. As it is possible to see from Table 36 with a fixed Cd of 0.455 the static mass flow rates agreement are quite good, some differences are due to the approximated value of the Cd and of the fuel density, interpolated by the tables presented in Reference Fluid Thermodynamic and Transport Properties Database [121].

Table 36: static mass flow hydrogen injector characterization

CALCULATED MASSFLOW RATE					
Flow Coefficient	-	0.455	0.455	0.455	0.455
Fuel Density	kg/m3	0.248	0.412	0.577	0.822
Fuel Temperature	°C	20	20	20	20
Hole Area(1 holes)	m2	9.68E-07	9.7E-07	9.68E-07	9.7E-07
Injection Pressure	bar	3	5	7	10
Cylinder Pressure	bar	1	1	1	1
Number of Holes	-	4	4	4	4
MF static - Hole	kg/h (one Hole)	0.50	0.91	1.32	1.93
MF static - Injector	kg/h (Injector)	2.00	3.64	5.27	7.71
CFD3D STATIC RESULT					
	Kg/s	0.00	0.00	0.00	0.00
	kg/h	2.14	3.64	5.13	7.37
	g/s	0.59	1.01	1.43	2.05

With the information of the maximum static mass flow rate for every injection pressure it is possible to calculate the real injection pattern. As previously said the experimental DOI is too short to fully open the injector for the tested cases, then a triangular shape for the injected fuel is more probable, interpolating the mass flow rate from zero to the static one calculated and make the whole injection duration coherent with the experimental one. From the imposed mass flow rate is easy to calculate the injected mass. If the injected mass is the same as the experimental results, the hypothesis on the triangular injection is coherent and the real injection pattern is reasonably correct.

It is interesting to underline that with 3bar pressure the injection time to inject the same hydrogen of the 5bar pressure is more than 2ms, so that the injector is fully open and the injection law is more "standard".

As an example in Figure 103 are reported 2 injection laws: the first is the one of 3 bar (a), considering the injected mass equal to the one of 5bar, while the second is the one related to 10bar (b) in which is represented also the interpolation to the mass flow rate if the injector is fully open.
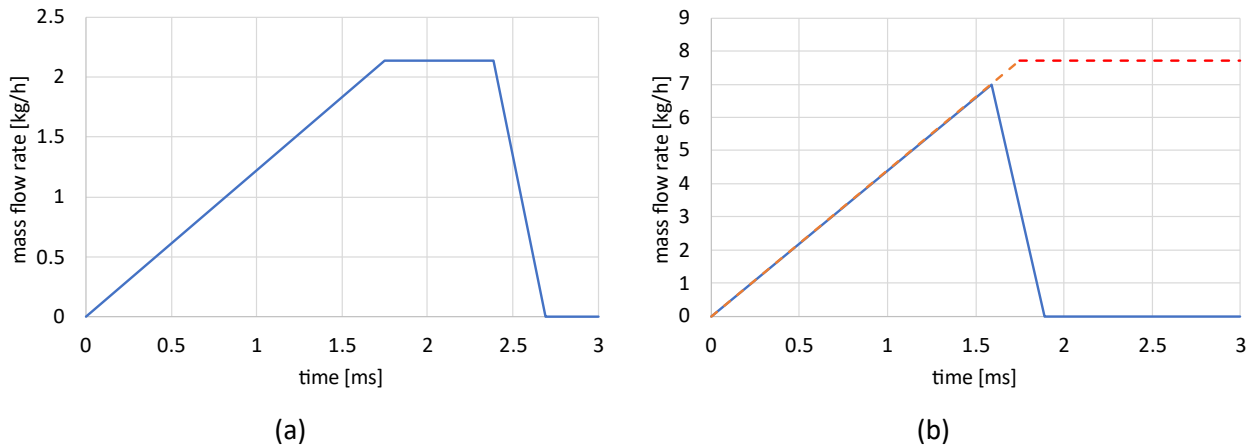
Figure 103: imposed injection mass flow rate for 3bar (a) and 10 bar (b)

Some of the main results are summarised in Table 37:

- the differences in term of injected mass between the simulated one and the one derived from experimental data are due to the differences in term of effective opening and closing of the injector tip, due to the very short time it is probable that the cycle-by-cycle variation can be quite relevant, moreover the imposed injection laws for different pressure are calculated using the same opening and closing timing, to reduce the amount of possible variables
- the expected maximum pressures in the triangular pattern are very close to the resulting from the simulations, confirming once again that the injector behavior is correctly represented

Table 37: real injection pattern CFD 3D results compared to experimental data

P_inj	DOI	DOI	exp. mass	CFD3D mass	expected P_max	CFD3D P_max
bar	deg	ms	mg		bar	Bar
10	55.53	1.54	1.70	1.75	9.07	9.09
7	52.82	1.46	0.98	1.05	5.86	5.64
5	61.87	1.71	0.98	1.00	4.91	4.94
3	86	2.39	0.98	0.99	3	3.2

Lastly is tested the dependency of the chamber backpressure on the mass flow rate only for the case with 5bar of injection pressure. As previously stated, the chamber backpressure is the only variable changed between every simulation, keeping constant the injection pressure law and therefore also the injected mass and mass flow rate. In Figure 104 are reported all the resulted curves of mass flow rates for different values of back-pressure, from the dotted 1bar (taken as a reference) up to 4.5bar (red line). As it can be expected at higher pressure gradient correspond higher velocity through the injector holes. If the Mach number rises the fuel density drop, reducing the mass flow increment. From Figure A.5 in appendix is possible to observe the dependency here described: the images are taken in the moment of maximum injection pressure and it is possible to observe that Mach 1 is reached for a backpressure of 3 bar, with higher pressure gradients the mass flow doesn't change anymore.
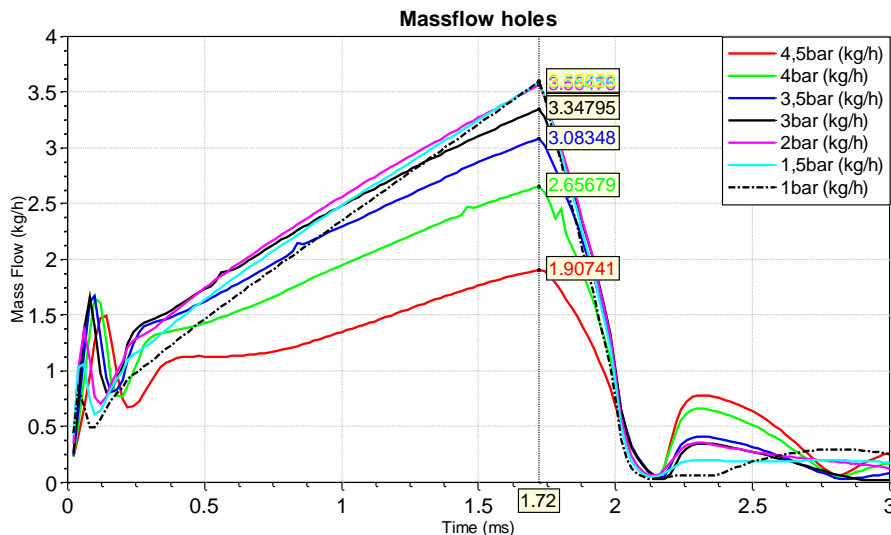
Figure 104: mass flow rate dependency from the chamber backpressure variation

6.3.4 Injection optimization

the process for evaluation of the fuel trapping efficiency can be summarize as follows:

- mesh of the whole engine, defining the symmetry plane and the piston movement;
- intake mass flow rate definition on the basis of previous experience but scaled on the basis of experimental mean value;
- injection strategy definition, related to the injector characterization just made;
- multi-cycle simulation with temperature reinitialization to obtain convergence in term of in cylinder mass distribution and developed flow field, thanks to experimental data the target in-cylinder pressure is fixed and it is possible to only modify the temperature; full residuals is imposed at every reinitialization since it happens right before EPO.

On the basis of this methodology the fuel trapping efficiency is calculated at the last cycle as in-cylinder fuel mass divided by injected mass. For the first group of simulations it is also compared the mean Lambda value with the experimental one, even if it could be affected by the distance from the cylinder and some fuel can be burnt outside the cylinder, it is interesting to analyze the trend.

From the results of the first set of simulations, the most promising solutions are further implemented and tested, making comparison also in terms of physical implementation and feasibility.

The selected operative condition is WOT 6000RPM because is one of the highest tested operative condition with a good combustion stability, the computational domain is made by the whole engine from the reed valve to the very end of the exhaust system. The intake boundary condition is a mass flow rate crank angle based considering the reed valve itself, doing so, when the valve should be closed because of the backpressure, the mass flow is simply set to zero. The reason to simulate the whole exhaust is to avoid the implementation and calibration of a CFD 1D model that could help to predict the pressure behavior but it need a bit of correlation with experimental data. Using the entire exhaust system is possible to set a fixed output pressure corresponding to the pressure in the test bench cell. The related mesh (Figure 105) is made by hexahedral cells with mean cell size of 2mm and refinement in the more interesting portions such as transfer and exhaust ports, cylinder, and injector volume. Thanks to the symmetry of the engine is possible to simulate only half of it, counting the total number of cells at BDC of 286000 cells.

The amount of cells will vary changing the injector position and especially the piston shape.
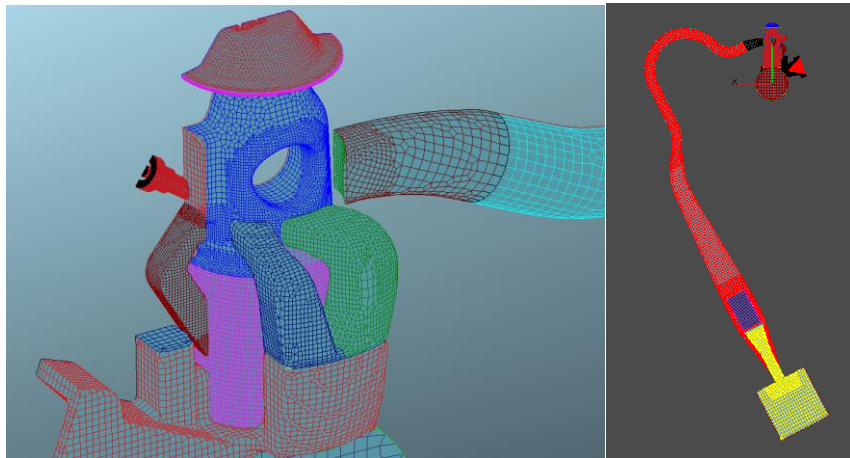
Figure 105: 2TE3 computational volume

In the first round of simulations the experimental setup is replied and it will be taken as a reference for the further comparisons. As depicted in Figure 106 the injector is positioned downward and the piston shape is standard. As for the injector characterization the considered injection pressure are 3-5-7-10 bar, with their specific injection laws. To define every injector modification during the whole project is used a nomenclature specific for every case: injection pressure that identify also the specific injection pattern + the major modification.

As an example in the first round is possible to identify the 5 bar simulation with the injector positioned in its standard position, i.e. DownWard, the simulation is named 5bar_DW.
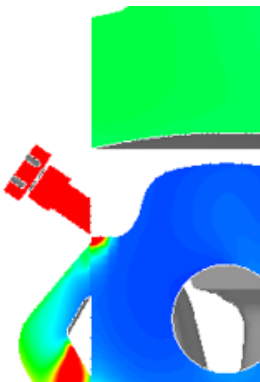
Figure 106: 2TE3 injector downward position

As an example, it is reported in Figure 107 the main in-cylinder results for the simulation with 10 bar of injection pressure and the injector positioned downward (reference name 10bar_DW) after 5 consecutive cycles. It is possible to see the cylinder reinitialization before every EPO in the cylinder pressure (a). At least 5 cycles are made to reduce the differences in term of equivalence ratio, even if for the total mass 3 cycle could be enough.
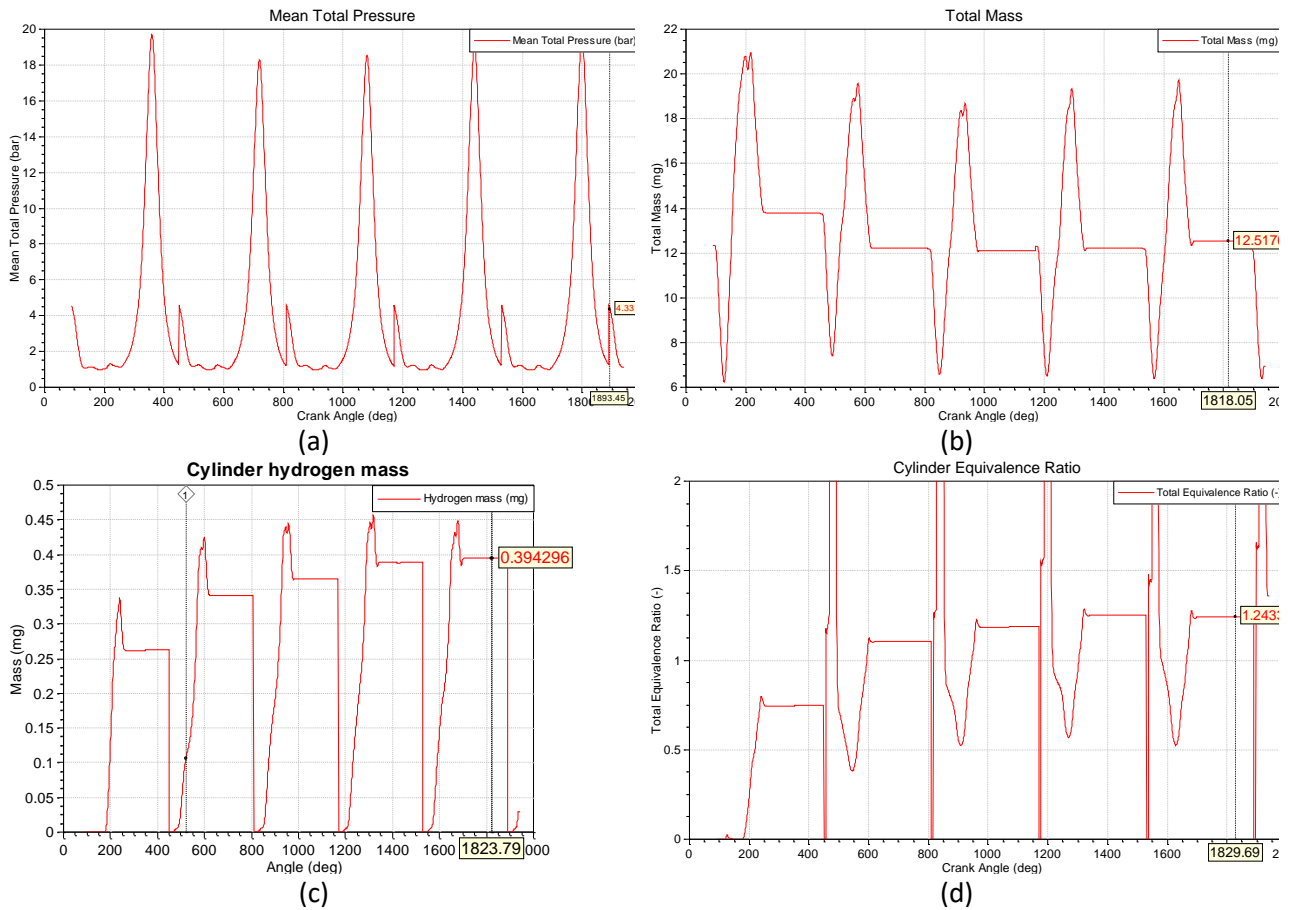
Figure 107: 2TE3 10 bar - downward simulation, in-cylinder pressure (a), in-cylinder mass (b), in-cylinder hydrogen mass (c), and equivalence ratio (d)

In Table 38 are reported the main results for the first round of simulations in terms of trapped hydrogen mass, trapping ratios and lambda values compared to the experimental one. As previously said the comparison with the experimental lambda is affected by the distance between the cylinder and the lambda sensor, that can cause a variation in the exhaust gas composition. To confirm this hypothesis at 10bar the injected mass is almost the double than in the other cases and the simulated lambda value is very rich, nevertheless the experimental lambda value is very lean and close to the others.

Table 38: 2TE3 results comparison from the first round of simulations

		3bar_DW	5bar_DW	7bar_DW	10bar_DW
tot H2 cyl	mg	0.571	0.544	0.516	0.789
injected h2	mg	0.99	1.001	1.001	1.76
trapping ratio	%	57.0	54.3	51.5	44.8
Lambda		1.25	1.31	1.26	0.81
exp lambda	-		1.36	1.46	1.21

For the second round of simulations, only the injection pressures at 3 bar and 5 bar were retained. The first one to further assess the importance of injection time, and the second one because it achieved a high trapping efficiency and has a medium injection value, between the minimum and the maximum.

The injector position is changed upside-down, with the injector tip directed upward, toward the head. As shown in Figure 108 only the injector is modified between the already tested geometry (a) and the new test (b). All the other geometry, mesh, boundary and initial conditions remain the same. Also here a full set of multi-cycle simulations are performed with in-cylinder pressure and composition reinitialization until stationary conditions are reached.

(a)   (b)
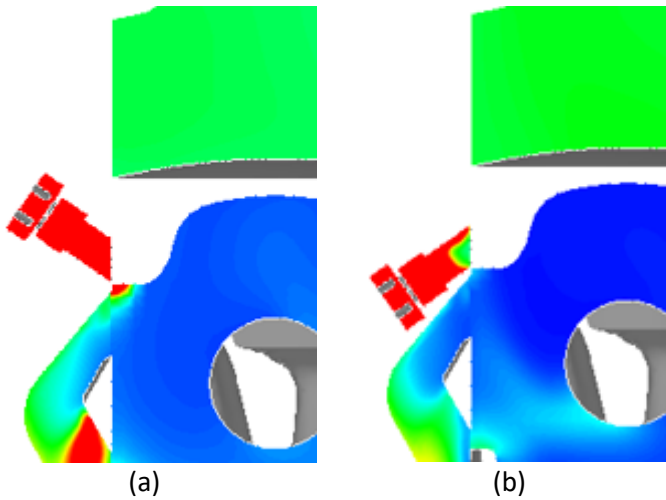
Figure 108: second round of simulations, injector downward (a) and upward (b)

In Table 39 are reported the main results of the second round of simulations, with the injector positioned UpWard. The trapping ratio is drastically increased for the 5bar injection, while is very close to the 57.1% of the 3bar_DW. In the Figure 109 are reported the simulations performed at 3 bar and 5 bar in the last cycle corresponding to 280CAD when the turbulence is high and the injected mass of hydrogen is still clearly visible before its complete mixing. Figure (a) and (b) are related to the simulations performed at 5bar with the injector positioned DW and UW. The same for figures (c) and (d) for the 3 bar injection pressure. The improvement in term of hydrogen mass inside the cylinder, the presence in the intake boost port and in the exhaust port is quite evident, moving the injector upward perform the best solution.

This new position is not further improved or optimize because it is impossible to implement in the real engine.

Table 39: upward injector simulations main results

		3bar UW	5bar UW
tot H2 cyl	mg	0.575	0.634
injected h2	mg	0.99	1.001
trapping ratio	%	58.1	63.3
Lambda		1.21	1.08

5bar_DW @280CAD (a)

5bar_UW @280CAD (b)

3bar_DW @280CAD (c)
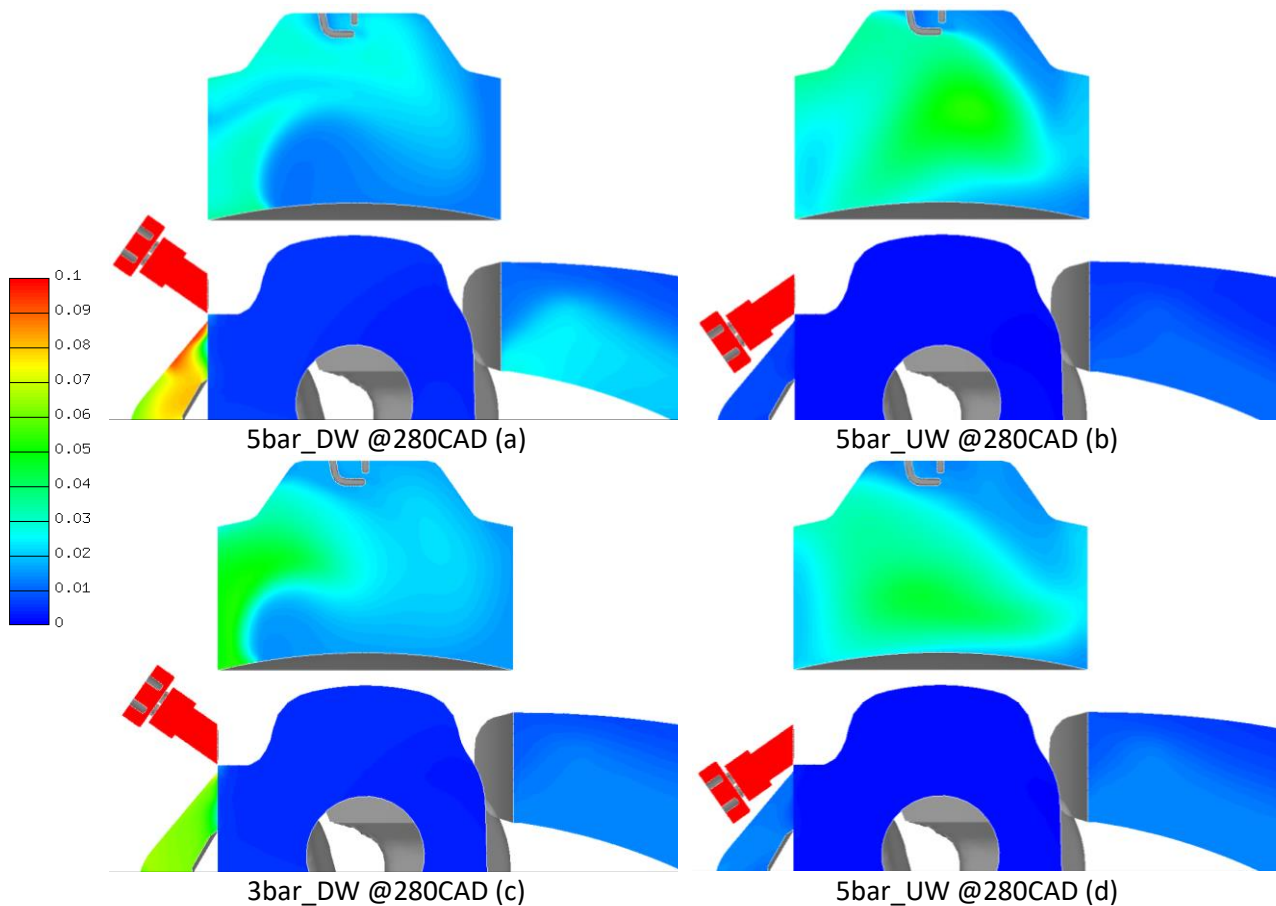
5bar_UW @280CAD (d)

Figure 109: hydrogen mass fraction at 280CAD for 5bar_DW(a), 5bar_UW(b), 3bar_DW(c), 3bar_UW(d)

For the third round of simulations, only the law at 5 bar pressure was considered. In this case the tests operated to see the influence of injector position and piston shape. Figure 110 report the focus on the two main modifications: in figure (a) and (b) the injector is in its standard DW position, while the piston shape is varied, designing a bowl with the purpose of create a fuel recirculation instead of exiting from the exhaust. In figure (c) is reported the injector positioned in a higher position with respect of the standard. The injector was raised so that injection could be postponed without excessively raising the temperature at the injector tip. As can be seen in Figure 112 the EOI was postponed from 232.5 deg to 243 deg.

Figure 111 shows the comparison in term of in-cylinder temperature (red line) and temperature inside the injector (blue lines). Positioning the injector higher, as expected, make the temperature increase up to 100°C. This outcome is probably too much high for the real injector but is still interesting for what may concern the trend analysis.

A set of multi-cycle simulations are performed with in-cylinder pressure and composition reinitialization until stationary conditions are reached.
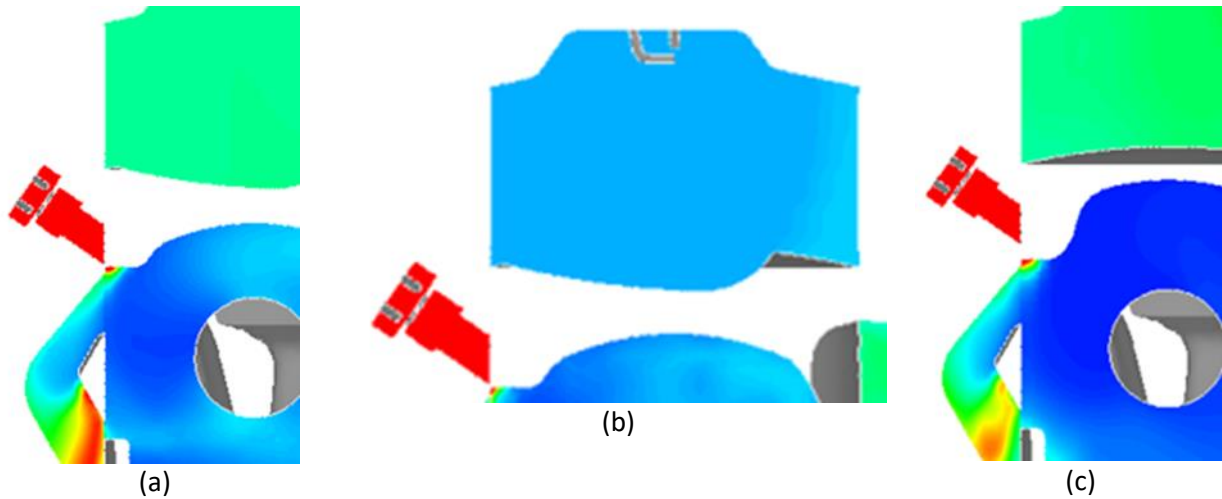
Figure 110: third round of simulations, injector DW with bowl(a), focus on the bowl shape(b) and injector DW higher position (c)
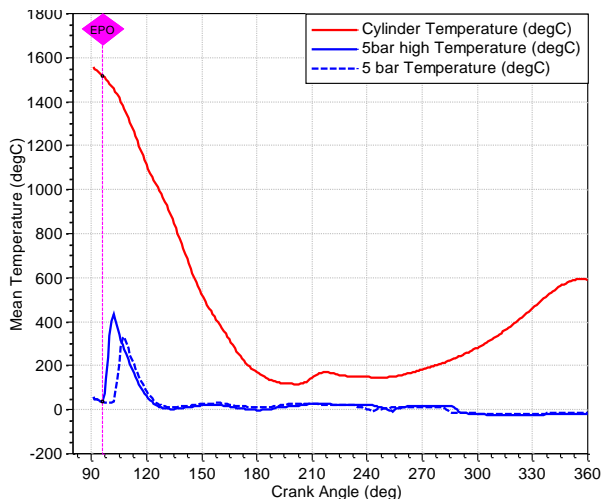
Figure 111:in-cylinder temperature compared with injector tip temperature for the standard and higher positions
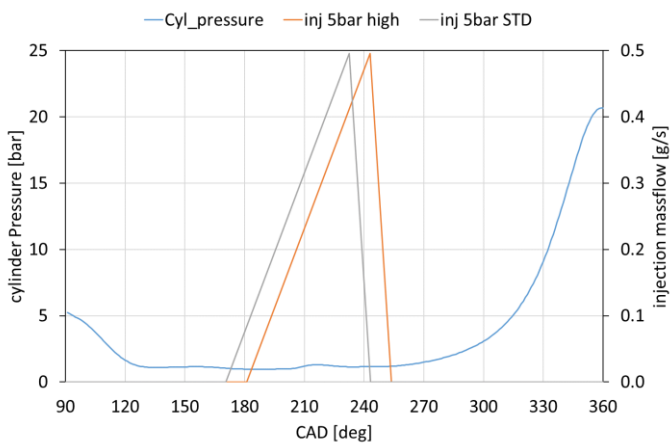
Figure 112: in-cylinder pressure and injectrion strategy comparison

144

Figure 113 shows the mass fraction of hydrogen at 245CAD, after closing the intake port and at the end of injection: in figure (a) the hydrogen slides over the piston bowl and exits the exhaust while in figure (b) the hydrogen remains inside the cylinder, showing significantly less hydrogen from the exhaust.

5bar_bowl @245CAD (a)
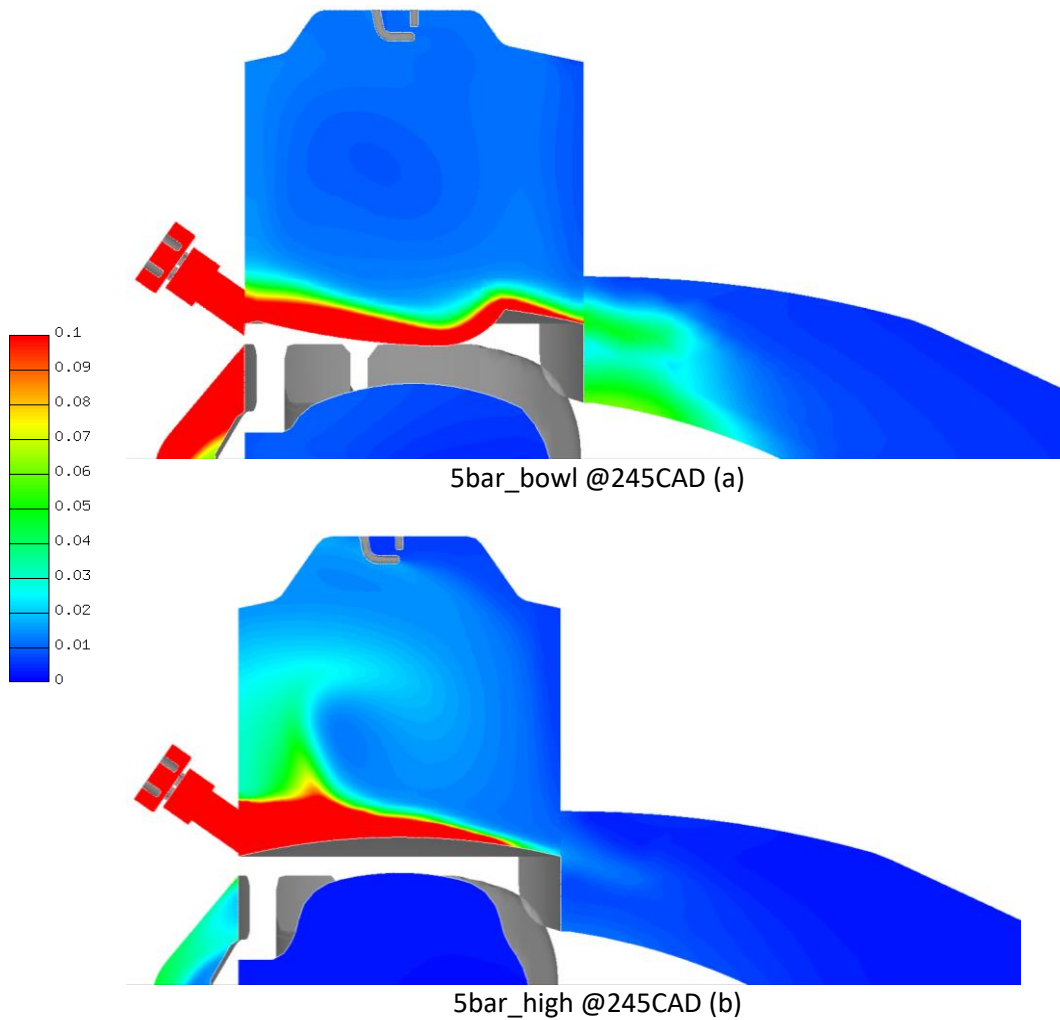
5bar_high @245CAD (b)

Figure 113: hydrogen mass fraction at 280CAD for 5bar_bowl @245CAD(a), 5bar_high @245CAD(b)

In Figure 114 the same comparison is made at 280 CAD, precisely when the injector is closed, and all volumes are in isolation. This allows us to analyze the masses of fuel in the cylinder, exhaust, and intake. Notably, there is a significant disparity in the exhaust between figures (a) and (b). The implication is that the specific design of the combustion chamber does not contribute to retaining hydrogen within the cylinder but rather aids in the formation of the tumble vortex.
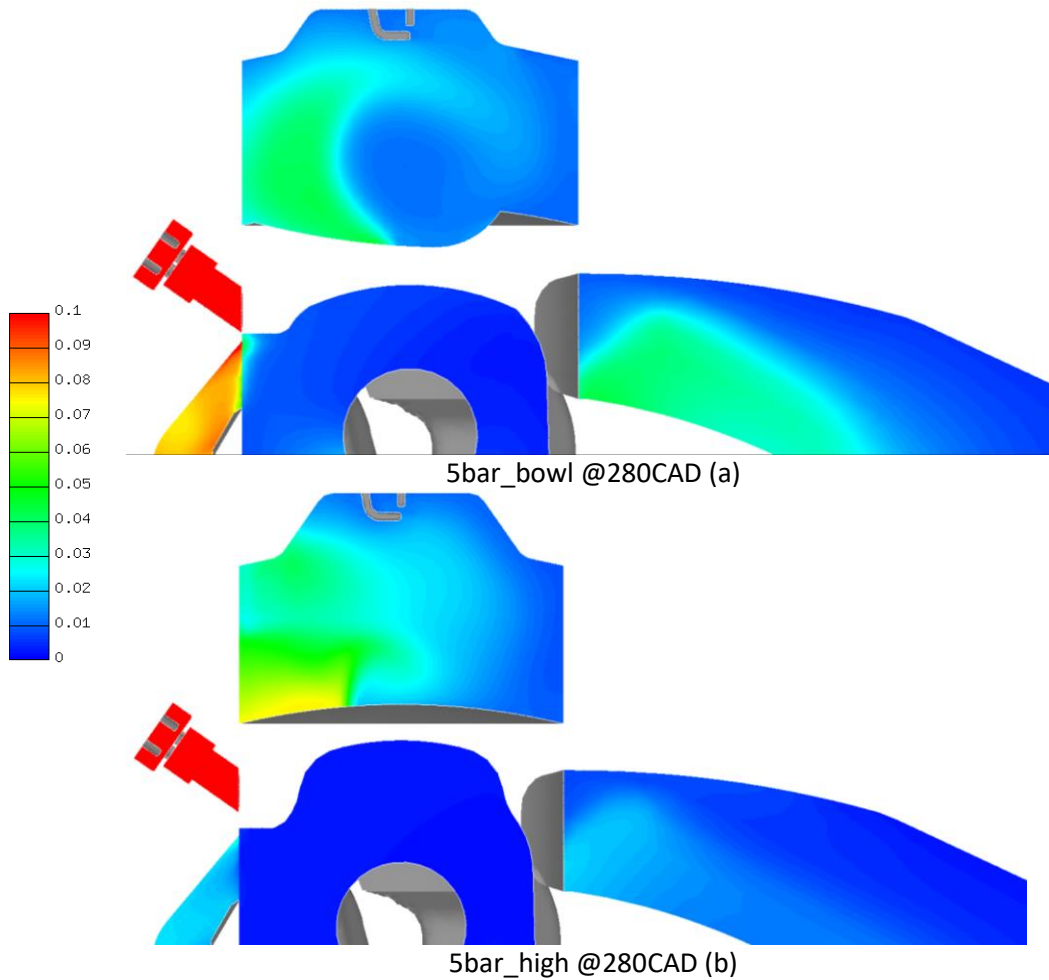
Figure 114: hydrogen mass fraction at 280CAD for 5bar_bowl @280CAD(a), 5bar_high @280CAD(b)

The results of the third-round simulations shown in Table 40 confirm what is shown in the images: the trapping efficiency of the piston with the bowl is lower than the standard case while the solution with the injector placed higher to delay the end of injection has an enhancing effect. As in the case of the upward injector, however, this solution is difficult to apply to the real case, opening the exhaust port and the injector tip together results in excessively high temperatures.

Table 40: 5 bar injector simulations main results with bowl shaped piston and higher injector

		5bar bowl	5bar high
tot H2 cyl	mg	0.517	0.63
injected h2	mg	1.001	1.001
trapping ratio	%	51.7	63
Lambda		1.39	1.12

As a final round of calculations, some configurations were tried that could improve aspects of all the above while keeping 5bar as the injection pressure:

- the height of the injector tip is left standard, so as to keep the temperature in the injector under control.
- the position of the injector in the "horizontal" configuration is drawn by placing the injector horizontally but with an upward deflection in order to direct the flow of hydrogen as the UW injector would do.
- the shape of the piston instead of being modified with a bowl is modified with two different fins, called "noses" of increasing size so as to use the STD configuration for the injector but be able to actively deflect the incoming hydrogen flow.

These considerations result in 3 geometries as in Figure 115 where they are shown in order: 5bar nose_01(a), 5bar nose_02(b) and 5bar horizontal(c).

| 5bar nose_01(a) | 5bar nose_02(b) | 5bar horizontal(c) |
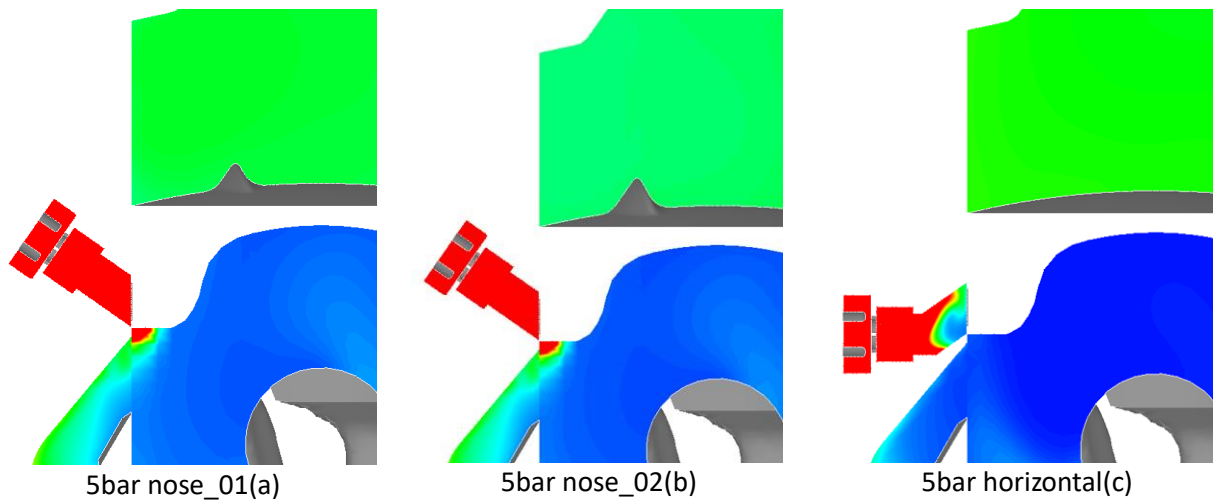
Figure 115: fourth round of simulations, 5bar nose_01(a), 5bar nose_02(b) and 5bar horizontal(c)

After The usual reinitialization cycles to obtain steady-state conditions the main results are shown in Table 41: contrary to expectation, by increasing the size in the nose the amount of hydrogen trapped decrease. The horizontal solution with the std piston on the other hand seems to be the best resuming the upward simulation result.

Table 41: 5 bar injector simulations main results with nose and horizontal configurations

		5bar nose_01	5bar nose_02	5bar horizontal
tot H2 cyl	mg	0.615	0.58	0.659
injected h2	mg	1.001	1.001	1.001
trapping ratio	%	61.4	57.9	65.8
Lambda		1.11	1.18	1.04

The results are presented at two characteristic engine angles: 245CAD after the end of injection and 280CAD time when the injector is closed, and all volumes are independent.

Figure 116 shows the mass fraction of the case with the smaller nose, the effectiveness of hydrogen diversion is clearly visible in fig (a), while fig (b) shows a good degree of in-cylinder charge homogeneity and little fuel at the exhaust.

Figure 117 (a) on the other hand shows that the larger nose works worse as a deflector, the hydrogen remains concentrated near the injector, as a result we have less trapping as more fuel returns to the boost port and will be lost to the next cycle, and results in less homogeneity of charge at 280CAD (fig (b)).

Figure 118, on the other hand, shows the mass fraction of hydrogen for the horizontal injector configuration, again at 245CAD and 280CAD. the 45deg upward directed injector port directs the hydrogen very well toward the centre of the cylinder, however a small fraction of fuel however tends to be attracted to the exhaust. At the end of injection much of the injected fuel remains in the cylinder as also shown in Table 41.

5bar nose_01 @245CAD (a)

5bar nose_01 @280CAD (b)
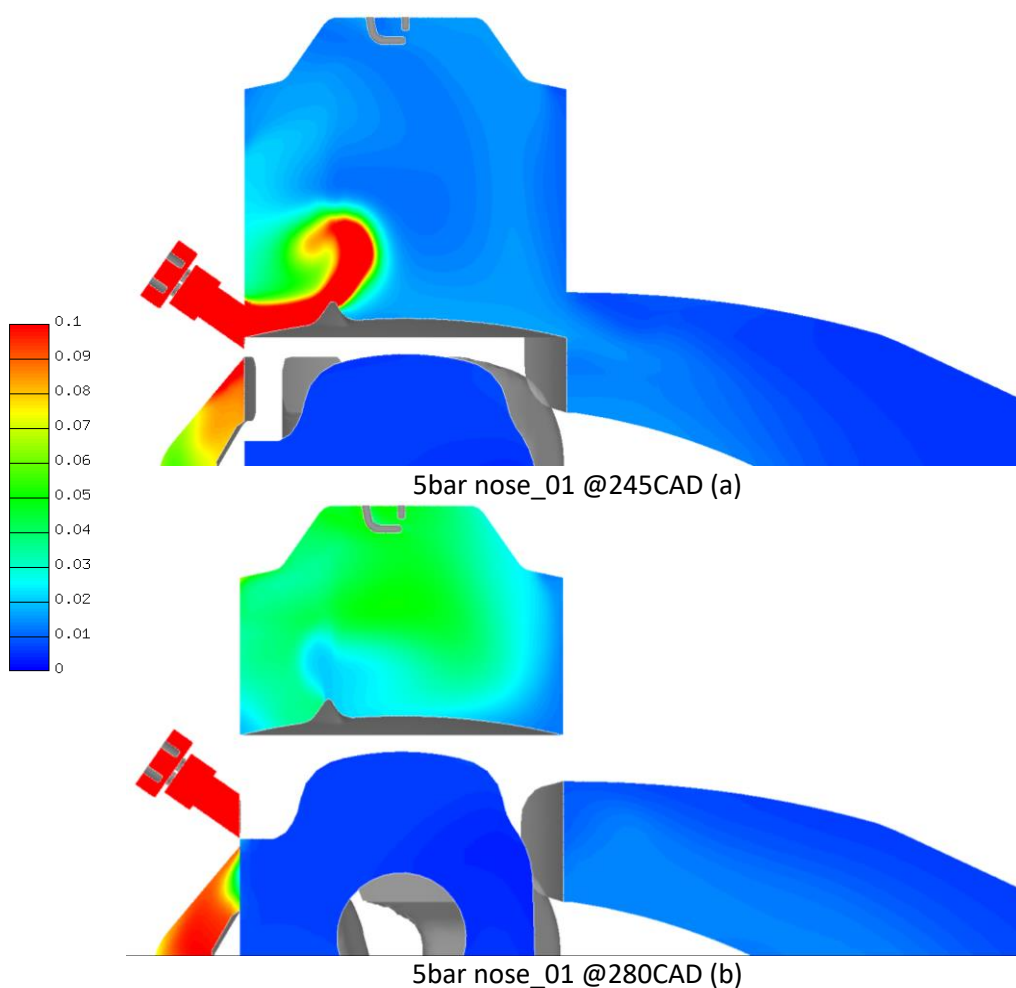
Figure 116: hydrogen mass fraction for 5bar nose_01@245CAD(a), 5bar nose_01@280CAD(b)

5bar nose_02 @245CAD (a)

5bar nose_02 @280CAD (b)
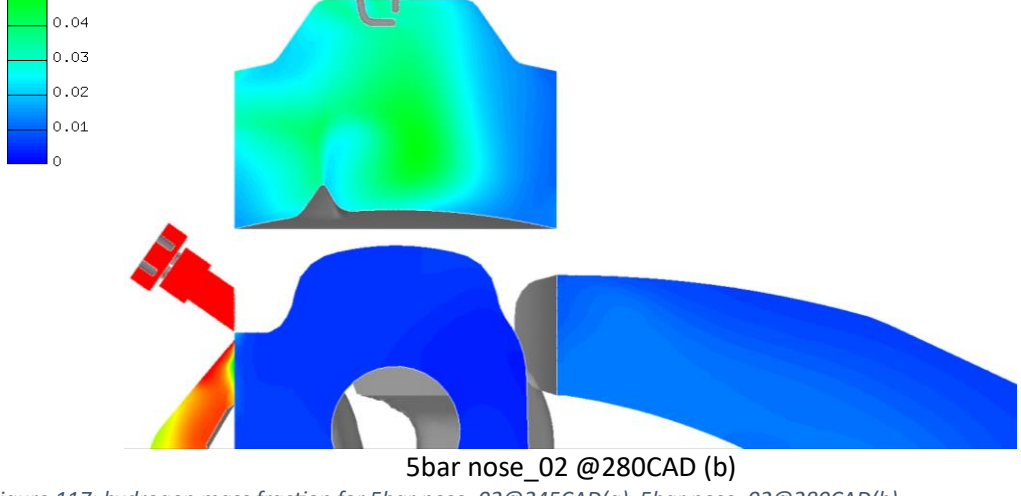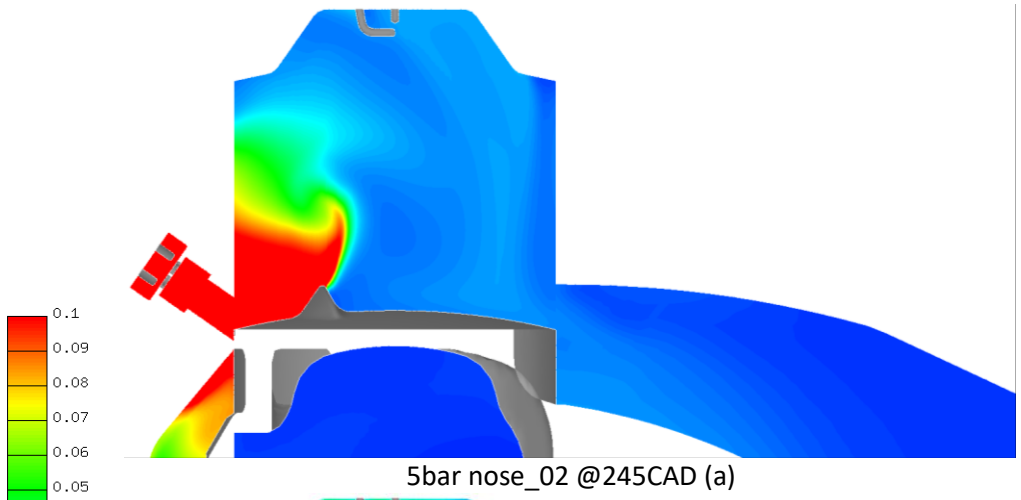
Figure 117: hydrogen mass fraction for 5bar nose_02@245CAD(a), 5bar nose_02@280CAD(b)

5bar horizontal @245CAD (a)
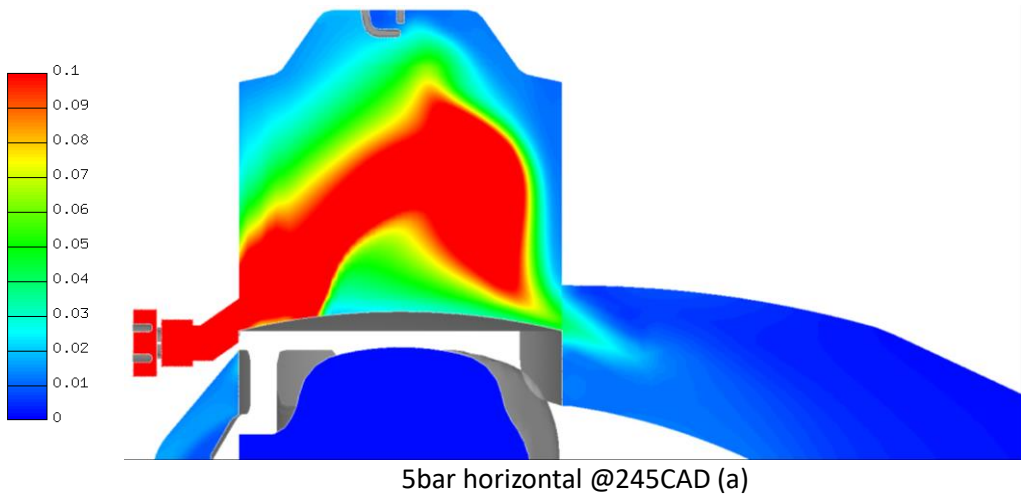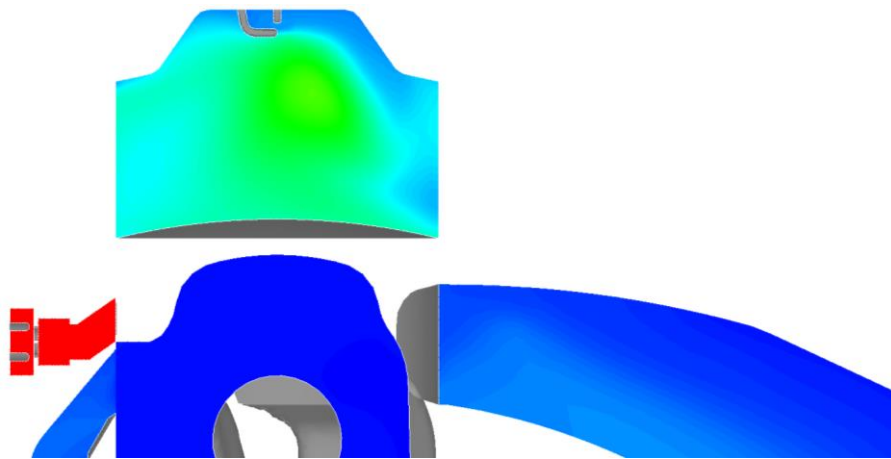
5bar horizontal @280CAD (b)

Figure 118: hydrogen mass fraction for 5bar horizontal@245CAD(a), 5bar horizontal@280CAD(b)

In conclusion Figure 119 report the hydrogen trapping efficiencies of the main tested solutions. 5bar with piston bowl has the worst result because of the slip of the hydrogen directly to the exhaust. The horizontal solution appears to be the best one also considering that the UW and 'high' are not feasible due to technical constrains. Considering only 5bar pressure injection strategies the overall H2 trapping efficiency is increased from 54.3% up to 65.8% (+21%).
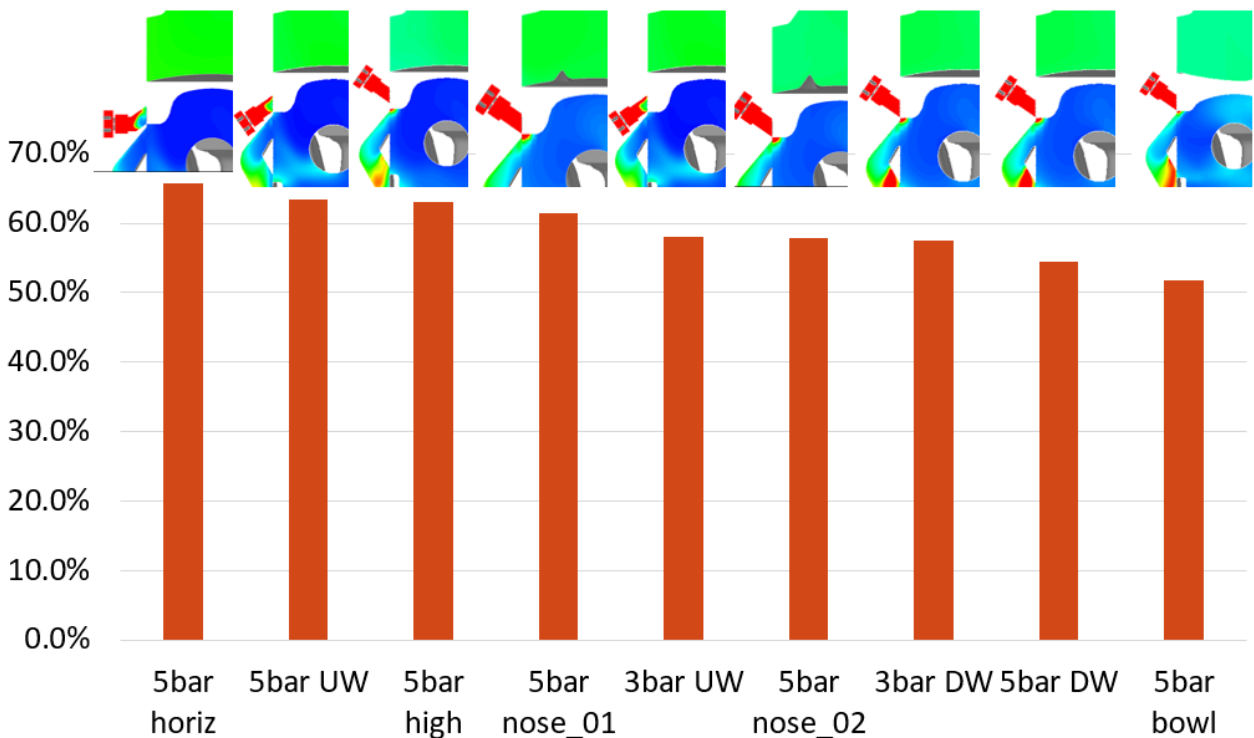
Figure 119: hydrogen trapping efficiency for all the simulations performed

150

6.4   Conclusions

This comprehensive study delves into the potential of 2-stroke cycle engines, focusing on hydrogen direct injection technology. 2-stroke engines, known for their exceptional power-to-weight ratios, can excel when utilizing lean lambda mixtures of hydrogen. Enhancing scavenging efficiency in these engines can nearly double the delivered brake power compared to their 4-stroke counterparts. Achieving this involves appropriately sized supercharging systems and potential hybrid solutions for greater control.

The initial study involves a CFD analysis of a 0.9 L H2 DI 2-stroke 3-cylinder engine with intake and exhaust poppet valves. Three supercharging systems are evaluated: 1) single mechanical supercharger; 2) variable geometry turbocharger with mechanical supercharger; 3) variable geometry turbocharger with an electric supercharger. The combustion process mirrors that of a conventional 4-stroke H2 DI engine, calibrated using published experimental data. CFD-3D simulations are conducted to optimize cylinder design, intake and exhaust port geometry, and combustion chamber configuration to enhance scavenging and trapping efficiency up to 74%.

Compared to a traditional 2-stroke loop scavenged engine with piston-controlled ports, poppet valves offer more flexible gas exchange control but pose challenges in avoiding fresh charge short-circuiting. The study compares different 2-stroke engine configurations and includes a real 4S H2 DI 4-cylinder 2.0 L engine as a reference. The results demonstrate undeniable advantages for the 2-stroke cycle, particularly in terms of brake performance, with specific power more than doubling and a higher and flatter specific torque curve. However, a reduction in thermal efficiency is observed at full load, primarily with the simpler design using a single mechanical supercharger. At partial load, the differences diminish, and the 2-stroke VGT engine with an electric supercharger becomes the most efficient configuration.

Preliminary CFD-1D simulations show limited advantages in using the electric supercharger compared to a standard mechanical supercharger with electronically controlled bypass.

Another aspect of the study focuses on a preliminary investigation of an Opposed Piston 2-Stroke single-cylinder engine designed for hydrogen operation. The engine, initially conceived as an electric generator, shows promise for various applications, including light commercial vehicles. CFD-1D simulations indicate that a 1.2 L OP H2 engine, assisted by a conventional mechanical supercharger, can deliver up to 45 kW at 3000 rpm with minimal pollutant emissions. Maximum BTE of approximately 50% is achieved at 2000 rpm, with the engine delivering maximum brake torque and power of about 170 Nm and 35 kW, respectively. The broad range of BTE above 40% covers all loads higher than 30%.

Lastly, the study involves the conversion of a more conventional 50cc small loop-scavenged engine to run on hydrogen. The low-pressure direct injection system positions a single injector over the intake boost port, with a hole in the piston allowing injection into either the cylinder or the crankcase. The primary focus is on enhancing hydrogen trapping efficiency, achieved through different injector configurations and piston shape modifications. Calibration of the CFD 3D injector involves multiple pressure levels and accounting for backpressure's influence on mass flow rates. Several injector positions are explored, especially at a 5-bar injection pressure, including rotation from downward to upward and horizontal positioning with a machining adaptation to deflect hydrogen upward. The latter configuration shows the most promise, improving hydrogen trapping efficiency by 21% and offering a practical solution with only the need to modify the injector casing.

7   Conclusions

The main goal of the thesis is to explore the potential of different types of 2-Stroke engines, including innovative combustion processes, such as Dual Fuel Reactivity Controlled Compression Ignition (DF-RCCI). In this context, as low-reactivity fuels in combination with diesel I considered: gasoline, biogas, and natural gas, along with different hydrogen blends to enhance combustion speed and efficiency. Some comparisons between 4-Stroke and 2-Stroke solutions are made in terms of Brake thermal efficiency (BTE), performance, and specific emissions, in both DF-RCCI mode and using pure hydrogen as a single fuel. Electrification, together with 2-Stroke engines can provide a series of benefits such as high specific power high power-to-weight ratios and higher energy efficiency in term of BTE and fuel consumption. These technologies are also being explored for use in aircraft engines and high-performance automotive engines, as the specific requirements in these two fields demand distinct solutions

The 2-stroke cycle with Uniflow scavenging (set of inlet ports controlled by the piston movement and exhaust poppet valves) demonstrates to be a promising platform for RCCI combustion systems. Passing from standard diesel to RCCI, regardless the number of strokes of the cycle, consistently leads to significant reductions in NOx and soot emissions of more than 1 order of magnitude, even if at the cost of an increase of HC and CO emissions (HC passes from 0.02 g/kWh to more than 2 g/kWh): however, this issue can be managed by means of a cost-effective Oxidation catalyst. Additionally, the switch to RCCI improves BTE and makes the 2-stroke engine as a very interesting alternative, especially for achieving high power density without affecting the complexity of the power-unit. Across the entire operational spectrum spanning from 1500 RPM to 3500 RPM, the 4-stroke RCCI model engine achieves a notably high BTE exceeding 40% at low to medium RPMs. However, as engine speed climbs above 3000 RPM, the 4-stroke engine experiences a drop in BTE, below that of the 2-stroke RCCI model. This reduction in BTE for the 4-stroke engine at higher RPMs is attributed to the increased weight of pumping and mechanical losses compared to the more efficient 2-stroke engine. Consequently, the 2-stroke engine manages to maintain a 38% BTE at these elevated engine speeds.

Considering medium and low loads, dual-fuel combustions may enhance the performance and the efficiency even in comparison to a standard diesel engine. Different piston bowl shapes are analyzed along with injector position and spray angle. The combustion chamber design is varied in a range between 23mm of radius and 38mm (28mm reference piston bowl radius): in this range it has been found that the standard piston bowl provides an excellent balance between efficiency and emissions at full load, also with an optimization of injector depth and spray angle for the different bowl shapes. Using a deeper cylindrical bowl with a smaller radius it is possible to extend the advantages also at partial load, resulting in a reduction up to 38% in NOx emissions at the same Gross Indicated Mean Effective Pressure (GIMEP) as the STD bowl. At very low loads (BMEP=2bar), with a diesel substitution of 80%, dual fuel combustion with Natural Gas presents major problems: BTE drops of about 12%, CO and NOx emissions rises abruptly due to combustion instabilities. The introduction of hydrogen up to 30 vol% strongly helps to speed up the combustion phase, increasing both combustion efficiency (about 31%) and stability, and also reducing emissions. CO and UHC emissions dropped significantly by 54.1% and 70.4%, respectively, and a NOx emissions reduction by 15.9% is demonstrating the overall environmental benefits of hydrogen addition.

The Uniflow 2-Stroke design is the mainstream technology for large bore diesels, but it requires a specific optimization when the displacement is medium or small. At the time of writing this thesis, emission

regulations in the aircraft field are not very restrictive, making it a good testbed for different 2-stroke solutions, such as the Uniflow with valves or the loop scavenged, running on diesel/kerosene or gasoline.

At first, a 2-stroke, 6-cylinder CI aircraft engine with a total displacement of 5.6 L was analyzed by means of CFD-1D simulations, supported by experimental data. Key performance features include the ability to deliver up to 400 HP for a short time at 2600 rpm, with a direct coupling to the propeller. The Brake Specific Fuel Consumption (BSFC) is expected at 210-215 g/kWh during typical cruise conditions, along with a peak cylinder pressure lower than 100 bar. The engine can be easily modified to run on different fuels, such as kerosene, making it suitable for military applications. The engine is simulated at both sea level and at high-altitude conditions (12000-18000 ft), optimizing turbo-matching and also taking care of aspects such as the operating conditions of the turbocharger remain far from the speed limit.

Another study in the aircraft field (highlighting the great adaptability of these 2S concepts on different field applications) consisted in the numerical optimization of a 2-stroke, 3-cylinder SI engine with a displacement of 1.2 L, rated at 110 kW at 6000 rpm. The engine features a parallel hybrid configuration, an external centrifugal compressor, and an innovative semi-direct low-pressure fuel injection system. The reasons for these choices are related to the high flexibility of the parallel hybrid configuration, enhancing high power output during take-off and offering the possibility to drive either the electric motor or the thermal engine during cruise conditions. The most important numerical results from CFD-1D simulations at full load include low average peak cylinder pressure (less than 60 bar), low thermal loads (BMEP less than 9 bar), and good Brake Thermal Efficiency (about 32%) at high speed. The engine also achieves BSFC less than 260 g/kWh at high-medium engine speed and high fuel trapping efficiency (over 90%) at medium-high speed thanks to the injection system made up of two low-pressure injectors positioned in the transfer ports facing the cylinder.

Hydrogen can be used as a fuel in addition to natural gas, as previously discussed, but also as a stand-alone fuel. Its implementation in 4-Stroke engines, however, is far from trivial as it requires significant modifications to the standard design. The combination of combustion stability and ultra-low NOx emissions can be typically found with ultra-lean mixtures (lambda=2.3-2.8), and therefore, a high amount of fresh air entering the cylinder is required. In a conventional 4-stroke engine, this generally results in a performance drop or the use of cumbersome supercharging systems. The 2-stroke cycle can counterweight this drop, reaching a good trade-off between emissions and brake output performance, but it requires some specific development.

The potential of a reverse loop engine with poppet valves for both intake and exhaust has been evaluated in the high-performance automotive field. A DI-SI 2-stroke 3-cylinder 0.9 L engine featuring three different types of supercharging layouts: 1) a single mechanical supercharger; 2) a variable geometry turbocharger supported by a mechanical supercharger; 3) a variable geometry turbocharger supported by an electric supercharger. The design of the 2S cylinder is supported by CFD 3D simulations: a particular reference to the geometry of the intake and exhaust ports and the implementation of a masking fin, helped to increase the scavenging and trapping efficiency up to 74%. The comparison shows that the 2-stroke cycle offers indisputable advantages in terms of brake performance (specific power is more than doubled, the specific torque curve is higher and flatter), with almost negligible NOx emissions. On the other hand, a reduction in BTE is observed at full load, particularly evident for the simpler design (single mechanical supercharger) due to the energy spent on driving the supercharger. For the 4S reference engine the BTE curve at full load is almost flat all over the operating range, with a maximum of 40% at 2500 RPM. The simplest solution, i.e. the 2S single stage, despite the high specific performances is strongly affected by the power absorbed by the supercharger that makes the BTE drops to a minimum of 26% at 3500 RPM, and never above 33%. However, at low loads, the most efficient configuration becomes the 2-stroke VGT engine with an electric supercharger. BTE are comparable for both full and partial load but the brake performances are more than

doubled at full load (almost 40kW/l for the 4S to almost 100kW/l for the 2S engine with VGT and electric supercharger).

The evaluation and improvement of trapping efficiency is analyzed in collaboration with the Technical University of Graz (TU Graz) for a small 50cc loop scavenged engine featuring a low-pressure direct injector positioned above the intake boost port. The detailed results show an improvement of up to 21% (from 54.3% to 65.8%) by changing the injector configuration without any other modifications. Specifically, instead of the baseline injector directed toward the piston, the injector is positioned horizontally with a hole in the injector housing to deflect the hydrogen flow upward.

The use of hydrogen in 2-Stroke engines is effective, but to ensure BTE and trapping efficiency as high as a 4-Stroke engine with all the benefits of a 2-stroke engine, a different architecture is needed: an opposed-piston engine running on hydrogen is preliminarily evaluated for a gen-set application. The 1.2 L opposed-piston H2 engine, assisted by a conventional mechanical supercharger, can deliver up to 45 kW at 3000 rpm, with near-zero pollutant emissions. Trapping efficiency is always above 90% but can reach 100%, 4S-like condition, modifying the pressure across cylinder by means of a backpressure valve positioned downstream the exhaust line. The condition of maximum BTE=50% is reached at 2000 rpm, where the engine delivers its maximum brake torque of about 170 Nm (BMEP=8.9 bar) and a brake power of about 35 kW.

In conclusion, 2-stroke engines can be very effective in improving BTE by improving air and fuel trapping for various applications. The use of dual-fuel combustion can be fully proficient in reducing NOx emissions and increasing combustion stability at low load. At higher engine speeds and loads, 2-stroke uniflow engines are very effective in RCCI mode, showing almost double the performance of corresponding 4-stroke engines, while also improving BTE and reducing NOx and soot emissions by about an order of magnitude. The use of hydrogen as a single fuel in 2-stroke engines is very promising for several reasons:

- Level of BTE comparable to or higher than corresponding 4-stroke engines
- Almost double performance for comparable operating conditions and lambda values
- More compact and flexible supercharging and turbocharging systems.

Further studies of this thesis should be directed towards two main paths: on one side, the conversion of existing diesel engines into more sustainable DF diesel-hydro methane combustion, with new piston bowls to experimentally test their real efficiency. On the other side, although the available experimental data in literature on 4-Stroke hydrogen engines seem very promising, a deeper investigation on unconventional 2-Stroke solutions proposed in this work can determine a suitable and environmentally effective green alternative for several application fields.

8 References

1. Heywood, J.B., "Internal combustion engine fundamentals," McGraw-Hill Education, 2018.

2. Ritchie, H., Roser, M., and Rosado, P., "CO₂ and Greenhouse Gas Emissions," *Our World in Data*, 2020.

3. Zeng, D., Dong, Y., Cao, H., Li, Y., Wang, J., Li, Z., and Hauschild, M.Z., "Are the electric vehicles more sustainable than the conventional ones? Influences of the assumptions and modeling approaches in the case of typical cars in China," *Resources, Conservation and Recycling* 167:105210, 2021, doi:10.1016/j.resconrec.2020.105210.

4. Reitz, R.D., Ogawa, H., Payri, R., Fansler, T., Kokjohn, S., Moriyoshi, Y., Agarwal, A.K., Arcoumanis, D., Assanis, D., and Bae, C., IJER editorial: The future of the internal combustion engine, *International Journal of Engine Research* 21(1):3–10, 2020.

5. Agarwal, A.K., Singh, A.P., and Maurya, R.K., "Evolution, challenges and path forward for low temperature combustion engines," *Progress in Energy and Combustion Science* 61:1–56, 2017.

6. Benajes, J., García, A., Monsalve-Serrano, J., and Boronat, V., "Achieving clean and efficient engine operation up to full load by combining optimized RCCI and dual-fuel diesel-gasoline combustion strategies," *Energy Conversion and Management* 136:142–151, 2017.

7. Monsalve-Serrano, J., Belgiorno, G., Di Blasio, G., and Guzmán-Mendoza, M., "1D simulation and experimental analysis on the effects of the injection parameters in methane–diesel dual-fuel combustion," *Energies* 13(14):3734, 2020.

8. Adzuan, M.A. and Yusop, A.F., "A review of dual fuel RCCI engine fundamental and effect on the performance, combustion and emission characteristic," Penang, Malaysia: 040001, 2022, doi:10.1063/5.0078962.

9. Hanson, R.M., Kokjohn, S.L., Splitter, D.A., and Reitz, R.D., "An experimental investigation of fuel reactivity controlled PCCI combustion in a heavy-duty engine," *SAE International Journal of Engines* 3(1):700–716, 2010.

10. Curran, S., Prikhodko, V., Cho, K., Sluder, C.S., Parks, J., Wagner, R., Kokjohn, S., and Reitz, R.D., "In-cylinder fuel blending of gasoline/diesel for improved efficiency and lowest possible emissions on a multi-cylinder light-duty diesel engine," SAE Technical Paper, 2010.

11. Kokjohn, S., Hanson, R., Splitter, D., Kaddatz, J., and Reitz, R., "Fuel reactivity controlled compression ignition (RCCI) combustion in light-and heavy-duty engines," *SAE International Journal of Engines* 4(1):360–374, 2011.

12. Benajes, J., Molina, S., García, A., Belarte, E., and Vanvolsem, M., "An investigation on RCCI combustion in a heavy duty diesel engine using in-cylinder blending of diesel and gasoline fuels," *Applied Thermal Engineering* 63(1):66–76, 2014.

13. Reitz, R.D. and Duraisamy, G., "Review of high efficiency and clean reactivity controlled compression ignition (RCCI) combustion in internal combustion engines," *Progress in Energy and Combustion Science* 46:12–71, 2015, doi:10.1016/j.pecs.2014.05.003.

14.   Kozarac, D., Sremec, M., Bozic, M., and Vucetic, A., "The performance and emissions of a conventional natural gas/diesel dual fuel engine at various operating conditions," SAE Technical Paper, 2019.

15.   Hutter, R., Ritzmann, J., Elbert, P., and Onder, C., "Low-load limit in a diesel-ignited gas engine," *Energies* 10(10):1450, 2017.

16.   Dimopoulos, P., Boulouchos, K., Rechsteiner, C., Soltic, P., and Hotz, R., "Combustion characteristics of hydrogen-natural gas mixtures in passenger car engines," *SAE Transactions* 1564–1576, 2007.

17.   Morrone, B. and Unich, A., "Numerical investigation on the effects of natural gas and hydrogen blends on engine combustion," *International Journal of Hydrogen Energy* 34(10):4626–4634, 2009.

18.   Mariani, A., Prati, M.V., Unich, A., and Morrone, B., "Combustion analysis of a spark ignition ic engine fuelled alternatively with natural gas and hydrogen-natural gas blends," *International Journal of Hydrogen Energy* 38(3):1616–1623, 2013.

19.   Fetting, C., "The European green deal," *ESDN Report* 53, 2020.

20.   Dincer, I., "Green methods for hydrogen production," *International Journal of Hydrogen Energy* 37(2):1954–1971, 2012, doi:10.1016/j.ijhydene.2011.03.173.

21.   Millo, F., Piano, A., Rolando, L., Accurso, F., Gullino, F., Roggio, S., Bianco, A., Pesce, F., Vassallo, A., and Rossi, R., "Synergetic Application of Zero-, One-, and Three-Dimensional Computational Fluid Dynamics Approaches for Hydrogen-Fuelled Spark Ignition Engine Simulation," *SAE Int. J. Engines* 15(4):561–580, 2021, doi:10.4271/03-15-04-0030.

22.   Verhelst, S. and Wallner, T., "Hydrogen-fueled internal combustion engines," *Progress in Energy and Combustion Science* 35(6):490–527, 2009, doi:10.1016/j.pecs.2009.08.001.

23.   Azeem, N., Beatrice, C., Vassallo, A., Pesce, F., Davide, G., Guido, C., and Rossi PhD, R., "Comparative Analysis of Different Methodologies to Calculate Lambda (λ) Based on Extensive And systemic Experimentation on a Hydrogen Internal Combustion Engine," Detroit, Michigan, United States: 2023-01–0340, 2023, doi:10.4271/2023-01-0340.

24.   Bao, L., Sun, B., Luo, Q., Li, J., Qian, D., Ma, H., and Guo, Y., "Development of a turbocharged direct-injection hydrogen engine to achieve clean, efficient, and high-power performance," *Fuel* 324:124713, 2022, doi:10.1016/j.fuel.2022.124713.

25.   Bao, L., Sun, B., and Luo, Q., "Optimal control strategy of the turbocharged direct-injection hydrogen engine to achieve near-zero emissions with large power and high brake thermal efficiency," *Fuel* 325:124913, 2022, doi:10.1016/j.fuel.2022.124913.

26.   Mattarelli, E., Cantore, G., and Alberto, C., "Advances in The Design of Two-Stroke, High Speed, Compression Ignition Engines," in: Ng, H. K., ed., *Advances in Internal Combustion Engines and Fuel Technologies*, InTech, ISBN 978-953-51-1048-4, 2013, doi:10.5772/54204.

27.   Hori, H., "Scavenging flow optimization of two-stroke diesel engine by use of CFD," SAE Technical Paper, 2000.

28.   2/4 SIGHT, https://www.brighton.ac.uk/advanced-engineering/research-projects/24-sight.aspx, Sep. 2023.

29.   Amsden, A.A., "KIVA-3: A KIVA program with block-structured mesh for complex geometries," LA-12503-MS, Los Alamos National Lab., NM (United States), 1993.

30.   K3prep_Diesel_Bowl_Demo.pdf.

31.   Nordin, P.N., "Complex chemistry modeling of diesel spray combustion," Chalmers University of Technology Sweden, 2001.

32.   Golovitchev, V.I. and Imren, A., "Development of dual fuel combustion models for direct injected heavy duty diesel engines," *Diesel Fuels: Characteristics, Performances and Environmental Impacts. Nova Pusblisher*, 2013.

33.   Golovitchev, V.I., Nordin, N., Jarnicki, R., and Chomiak, J., "3-D diesel spray simulations using a new detailed chemistry turbulent combustion model," *SAE Transactions* 1391–1405, 2000.

34.   Lipatnikov, A.N. and Chomiak, J., "Turbulent flame speed and thickness: phenomenology, evaluation, and application in multi-dimensional simulations," *Progress in Energy and Combustion Science* 28(1):1–74, 2002.

35.   Su, T.F., Patterson, M.A., Reitz, R.D., and Farrell, P.V., "Experimental and numerical studies of high pressure multiple injection sprays," *SAE Transactions* 1281–1292, 1996.

36.   Reitz, R., "Modeling atomization processes in high-pressure vaporizing sprays," *Atomisation and Spray Technology* 3(4):309–337, 1987.

37.   Ricart, L.M., Xin, J., Bower, G.R., and Reitz, R.D., "In-cylinder measurement and modeling of liquid fuel spray penetration in a heavy-duty diesel engine," *SAE Transactions* 1622–1640, 1997.

38.   Kee, R.J., Grcar, J.F., Smooke, M.D., Miller, J.A., and Meeks, E., "PREMIX: a Fortran program for modeling steady laminar one-dimensional premixed flames," *Sandia National Laboratories Report* (SAND85-8249), 1985.

39.   Manual, G.-P.U. and User's, P., "GT-Suite version 2016," *Gamma Technologies Inc*, 2017.

40.   ANSYS Forte Theory Manual, https://ansyshelp.ansys.com/Views/Secured/corp/v211/en/forte_th/forte_th.html, May 2021.

41.   Manual, F.-M. and User's, A., "Fire-M R2022.2," *AVL List GmbH*, 2022.

42.   Wei, L. and Geng, P., "A review on natural gas/diesel dual fuel combustion, emissions and performance," *Fuel Processing Technology* 142:264–278, 2016, doi:10.1016/j.fuproc.2015.09.018.

43.   Lounici, M.S., Loubar, K., Tarabet, L., Balistrou, M., Niculescu, D.-C., and Tazerout, M., "Towards improvement of natural gas-diesel dual fuel mode: An experimental investigation on performance and exhaust emissions," *Energy* 64:200–211, 2014.

44.   Papagiannakis, R.G., Rakopoulos, C.D., Hountalas, D.T., and Rakopoulos, D.C., "Emission characteristics of high speed, dual fuel, compression ignition engine operating in a wide range of natural gas/diesel fuel proportions," *Fuel* 89(7):1397–1406, 2010, doi:10.1016/j.fuel.2009.11.001.

45.   Rahnama, P., Paykani, A., and Reitz, R.D., "A numerical study of the effects of using hydrogen, reformer gas and nitrogen on combustion, emissions and load limits of a heavy duty natural gas/diesel RCCI engine," *Applied Energy* 193:182–198, 2017.

46.   Liu, F., Kang, Y., Wu, H., Lee, C.-F., and Li, Y., "Effect of hydrogen volume ratio on the combustion characteristics of CNG-diesel dual-fuel engine," SAE Technical Paper, 2017.

47.   Giurcan, V., Movileanu, C., Musuc, A.M., and Mitu, M., "Laminar Burning Velocity of Biogas-Containing Mixtures. A Literature Review," *Processes* 9(6):996, 2021, doi:10.3390/pr9060996.

48.   Mattarelli, E., Rinaldini, C.A., Savioli, T., and Scrignoli, F., "Optimization of a High-Speed Dual-Fuel (Natural Gas-Diesel) Compression Ignition Engine for Gen-sets," *SAE Int. J. Engines* 14(3):03-14-03–0022, 2021, doi:10.4271/03-14-03-0022.

49.   Cameretti, M.C., De Robbio, R., and Tuccillo, R., "Performance Improvement and Emission Control of a Dual Fuel Operated Diesel Engine," 2017-24–0066, 2017, doi:10.4271/2017-24-0066.

50.   Nieman, D.E., Dempsey, A.B., and Reitz, R.D., "Heavy-Duty RCCI Operation Using Natural Gas and Diesel," *SAE Int. J. Engines* 5(2):270–285, 2012, doi:10.4271/2012-01-0379.

51.   Zhou, D.Z., Yang, W.M., An, H., Li, J., and Shu, C., "A numerical study on RCCI engine fueled by biodiesel/methanol," *Energy Conversion and Management* 89:798–807, 2015, doi:10.1016/j.enconman.2014.10.054.

52.   Liu, J., Yang, F., Wang, H., and Ouyang, M., "Numerical study of hydrogen addition to DME/CH4 dual fuel RCCI engine," *International Journal of Hydrogen Energy* 37(10):8688–8697, 2012, doi:10.1016/j.ijhydene.2012.02.055.

53.   Li, Y., Jia, M., Liu, Y., and Xie, M., "Numerical study on the combustion and emission characteristics of a methanol/diesel reactivity controlled compression ignition (RCCI) engine," *Applied Energy* 106:184–197, 2013, doi:10.1016/j.apenergy.2013.01.058.

54.   Molina, S., García, A., Pastor, J.M., Belarte, E., and Balloul, I., "Operating range extension of RCCI combustion concept from low to full load in a heavy-duty engine," *Applied Energy* 143:211–227, 2015, doi:10.1016/j.apenergy.2015.01.035.

55.   Dempsey, A.B., Walker, N.R., and Reitz, R.D., "Effect of Piston Bowl Geometry on Dual Fuel Reactivity Controlled Compression Ignition (RCCI) in a Light-Duty Engine Operated with Gasoline/Diesel and Methanol/Diesel," *SAE Int. J. Engines* 6(1):78–100, 2013, doi:10.4271/2013-01-0264.

56.   Lee, S. and Park, S., "Optimization of the piston bowl geometry and the operating conditions of a gasoline-diesel dual-fuel engine based on a compression ignition engine," *Energy* 121:433–448, 2017, doi:10.1016/j.energy.2017.01.026.

57.   Prajapati, H.N., "Emission analysis of biogas premixed charge diesel dual fuelled engine," *IOSRJEN* 4(5):54–60, 2014, doi:10.9790/3021-04535460.

58.   Molina, S., García, A., Pastor, J.M., Belarte, E., and Balloul, I., "Operating range extension of RCCI combustion concept from low to full load in a heavy-duty engine," *Applied Energy* 143:211–227, 2015, doi:10.1016/j.apenergy.2015.01.035.

59.   Benajes, J., García, A., Monsalve-Serrano, J., and Boronat, V., "Achieving clean and efficient engine operation up to full load by combining optimized RCCI and dual-fuel diesel-gasoline combustion strategies," *Energy Conversion and Management* 136:142–151, 2017, doi:10.1016/j.enconman.2017.01.010.

60.   shimamoto, yuzuru, A study of squish in open combustion chambers of a diesel engine, 1970.

61.   Arcoumanis, C., Bicen, A.F., Vafidis, C., and Whitelaw, J.H., "Three-Dimensional Flow Field in Four-Stroke Model Engines," *SAE Transactions* 93:978–987, 1984.

62.   Scrignoli, F., Vecchio, F., Legrottaglie, F., Mattarelli, E., and Rinaldini, C.A., "Numerical Investigation of Dual Fuel Combustion on a Compression Ignition Engine Fueled with Hydrogen/Natural Gas Blends," *Fuels* 3(1):132–151, 2022, doi:10.3390/fuels3010009.

63.   Legrottaglie, F., Mattarelli, E., Rinaldini, C.A., and Scrignoli, F., "Application to micro-cogeneration of an innovative dual fuel compression ignition engine running on biogas," *International Journal of Thermofluids* 10:100093, 2021, doi:10.1016/j.ijft.2021.100093.

64.   Cantore, G., Mattarelli, E., Rinaldini, C.A., Savioli, T., and Scrignoli, F., "Numerical optimization of the injection strategy on a light duty diesel engine operating in dual fuel (CNG/diesel) mode," *International Journal of Heat and Technology* 37(3):682–688, 2019, doi:10.18280/ijht.370303.

65.   Legrottaglie, F., Mattarelli, E., Rinaldini, C.A., Savioli, T., and Scrignoli, F., "Experimental investigation on a diesel engine operated in RCCI combustion mode," *AIP Conference Proceedings*, 2019, doi:10.1063/1.5138829.

66.   PR_170725_TC CD-300_EN_final.pdf, Feb. 2022.

67.   Portfolio, https://www.flyrotax.com/p/products/engines, Feb. 2022.

68.   Engines, https://www.lycoming.com/engines, Feb. 2022.

69.   Heywood, J.B. and Sher, E., "The Two-Stroke Cycle Engine: Its Development, Operation, and Design," Routledge, ISBN 978-0-203-73485-8, 2017, doi:10.1201/9780203734858.

70.   Brouwers, A.P., "150 and 300 kW Lightweight Diesel Aircraft Engine Study," National Aeronautics and Space Administration, Scientific and Technical …, 1980.

71.   Mattarelli, E., Rinaldini, C.A., and Wilksch, M., "2-Stroke High Speed Diesel Engines for Light Aircraft," *SAE International Journal of Engines* 4(2):2338–2360, 2011.

72.   Mattarelli, E., Paltrinieri, F., Perini, F., Rinaldini, C.A., and Wilksch, M., "2-Stroke Diesel Engine for Light Aircraft: IDI vs. DI Combustion Systems," SAE Technical Paper 2010-01–2147, SAE International, Warrendale, PA, 2010, doi:10.4271/2010-01-2147.

73.   DeltaHawk - Jet Fuel Engines, https://deltahawk.com/, Feb. 2022.

74.   zoche_brochure.pdf, Feb. 2022.

75.   Faruoli, M., Coclite, A., Viggiano, A., Caso, P., and Magi, V., "A comprehensive numerical analysis of the scavenging process in a uniflow two-stroke diesel engine for general aviation," *Energies* 14(21):7361, 2021.

76.   Foxhall, N., "Inside the new 850cc BRP-Rotax 2 stroke DI Snowmobile engine," 2018.

77.   Sturm, S., Lang, M., and Schmidt, S., "Simulation Analysis of the Scavenging Process of a Uniflow and Loop Scavenging Concept," 9.

78.   Design and Simulation of Two-Stroke Engines, https://www.sae.org/publications/books/content/r-161/, May 2021.

79. The Two-Stroke Cycle Engine : Its Development, Operation, and Design, Routledge, ISBN 978-0-203-73485-8, 2017, doi:10.1201/9780203734858.

80. Balduzzi, F., Vichi, G., Romani, L., Ferrara, G., Trassi, P., Fiaschi, J., and Tozzi, F., "Development of a Low Pressure Direct Injection System for a Small 2S Engine. Part I - CFD Analysis of the Injection Process," *SAE Int. J. Engines* 8(4):1885–1897, 2015, doi:10.4271/2015-01-1727.

81. Romani, L., Vichi, G., Ferrara, G., Balduzzi, F., Trassi, P., Fiaschi, J., and Tozzi, F., "Development of a Low Pressure Direct Injection System for a Small 2S Engine. Part II - Experimental Analysis of the Engine Performance and Pollutant Emissions," SAE Technical Paper 2015-01–1730, SAE International, Warrendale, PA, 2015, doi:10.4271/2015-01-1730.

82. Krimplstätter, S., Winkler, F., Oswald, R., and Kirchberger, R., "Air Cooled 50cm^3 Scooter Euro 4 Application of the Two-Stroke LPDI Technology," 2014-32–0008, 2014, doi:10.4271/2014-32-0008.

83. Oswald, R., Ebner, A., and Kirchberger, R., "High Efficient 125- 250 cm^3 LPDI Two-Stroke Engines, a Cheap and Robust Alternative to Four-Stroke Solutions?," 2010-32–0019, 2010, doi:10.4271/2010-32-0019.

84. Winkler, F., Oswald, R., Schögl, O., Abis, A., Krimplstätter, S., and Kirchberger, R., "Layout and Development of a 300 cm^3 High Performance 2S-LPDI Engine," 12.

85. Oliveira, A.M., Beswick, R.R., and Yan, Y., "A green hydrogen economy for a renewable energy society," *Current Opinion in Chemical Engineering* 33:100701, 2021, doi:10.1016/j.coche.2021.100701.

86. Bockris, J.O., "A Hydrogen Economy," *Science* 176(4041):1323–1323, 1972, doi:10.1126/science.176.4041.1323.

87. Hosseini, S.E. and Butler, B., "An overview of development and challenges in hydrogen powered vehicles," *International Journal of Green Energy* 17(1):13–37, 2020, doi:10.1080/15435075.2019.1685999.

88. Millo, F., Piano, A., Rolando, L., Accurso, F., Gullino, F., Roggio, S., Bianco, A., Pesce, F., Vassallo, A., and Rossi, R., "Synergetic Application of Zero-, One-, and Three-Dimensional Computational Fluid Dynamics Approaches for Hydrogen-Fuelled Spark Ignition Engine Simulation," *SAE Int. J. Engines* 15(4):561–580, 2021, doi:10.4271/03-15-04-0030.

89. Ramognino, F., Sforza, L., D'Errico, G., Gomez-Soriano, J., Onorati, A., and Novella, R., "CFD Modelling of Hydrogen-Fueled SI Engines for Light-Duty Applications," SAE Technical Paper 2023-24–0017, SAE International, Warrendale, PA, 2023, doi:10.4271/2023-24-0017.

90. Verhelst, S. and Wallner, T., "Hydrogen-fueled internal combustion engines," *Progress in Energy and Combustion Science* 35(6):490–527, 2009, doi:10.1016/j.pecs.2009.08.001.

91. Ji, C., Hong, C., Wang, S., Xin, G., Meng, H., Yang, J., and Qiang, Y., "Evaluation of the variable valve timing strategy in a direct-injection hydrogen engine with the Miller cycle under lean conditions," *Fuel* 343:127932, 2023, doi:10.1016/j.fuel.2023.127932.

92. Ma, D.-S. and Sun, Z.Y., "Progress on the studies about NOx emission in PFI-H2ICE," *International Journal of Hydrogen Energy* 45(17):10580–10591, 2020, doi:10.1016/j.ijhydene.2019.11.065.

93. Azeem, N., Beatrice, C., Vassallo, A., Pesce, F., Davide, G., Guido, C., and Rossi PhD, R., "Comparative Analysis of Different Methodologies to Calculate Lambda (λ) Based on Extensive And systemic

Experimentation on a Hydrogen Internal Combustion Engine," Detroit, Michigan, United States: 2023-01–0340, 2023, doi:10.4271/2023-01-0340.

94. Stępień, Z., "A Comprehensive Overview of Hydrogen-Fueled Internal Combustion Engines: Achievements and Future Challenges," *Energies* 14(20):6504, 2021, doi:10.3390/en14206504.

95. Bulgarini, M., Torre, A.D., Barillari, L., Montenegro, G., Onorati, A., Gullino, F., and Tonelli, R., "Towards H$_2$ High-Performance IC Engines: Strategies for Control and Abatement of Pollutant Emissions," SAE Technical Paper 2023-24–0108, SAE International, Warrendale, PA, 2023, doi:10.4271/2023-24-0108.

96. Bao, L., Sun, B., Luo, Q., Li, J., Qian, D., Ma, H., and Guo, Y., "Development of a turbocharged direct-injection hydrogen engine to achieve clean, efficient, and high-power performance," *Fuel* 324:124713, 2022, doi:10.1016/j.fuel.2022.124713.

97. Bao, L., Sun, B., and Luo, Q., "Optimal control strategy of the turbocharged direct-injection hydrogen engine to achieve near-zero emissions with large power and high brake thermal efficiency," *Fuel* 325:124913, 2022, doi:10.1016/j.fuel.2022.124913.

98. Blair, G., "Design and Simulation of Two-Stroke Engines," SAE International, ISBN 978-0-7680-2516-3, 1996.

99. Heywood, J., "Two-stroke cycle engine: it's development, operation and design," Routledge, 2017.

100. Liu, X., Liu, F., Zhou, L., Sun, B., and Schock, Harold.J., "Backfire prediction in a manifold injection hydrogen internal combustion engine," *International Journal of Hydrogen Energy* 33(14):3847–3855, 2008, doi:10.1016/j.ijhydene.2008.04.051.

101. Hydrogen engine operation strategies: Recent progress, industrialization challenges, and perspectives | Elsevier Enhanced Reader, https://reader.elsevier.com/reader/sd/pii/S0360319922044962?token=D971A1C7B1DBD680773006B391385906C8E9F50EC524DC046E95AC77D4FCE0D345AD22CF8AB7D3586443212920AB1D47&originRegion=eu-west-1&originCreation=20230521143825, May 2023, doi:10.1016/j.ijhydene.2022.09.256.

102. Babayev, R., Andersson, A., Dalmau, A.S., Im, H.G., and Johansson, B., "Computational characterization of hydrogen direct injection and nonpremixed combustion in a compression-ignition engine," *International Journal of Hydrogen Energy* 46(35):18678–18696, 2021, doi:10.1016/j.ijhydene.2021.02.223.

103. White, C.M., Steeper, R.R., and Lutz, A.E., "The hydrogen-fueled internal combustion engine: a technical review," *International Journal of Hydrogen Energy* 31(10):1292–1305, 2006.

104. Mohammadi, A., Shioji, M., Nakai, Y., Ishikura, W., and Tabo, E., "Performance and combustion characteristics of a direct injection SI hydrogen engine," *International Journal of Hydrogen Energy* 32(2):296–304, 2007.

105. Nomura, K., "Development of a new two stroke engine with poppet-valves: Toyota S-2 Engine," *IFP Int. Seminar 1993'A New Generation of Two-Stroke Engines', 29-30 November 1993*, 1993.

106. Osborne, R.J., Stokes, J., Lake, T.H., Carden, P.J., Mullineux, J.D., Helle-Lorentzen, R., Evans, J.C., Heikal, M.R., Zhu, Y., Zhao, H., and Ma, T., "Development of a Two-Stroke/Four-Stroke Switching Gasoline Engine - The 2/4SIGHT Concept," SAE Technical Paper 2005-01–1137, SAE International, Warrendale, PA, 2005, doi:10.4271/2005-01-1137.

107. Bao, L., Sun, B., and Luo, Q., "Optimal control strategy of the turbocharged direct-injection hydrogen engine to achieve near-zero emissions with large power and high brake thermal efficiency," *Fuel* 325:124913, 2022, doi:10.1016/j.fuel.2022.124913.

108. Bao, L., Sun, B., Luo, Q., Li, J., Qian, D., Ma, H., and Guo, Y., "Development of a turbocharged direct-injection hydrogen engine to achieve clean, efficient, and high-power performance," *Fuel* 324:124713, 2022, doi:10.1016/j.fuel.2022.124713.

109. Manual, G.-P.U. and User's, P., "GT-Suite version 2016," *Gamma Technologies Inc*, 2017.

110. Ma, F., Zhao, C., and Zhang, S., "Study on Dual-spark Ignition Rapid Combustion Characteristic of Opposed-piston Two-stroke GDI Engine," *Energy Procedia* 61:722–725, 2014, doi:10.1016/j.egypro.2014.11.951.

111. Pirault, J.-P. and Flint, M.L., "Opposed Piston Engines," SAE International, Warrendale, PA, ISBN 978-0-7680-2175-2, 2009, doi:10.4271/R-378.

112. Naik, S., Johnson, D., Fromm, L., Koszewnik, J., Redon, F., Regner, G., and Abani, N., "Achieving Bharat Stage VI Emissions Regulations While Improving Fuel Economy with the Opposed-Piston Engine," *SAE Int. J. Engines* 10(1):17–26, 2017, doi:10.4271/2017-26-0056.

113. Herold, R.E., Wahl, M.H., Regner, G., Lemke, J.U., and Foster, D.E., "Thermodynamic Benefits of Opposed-Piston Two-Stroke Engines," 2011-01–2216, 2011, doi:10.4271/2011-01-2216.

114. Regner, G., Johnson, D., Koszewnik, J., Dion, E., Redon, F., and Fromm, L., "Modernizing the Opposed Piston, Two Stroke Engine for Clean, Efficient Transportation," 2013-26–0114, 2013, doi:10.4271/2013-26-0114.

115. Technology Assessment Of A Fuel Cell Vehicle: 2017 Toyota Mirai | Argonne National Laboratory, https://www.anl.gov/argonne-scientific-publications/pub/144774, Apr. 2023.

116. Mattarelli, E., Rinaldini, C., Savioli, T., Cantore, G., Warey, A., Potter, M., Gopalakrishnan, V., and Balestrino, S., "Scavenge Ports Ooptimization of a 2-Stroke Opposed Piston Diesel Engine," 2017-24–0167, 2017, doi:10.4271/2017-24-0167.

117. Richards, K.J., Senecal, P.K., and Pomraning, E., CONVERGE 3.1, 2023.

118. Naik, S., Redon, F., Regner, G., and Koszewnik, J., "Opposed-Piston 2-Stroke Multi-Cylinder Engine Dynamometer Demonstration," 2015-26–0038, 2015, doi:10.4271/2015-26-0038.

119. Winkler, F., Kirchberger, R., Schögl, O., and Schmidt, S., "Strategies to Reduce Scavenge Losses of Small Capacity 2-Stroke Engines, Pressurized by the Common Market Costs," SAE Technical Paper, 2005.

120. Winkler, F., Schögl, O., Oswald, R., and Kirchberger, R., "Development of a Low Emission Two-Stroke Engine with Low Pressure Fuel Injection," 2006-32–0065, 2006, doi:10.4271/2006-32-0065.

121. Reference Fluid Thermodynamic and Transport Properties Database (REFPROP), *NIST*, Oct. 2023.

9 Appendix

Crank angle [°AFTDC]	Temperature [K] 0.000e+00 6.250e+02 1.250e+03 1.875e+03 2.500e+03	NC10H22.Mole Fractions 0.000e+00 2.000e-04 4.000e-04 6.000e-04 8.000e-04	CH4.Mole Fractions 0.000e+00 7.500e-03 1.500e-02 2.250e-02 3.000e-02	OH.Mole Fractions 0.000e+00 1.000e-03 2.000e-03 3.000e-03 4.000e-03
-16.9905				
-11.9505				
-6.9105				
-1.9857				
3.0166				
8.04966				
13.05				
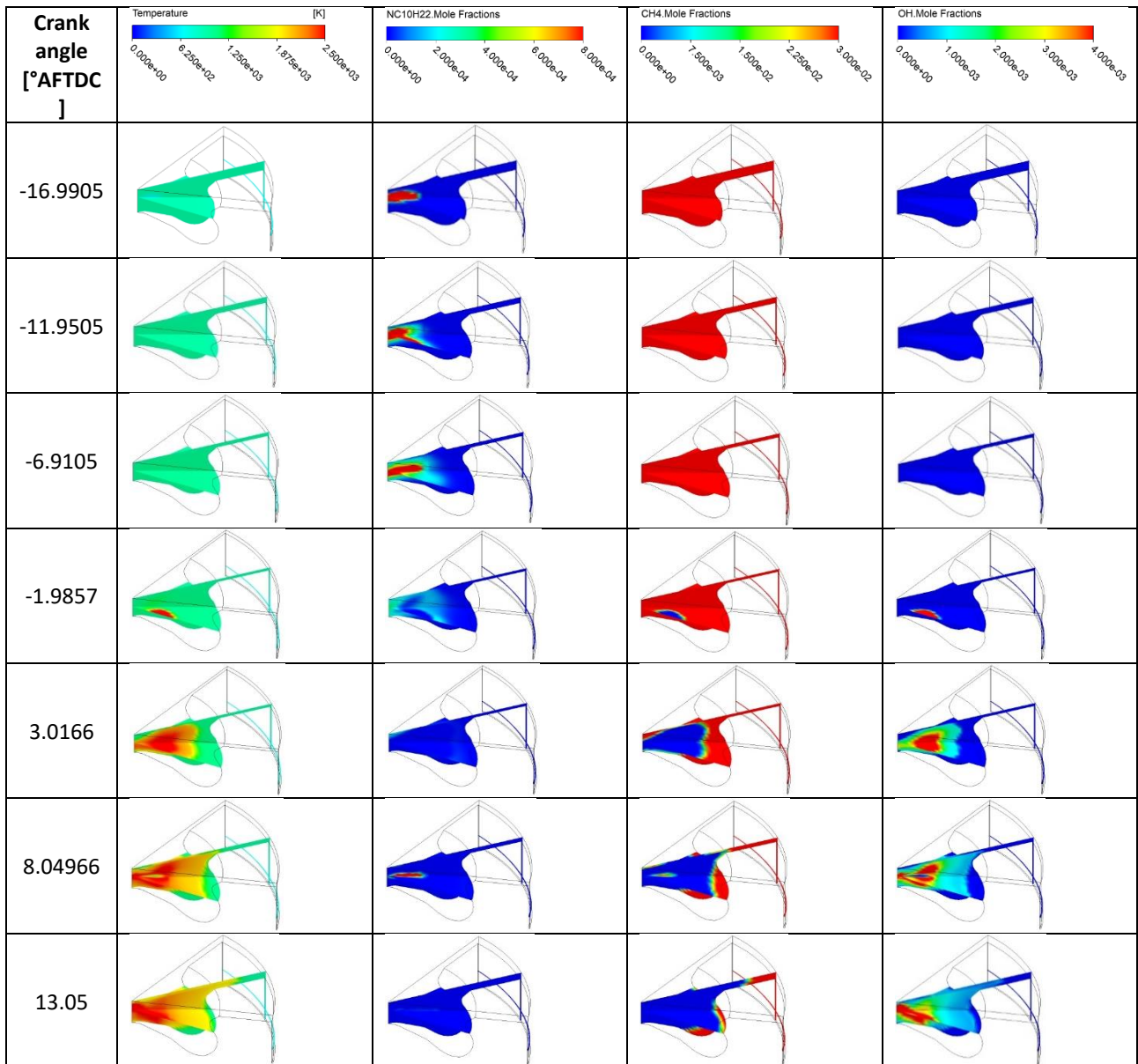
Figure A. 1: Temperature, n-C10H22 mole fraction, CH4 mole fraction and OH mole fraction on two cut planes coincident with the diesel spray axis at different CAD (DF NG-diesel combustion, H2 content: 30 vol%)
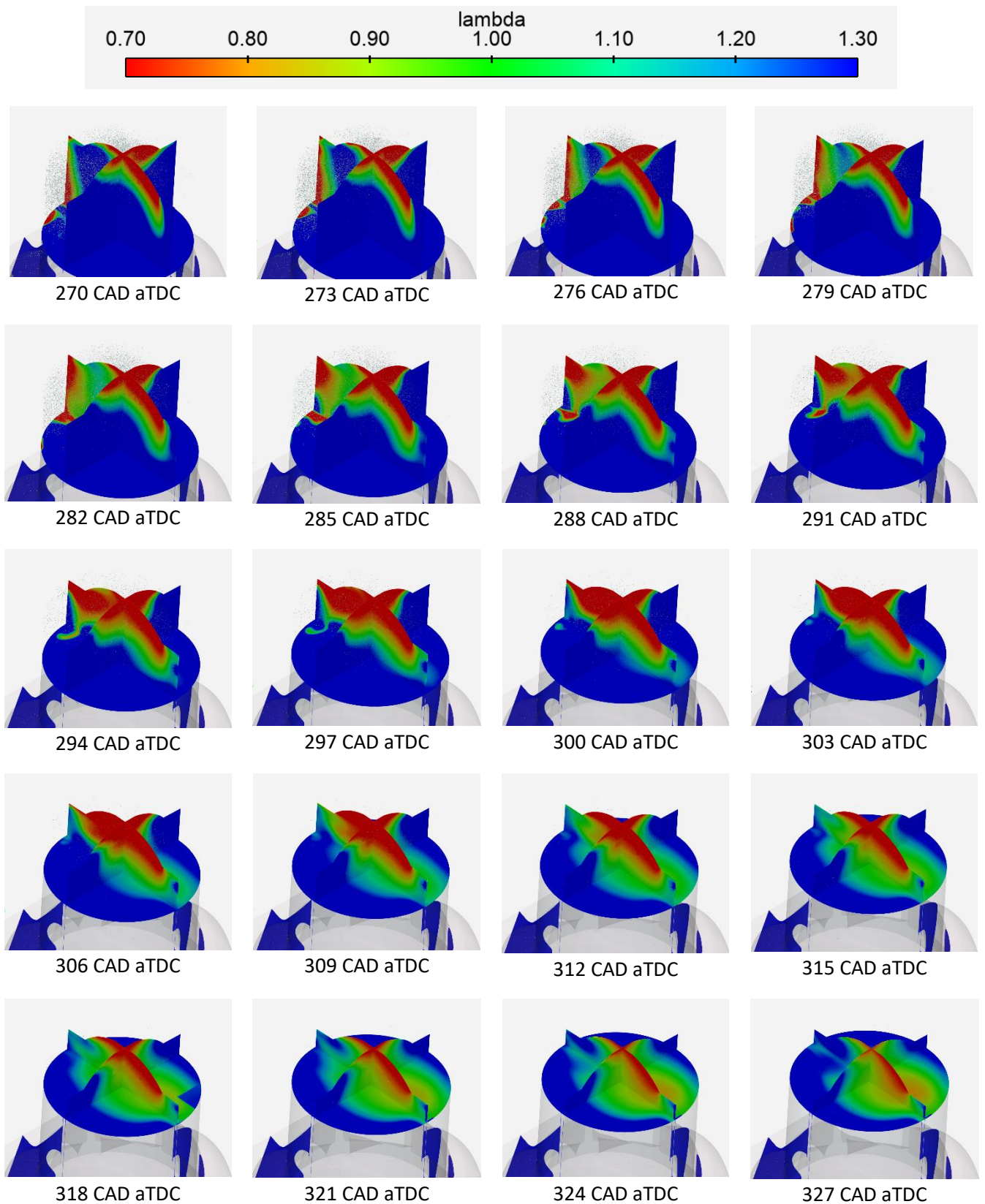
Figure A. 2: Charge mixing process from 270 CAD aTDC to 327 CAD aTDC. Three orthogonal planes in the combustion chamber are displayed together with the lambda value of the mixture. The exhaust port is located at bottom right side of every image. It is possible to see also fuel droplets from 270 to 291 CAD aTDC during their mixing process. At 327 CAD ATDC there is a rich volume under the injector but a very lean area in the combustion chamber outline, reducing the risk of auto-ignition due to end gas.
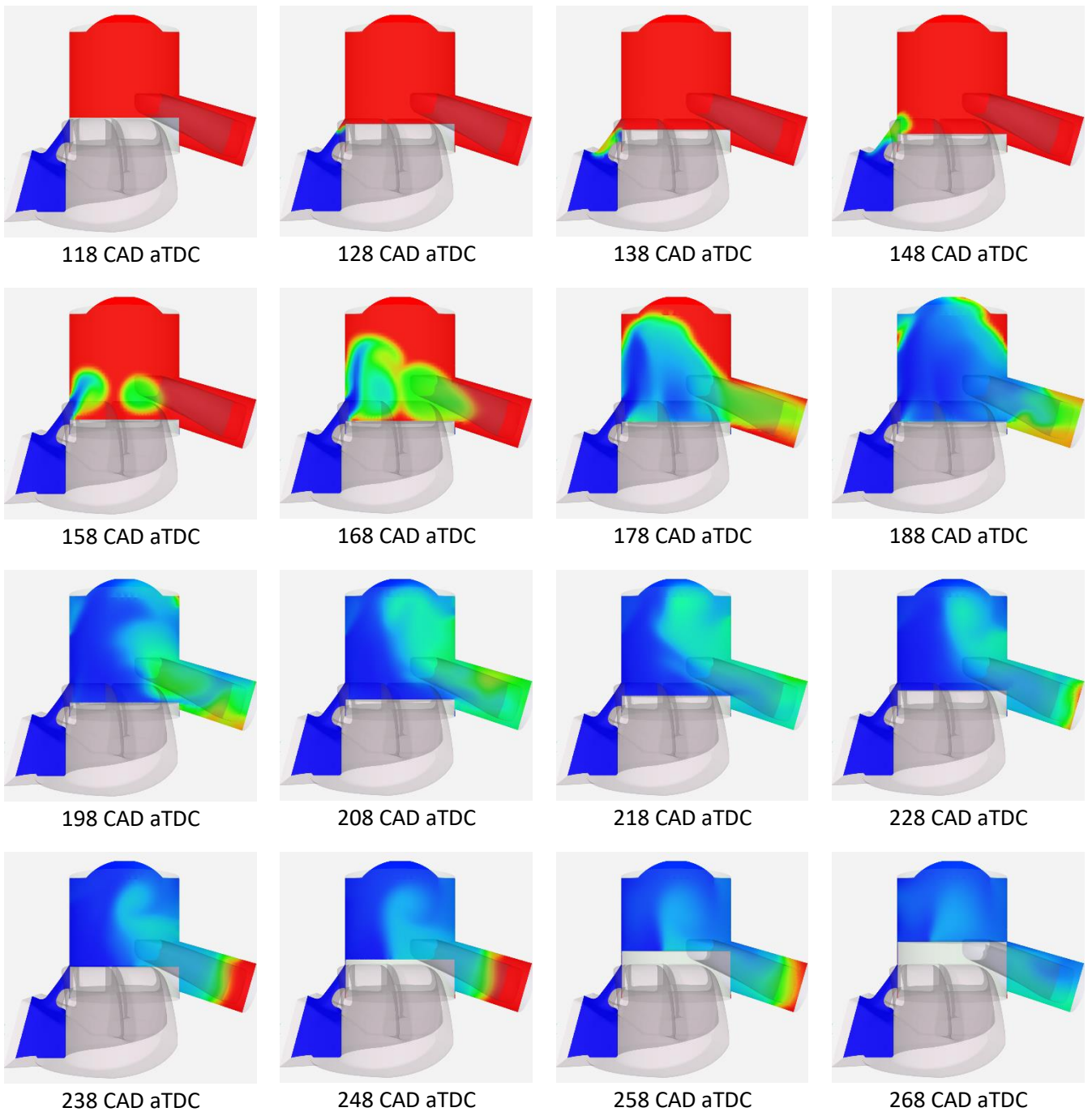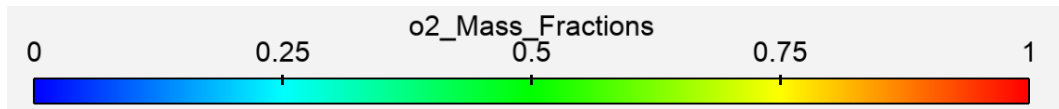
Figure A. 3: Scavenging process between 118 CAD aTDC to 268 CAD aTDC of the geometry called EVO running at 6000 rpm. O2 mass fraction is visualized in order to fully understand the gas exchange process. The loop formed by the fresh charge flux is clearly visible at 248 CAD aTDC. Two waves are evident: the first one from the cylinder to the intake volume at transfer port opening while the second one during the transfer port closing from the exhaust to the cylinder.
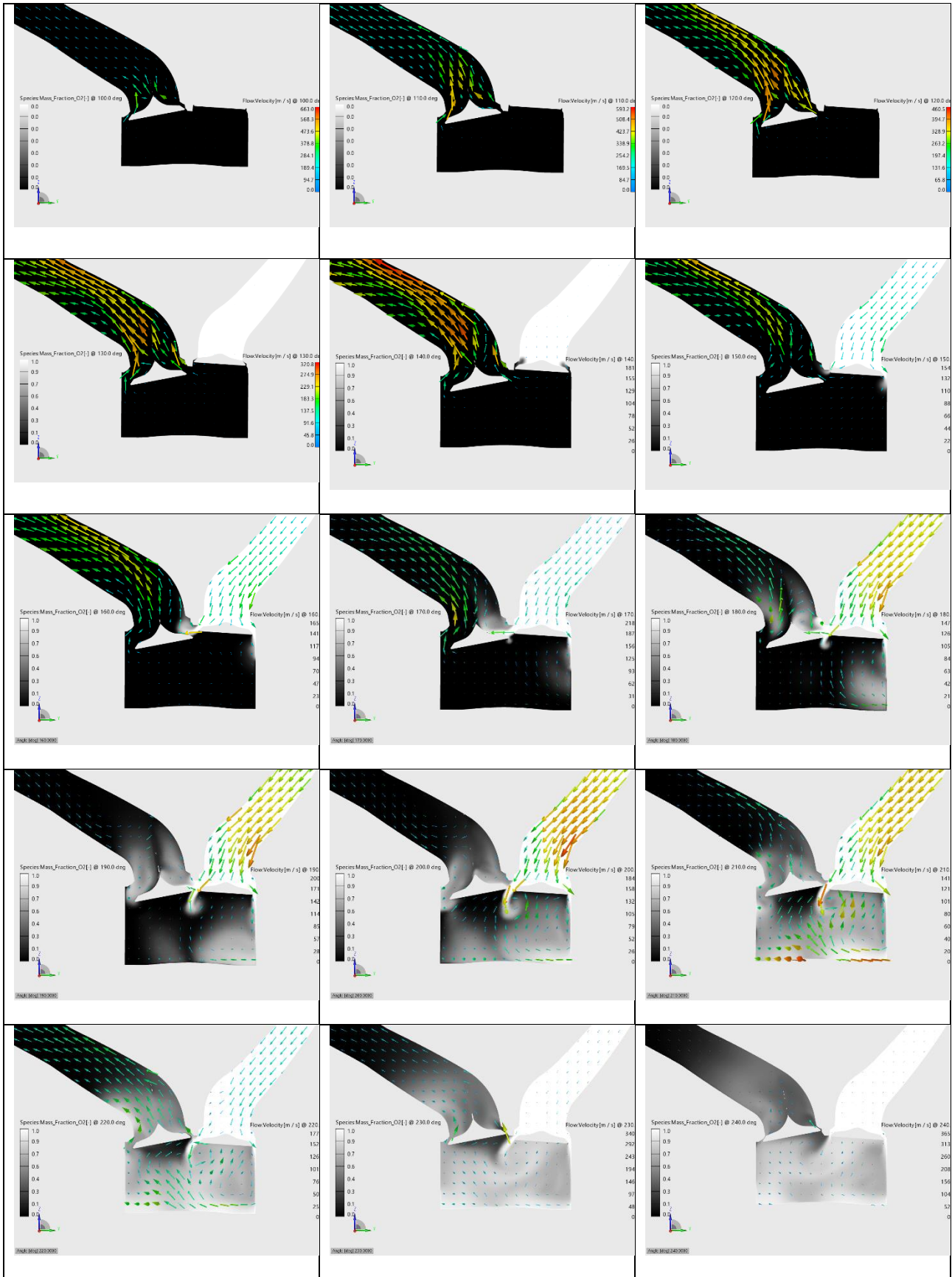
Figure A. 4: velocity field and scavenging process in a cylinder cross-section of the reverse loop best CAD configuration
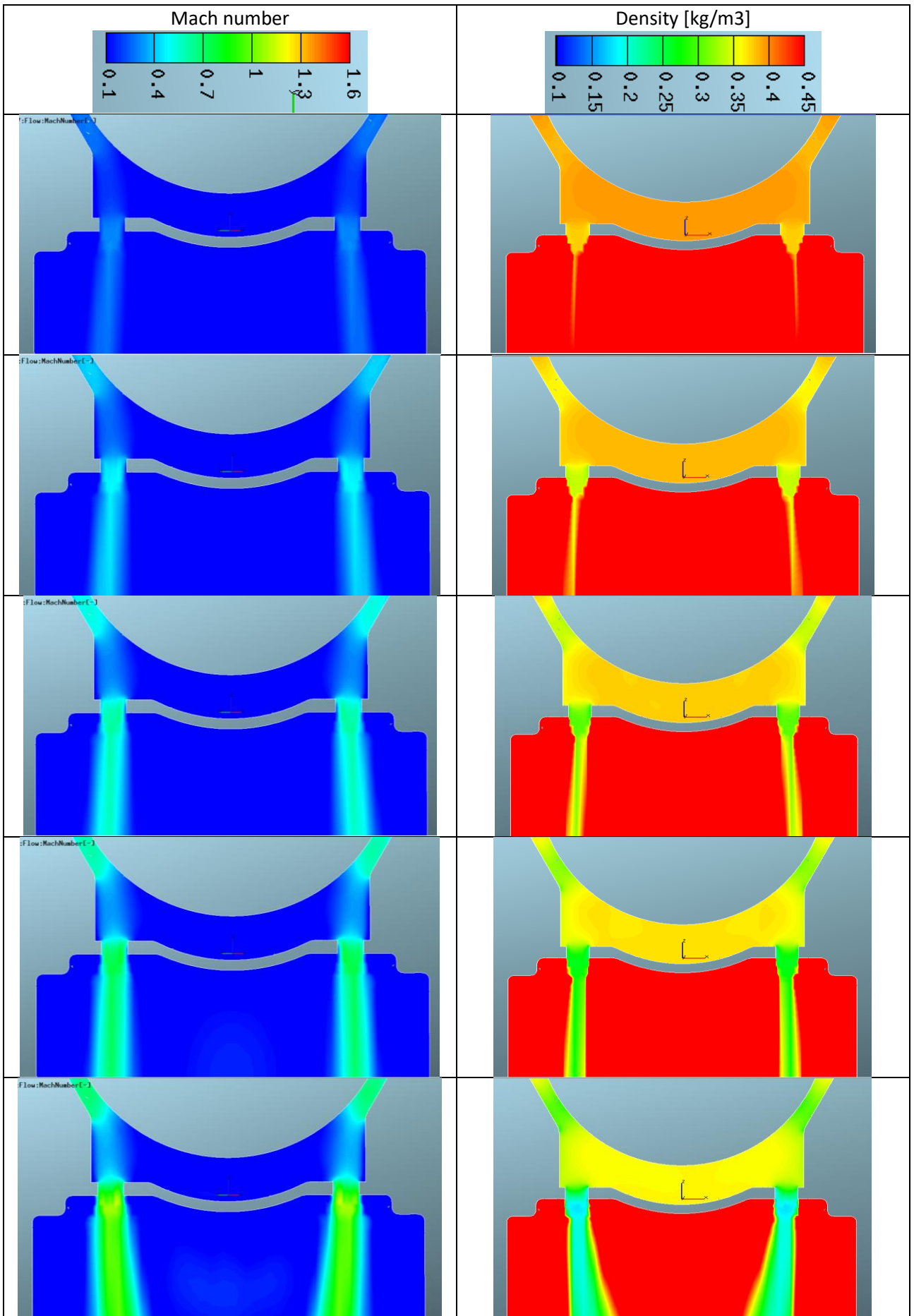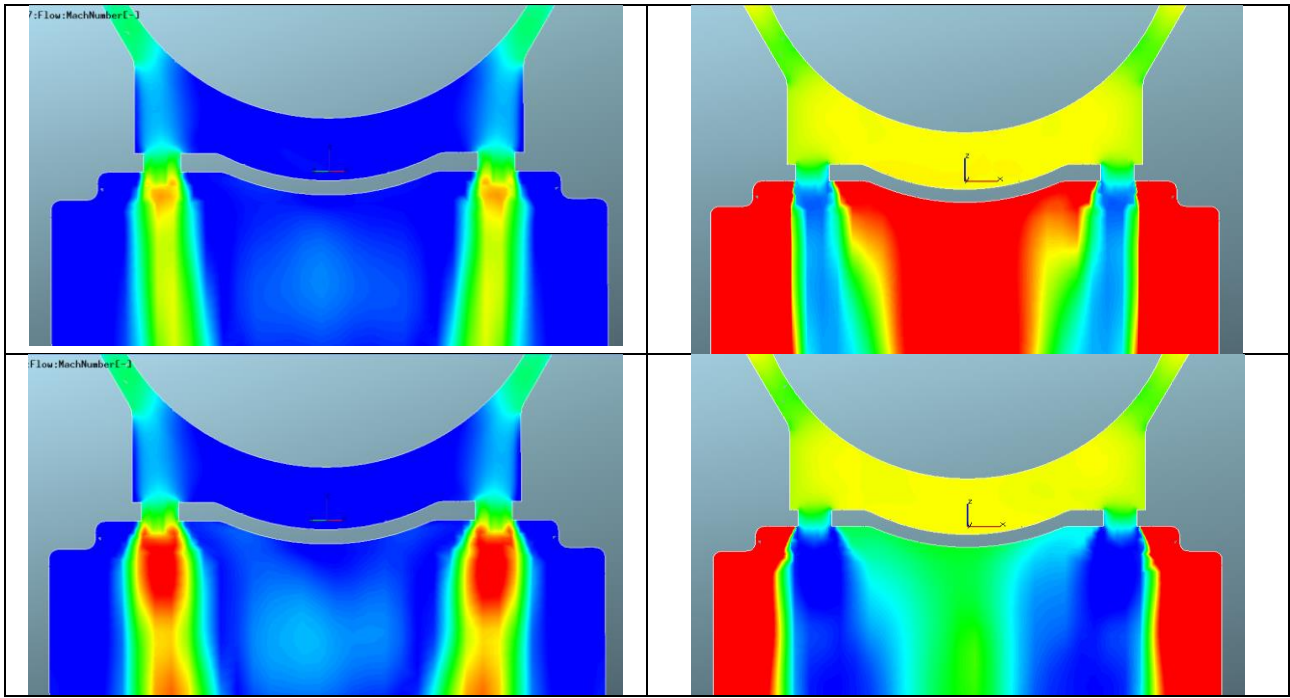
Figure A. 5: Mach number and flow density dependency from the chamber back pressure for the triangle 5bar injection strategy